WA School of Mines: Minerals, Energy and Chemical Engineering

Faculty of Science and Engineering

Fluid-Shale Geochemical Characterization and Its Relation to Geomechanics: Implications for Low Recovery of Flowback Water during Hydraulic Fracturing in Shale Reservoirs

Lingping Zeng

0000-0002-1584-1692

This thesis is presented for the Degree of

Doctor of Philosophy

of

Curtin University

March 2021

Declaration

To the best of my knowledge and belief this thesis contains no material previously published by any other person except where due acknowledgment has been made.

This thesis contains no material which has been accepted for the award of any other degree or diploma in any university.

Signature: ....

Date: .... 21/02/2021 ....

Abstract

Megatons of low salinity water with associated additives are injected into shale gas reservoirs during the hydraulic fracturing process to stimulate formation and improve flow efficiency thus produce hydrocarbon economically. However, industry reports that the flowback water has relatively low recovery factor (only 10 to 50% for most shale reservoirs) with extremely high salinity (sometimes can be up to 280,000 mg/L). The majority of injected hydraulic fracturing fluids are trapped underground, which raises both technical and environmental concerns. Although several mechanisms have been proposed to explain the water loss, most previous works are only descriptive in nature through the laboratory experiments, very few research quantitatively investigate how the water uptake is controlled by fluid-rock interactions associated wettability alteration from geochemical perspective. Moreover, much fewer works have been conducted to explore the impact of geochemistry on shale surface energy and mechanical properties, which determines the *in-situ* micro-fracture propagation and thus the extra water uptake. This study aims to systematically reveal the role of fluid-rock interactions on water uptake during hydraulic fracturing in shales from (1) geochemical properties, including the surface species concentrations, surface potential, wettability alteration and flowback water chemistry such as pH, ion concentration, oxidation-reduction potential and electrical conductivity, and (2) geomechanical properties, including surface energy, energy release rate at the tip of crack, bulk strength, Young's modulus and surface roughness.

To achieve the objectives, we hypothesized that (1) geochemistry controls over wettability alteration in shale gas reservoirs. (2) Fluid-rock interactions play minor role in the contribution of high total dissolved solids of flowback water during hydraulic fracturing. (3) Wettability alteration induced hydrophilicity would decrease the surface energy threshold for fracture initiation and thus facilitate fracture propagation. (4) Edge-charged minerals such as calcite and quartz and basal-charged mineral typically illite play different roles in shale weakening during hydraulic fracturing. (5) Fluid-rock interactions carry predominant weights on shale mechanical behaviours at microscale.

To test these hypotheses, geochemical modelling such as surface complexation, ion exchange, mineral dissolutions and disjoining pressure isotherm were developed to interpret the *in-situ* gas-brine-shale interactions and associated wettability alteration.

Spontaneous imbibition tests with combination of ion selective electrodes were performed to test the shale rocks water uptake ability and monitor fluid chemistry change. Furthermore, the nano-indentation experiments with atomic force microscope and scanning electron microscopy measurements were also carried out to demonstrate the established physicochemical models and to further examine the impact of fluid-rock interactions on shale mechanical properties at microscale.

The results from geochemical simulation show that brines salinity and pH significantly affect shale wettability by controlling surface species concentration of organic matter and inorganic minerals and thus surface potential. At *in-situ* pH, decreasing salinity usually triggers a greater positive surface potential on organic matter surfaces, implying a greater electrical double layer expansion thus hydrophilicity. For inorganic minerals such as calcite and quartz, decreasing salinity drives the surface potential to more negative. The disjoining pressure isotherm indicates that decreasing salinity would shift the disjoining pressure to more positive, providing a repulsion force between oil and shale thus the water-wet. Furthermore, spontaneous imbibition experiments show shales with higher content of calcite and low content of organic matter can uptake more water. Experimental results also show that the salinity increment induced by the fluid-shale interactions is less than 3% of flowback water salinity reported by industry, suggesting a minor impact of fluid-shale interactions on salinity increment.

The simulation results from the newly developed physicochemical model suggests that shale mechanical properties can be affected by the *in-situ* geochemistry. Lowering ionic strength usually decreases the rock surface energy and the energy release rate at the tip of the crack, facilitating micro-cracks propagation. Moreover, water saturation process can weaken shale strength. Decreasing salinity would further decrease the Young's modulus, and calcite-rich shale has a higher reduction than clay-rich shale, suggesting the contribution of mineralogy to shale mechanical properties. Finally, the extent of mineral dissolution for almost all minerals at neutral pH is negligible regardless of the salinity, implying that mineral dissolution plays a minor role in shale weakening. The greater repulsion force between adjacent mineral sublayers or particle surfaces, which is caused by the disjoining pressure change as the result of fluid-rock

interactions, is proposed to account for the shale weakening after low salinity hydraulic fluids injection during hydraulic fracturing.

Acknowledgements

I would like to express my deep and sincere gratitude to my research supervisor, Dr. Quan Xie for giving me the opportunity to conduct research and providing invaluable guidance throughout this work. His dynamism, wisdom, vision, sincerity and motivation have deeply inspired me. He has taught me the methodology to efficiently carry out the high-quality research works and to clearly present the research deliverables. It was a great privilege and honour to work and study under his guidance and supervision. I am extremely grateful for what he has offered me. I would also like to thank him for his friendship, empathy and patience. I could not have imagined having a better advisor and mentor for my PhD study.

I would like also give my thanks to my thesis committee: the Chairperson Prof. Reza Rezaee, Co-supervisor A/Prof Ali Saeedi and A/Prof Md Mofazzal Hossain for their insightful comments, encouragement and administrative supports. My sincere thanks are also expressed to the other staff members and students in the Discipline of Petroleum Engineering, particularly Dr. Mohammad Sarmadivaleh, Dr. Christopher Lagat, Ms. Nichole Sik, Ms. Surudee Bunpitakgate and Dr. Nathan Tarom.

I cannot express enough thanks to Dr. Jeremie Dautriat, Dr. Joel Sarout, Mr. Shane Kager, Mr. David Nguyen, Mr. Ludwig Monmusson and Mr. Neil Sturrock from CSIRO Energy for the supervision and supports of laboratory works in the Geomechanics and Geophysics Laboratory. My sincere thanks are also expressed to Dr. Nathan Reid from CSIRO Minerals for his supervision and supports of laboratory works in the Cooperative Research Centre for Landscope Environments and Mineral Exploration. I would like to extend my appreciations to Prof. Yunhu Lu from China University of Petroleum (Beijing), Dr. Alireza Keshavarz and Mr. Hamed Akhondzadeh from Edith Cowan University, Dr. Yongqiang Chen from The University of Manchester and Prof. Hon-Chung Lau from National University of Singapore for their efforts through the collaborative works.

Last but not least, the deepest appreciation to my parents is beyond words. I am extremely grateful to them for their love, caring and sacrifices for not only the PhD study but also throughout my whole life. I would like to express my thanks to my girlfriend for her love and support. My sincere thanks also go to all the other family members for their supports. Special thanks give to my landlord's family in Perth. I love you all.

Acknowledgement of Country

I acknowledge that Curtin University works across hundreds of traditional lands and custodial groups in Australia, and with First Nations people around the globe. I wish to pay my deepest respects to their ancestors and members of their communities, past, present, and to their emerging leaders. My passion and commitment to work with all Australians and peoples from across the world, including our First Nations peoples are at the core of the work we do, reflective of our institutions' values and commitment to our role as leaders in the Reconciliation space in Australia.

Copyright Statement

I have obtained permission from the copyright owners to use any third-party copyright material reproduced in the thesis (e.g. questionnaires, artwork, unpublished letters), or to use any of my own published work (e.g. journal articles) in which the copyright is held by another party (e.g. publisher, co-author).

Signature: ....

Date: ....21/02/2021..........

Table of Contents

List of Figures

List of Tables

List of Publications

(Publications forming parts of the thesis as standalone chapters)

Chapter 4

Zeng, L., Chen, Y., Hossain, M. M., Saeedi, A., & Xie, Q. (2019). Wettability alteration induced water uptake in shale oil reservoirs: A geochemical interpretation for oil-brine-OM interaction during hydraulic fracturing. *International Journal of Coal Geology, 213*, 103277.

Chapter 5

Zeng, L., Chen, Y., Lu, Y., Lau, H. C., Hossain, M. M., Saeedi, A., & Xie, Q. (2019). Interpreting water uptake by shale with ion exchange, surface complexation, and disjoining pressure. *Energy & Fuels, 33*(9), 8250-8258.

Chapter 6

Zeng, L., Reid, N., Lu, Y., Hossain, M. M., Saeedi, A., & Xie, Q. (2020). Effect of the fluid–shale interaction on salinity: implications for high-salinity flowback water during hydraulic fracturing in shales. *Energy & Fuels, 34*(3), 3031-3040.

Chapter 7

Zeng, L., Iqbal, M. A., Reid, N., Lagat, C., Hossain, M. M., Saeedi, A., & Xie, Q. (2020, November). Effect of Pyrite Oxidation on Flowback Water Properties During Hydraulic *Fracturing in Calcite-Rich Shales. In SPE Asia Pacific Oil & Gas Conference and Exhibition*. Society of Petroleum Engineers.

Chapter 8

Zeng, L., Chen, Y., Lu, Y., Hossain, M. M., Saeedi, A., & Xie, Q. (2020). Role of brine composition on rock surface energy and its implications for subcritical crack growth in calcite. *Journal of Molecular Liquids*, *303*, 112638.

Chapter 9

Zeng, L., Lu, Y., Al Maskari, N. S., Chen, Y., Hossain, M. M., Saeedi, A., ... & Xie, Q. (2020). Interpreting micromechanics of fluid-shale interactions with geochemical modelling and disjoining pressure: Implications for calcite-rich and quartz-rich shales. *Journal of Molecular Liquids, 319*, 114117.

Nomenclature

μ Chemical potential [J]

Ψ Electrostatic potential [V]

z   Ion valency

e   Charge of the ion [C]

k   Boltzmann constant, 1.381×10^{-23} [J/K]

T   Absolute temperature [K]

ρ Ion number density

ε_0 Dielectric constant of vacuum, 8.85×10^{-12} [C/(V m)]

ε Relative permittivity of water, 78.4 [C/(V m)]

ρ_s Surface number density

Ψ_s Surface potential [mV]

E_s Surface electric field

σ Surface charge density [C/m^2]

ΔG_{tot} Total Gibbs energy [J/mol]

ΔG_{ads} Chemical adsorption energy [J/mol]

F   Faraday constant, 96485 [C/mol]

$\Delta H^{\ominus}$ Standard enthalpy change [J/mol]

R   Ideal gas constant, 8.314 [J /(mol·K)]

κ Reciprocal Debye length [m^{-1}]

Z   Interaction constant [J m^{-1}]

D   Thickness of the film on mineral surface [m]

$\rho_{\infty i}$ Number density of ion i at bulk solution

γ Surface tension [J/m^2]

f Surface stress [J/m^2]

c Double layer capacitance [F/m^2]

G_0 Energy release rate at tip of crack

M   Indentation modulus [GPa]

E   Young's modulus [GPa]

ν Poisson's ratio

This page intentionally left blank

1. Introduction

1.1. Importance of Fluid-shale Interactions and Problem Statements

During the transition of world energy structure from traditional fossil fuels to renewable energy (e.g., hydrogen), unconventional resources typically the shale gas reservoirs play an important role because of its abundant deposit and low carbon emission than conventional coal and oil [1-3]. Shales are fine-grained sedimentary rocks which mainly consist of certain amounts of organic matter (kerogen) and inorganic materials such as quartz, calcite, dolomite, pyrite and clay minerals (e.g., kaolinite, smectite and illite, etc.) [4-7]. Given the low porosity and relatively low permeability (ranges from nanodarcy to millidarcy [8-10]), the commercial production of shale gas cannot be achieved without stimulating formation to enhance the reservoir connectivity. Currently, large-scale multi-stage hydraulic fracturing with combination of horizontal drilling are widely applied in the industry to generate new fractures and activate pre-existing natural fractures and thus improve reservoir transmissibility and the ultimate productivity. To stimulate reservoirs, hydraulic fracturing fluids containing low salinity slick water (typically less than 5,000 mg/L), proppants, corrosion inhibitors, anti-erosion additives, friction reducers and other additives are injected underground at high pressure [11-14]. It is estimated that 10,000 to 75,000 m^3 water is needed during the implementation of hydraulic fracturing for a single well per annum [14]. However, industry reports that for some shale reservoirs only less than 10 to 50% of hydraulic fluids can be recovered after fracturing, and the majority of injected hydraulic fluids would remain in reservoirs and cannot be recovered [15-18], which raises the concerns from both technical [19-21] and environmental perspectives [22-24]. Therefore, it is of vital importance to understand the controlling factor(s) behind the low recovery of flowback water during hydraulic fracturing in shales.

To understand the loss of hydraulic fracturing fluids, several mechanisms have been proposed such as gravity induced water segregation and retention at main fractures [19, 20], clay hydration and swelling [21], chemical osmotic effect [22-24], micro-fracture extension [25, 26], and capillary force [26-29] which is associated with shale wettability. While extensive efforts have been paid on laboratory works to investigate the mechanisms behind water uptake by shale, much of researches up to now have just been descriptive in nature, and few works quantitatively characterize the water uptake

capacity and water chemistry change during spontaneous imbibition in shales. Moreover, much fewer researches interpret how the water uptake would be controlled by fluid-rock interactions from geochemical perspective. To better constrain the intrinsic uncertainties of the water uptake during hydraulic fracturing in shale gas reservoirs, more quantitative works need to be made to understand how fluid-shale interactions affect *in-situ* geochemistry such as mineral surface species concentrations, surface potential and surface energy, which would directly determines shale system's wettability thus the water update potential.

Furthermore, fluid-shale interactions can also affect rock mechanical behaviours. To improve hydraulic fracturing performance, the reservoir and rock parameters must be considered, including permeability, porosity, compressibility, Young's modulus, Poisson's ratio, toughness and in-situ stress, etc. [25, 26] Considering that shales contain high salinity formation brine (sometimes can be up to 280,000 mg/L [27]), when the low salinity water-based hydraulic fracturing fluids enter the reservoirs, the mixing process would not only affect the *in-situ* geochemistry, but also influence the aforementioned engineering design factors [28]. Therefore, it is significant to investigate how the fluid-shale interactions would affect rock strength, which controls the fracture conductivity and flow efficiency and thus the productivity.

Laboratories experiments from last two decades have demonstrated that saturating rock with water would weaken or soften the rock and change its mechanical properties such as compressive strength [29-34], Young's modulus [35-38], brittleness index [37, 39], and may also affect the crack growth even under subcritical conditions [40-46]. However, it is still far from clear to understand the role of water in rock weakening. Current proposed mechanisms of fluid-rock interactions induced rock strength reduction include mineral dissolution and degradation [35, 47-53], clay hydration and swelling [30, 31, 54-56], pyrite oxidation and associated secondary carbonate dissolution [57-59], and the change of rock surface energy and disjoining pressure [40, 60-62]. However, most of the research up to now lack of quantitative characterization of fluid-rock interactions induced rock weakening. Moreover, much fewer works have been conducted to interpret how *in-situ* geochemistry can affect micromechanics of shales with different mineralogy. In conclusion, the existing accounts fail to capture the geochemical contributions to shale weakening during the mixing of low salinity

hydraulic fluids and high salinity per-existing formation brine. Therefore, pressing and urgent needs are calling to quantitatively study the effect of fluid-rock interactions on shale mechanical properties and fracture propagation during hydraulic fracturing from the physicochemical perspective.

1.2. Research Objectives

This thesis aims to systematically understand the role of fluid-rock interactions in shale system's (1) geochemical properties, including the surface species concentrations, surface potential, wettability alteration and flowback water chemistry such as pH, ion concentration, oxidation-reduction potential and electrical conductivity, and (2) geomechanical properties, including surface energy, energy release rate at the tip of crack, bulk strength, Young's modulus and surface roughness. To achieve these objectives, five main hypotheses have been proposed and listed as follows.

Hypothesis #1 - Geochemistry controls over wettability alteration in shale reservoirs.

Hypothesis #2 - Fluid-rock interactions play a minor role in the contribution of high total dissolved solids of flowback water during hydraulic fracturing.

Hypothesis #3 - Wettability alteration induced hydrophilicity would decrease the surface energy threshold for fracture initiation and thus facilitate fracture propagation.

Hypothesis #4 - Edge-charged minerals such as calcite and quartz and basal-charged mineral typically illite play different roles in shale weakening during hydraulic fracturing.

Hypothesis #5 - Fluid-rock interactions carry predominant weights on shale mechanical behaviours at microscale.

To test these hypotheses, geochemical modelling such as surface complexation, ion exchange, mineral dissolutions and disjoining pressure isotherm were developed to interpret the *in-situ* gas-brine-shale interactions and associated wettability alteration. Spontaneous imbibition tests with combination of ion selective electrodes were performed to test the shale rocks water uptake capacity and monitor fluid chemistry change. Furthermore, physicochemical models on calcite and quartz surface were

developed to explore how fluid-rock interactions would affect rock surface energy and control micro-fracture propagation. The nano-indentation experiments with atomic force microscope and scanning electron microscopy measurements were also carried out to demonstrate the established physicochemical models and to further examine the impact of fluid-rock interactions on shale mechanical properties at microscale.

1.3. Thesis Structure

The thesis mainly consists of ten chapters. Chapter 1 introduces importance and urgency of conducting research works of fluid-rock interactions on shale geochemical and geomechanical properties, defining the main engineering problems and the five research objectives. In Chapter 2, detailed literature of fluid-shale interactions has been reviewed in terms of four sub-problems: shale wettability, water uptake capacity, flowback water chemistry and geomechanical behaviours. Chapter 3 is the methodology of the entire thesis, which addresses each of aforementioned sub-problems. In Chapters 4 and 5, geochemical modelling with consideration of surface complexation, ion exchange, mineral dissolution and disjoining pressure prediction have been conducted to understand the fluid-rock interactions induced wettability alteration of shale organic matter and inorganic minerals. Then the developed geochemical models were applied to interpret the results of water uptake capacity and fluid chemistry change during spontaneous imbibition process from both mineralogy and pyrite oxidation perspectives, which are detailed in Chapters 6 and 7. In Chapters 8 and 9, a physicochemical model combined with disjoining pressure isotherm were developed to predict the calcite and quartz surface energy change as the result of fluid-rock interactions, and to explain why *in-situ* geochemistry would affect subcritical crack growth and shale micromechanics. To further verify the established theory, in Chapter 10, the nano-indentation experiments combined with atomic force microscope measurements were conducted to test how shales with different mineralogy can be impacted by the water saturation and brine salinity. Chapter 11 summarizes the main conclusions and provide suggestions for the future works.

A brief introduction of each of the main Chapters are listed below.

In Chapter 4, it is hypothesized the hydraulic fracturing fluid (usually slick water with low salinity < 5000 ppm) increases the hydrophilicity of oil-brine-OM system thereby

contributing water uptake in shale. To be more specific, lowering salinity particularly in Ca^{2+} and Mg^{2+} increases oil and organic matter surface potentials and facilitates electrical double layer expansion, and thus triggers the hydrophilicity. To test the hypothesis, geochemical simulation using literature data [27] was conducted to account for the incremental oil recovery from shale oil rocks in low salinity brines. Surface species and surface potential of oil and organic matters were computed as a function of pH for different brine salinity (280,000, 140,000 and 28,000 ppm of formation brine and 20,000 ppm of KCl) at different temperature (25 °C, 60 °C and 100 °C). The disjoining pressure between the interfaces of brine-oil and brine-OM was also examined.

In Chapter 5, geochemical modelling were performed to explain the results of spontaneous imbibition experiments by published work [63]. We calculated the surface potential of organic matter, quartz, and calcite in the presence of 0.1−20 wt % NaCl. Moreover, the *in-situ* pH was predicted using PHREEQC with consideration of ion exchange and mineral dissolution. Disjoining pressure under constant charge conditions was also calculated to explain the fluid-shale interactions induced water uptake.

In Chapter 6, spontaneous imbibition experiments were performed using outcrops from Marcellus, Barnett, and Eagle Ford shales to examine the effect mineralogy on water uptake. The fluid chemistry such as pH, electrical conductivity, and ion concentrations (Cl^-, K^+, Ca^{2+}, NO^{3-}, F^-, Br^-, and NH^+) of the surrounding water were monitored during the spontaneous imbibition process in four consecutive weeks.

In Chapter 7, the impact of *in-situ* pyrite oxidation on fluid-shale interactions, particularly the calcite dissolutions, were investigated to screen and design hydraulic fracturing fluids in shales. Spontaneous imbibition experiments were performed using Marcellus shale samples under three conditions: i) ambient conditions, where the fluid was in equilibrium with atmospheric air throughout the tests, ii) limited O_2 condition, where the fluid was free equilibrated with air in a sealed cylinder and iii) vacuum condition, where the fluid in a sealed cylinder was degassed. The pH and ion concentrations were also measured at the end of experiments.

In Chapter 8, to relate fluid-calcite interaction in particular surface potential to surface energy in light of capacitance theory, a physicochemical model was developed. To test the model, calcite surface chemical species and surface potential were calculated as a function of pH, ion types and fluid salinity using surface complexation modelling. Moreover, the predicted surface energy was compared with Bergsaker et al.'s [64] experimental measurements.

In Chapter 9, it was proposed that fluid-mineral interactions likely generate electrical double layer force between mineral surfaces which would shift the disjoining pressure from strongly negative (mineral-air-mineral) to less negative or even positive (mineral-fluid-mineral) thus triggering Young's modulus reduction. To test the hypothesis, geochemical modellings including minerals dissolution (calcite, dolomite, quartz, pyrite and illite) and surface complexation were performed together with disjoining pressure isotherm using literature experimental data [35], accounting for the Young's modulus reduction induced by fluid-shale interactions.

In Chapter 10, the strength of shale samples (calcite-, quartz- and illite- rich shales) at different saturation conditions (dry, high salinity and low salinity $NaCl + CaCl_2$) were measured using nano-indentation techniques together with scanning electron microscopy (SEM) and atomic force microscopy (AFM). The developed physicochemical model was also applied to explain the shale weakening after water saturation and salinity reduction.

2. Literature Review

2.1. Fluid-rock Interactions Control Wettability Alteration in Shales

Shale wettability is the defined as the ability of a liquid (gas, oil or water) to maintain contact with a surface on both organic matter and inorganic minerals, and it is determined by the balance between the adhesive force (liquid to solid surface) and cohesive force (liquid to liquid) [65, 66]. As one of the main factors dominating the hydrocarbon production, understanding shale wettability is of crucial importance of designing the hydraulic fluids to enhance the ultimate hydrocarbon recovery. To characterize shale wettability, contact angle measurements and spontaneous imbibition experiments are the most commonly used methods [67]. However, due to shale complex compositions and strong heterogeneity, the assessment results from aforementioned two methods are sometimes contrary to each other, which impedes the thorough interpretation of shale wettability. For example, results from contact angle measurement indicate that the air/water/shale systems present strong to mediate hydrophilicity, where the contact angle is typically less than 60° [68-79]. However, the spontaneous imbibition tests show that the intact shale samples can imbibe more oil than water, implying that shales tend to be oil-wet [63, 75, 80]. Therefore, there is a pressing need to gain a deeper understanding of the effect of fluid-rock interactions on shale wettability from geochemical perspective particularly the pH and salinity.

In-situ pH appears to play an important role in shale wettability. For instance, Morsy et al. [71] measured the contact angle on Mancos shale surface in the presence of different pH. Compared to the base case where samples were treated with 30 wt% KCl brine with pH $\sim$ 8, decreasing pH by adding HCl (pH $\sim$ 0.39, 0.4 and 0.57) or increasing by adding NaOH (pH $\sim$ 11.8, 11.9 and 13) can decrease the contact angle. Meanwhile, the oil recovery was also improved up to 53% by low pH solutions. Similar observations were reported by Takahashi and Kovscek [81], who found that the siliceous shales presented highest contact angle (30°) at pH ranging from 4 to 6. Decrease or increase pH from this range would decrease the contact angle. Given that fluid-rock interactions dominate the *in-situ* pH [21, 82-84] through the ion-exchange process particularly in illite-rich shales, it is of vital importance to quantify the pH through geochemical reactions and thus characterize the *in-situ* wettability.

Shale wettability is also affected by the ion concentrations through the surface complexation process [21, 85, 86]. By changing fluid salinity, bonding-capable ions such as Ca^{2+}, Ma^{2+} and SO_4^{2-} can either attach or detach from surface charge sites to affect surface potential and electrical double layer expansion and thus affect the wettability [87-90]. For example, Roshan et al. [91] measured the air/brine contact angle on shale surface in the presence of 0.1 to 1.0 M NaCl, KCl, $CaCl_2$ and $MgCl_2$ solution under both atmospheric and reservoirs conditions, respectively. The results show that decreasing salinity decreases the contact angle for all tested solutions. These findings were confirmed by Pan et al. [92], who reported that decreasing brine salinity would slightly decrease the contact angle in CH_4-brine-shale system. Similar observations were also reported by Mirchi et al. [93], Roshan et al. [94] and Xie et al. [95].

Although aforementioned laboratory experiments typically the contact angle measurements have been extensively conducted to test the shale wettability, most of them are only descriptive in nature. Few works investigate the fundamental nature behind the observations, and much fewer of them quantitatively analyse how the fluid-rock interaction can affect shale surface charge, surface potential and the associated disjoining pressure in air-brine-shale system, which fails to capture the geochemical contributions to the fluid-rock interactions induced wettability alteration. Therefore, in the study, we aim to systematically interpret the basic physics behind shale wettability alteration during hydraulic fracturing through the modelling of surface complexation, ion exchange, mineral dissolution and disjoining pressure isotherm.

2.2. The Hydraulic Fracturing Fluid Loss and Water Uptake in Shale Reservoirs

Since 1919 when the water retention issue in oil/gas reservoirs was first reported by Mills and Wells [96], industry has never stopped making the efforts to understand fluid loss. This is typically true for shale gas reservoirs [20]. Due to the low porosity and ultralow permeability (ranges from nanodarcy to millidarcy), horizontal drilling with combination of multi-stage hydraulic fracturing are widely implemented to stimulate reservoir and enhance flow efficiency. During hydraulic fracturing, approximately 10,000 to 75,000 m^3 water with proppants and other additives are pumped underground for a single well per annum [14]. However, industries report that for some shale

reservoirs only less than 10 to 50% of hydraulic fluids can be recovered after fracturing, and the majority of injected slick water just remain in reservoirs and cannot be recovered [15-18]. For example, Mantell [11] reported that the average recovery of flowback water is only 6% to 10% across shale plays in U.S.. Vidic et al. [15] concluded that the range of flowback water recovery in Marcellus formation is 9% to 53%. Nicot and Scanlon [14, 16] reported that more than 80% of hydraulic fluids disappeared in Eagle Ford shale play. These large amounts of hydraulic fluids with chemical additives may leak into aquifers thus possibly contaminating potable water [17]. Moreover, the trapped fluid in shale reservoirs would significantly decrease the relative permeability of gas phase thus the hydrocarbon production [10, 18]. Therefore, there is a pressing need to decipher the controlling factor(s) of the low recovery of flowback water during hydraulic fracturing in shale reservoirs.

Current proposed mechanisms of water uptake in shales from literature can be summarized into two categories: capillary forces induced imbibition and electrochemical forces induced imbibition. For the capillary forces, wettability has been recognized as the core reason to control the imbibition dynamics by affecting pore-networks' capillary pressure [63, 68, 97, 98]. Besides, given the strong shale heterogeneity and complex system, capillary forces associated water uptake are also affected by internal pore connectivity, which is controlled by the distribution of micro-fractures and fractures [80, 94, 99-103]. For the electrochemical forces, clay hydration [80, 104-106] and osmosis effect [27, 63, 107, 108] are believed as the main factor contributing extra water uptake. Overall, both capillary forces and electrochemical forces affecting the water uptake during hydraulic fracturing are governed by the fluid-rock interactions, including surface complexation (e.g., calcite, dolomite, quartz, kaolinite, etc.), ion exchange (particularly in illite) and mineral dissolution process. Therefore, quantitatively understanding these basic geochemical reactions in shale gas reservoirs is of vital importance.

2.3. The *In-situ* Geochemistry Change during Hydraulic Fracturing in Shale Reservoirs

The salinity increment of flowback water after hydraulic fracturing in shale reservoirs has been widely reported. For instance, Kurtoglu [109] investigated the water chemistry of three samples from Middle Bakken reservoir. The average total dissolved

solids (TDS) is 285,000 mg/L. Hayes [110] reported that the level of TDS of produced water from Marcellus shale play can be as high as 300,000 mg/L with high concentration of Na, Ca, Cl and relatively high level of Ba, Br and Sr. Zolfaghari et al. [111] measured the salinity of flowback water from three formations in Horn River Basin. They reported that the fluid salinity ranges from 40,000 to 70,000 mg/L. Haluszczak et al. [112] found that the salinity of produced water from Marcellus gas formation after three months fracking increased up to 170,000 mg/L, where the salinity of local fracturing fluid is only within 1,000 mg/L. Similar trends of salinity increasing of flowback water are also reported by Blauch et al. [113], Jiang et al. [114] and Zolfaghari et al. [115].

To understand the origin of high salinity flowback water, several potential mechanisms have been proposed, such as i) fluid-fluid interactions which include the mixing of low salinity hydraulic fluids with initial high salinity formation brine [112, 116-118], and diffusion osmosis [29, 115, 119]; ii) fluid-salt interactions, which likely results in a salinity increment due to the dissolution of precipitated salts on fracture surfaces [20, 113, 119]; iii) fluid-shale interactions in particular mineral dissolution [113-115, 117, 119, 120], ion exchange process [21, 115] and surface complexation [85, 88]. For instance, Rowan et al. [121] measured $^{228}Ra/^{226}Ra$ and ^{226}Ra activity of 13 produced water samples from the Marcellus shale play. They concluded that the high saline flowback water was the result of mixing injected slick water with high salinity formation brine. Ghanbari et al. [108] proposed that the salt precipitating on pore and fracture surface may be another source of ions. Zolfaghari et al. [115] performed spontaneous imbibition experiments using shales from Horn River Basin. They attributed the high salinity to the exchangeable ion mobilization from clay minerals. Chermak and Schreiber [120] analysed the trace element data from 9 shale gas reservoirs in the U.S. and proposed that the high saline flowback water was caused by the mineral dissolution. However, Stewart et al. [116] found the opposite, arguing that dissolution of soluble components cannot release enough ions to match the high salinity of produced water, although more quantitative works need to be conducted. Roshan et al. [91] performed contact angle measurements on shale sample with consideration of different ion concentrations and types. Their results imply that the potential determined ions (PDIs) typically the bivalent ions are able to adsorb on the mineral surface through surface complexation and ion exchange, which likely affects

the *in-situ* fluid salinity. Teppen and Miller [122], Ali and Hascakir [47], Abdulsattar et al. [123] pointed out that, for the shales containing a certain amount of clays with high value of cation exchange capacity (CEC) such as smectite and zeolite, cations can be held on the rock negatively charged surfaces of the rock, thereby affecting the flowback water chemistry.

Overall, there is still no consensus on the core mechanism(s) behind the salinity increment in flowback water. To better explore where the salts come from after hydraulic fracturing, more detailed spontaneous imbibition tests are required to conduct to not only measure the brine salinity, but also other geochemical properties such as pH, electrical conductivity and oxidation-reduction potential using shales with different mineralogy and under different oxidizing environment. Besides, more quantitatively works need to be performed to examine the weights of fluid-rock interactions typically the mineral dissolution in the contribution to the salinity increasing in flowback water.

2.4. Impact of Fluid-rock Interactions on Shale Mechanical Behaviours

The issue of rock weakening triggered by fluid saturation has been extensively reported in carbonate [51-53, 62, 124-127] and sandstone [38, 54, 128-132] reservoirs since last two decades. However, more recently this problem has been revisited in the terms of shales during hydraulic fracturing as shale is more sensitive to water because of high content of clay minerals and complex internal pore structures [31, 50, 133, 134]. The injected fluids which usually contain certain types of ions such as Na^+, K^+, and Ca^{2+} can react with shale matrix and affect the mechanical properties, including compressive strength [29-33, 53], Young's modulus [35-38], brittleness index [37, 39], and subcritical crack growth [40-42, 64, 135]. The fluid-rock interactions induced shale mechanical properties alteration would also impact reservoir integrity and thus control the efficiency of oil and gas production [136]. Moreover, for some long-term underground storage projects such as CO_2 [137-139] and H_2 [140-142] storage, the shale caprock stability is crucially important as fluid-rock interactions would also take place. Therefore, understanding how fluid-rock interactions affect shale properties is of fundamental interest for entropic sub-surface activities involving the water-based fluid injection.

Such studies on the impact of fluid-shale interactions on mechanical behaviours have been massively approached mainly through the laboratory-scale geophysics and geomechanical experiments. For example, Al-Bazali et al. [133] measured shale compressive strength under different water saturation in biaxial test. The results show that exposing shale with higher content of water can lead to a larger shale strength decrease, which is mainly caused by the calcite dissolution. Lin and Lai [143] reported that for Barnett shale, increasing 1% of water content would roughly decrease Young's modulus by 6.1 ‰. Liu et al. [144] tested the compressive strength and Young's modulus of shale through water absorption and uniaxial compression experiments. Their results indicate that the rock mechanical properties are also affected by the system wettability: the compressive strength and Young's modulus would decrease when shale is under 'water-absorbing' state. Lyu et al. [18] performed uniaxial compressive strength tests on shale rocks saturated with deionised water, NaCl, KCl and $CaCl_2$ solution. They reported that samples with saline water presented lower swelling tendency and strength reduction compared to the pure water. Adding K^+ can further decrease the strength reduction by preventing clay swelling. Similar observations were also reported by Zhang et al. [145], Hemphill et al. [146], Khodja et al. [147], Akrad et al. [35], Gomez and He [148], Aderbigbe and Lane [149], Pagels et al. [150], Almasoodi et al. [151], Corapcioglu et al. [48], Pedlow and Sharma [56], Yuan et al. [152], Dieterich et al. [49], Yang et al. [153], Ali et al. [47], Du et al.[50], Lyu et al. [30] and Lu et al. [55]. These results from mesoscale tests typically the uniaxial compression test and triaxial compression test, and microscale tests particularly the nano-indentation have clearly demonstrated that fluid-rock interactions would undoubtedly soften shale rocks.

To understand the role of fluid saturation in shale weakening, several mechanisms have been proposed, including the reduction of friction angle and cohesion force [34, 154-157], mineral dissolution and degradation [35, 47-53], clay hydration and swelling [30, 31, 54-56], pyrite oxidation and associated secondary carbonate dissolution [57-59], and the change of rock surface energy and disjoining pressure [40, 60-62]. Although fluid-rock interactions induce shale weakening has been commonly recognized as the comprehensive result of aforementioned mechanical and chemical reactions, most of the researches up to now only report how pure water saturation affect shale mechanical properties. However, the impact of fluid geochemistry on shale

mechanical behaviors lacks of detailed investigation. In fact, the injected hydraulic fracturing fluids and the pre-existing formation brine contain a certain amount of monovalent ions such as Na^+, K^+, and Cl^- and divalent ions such as Ca^{2+}, Mg^{2+}, and SO_4^{2-} etc. The aqueous ions can react with rock by attaching to or detaching from the specific functional groups on mineral surfaces, change shale surface chemistry, lead to electrical double layer expansion and generate repulsion force between two adjacent mineral particles or sublayers, and thus control the rock strength [60, 61]. Therefore, more efforts are required to quantitatively interpret how the fluid-rock interactions can affect shale surface energy and mechanical properties from geochemical perspective. Meanwhile, the effect of mineralogy on shale weakening during hydraulic fracturing has not been fully studied. We already know that for 'soft' clay-rich shales, the injected slick water can soften the rock and intensify the issues of proppants embedment on fracture surfaces [158-160]. In this case, the hydraulic fracture conductivity would dramatically decrease and impede the hydrocarbon flow and ultimate productivity [161]. However, when shales are rich in 'hard' edge-charged minerals such as calcite and quartz, the low salinity fracturing fluids may decrease the minimum surface energy and thus reduce the fracture toughness, which triggers existing micro-fracture propagation [64, 162]. As the result, the hydraulic fracturing performance in calcite- and quartz-rich shales would be more pronounced as the fracture networks in these reservoirs can be better developed, which improves the formation connectivity and thus the production efficiency. Therefore, pressing and urgent needs are calling to develop new physicochemical models and quantitatively study the effect of fluid-rock interactions on surface energy and its relation to the mechanical behaviours of shales with different mineralogy during hydraulic fracturing.

3. Research Framework and Methodology

3.1. Research Framework

In this section, the whole research framework is presented to address the main problem that being framed: how does the fluid-shale interactions contribute to the low recovery of flowback water after hydraulic fracturing in shale reservoirs. To better address this problem, five sub-objectives are further defined: (1) geochemistry controls over wettability alteration in shale reservoirs. (2) Fluid-rock interactions play minor role in the contribution of high total dissolved solids of flowback water during hydraulic fracturing. (3) Wettability alteration induced hydrophilicity would decrease the surface energy threshold for fracture propagation. (4) Edge-charged minerals such as calcite and quartz and basal-charged mineral typically illite play different roles in shale weakening during hydraulic fracturing. (5) Fluid-rock interactions carry predominant weights on shale mechanical behaviours at microscale. To achieve these objectives, various methodologies from geochemical modelling to spontaneous imbibition experiments and nano-indentation tests have been conducted, which are detailed in the following sub-sections. Figure 3-1 illustrates the primary framework of this research.

(Main objective)

Fluid-Shale Geochemical Characterization and Its Relation to Geomechanics: Implications for Low Recovery of Flowback Water during Hydraulic Fracturing in Shale Reservoirs.

(Sub-objectives)   (Nano-scale)   (Meso-scale)

Geochemistry controls over wettability alteration in shale reservoirs.

Comprehensive geochemical modelling with combination of surface complexation, ion exchange, mineral dissolution and disjoining pressure isotherm to interpret fluid-shale interactions induced wettability alteration.

Fluid-rock interactions play minor role in the contribution of high total dissolved solids of flowback water during hydraulic fracturing.

Spontaneous imbibition tests to monitor shale water uptake and flowback water chemistry in terms of (1) mineralogy, and (2) O_{2aqu} content (pyrite oxidation).

Wettability alteration induced hydrophilicity would decrease the surface energy threshold for fracture initiation and thus facilitate fracture propagation.

Extended physicochemical modelling to relate fluid-rock interaction in particular surface potential to surface energy in light of capacitance theory.

Edge-charged minerals such as calcite and quartz and basal-charged mineral typically illite play different roles in shale weakening during hydraulic fracturing.

(Future work)

Nano-indentation tests with combination of Atomic Force Microscope measurement and Scanning Electron Microscopy analysis to interpret the role of fluid-rock interactions on shale micro-mechanical properties.

Triaxial compression tests with combination of micro-seismicity monitoring and micro/medical CT imaging to investigate the effect of fluid-rock interaction on shale meso-mechanical properties.

Fluid-rock interactions carry predominant weights on shale mechanical behaviors at microscale.

Figure 3-1 The primary research framework.

15

3.2. Methodology

3.2.1. Geochemistry controls over wettability alteration in shale reservoirs

While it has been widely accepted that that water uptake in shale reservoirs is a complex function of physicochemical processes in particular capillary forces, much of the studies up to now are just descriptive in nature. Moreover, little attention has been paid to quantitatively characterize the fluid-shale interactions and, thus, the surface forces from geochemical perspective, impeding better managing and predicting flowback water recovery. To understand the basic physics behind the fluid-shale interactions induced wettability alteration, in this subsection, the comprehensive geochemical modellings have been developed in terms of five aspects (Chapters 4 and 5): (1) fundamentals of surface potential in electrolyte solution. (2) Surface complexation modelling on OM, quartz, calcite and dolomite surface. (3) Ion exchange modelling in illite to predict *in-situ* pH. (4) Mineral dissolution-precipitation. (5) Disjoining pressure isotherm.

- Fundamentals of Surface Potential in Electrolyte Solution

To calculate the mineral surface potential in electrolyte solution, it is better to consider a simple case first that two similar charged flat surfaces separated by pure water, which means that the fluid does not contain any dissociated electrolyte ion, and all the ions are from the surfaces (such system is called "counter-ions only system" [163]). Given by the Boltzmann distribution of molecules in the system, the ion chemical potential can be expressed as [164]:

$$\mu = ze\Psi + kTlog\rho \qquad \qquad \text{Eq. 3-1}$$

where μ is the chemical potential, J; Ψ is the electrostatic potential, volt; z is the ion valency; e is the charge of the ion, C; k is the Boltzmann constant, 1.381×10^{-23} J/K; T is the absolute temperature, K; ρ is the ion number density (e.g., 1 M corresponds to the number density of 6.022×10^{26} m^{-3}).

For the case when system equilibrium is reached that the chemical potential is universally the same, the ion number density at the distance x from the mid-plane of two surfaces can be written as [163]:

$$\rho = \rho_0 e^{-ze\Psi/kT}$$ Eq. 3-2

which is also well known as Nernst equation. ρ_0 is the number density at mid-plane.
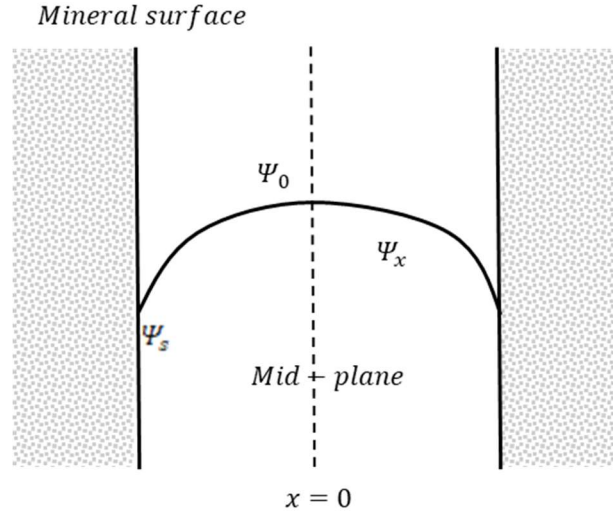
Figure 3-2 Electrostatic potential distribution between two similar surfaces (after Israelachvili [163]).

On the other hand, the Poisson equation shows the distribution of net excess charge density at x [165]:

$$ze\rho = -\varepsilon_0\varepsilon(d^2\Psi/dx^2)$$ Eq. 3-3

where ε_0 is the dielectric constant or permittivity of vacuum, 8.85×10^{-12} C/(V m); ε is the relative permittivity of water, 78.4 C/(V m). Combining the Eq. 3-2 with Eq. 3-3, we have the Poisson-Boltzmann (PB) equation [163, 166]:

$$d^2\Psi/dx^2 = -(ze\rho_0/\varepsilon_0\varepsilon)e^{-ze\Psi/kT}$$ Eq. 3-4

The PB equation relates the ion number density with the potential and also the electric field $E = \dfrac{\partial\Psi}{\partial x}$. Here we define the surface number density, surface potential and the surface electric field as ρ_s, Ψ_s and E_s.

To solve the nonlinear second-order differential Poisson-Boltzmann equation, two boundary conditions are required. The first one is that the electric field must vanish at the mid of two surfaces, namely that $E_0 = -(d\Psi/dx)_0 = 0$ [163]. The second condition follows the basic rule that the total charges on the surfaces are quantatively

equal but with opposite sign to the charges in water between the surfaces. The Gauss Law relates the surface charge density σ (C/m^2) to the electric field E_s at the surface and gives the second boundary condition as:

$$E_s = -\sigma/\varepsilon_0\varepsilon$$ Eq. 3-5

By differentiating Eq. 3-2 and considering Eq. 3-4, we have

$$\frac{d\rho}{dx} = -\left(\frac{ze\rho_0}{kT}\right)e^{-\frac{ze\Psi}{kT}}\left(\frac{d\Psi}{dx}\right) = \frac{\varepsilon_0\varepsilon}{kT}\left(\frac{d\Psi}{dx}\right)\left(\frac{d^2\Psi}{dx^2}\right) = \frac{\varepsilon_0\varepsilon}{2kT}\frac{d}{dx}\left(\frac{d\Psi}{dx}\right)^2$$

Given that,

$$\rho_x - \rho_0 = \int_0^x d\rho = \frac{\varepsilon_0\varepsilon}{2kT}\int_0^x d\left(\frac{d\Psi}{dx}\right)^2 = \frac{\varepsilon_0\varepsilon}{2kT}\left(\frac{d\Psi}{dx}\right)_x^2$$

Therefore,

$$\rho_x = \rho_0 + (\varepsilon_0\varepsilon/2kT)(d\Psi/dx)_x^2$$ Eq. 3-6

At the surface where $x = D/2$ and with consideration of Eq. 3-5, the ion number density is expressed as:

$$\rho_s = \rho_0 + \sigma^2/2\varepsilon_0\varepsilon kT$$ Eq. 3-7

Now we turn to the system with electrolyte ions. For an isolated surface in aqueous solution, we now set $x = 0$ at the surface for the calculation convenience. In this case, the Eq. 3-2 for the ion i at distance from the surface x is written as:

$$\rho_{xi} = \rho_{\infty i}e^{-z_ie\Psi_x/kT}$$ Eq. 3-8

where $\rho_{\infty i}$ is the number density of ion i at bulk solution.

At the surface where $x = 0$, the number density ρ_{0i} (referred to as ρ_{si} for counter-ions only system) becomes:

$$\rho_{0i} = \rho_{\infty i}e^{-z_ie\Psi_0/kT}$$ Eq. 3-9

where Ψ_0 now is the surface potential (referred to as Ψ_s for counter-ions only system). Substituting Eq. 3-8 and 3-9 to Eq. 3-7, we have the ions number density at isolated surface with charge density σ:

$$\sum_i \rho_{0i} = \sum_i \rho_{\infty i} + \sigma^2/2\varepsilon_0\varepsilon kT \qquad \text{Eq. 3-10}$$

Or

$$\sigma^2 = 2\varepsilon_0\varepsilon kT(\sum_i \rho_{0i} - \sum_i \rho_{\infty i}) \qquad \text{Eq. 3-11}$$

Eq. 3-11 gives the correlation between the surface potential and surface charge density.

- Surface complexation modelling on OM, quartz, calcite and dolomite surface

Among all mineral compositions of shale reservoirs such as quartz, calcite, dolomite, illite, etc., organic matter (OM) plays a vital role in shale oil and gas generation and reserves. Although OM usually takes only 5 wt% of shale rocks, it significantly contributes to the shale gas and oil adsorption [167, 168]. For example, Zhang et al. [169] reported that higher total organic content (TOC) always corresponds to higher hydrocarbon adsorption potential. Given that OM has a great capacity of adsorbing shale oil and gas, we assumed that OM likely controls solid surface chemistry thus surface potentials. It is worth noting that in oil and organic matter surface complexation models, the adsorption is a function of both chemical and electrostatic energy [170]:

$$\Delta G_{tot} = \Delta G_{ads} + zF\psi \qquad \text{Eq. 3-12}$$

Where ΔG_{tot} is the total Gibbs energy (J/mol); ΔG_{ads} is chemical adsorption energy (J/mol); z is charge number of the adsorbed species; F is Faraday constant (96485 C/mol); ψ is the surface potential (mV). Increasing the Gibbs energy leads to weaker adsorption [170]. Consequently, co-ions would be expelled by the surface due to the same sign charge, while counter-ion is adsorbed electrostatically on the surface because of the opposite sign charge.

Aforementioned co-ions repulsion and counter-ions attraction can be denoted by the electrical double layer (EDL). The inner layer, or stern layer, consists of ions which have the opposite sign against oil and organic matter surface. The outer layer, or

diffuse layer, is composed of ions with the same sign of stern layer but loosely attracted to the surface so that the ions can move freely to the solution. Combining with stern layer and diffuse layer, the EDL can impose an electrical repulsive force owing to the same charge sign on oil and OM surfaces [27, 171].

To quantify this repulsion, we used surface potential to represent the oil-OM affinity. Surface potential is defined as the electrical potential difference between the inner and outer layer of oil and OM [172]. A strong repulsion appears when oil and OM have large positive sign surface potentials and this will trigger hydrophilicity. When the potentials decline, oil will tend to adsorb on the OM surface because of Van Der Waals force, which is always negative, meaning attractive forces [173]. It is worth noting that the surface potential is a function of brine composition and surface charge, while the latter is governed by the surface complexation constants. For details of the procedure on surface potential calculation please refer to the PHREEQC user manual [170, 174].

To compute the surface potential of oil and OM surfaces, the following two assumptions were made in our surface complexation modelling.

1. The total oil and OM surface carboxylate and nitrogen base group numbers are represented by acid and base number [84].
2. Surface species and chemical reactions on both oil-brine and brine-OM interface are set the same due to their essence of hydrocarbon.

The number of chemical species and surface potential on oil and organic matter surface at different pH and salinity are calculated by PHREEQC version 3 [175]. Table 1 lists the chemical reactions used in our model. The BN/AN of oil is set to be 13:1, which is consistent with Bakken oil measurement [109].

For organic matter or kerogen, BN/AN is set as 10:1 (5:0.5 in sites per square nanometer) and the specific area is 200 m^2/g [176], which was verified by solid-state ^{13}C nuclear magnetic resonance (NMR), X-ray photoelectron spectroscopy (XPS) and sulphur X-ray absorption near edge structure (S-XANES) techniques [177], and Fourier transform infrared (FTIR) spectroscopy [178]. It is worth noting that the ratio of BN/AN used in our geochemical modelling may not represent the absolute value of the ratio for the Bakken Formation, but our results provide a visualization of the effect

of hydraulic fracturing fluids (low salinity water) affects oil-brine-OM interaction thus wettability.

Table 3-1 Chemical reactions on oil and OM surface in surface complexation model.

Number	Reaction [a]	log $K_{25°C}$ [b][c]	log $K_{60°C}$ [d]	log $K_{100°C}$ [d]
1	$-NH^+ \leftrightarrow -N + H^+$	-6.00	-5.50	-4.80
2	$-COOH \leftrightarrow -COO^- + H^+$	-5.00	-5.00	-5.00
3	$-COOH + Ca^{2+} \leftrightarrow -COOCa^+ + H^+$	-3.80	-3.78	-3.76
4	$-COOH + Mg^{2+} \leftrightarrow -COOMg^+ + H^+$	-4.00	-3.98	-3.96

[a] '−' indicates the chemical group which is linked to oil surface. ">" will be used when the chemical group is linked to OM surface [179, 180].

[b] Equilibrium constants at 25°C of reactions 1-3 are obtained from Brady and Krumhansl [179].

[c] log $K_{25°C}$ for reaction 4 is obtained from Brady et at. [89].

[d] log $K_{60°C}$ and $K_{100°C}$ for all the reactions are calculated based on van't Hoff equation [181]:

$$\ln \frac{K_2}{K_1} = \frac{-\Delta H^\ominus}{R} \left(\frac{1}{T_2} - \frac{1}{T_1} \right)$$

where K_1 and K_2 are equilibrium constant, T_1 and T_2 are the absolute temperatures (K), $\Delta H^\ominus$ is the standard enthalpy change (J/mol) and R is the ideal gas constant (8.314 J / mol·K).

The surface complexation reactions in the presence of quartz, calcite and dolomite surface are shown in Table 3-2. In this study, the surface site density for quartz, calcite and dolomite are set to 3.84 [182], 5 [90, 179] and 8 μmol/m^2 [183, 184], and the specific area are set to 0.1, 2.8 and 1.7 m^2/g [21, 85], respectively. For organic matter, the site density for acid number (AN) and base number (BN) are set to 0.5 and 5 μmol/m^2 and the specific area is 200 m^2/g [85]. All the surface complexation reactions are simulated with consideration of aforementioned mineral dissolution-precipitation process. Besides, the effect of CO_2 and O_2 in atmosphere is also incorporated in the

simulation to better mimic the experimental conditions. The aqueous CO_2 can generate extra H^+ that affects the complexation reaction on mineral surface as shown in Table 3-2, while the dissolved O_2 can affect electrolyte salinity, pH and accelerate pyrite oxidation [185]. The log of partial pressure of CO_2 and O_2 is set to -3.4 and -0.67, which represents the corresponding content in the atmosphere [21].

Table 3-2 Surface complexation reactions of organic matter, quartz, calcite and dolomite and corresponding equilibrium constants.

Number	Reaction	$\log K_{298K}$
	Quartz[a]	
5	$>SiOH \leftrightarrow >SiO^- + H^+$	-4.0
6	$>SiOH + Ca^{2+} \leftrightarrow >SiOCa^+ + H^+$	-9.7
7	$>SiOH + CaOH^+ \leftrightarrow >SiOCaOH + H^+$	-4.5
	Calcite[a]	
8	$>CaOH + H^+ \leftrightarrow >CaOH_2^+$	11.9
9	$>CaOH + HCO_3^- \leftrightarrow >CaCO_3^- + H_2O$	5.8
10	$>CaOH_2^+ + SO_4^{2-} \leftrightarrow >CaSO_4^- + H_2O$	2.1
11	$>CO_3H \leftrightarrow >CO_3^- + H^+$	-5.1
12	$>CO_3H + Ca^{2+} \leftrightarrow >CO_3Ca^+ + H^+$	-2.6
	Dolomite[b]	
13	$>MgOH + H^+ \leftrightarrow >MgOH_2^+$	10.6
14	$>MgOH - H^+ \leftrightarrow >MgO^-$	-12.0
15	$>MgOH + CO_3^{2-} + 2 H^+ \leftrightarrow >MgHCO_3 + H_2O$	23.5
16	$>MgOH + CO_3^{2-} + H^+ \leftrightarrow >MgHCO_3^- + H_2O$	15.4
17	$>MgOH + HCO_3^- \leftrightarrow >MgCO_3^- + H_2O$	5.8
18	$>MgOH_2^+ + SO_4^{2-} \leftrightarrow >MgSO_4^- + H_2O$	2.1
19	$>CO_3H \leftrightarrow >CO_3^- + H^+$	-4.8
20	$>CO_3H + Mg^{2+} \leftrightarrow >CO_3Mg^+ + H^+$	-2.0

[a] The reactions for calcite and dolomite are obtained from Brady et al. [89, 182] and Chen et al. [186].

[b] The reactions for $>MgOH$ of dolomite are obtained from Pokrovsky et al. [183, 184]. Reactions for $>CaOH$ of dolomite are set as same as the calcite.

- Ion exchange modelling in illite to predict *in-situ* pH

Ion exchange between basal-charged clays in particular the high-content of illite and brine can significantly affect the local pH [82, 84, 187, 188]. This triggers the variation of the chemical surface species at organic matter and inorganic minerals thus surface potential [88, 189, 190]. We therefore performed ion-exchange modelling to determine the *in-situ* pH which would be used as a reference to obtain surface potentials of brine-shale and to calculate the disjoining pressure. To achieve this, we consider the geochemical reactions and corresponding equilibrium constants which are shown in Table 3. Zolfaghari et al. [115] reported that the cation exchange capacity (CEC) based on the ammonium acetate method is 3.5 cmol/kg. Therefore, the absolute amount of exchangeable sites in our model is set as 0.007 mol (the typical CEC of kaolinite is about 10 cmol/kg, and illite and smectite have CEC ranging from 25 to 100 cmol/kg [191]).

Table 3-3 Input parameters of mineral surface ion-exchange [90, 187].

Number	Reaction	log $K_{25°C}$
1	$>Na + H^+ \leftrightarrow >H + Na^+$	4.6
2	$2>Na + Ca^{2+} \leftrightarrow >Ca + 2Na^+$	0.8
3	$>Na + K^+ \leftrightarrow >K + Na^+$	0.7
4	$2>Na + Mg^{2+} \leftrightarrow >Mg + 2Na^+$	0.6

- Mineral Dissolution-precipitation

The extent of such dissolution-precipitation of any mineral can be represented by the saturation index as shown in Eq. 3-13 [175]:

$$Saturation\ Index(mineral) = log\left(\frac{IAP}{K}\right),$$ Eq. 3-13

where *IAP* is the ion activity product of the solution, and *K* is the equilibrium constant of the dissolution-precipitation reaction for a given mineral. The mineral will tend to dissolve into the solutions when the saturation index is negative, whereas it would precipitate when that value is positive [21, 175]. The corresponding dissolution reactions and equilibrium constants for minerals such as quartz (SiO_2), calcite ($CaCO_3$), dolomite ($CaMg(CO_3)_2$), pyrite (FeS_2) and illite ($K_{0.6}Mg_{0.25}Al_{1.8}Al_{0.5}Si_{3.5}O_{10}(OH)_2$) are listed in Table 4, which are defined by the Lawrence Livermore National Laboratory (LLNL) thermo.com.V8.R6.230 database

[175]. PHREEQC V3.5.0 was used to perform the modelling of mineral dissolution and the surface complexation which will be introduced in the following subsection.

Table 3-4 Dissolution-precipitation reactions and equilibrium constants for quartz, calcite, dolomite, pyrite and illite [21, 175]. Calcite, dolomite and illite tend to dissolve in the solution while quartz and illite tend to precipitate at room temperature.

Number	Reactions	log K_{298K}
1	$SiO_2 = SiO_2$	-3.99
2	$CaCO_3 + H^+ = Ca^{2+} + HCO_3^-$	1.85
3	$CaMg(CO_3)_2 + 2 H^+ = Ca^{2+} + Mg^{2+} + 2 HCO_3^-$	2.51
4	$FeS_2 + H_2O = 0.25 H^+ + 0.25 SO_4^{2-} + Fe^{2+} + 1.75 HS^-$	-24.65
5	$K_{0.6}Mg_{0.25}Al_{1.8}Al_{0.5}Si_{3.5}O_{10}(OH)_2 + 8 H^+ = 0.25 Mg^{2+} + 0.6 K^+ + 2.3 Al^{3+} + 3.5 SiO_2 + 5 H_2O$	9.026

- Disjoining pressure isotherm

The interaction between two surfaces should incorporate both electrostatic force and van der Waals force, which was first proposed by Derjaguin, Landau, Verwey and Overbeek and is well-known as the DLVO theory [192]. Although the more updated DLVO theory furtherly considers the structural force, given its short range interaction (less than 5 nm), it is usually omitted without significant error if compared with the long range electrostatic and van der Waals forces [193]. Therefore, in this work, the disjoining pressure based on DLVO theory is calculated by Eq. 3-14:

$$\Pi_{Total} = \Pi_{van\ der\ Waals} + \Pi_{electrostatic} \qquad \text{Eq. 3-14}$$

where Π_{Total} is the total disjoining pressure between two surfaces, Pa; $\Pi_{van\ der\ Waals}$ is the van der Waals force, Pa; and $\Pi_{electrostatic}$ is the electrostatic force, Pa. It is worth noting that the disjoining pressure between mineral surfaces can represent the rock strength to a certain extent [54]. The negative disjoining pressure corresponds to adhesive force which can attract the adjacent mineral surfaces and therefore indicates a high rock strength, whereas the positive disjoining pressure represents the repulsive force which tends to separate surfaces [54, 163].

At an air condition, only van der Waals force contributes to the disjoining pressure because the electrical double layer (EDL) is assumed to be negligible without fluid-rock interaction [163]. The van der Waals force of two similar flat surfaces (the geometric contact of calcite-calcite and quartz-quartz is assumed to be the plane-plane) is defined by [163, 194]:

$$\Pi_{van\ der\ Waals} = -\frac{H}{6\pi D^3} \qquad \text{Eq. 3-15}$$

Where H is the Hamaker constant, J.

At a fluid condition, fluid-rock interactions affect the rock surface chemical species thus surface charge density. Therefore, electrostatic force needs to be considered together with van der Waals force in the disjoining pressure isotherm calculation. The electrostatic force for two similar flat surfaces with constant surface potential is given by [163, 194]:

$$\Pi_{electrostatic} = \left(\frac{\kappa^2}{2\pi}\right) Z e^{-\kappa D} \qquad \text{Eq. 3-16}$$

where κ is the reciprocal Debye length, m^{-1}; Z is the interaction constant, J m^{-1}; D is the thickness of the film on mineral surface, m. The reciprocal Debye length is expressed by:

$$\kappa = \left(\sum_i \rho_{\infty i} e^2 z_i^2 / \varepsilon_0 \varepsilon k T\right)^{0.5} \qquad \text{Eq. 3-17}$$

where $\rho_{\infty i}$ is the number density of ion i at bulk solution; e is the electronic charge, C; z_i is the valency of ion i, ε_0 is the dielectric constant or permittivity of vacuum, C/(V m); ε is the relative permittivity of water, C/(V m); k is the Boltzmann constant, J/K; T is the absolute temperature, K.

The interaction constant Z in Eq. 3-16 is defined by:

$$Z = 64\pi\varepsilon_0\varepsilon(kT/e)^2 tanh^2(ze\Psi_0/4kT), \qquad \text{Eq. 3-18}$$

where Ψ_0 is the surface potential, mV.

In this simulation, the electronic charge e is set to be 1.602×10^{-19} C, dielectric constant ε_0 is 8.85×10^{-12} C/(V m), the relative permittivity of water ε is 78.4 C/(V m), and the

Boltzmann constant k is 1.381×10^{-23} J/K [163, 193]. The Hamaker constant for calcite and quartz is set to be 10.1×10^{-20} and 8.86×10^{-20} J at vacuum or air condition, and 1.44×10^{-20} and 1.02×10^{-20} J at water condition at temperature of 298K, respectively [195].

3.2.2. Fluid-rock interactions play minor role in the contribution of high total dissolved solids of flowback water during hydraulic fracturing

Hydraulic fracturing has been widely implemented to enhance hydrocarbon production from shale reservoirs. However, one of the main challenges during hydraulic fracturing is to understand what factor(s) triggers high salinity of flowback water, which sometimes can be up to 300,000 mg/L. While several mechanisms have been proposed to explain the controlling factor behind the high salinity of flowback water, there has been little discussion about the effect of fluid-shale interactions (e.g., mineral dissolution and surface complexation) on the high salinity, and far less attention has been paid to quantify the contribution of fluid-shale interactions. We thus conducted spontaneous imbibition experiments to monitor the surrounding water chemistry change and quantify the shale water uptake ability (Chapters 6 and 7).

Spontaneous imbibition experiments under ambient conditions were performed as the following procedures: (i) intact shale plugs from Kocurek Industries INC. were cut into small cylinders with a diameter of 38.20 mm and height of 9.85 mm in the Geomechanics and Geophysics laboratory at Commonwealth Scientific and Industrial Research Organization (CSIRO, Perth); (ii) the samples were heated at 105 °C in an oven for 48 hours to evaporate moisture; (iii) the mass of dried sample was measured before the imbibition test; (iv) samples without naked-eye micro-fractures were immersed in deionised (DI) water with volume of 700 mL (Figure 3-3a); (v) the weight of wet samples was measured every 24 hours in the consecutive four weeks to examine the effect of fluid-shale interactions to the water uptake. It is worth noting that only the samples with no visible micro-fractures were selected for spontaneous imbibition tests, which can avoid any hydration-generated micro-fractures.
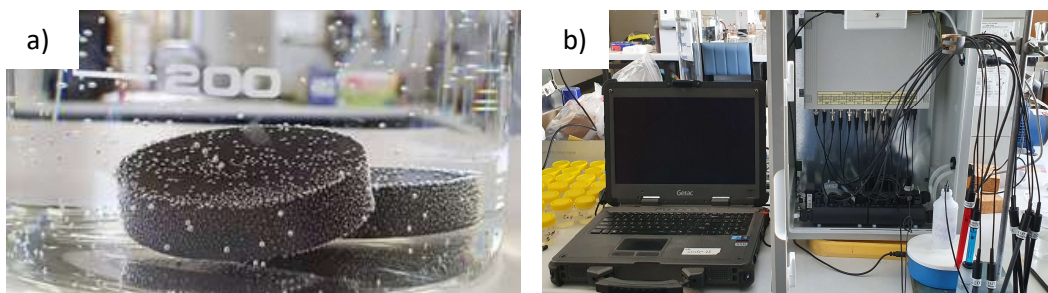
Figure 3-3 a) Spontaneous imbibition experiments using shale samples with DI water. Air bubbles were expelled away from samples' pore network during the imbibition process, and b) ion selective electrodes and monitoring system for water chemistry investigation.

To better characterize the role of fluid-shale interactions in the salinity increment of flowback water, we also continuously monitored the surrounding water chemistry using ion selective electrodes (Figure 3-3b). Fluid properties such as pH, conductivity, and concentration of ions (Cl^-, K^+, Ca^{2+}, NO_3^-, F^-, Br^- and NH^+) were monitored using the corresponding electrodes, which were connected to the ELIT Compact On-Site Fluid Analyser (NICO 2000 LTD.). It is worth noting that the concentration of other ions such as Na^+, Ba^{4+}, SO_4^{2-} were not measured in this study due to the significant interference from other ions. Before water chemistry measurement, all the electrodes were calibrated using standard pH buffers (pH = 10, 7 and 4) and standard solutions (1000, 100, 10 and 1 mg/L for selected ions). The results were recorded when the value of aforementioned parameters had reached a steady state at each measurement.

Meanwhile, to further examine the role of pyrite oxidation in mineral dissolution and the subsequent fluids' salinity increment, spontaneous imbibition experiments were performed under three different conditions: (i) ambient condition, where fluid was eligible to access the O_2 from atmosphere throughout the tests, (ii) limited O_2 condition, where fluid would only react with air in limited space of a sealed cylinder, and (iii) vacuumed condition, where fluid in the sealed cylinder was fully degassed (Figure 3-4). The difference between ambient and limited air conditions is that for ambient condition, aqueous O_2 can be always supplemented by equilibration with atmosphere after consumption, while for limited air condition, no more $O_{2(aq)}$ is available once it is consumed before the sealed system is opened.
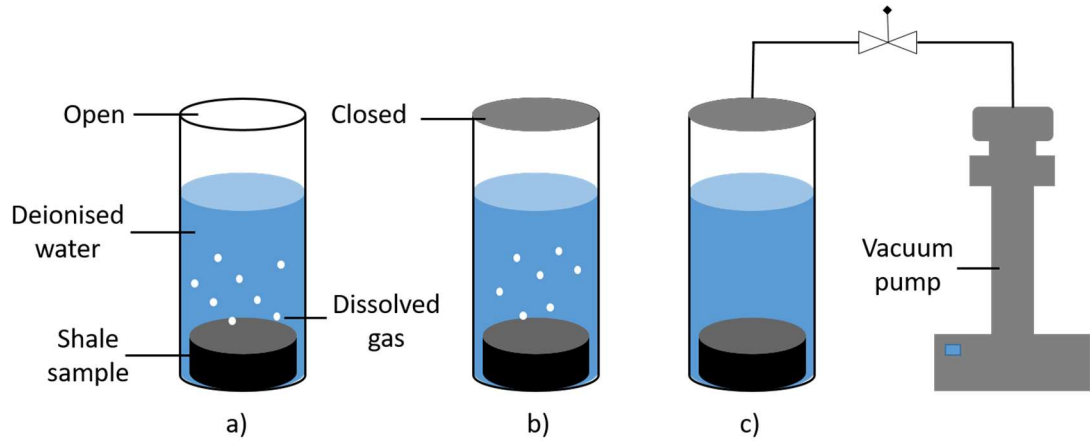
Figure 3-4 Schematic of spontaneous imbibition for a) ambient condition, b) limited O₂ condition and c) vacuum condition.

3.2.3. Wettability alteration induced hydrophilicity would decrease the surface energy threshold for fracture initiation and thus facilitate fracture propagation

The fluid-shale interactions induced wettability alteration can affect the mineral surface charge site density (surface species concentration) and surface potential, and thus the surface energy needed for crack propagation. On the basis of aforementioned geochemical modelling, a new physicochemical model has been developed to relate surface potential to the energy release rate of rupture (Chapter 8). This correlation is built on the basis of capacitance theory and can be presented through Lippmann classical equation. The Lippmann classical equation describes the change of surface tension of interface between the polarizable electrode and ionic solution [196, 197]. It has been widely applied on liquid-solid interface to interpret the wetting phenomenon [198-201]. According to the derivation made by Kramer [199] and Linford [202], for liquid electrodes, if the boundary conditions of derivation like constant temperature T, pressure p, chemical potential μ and strain ε are considered explicitly, we have

$$\left(\frac{\partial \gamma}{\partial E}\right)_{T,p,\mu,\varepsilon} = -q \qquad\qquad \text{Eq. 3-19}$$

where γ, E and q represent surface tension (J/m²), electrode potential (V) and charge (C), respectively. For general solid electrodes, if the strain is potential-dependent, we have the generalized Lippmann equation [201, 203]

$$\frac{d\gamma}{dE} = -q - (\gamma - f)\frac{d\varepsilon}{dE} \qquad\qquad \text{Eq. 3-20}$$

where f is the surface stress (J/m^2). For most of the solid electrodes especially the planar flat electrode, the dε/dE can be neglected [199, 201]. Therefore, the classical Lippmann equation is given by

$$\frac{d\gamma}{dE} = -q \qquad \qquad \text{Eq. 3-21}$$

Van Cappellen et al. [204] developed a constant capacitance model (CCM) using surface complexation on carbonatite-brine interface. The results imply that for carbonated surface such as calcite and dolomite, the double layer capacitance c (F/m^2) can be set as a constant in the presence of homogeneous solution. This is because the change of capacitance by a factor of two would not significantly affect the surface charges [204, 205]. For example, the surface charge difference of $MnCO_3$ is less than 0.005 mmol/m^2 in presence of high ($I = 1$ M) and low ($I = 0.032$ M) ionic strength [204]. The results have also been confirmed by microscopic and spectroscopic investigations [204, 206-211]. Meanwhile, a more complex model named Charge Distribution MUltiSIte Complexation (CD-MUSIC) also uses the constant capacitance [211, 212], although it specifies two capacitances, where c_1 is the capacitance of the interface between solid surface and the centre of the Stern layer, and c_2 corresponds to the capacitance from Stern layer centre to the starting point of the EDL [170, 174]. Therefore, if capacitance at specific ionic strength is considered as potential-independent, Eq. 3-21 can be rearranged as

$$\gamma - \gamma_0 = -\frac{1}{2}c(E - E_0)^2 = -\frac{1}{2}\frac{q^2}{c} \qquad \qquad \text{Eq. 3-22}$$

If we define the uncharged surface potential as Φ, then

$$\Phi = E - E_0 \qquad \qquad \text{Eq. 3-23}$$

Subsequently, the general Lippmann Equation can be stated as

$$\gamma - \gamma_0 = -\frac{1}{2}c\Phi^2 = -\frac{1}{2}\frac{q^2}{c} \qquad \qquad \text{Eq. 3-24}$$

Eq. 3-24 suggests that if the surface potential changes from Φ_1 to Φ_2, the surface tension would change as

$$\gamma_2 - \gamma_1 = -\frac{1}{2}(c_2\Phi_2^2 - c_1\Phi_1^2) \qquad \qquad \text{Eq. 3-25}$$

where γ_1 and γ_2, Φ_1 and Φ_2, c_1 and c_2 are the surface tension or surface energy, surface potential, and capacitance at different ionic strength, respectively. By substituting Eq. 3-19 into Eq. 3-25, we finally get the correlation between surface potential and energy release rate during fracture propagation.

$$G_{02} - G_{01} = -(c_2\Phi_2^2 - c_1\Phi_1^2)$$ Eq. 3-26

where G_{01} and G_{02} are the energy release rate at different ionic strength. Eq. 3-26 indicates that the change of surface energy is affected by both capacitance of EDL and surface potential.

3.2.4. Edge-charged minerals such as calcite and quartz and basal-charged mineral typically illite play different roles in shale weakening during hydraulic fracturing

The minerals in shales can be classified into two categories: edge-charged (Chapter 9) and basal-charged minerals (Chapter 10). For edge-charged minerals such as calcite and quartz, the surface species or functional groups present on the edge or surface of mineral [61, 179]. Therefore, the surface species, such as >CaOH and >CO$_3$H for calcite and >SiOH for quartz, can interact with surrounding brine and release H$^+$ or attach aqueous ions (the extent of reaction depends on the equilibrium constant and ion concentrations). In other words, brine chemistry would control the surface charge, surface potential, surface energy and also affect the disjoining pressure for edge-charged minerals, and thus plays a significant role in rock weakening. However, for basal-charged mineral particularly the illite, the majority of function groups locate in the basal or inner part of the rock [21]. Therefore, illite tends to react with fluid through the ion exchange process rather than surface complexation [90]. Consequently, illite-rich shales becomes less sensitive to saturated brine and has lower indentation modulus reduction than calcite and quartz.

To verify this hypothesis, nano-indentation tests were performed on calcite-, quartz- and illite-rich shales to evaluate the shale strength through the indentation modulus. The indentation modulus were measured using Fischer-Cripps Ultra Micro Indentation System equipped with a Berkovich indenter [213]. In each test, we examined 64 test points on an 8 × 8 network with 50 μm spacing between adjacent points. It is worth noting that the directly acquired data from this measurement is indentation modulus.

The relationship between indentation modulus and Young's modulus is given by [214]:

$$M = \frac{E}{1-\nu^2}$$

Eq. 3-27

Where M is indentation modulus, GPa; E is the Young's modulus, GPa; ν is the Poisson's ratio. Given the constant Poisson's ratio of the sample, we can indirectly quantify the change of Young's modulus of the rocks before and after brine exposure by comparing the change of indentation modulus, and thus characterize the effect of fluid-rock interactions on shale mechanical behavior.

3.2.5. Fluid-rock interactions carry predominant weights on shale mechanical behaviours at microscale

As aforementioned, the fluid-rock interactions can change the shale surface geochemistry particularly the surface potential and the disjoining pressure between adjacent surfaces of mineral particles or sublayers, thus affect the shale strength. By combining the surface complexation simulation and disjoining pressure isotherm, the disjoining pressure on calcite and quartz surface at dry and saturated conditions (with different brine salinity) has been calculated. Futhermore, the attraction/repulsion force inside the rock at nano-scale has been characterized. Meanwhile, this physicochemical simulation accounts for the experimental results from the nano-indentation tests. Detailed surface thermodynamic reactions have been introduced in the subsection 3.2.1.

4. Chapter 4 Wettability Alteration Induced Water Uptake in Shale Oil Reservoirs: A Geochemical Interpretation for Oil-Brine-OM Interaction during Hydraulic Fracturing

4.1. Abstract

Multi-stage hydraulic fracturing is an indispensable approach to enable shale oil available and affordable. However, a low flowback water recovery (usually <30%) after fracturing has been widely observed, triggering both technical and environmental concerns. While it has been confirmed that water uptake is a complex function of physicochemical processes in particular capillary forces, there have been few direct investigations on the characterization of the wettability of oil-brine-shale from the geochemical perspective, especially organic matter (OM), which impedes to better manage and predict flowback water recovery. To gain a deeper understanding of the system wettability, we hypothesized the hydraulic fracturing fluid (usually slick water with low salinity less than 5000 ppm) increases the hydrophilicity of oil-brine-OM system thereby contributing water uptake in shale. To be more specific, lowering salinity particularly in Ca^{2+} and Mg^{2+} increases oil and organic matter surface potentials and facilitates electrical double layer expansion, and thus triggers the hydrophilicity. To test our hypothesis, we conducted a geochemical simulation using literature data to account for the incremental oil recovery from shale oil rocks in low salinity brines. We computed surface species and surface potential of oil and organic matters as a function of pH for different brine salinity (280,000, 140,000 and 28,000 ppm of formation brine and 20,000 ppm of KCl) at different temperature (25 °C, 60 °C and 100 °C). We also examined the disjoining pressure between the interfaces of brine-oil and brine-OM.

Surface complexation modelling results show that the oil-brine-OM system wettability is primarily controlled by *in-situ* salinity and secondarily affected by pH and temperature. At a given pH, decreasing salinity triggers a greater positive surface potential for both oil and OM surfaces, implying a greater electrical double layer expansion thus hydrophilicity. Moreover, the surface potential for oil and OM decreases with increasing pH, which even would be shifted from positive to negative in the presence of low salinity water. Furthermore, the surface potential of both oil and

OM decreases with increasing temperature at *in-situ* pH (from 3.5 to 7). The disjoining pressure results show that saturating sample from high salinity formation brine into the low salinity KCl solution will shift the disjoining pressure from negative values (attraction) to positive values (repulsion). Our results support the hypothesis that lowering salinity increases hydrophilicity of oil-brine-OM, which likely contributes to water uptake by shale. We also argue that geochemical modelling would be an effective tool to characterize the interaction of oil-brine-OM, providing insights into water uptake and enhanced oil recovery in shales.

Keywords: Shale oil, Water uptake, Wettability alteration, Surface complexation modelling, Disjoining pressure.

4.2. Introduction

Multi-stage hydraulic fracturing in shale reservoirs appears to be an indispensable and cost-effectively means to unlock oil and gas resources due to the ultra-low permeability of shale, which ranges from tens of nano-darcy to 1 milli-darcy. To fracture shale reservoirs, low salinity hydraulic fluids (usually < 5000 ppm), namely slick water which consists of water, proppants and other additives, are injected into a horizontal well at high pressures [13]. Therefore, the existing fractures can be reopened together with creating new fractures and thus enhances formation connectivity [215]. Existing literature show that multi-stage hydraulic fracturing with 5 to 7 stages or segments would efficiently increase shale oil production [216, 217].

However, some researchers have reported that the recovery of flowback water after multi-stage hydraulic fracturing is relatively low, which not only leads to the technical issues, but also the environmental concerns. For example, Vidic et al. [17] reported that the recovery of flowback water in Marcellus formation in Pennsylvania ranges from 9 to 53%. Scanlon et al. [15, 16] claimed that up to 90% of hydraulic fluids disappeared in Eagle Ford shale play. Technically, the trapped fluids in fractures uptake into the matrix due to capillary force and hinder shale oil to be recovered. Meanwhile, well productivity would significantly decrease because the relative permeability of hydrocarbon in fractures can be severely reduced during flow back process [19]. Moreover, the fracturing process may propagate micro-fractures from reservoir stratum to upper aquifer. Therefore, the injected fluids, which contain both

introduced chemicals and formation chemicals after reacting with the matrix, likely contaminate potable water and negatively affect animals and plants [22]. Consequently, to relieve the aforementioned concerns, it is of vital importance to understand where and how the fracturing fluids disappear.

Several mechanisms have been proposed to decipher the controlling factor(s) of the low recovery of flowback water during hydraulic fracturing in shale reservoirs, including main fractures' trapping due to gravity segregation and multiphase capillary, micro-fractures expansion and propagation [75, 108], mineral hydration [80] and chemical osmosis [27]. For example, Fakcharoenphol et al. [27] conducted spontaneous imbibition tests using Middle Bakken shale samples in the presence of high salinity formation brine (280,000 ppm) and low salinity KCl solution (20,000 ppm). They argue that the osmotic pressure is the controlling factor to trigger higher oil recovery and high water loss in the presence of low salinity water, implying that osmotic pressure governs the low recovery of slick water. It is widely accepted that water uptake into shale is a complex function of these physicochemical processes, which are associated with capillary forces [20, 74]. Therefore, more delicate works are needed to quantify the contribution of these processes in particular capillary pressure with respect to water uptake.

To understand how capillary pressure is associated with water uptake into shale, Roshan et al. [91] measured contact angle on shale surface in the presence of oil and brines with various ion types and concentrations. The results show that divalent ions (e.g. Ca^{2+} and Mg^{2+}) can increase the contact angle compared to monovalent ions, implying that ion types and concentrations play a vital of role in the interaction of oil-brine-shale system and thus wettability. To gain a deeper understanding of the controlling factor of the wettability alteration, a physical model was proposed [91] in light of the diffuse double layer theory. However, Roshan et al.'s physical model cannot answer the question that how the oil and organic matter surface chemistry control over wettability alteration. Moreover, while geochemical modelling has been widely used to understand the wettability in low salinity water (LSW) injection to improve formation hydrophilicity and oil recovery in conventional reservoirs, namely how the LSW alters the wettability of quartz [182, 218], calcite and dolomite [83, 87, 88, 219, 220], and basal-charged clay minerals (e.g., muscovite, illite, smectite and

chorite) [82, 84, 221, 222], few works have been done to directly investigate the interaction of oil-brine-organic matter (OM) in shale, presenting a substantial impediment to understand the disappearance of the slick water during the hydraulic fracturing in shale reservoirs. It is worth noting that although OM (which represents the kerogen in this work, and is used to differentiate the inorganic materials) usually takes only 5 wt% of shale rocks, organic matters likely play a certain role in shale gas and oil adsorption due to the high specific area (more than 200 m^2/g in general) through tremendous numbers of nanopores. Besides, organic matters with high connectivity [176, 178] also provide pathways to allow hydrocarbon to flow between inorganic and organic materials, which is largely governed by oil-brine-OM system wettability. We thus aimed to reveal how organic matter contributes the shale wettability from geochemical perspective. In particular, we hypothesized that lowering the salinity of slick water increases oil and OM surface potentials thus facilitates electrical double layer expansion, leading to a greater repulsive force between oil/OM surfaces, and thus the hydrophilicity (see Figure 4-1). To test the hypothesis, a geochemical simulation was performed to understand the results of spontaneous imbibition reported by Fakcharoenphol et al. [27]. We first present the effect of brine salinity and pH on the surface chemical species concentrations of organic matter. We then show the effect of brine chemistry and temperature on OM surface potential of the electrical double layer (EDL), which is directly dependent on the distribution of surface species. Finally, we present the disjoining pressure between the interfaces of brine-oil and brine-OM, which directly represents the ability of oil attaching or detaching from OM.
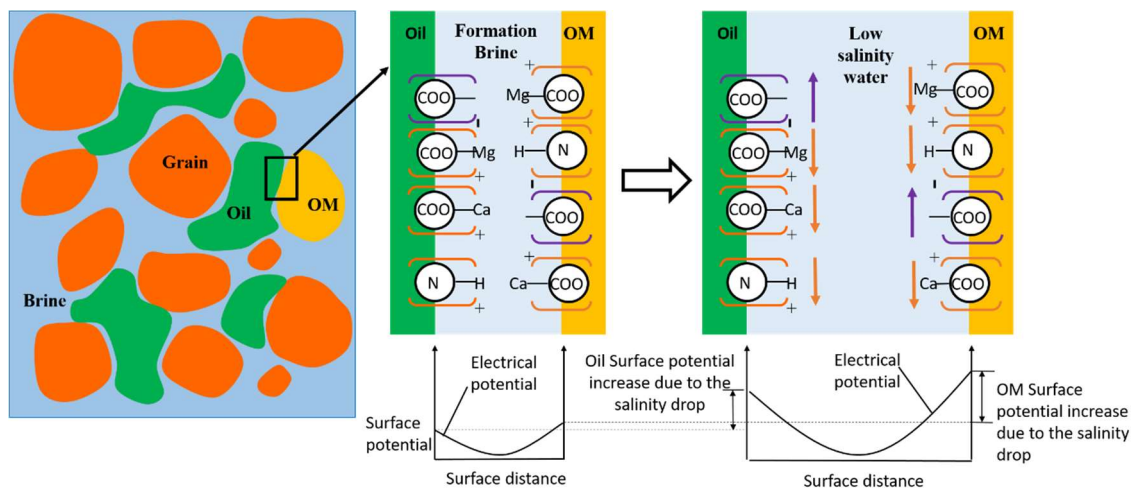
Figure 4-1 Schematic of oil/brine/OM wettability alteration due to brine salinity decreasing after Song et al. [223]. After low salinity water injection, the site density of –COO$^-$ increases, and that of –NH$^+$, –COOCa$^+$ and –COOMg$^+$ decrease due to the salinity drop.

4.3. Experimental Data from Literature

4.3.1. Middle Bakken formation mineralogy

The mineralogy of shale rock is important for the evaluation of fluid-rock system wettability, fracturing fluid loss and oil production. Table 4-1 shows the Middle Bakken formation mineralogy using Quantitative Evaluation of Minerals by Scanning Electron Microscopy (QEMSCAN) [224]. The results indicate that the sample is dominated by quartz, calcite and dolomite, followed by K-feldspar and plagioclase, whereas illite is the major type of clay minerals. It is worth noting that the mineralogy from X-ray diffraction (XRD) data reveal that the sample consists more illite than dolomite [224]. Singh [20] and Li et al. [225] attribute this mineralogy complexity to the high reservoir heterogeneity.

Given that clay minerals are coated with organic matters which likely governs shale surface chemistry [226], total organic carbon (TOC) and the chemical surface species are important to regulate oil-brine-shale wettability. Smith and Bustin [227] investigated the TOC of different Bakken members using Rock-eval and pointed out that the average contents of organic carbon vary from 1 to 10%. Table 4-2 illustrates the average and maximum organic carbon content by weight at lower, middle and upper Bakken member, respectively.

Table 4-1 Mineralogy from QEMSCAN [224].

Minerals Composition (Area %)	Quartz	Calcite	Dolomite	Plagioclase	K-feldspar	Muscovite/Kaolinite	Rutile
	46.47	13.4	15.01	5.12	7.04	0.56	0
	Biotite	Chlorite	Apatite	Illite	Pyrite	Ti-mineral	Others
	0.1	0.31	0.06	10.65	0.45	0.55	0.27

Table 4-2 Organic carbon content in Middle Bakken formation [227].

	Lower member	Middle member	Upper member
Average TOC, %	8	1	10
Maximum TOC, %	20	7	35

4.3.2. Formation water properties

To compute the oil-brine and OM-brine surface potentials, formation brines listed in Table 4-3 were used to compute surface species at oil and OM surfaces. Kurtoglu [109] investigated the Bakken formation water compositions with samples from three different wells (Table 4-3). The results show that sodium and calcium are the main types of cations while chloride dominates the anion. The formation water is of high salinity, averaging 285,000 ppm, whereas the typical salinity of fracturing fluid is less than 5000 ppm [228].

Table 4-3 Bakken formation water composition [109].

Sample #	Field Name	Concentration (ppm)									TDS (ppm)	pH
		Na^+	Ca^{2+}	Mg^{2+}	Fe	Ba^{2+}	Sr^{2+}	Cl^-	SO_4^{2-}	HCO_3^-		
1	Reunion Bay	85,739	19,790	1253	333	23	1458	172,500	223	122	281,448	5.8
2	Murphy Creek	87,277	16,750	1468	30	10	1200	169,500	291	37	276,569	5.6
3	Bailey	84,966	24,980	1753	241	16	1921	182,200	270	110	296,463	5.8

4.3.3. Oil properties

To compute oil surface species and surface potential, we assumed that oil surface chemistry is governed by carboxylic and amino functional groups [84, 88, 229]. The total oil acid number (AN) and base number (BN) are thought to be approximately representative of total carboxylate and amino base groups at oil surface [88]. Kurtoglu et al. [109] report that the acid number of crude oil in Bakken shale is extremely low due to the low percentage of resin and asphaltene (e.g., AN=0.09 mg KOH/g for Bailey field, and 'not detected' for Reunion Bay field oil). The total BN is 1.16 mg KOH/g for Reunion Bay oil.

4.3.4. Spontaneous imbibition experiments [27]

Spontaneous imbibition experiments were conducted by Fakcharoenphol et al. using Middle Bakken shale samples in the presence of high and low salinity brine, respectively. After saturated by oil, the core was immersed in high salinity solution (282,000 ppm) (Table 4-4) for five days then immersed in 20,000 ppm KCl solution for one day. Results show that a negligible number of oil droplets appeared at the surface of the core plug in the presence of high salinity water, whereas measurable oil droplets were observed when the core was placed in the low salinity brine, indicating a shift of wettability towards more water-wet (see Figure 4-2).

Table 4-4 High-salinity experimental water composition [27].

Ion	Concentration(ppm)	Molality(mol/L)
Ca^{2+}	20,507	0.51
Mg^{2+}	1,491	0.06
Na^+	85,994	3.74
Cl^-	174,733	4.92
Total	282,725	9.23
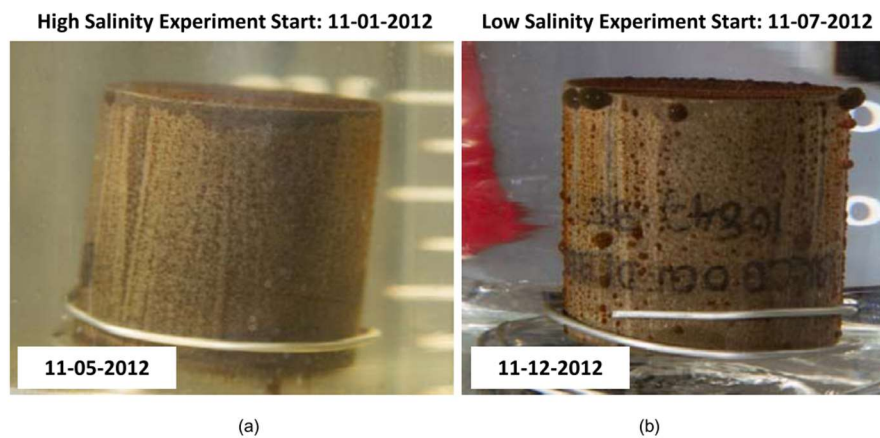
Figure 4-2 Spontaneous imbibition results in the presence of (a) 282,000 ppm high salinity flowback water and (b) 20,000 ppm KCl brine, respectively [27].

4.4. Geochemical Modelling

Among all mineral compositions of shale reservoirs such as quartz, calcite, dolomite, illite, etc., organic matter (OM) plays a vital role in shale oil and gas generation and reserves. Although OM usually takes only 5 wt% of shale rocks, it significantly

contributes to the shale gas and oil adsorption [167, 168]. For example, Zhang et al. [169] reported that higher TOC always corresponds to higher hydrocarbon adsorption potential. Given that OM has a great capacity of adsorbing shale oil and gas, we assumed that OM likely controls solid surface chemistry thus surface potentials. It is worth noting that in oil and organic matter surface complexation models, the adsorption is a function of both chemical and electrostatic energy [170]:

$$\Delta G_{tot} = \Delta G_{ads} + z F \psi \qquad \text{Eq. 4-1}$$

Where ΔG_{tot} is the total Gibbs energy (J/mol); ΔG_{ads} is chemical adsorption energy (J/mol); z is charge number of the adsorbed species; F is Faraday constant (96485 C/mol); ψ is the surface potential (mV). Increasing the Gibbs energy leads to weaker adsorption [170]. Consequently, co-ions would be expelled by the surface due to the same sign charge, while counter-ion is adsorbed electrostatically on the surface because of the opposite sign charge.

Aforementioned co-ions repulsion and counter-ions attraction can be denoted by the electrical double layer (EDL). The inner layer, or stern layer, consists of ions which have the opposite sign against oil and organic matter surface. The outer layer, or diffuse layer, is composed of ions with the same sign of stern layer but loosely attracted to the surface so that the ions can move freely to the solution. Combining with stern layer and diffuse layer, the EDL can impose an electrical repulsive force owing to the same charge sign on oil and OM surfaces [27, 171].

To quantify this repulsion, we used surface potential to represent the oil-OM affinity. Surface potential is defined as the electrical potential difference between the inner and out layer of oil and OM [172]. A strong repulsion appears when oil and OM have large positive sign surface potentials and this will trigger hydrophilicity. When the potentials decline, oil will tend to adsorb on the OM surface because of Van Der Waals force, which is always negative, meaning attractive forces [173]. It is worth noting that the surface potential is a function of brine composition and surface charge, while the latter is governed by the surface complexation constants. Details of the procedure on surface potential calculation please refer to the PHREEQC user manual [170, 174].

To compute the surface potential of oil and OM surfaces, the following two assumptions were made in our surface complexation modelling.

1. The total oil and OM surface carboxylate and nitrogen base group numbers are represented by acid and base number [84].
2. Surface species and chemical reactions on both oil-brine and brine-OM interface are set the same due to their essence of hydrocarbon.

The number of chemical species and surface potential on oil and organic matter surface at different pH and salinity are calculated by PHREEQC version 3 [175]. Table 5 lists the chemical reactions used in our model. The BN/AN of oil is set to be 13:1, which is consistent with Bakken oil measurement [109].

For organic matter or kerogen, BN/AN is set as 10:1 (5:0.5 in sites per square nanometer) and the specific area is 200 m^2/g [176], which was verified by solid-state ^{13}C nuclear magnetic resonance (NMR), X-ray photoelectron spectroscopy (XPS) and sulphur X-ray absorption near edge structure (S-XANES) techniques [177], and Fourier transform infrared (FTIR) spectroscopy [178]. It is worth noting that the ratio of BN/AN used in our geochemical modelling may not represent the absolute value of the ratio for the Bakken Formation, but our results provide a visualization of the effect of hydraulic fracturing fluids (low salinity water) affects oil-brine-OM interaction thus wettability.

Table 4-5 Chemical reactions on oil and OM surface in surface complexation model.

Number	Reaction [a]	log $K_{25°C}$ [b c]	log $K_{60°C}$ [d]	log $K_{100°C}$ [d]
1	$-NH^+ \leftrightarrow -N + H^+$	-6.00	-5.50	-4.80
2	$-COOH \leftrightarrow -COO^- + H^+$	-5.00	-5.00	-5.00
3	$-COOH + Ca^{2+} \leftrightarrow -COOCa^+ + H^+$	-3.80	-3.78	-3.76
4	$-COOH + Mg^{2+} \leftrightarrow -COOMg^+ + H^+$	-4.00	-3.98	-3.96

[a] "−" indicates the chemical group which is linked to oil surface. ">" will be used when the chemical group is linked to OM surface [179, 180].

[b] Equilibrium constants at 25°C of reactions 1-3 are obtained from Brady and Krumhansl [179].

[c] log $K_{25°C}$ for reaction 4 is obtained from Brady et at. [89].

[d] log $K_{60°C}$ and $K_{100°C}$ for all the reactions are calculated based on van't Hoff equation [181]:

$$\ln\frac{K_2}{K_1} = \frac{-\Delta H^\ominus}{R}\left(\frac{1}{T_2} - \frac{1}{T_1}\right)$$

where K_1 and K_2 are equilibrium constant, T_1 and T_2 are the absolute temperatures (K), $\Delta H^\ominus$ is the standard enthalpy change (J/mol) and R is the ideal gas constant (8.314 J / mol·K).

4.5. Results and Discussions

4.5.1. Effect of brine salinity and pH on surface species

Aqueous ion concentration strongly affects the number of chemical groups on oil surfaces (Figure 4-3). To compute surface potentials, we first calculated the surface species at oil and OM surfaces in the presence of formation brine with 280,000 ppm (FB), 2-fold dilution formation brine with 140,000 ppm (2dFB), 10-fold dilution formation brine with 28,000 ppm (10dFB) and low salinity KCl solution with 20,000 (LSW) at 25°C. For example, at pH = 5.75 (the average value of Kurtoglu's [109] measurement for Middle Bakken formation water), the concentration of $-NH^+$ decreases from 4.17 (FB) to 3.87 (2dFB), 2.79 (10dFB) and 2.41 μmol/m^2 (LSW), while the concentration of $-COO^-$ increases from 0.32 (FB) to 0.80 (2dFB), 0.92 (10dFB) and 0.93 μmol/m^2 (LSW) with decreasing brine salinity. The decline of $-NH^+$ concentration indicates a stronger deprotonation of $-NH^+$ at lower salinity, and the decline of $-COO^-$ concentration can be explained by Reactions 2 and 3, showing that decreasing concentration of Ca^{2+} leads to an increase of $-COOH$ (Reaction 2), and further increases $-COO^-$ level (Reaction 3). Similar trends are found on organic matter surface, as shown in Figure 4-4.
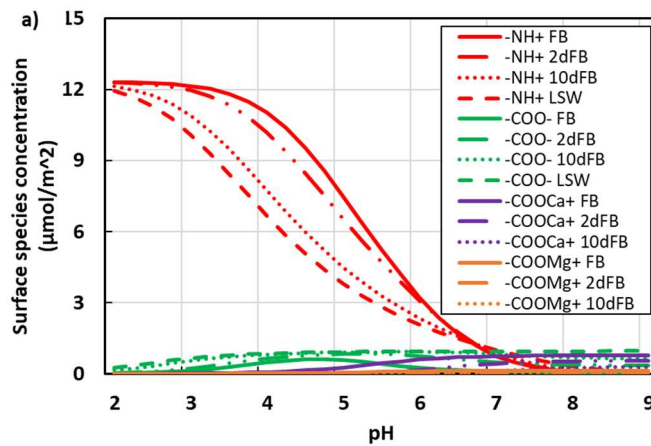
Figure 4-3 a) Oil surface species concentration as a function of pH at 25°C, b) amplifying picture for low surface species concentration area. FB, 2dFB, 10dFB and LSW correspond to high salinity formation brine, 2-fold dilution formation brine, 10-fold dilution formation brine and low salinity KCl solution, respectively.

Figure 4-4 a) OM surface species concentration as a function of pH at 25°C, b) amplifying picture for low surface species concentration area. For oil and OM surface species concentration at 60°C and 100°C, please see Supplemental Materials.

pH also affects surface species at oil and OM surfaces (Figures 4-3 and 4-4) especially for $-NH^+$ which decreasing dramatically with increasing pH. In the presence of formation brine, the concentration of $-NH^+$ decreases from 11.02 to 0.74 $\mu mol/m^2$ with increasing pH from 4 to 7. Unlike $-NH^+$, $-COOCa^+$ increases slowly from 0.07 to 0.74 $\mu mol/m^2$ with increasing pH from 4 to 7, then remaining constant. However, $-COO^-$ slightly increases with increasing pH and reaches the summit of 0.59 $\mu mol/m^2$ at pH $=$ 4.5. Further increasing pH leads to the concentration decrease. A similar trend was observed by Brady et al. [88] and Chen et al. [82]. The minor effect of pH on $-COOMg^+$ concentration variation is observed due to the low level of Mg^{2+} in formation brine. For low salinity water, increasing pH also intensely decreases $-NH^+$ concentration although a slight difference regarding the degree of decrease is shown in Figure 4-3. Analogously, the effect of pH on surface species at OM surfaces follows the same trend as the oil with pH (see Figure 4-4).

4.5.2. Effect of brine salinity and pH on surface potential

Brine salinity significantly affects the surface potential of oil and organic matter (Figure 4-5). For example, for oil surfaces at pH $=$ 5.75, decreasing salinity from 280,000 to 140,000, 28,000 and 20,000 ppm increase the surface potential from 32 to 35, 46 and 51 mV, respectively. Similarly, the same amount of surface potential increase is observed at organic matter surfaces. When pH increases to 9, both oil and OM surface potential in the presence of low salinity water decreases to a negative level (-34 mV, -52 mV), but the absolute sum of oil and OM potential of low salinity is still greater than that of high salinity (6 mV, 10 mV), implying that decreasing brine salinity constantly increases electrical double layer expansion, which in return triggers a greater repulsive force between oil/OM surfaces, thus hydrophilicity. For oil and OM surface potential at 60ºC and 100ºC, please see Supplemental Materials.
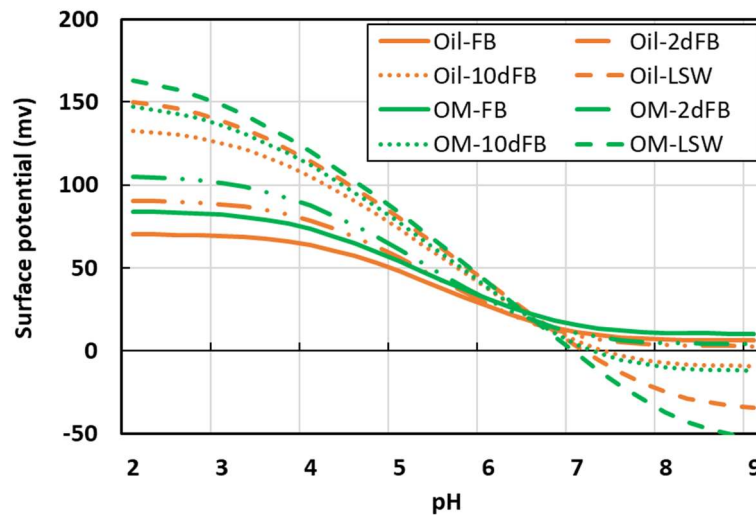
Figure 4-5 Surface potential on oil and organic matter surface as a function of pH at 25°C.

The surface potential of both oil and OM decreases monotonically with increasing pH regardless of salinity (Figure 4-5). For instance, the potential of oil surface drops from 69 to 7 mV with increasing pH from 3 to 8 in the presence of high formation brine. Figure 5 reveals that lowering pH likely leads to desorption of oil from OM surface thus more water wet due to a greater electrical double layer expansion. This result is in agreement with Takahashi and Kovscek's observation [230], which shows that lower pH brine (pH =3) yielded a lower residual oil saturation in shale from spontaneous imbibition experiments.

The surface potential of oil and OM remains positive in the presence of formation brine with increasing pH. Yet, for low salinity water, negative surface potentials are observed as pH > 7 (Figure 4-5). This can be explained by the correlation between –NH^+ and –COO- as a function of pH. Decreasing H^+ level will proceed deprotonation of –NH^+ and –COOH (Reactions 1 and 2), thereby a higher concentration of –COO-than –NH^+ is observed as pH is greater than 7 (Figure 4-3 and Figure 4-4). Note that the absolute value of the oil and OM surface potential sum in presence of LSW is less than that of FB when pH ranges from 6.6 to 7.3. This means that oil tends to desorb from OM at highly acidic and alkali conditions. However, the absolute potential sum at high alkali (pH > 9) is still less than that at highly acid (pH < 5). Therefore, for Middle Bakken oil with high BN/AN, decreasing pH leads to a strong repulsion between oil/OM surfaces thus more water-wet oil/brine/OM system.

4.5.3. Effect of temperature on surface potential

Figure 4-6 Surface potential on the oil surface as a function of pH. Colour blue represents 25ºC and red represents 100ºC, respectively. The effect of temperature on surface potential varies with salinity and pH. Kurtoglu reported that the average reservoir temperature of Middle Bakken is 115ºC [109], which is close to the high temperature used in the simulation. However, at reservoir condition of pH ranging from 3.5 to 7, at a given pH, the surface potential of both oil and OM decreases with increasing temperature (Figures 4-6 and 4-7). Given that the pH of Middle Bakken formation water is approximately equal to 5.7, the simulation results indicate that lowering temperature can increase both oil and OM surface potential, thus increasing electrical double layer expansion and hydrophilicity. This provides a quantitative explanation of hydraulic fracturing loss and disappearance due to the water uptake as a result of capillary forces. Although it is not practical to decrease reservoir temperature, the results of room temperature can directly explain the experimental results, while the results of high temperature show the characterization of surface species and surface potential at reservoir conditions.
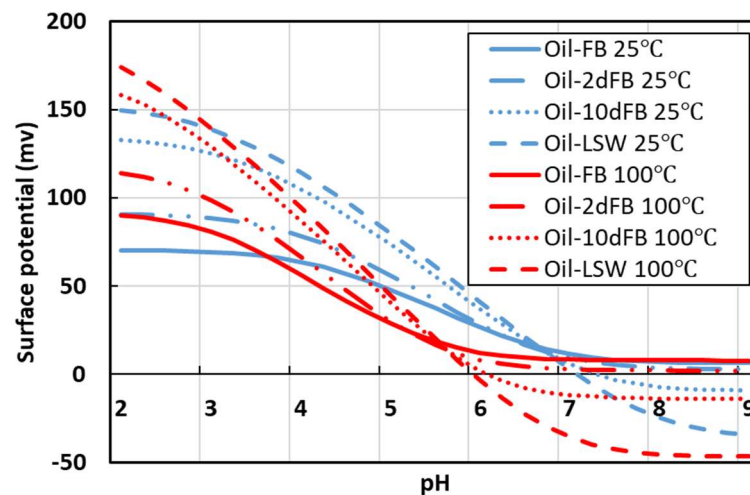
Figure 4-6 Surface potential on oil surface as a function of pH. Colour blue represents 25ºC and red represents 100ºC, respectively.

45

Figure 4-7 Surface potential on OM surface as a function of pH. Colour blue represents 25°C and red represents 100°C, respectively.

4.5.4. Effect of cation type and salinity on disjoining pressure

To investigate the effects of low salinity water on desorption/detachment of oil from OM, we calculate the intermolecular forces, namely total disjoining pressure, between the interfaces of brine-oil and brine-OM. The basic theory of disjoining pressure is introduced first, then we present the calculation results of different salinity for formation brine and low salinity KCl solution.

4.5.4.1. Theory of disjoining pressure

The disjoining pressure is defined as the pressure of the specific intermolecular interaction that indicates the interactive forces between interfaces of water-oil and water-rock [193, 231]. It consists of van der Waals forces, electrical forces and structural forces as follows [232, 233]:

$$\prod_{Total} = \prod_{Van\ der\ Waals} + \prod_{electrical} + \prod_{structural} \qquad \text{Eq. 4-2}$$

where $\prod_{Total}$ is the total disjoining pressure, $\prod_{Van\ der\ Waals}$ is Van der Waals force, $\prod_{electrical}$ is the electrical force and $\prod_{structural}$ is the structural force. Usually, we did not consider the structural forces because comparing to the London-van der Waals and electrical double layer forces, which are long-range interactions, the structural forces are short-range interactions (a distance of less than 5 nm) [163]. Therefore, the total disjoining pressure is calculated as:

$$\Pi_{Total} = \Pi_{electrical} - \frac{H}{6\pi L^3}$$ <div style="text-align: right">Eq. 4-3</div>

where $\frac{H}{6\pi L^3}$ represents the Van der Waals force. The negative sign here indicates that the Van der Waals forces are negative for the oil-brine-rock system. Details of the disjoining pressure and the calculations please refer to Xie et al. [193]. Table 6 shows the input parameters used in this work:

Table 4-6 The input parameters used to calculate total disjoining pressure.

Parameter	Value
Hamaker constant (A)	0.81×10^{-20} J
London wavelength (λ)	100 nm
electron charge (e)	1.60×10^{-19} C
Dielectric permittivity of vacuum (ε_0)	8.854×10^{-12}
Relative permittivity of electrolyte solution (ε_r)	78.4
Valence of a symmetrical electrolyte solution (Z)	1

4.5.4.2. *Results of disjoining pressure*

The results show that ion types and salinity strongly affect the disjoining pressure, as shown in Figure 4-8. For formation brine which comprises of divalent cations like Ca^{2+} and Mg^{2+}, lowing salinity from 280,000 (FB) to 140,000 (2dFB) and 28,000 ppm (10dFB) decreases a negligible disjoining pressure. However, lowing the salinity of monovalent cation (K^+ in this work) from 20,000 (LSW) to 5,000 ppm (4dLSW, which corresponds to the salinity of the typical fracturing fluid [13]) and 2,000 ppm (10dLSW) significantly decreases the negative disjoining pressure, and it even shifts to positive value. Note that positive and negative disjoining pressure represent repulsive and contractive forces, respectively [193]. Therefore, by saturating the sample in low salinity KCl solution, disjoining pressure of the oil-brine-rock interface will act as a repulsive force, which induces the desorption/detachment of oil from OM thus alters the system wettability to strong water wet. Similar results were reported by Xie et al. [193], which shown that divalent cations show negative disjoining pressure while monovalent cations exhibit positive values.
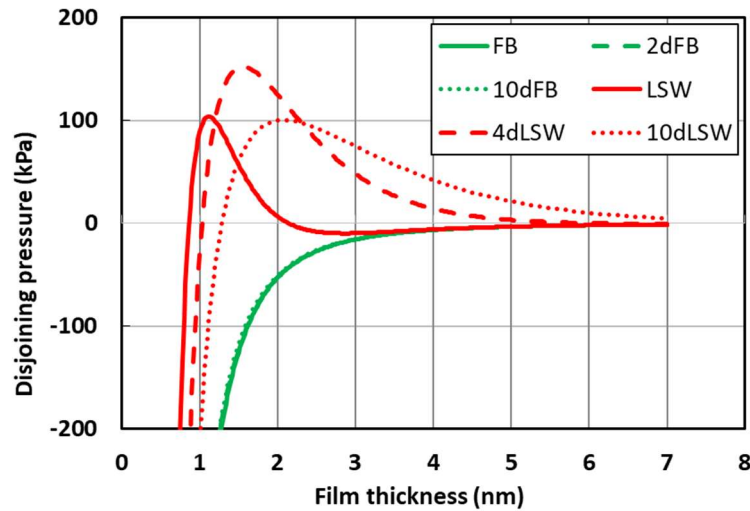
Figure 4-8 Total disjoining pressure as a function of film thickness at constant surface potential. Colour green represents formation brine and red represents low salinity water, respectively.

4.6. Implications and Conclusions

A large amount of hydraulic fracturing fluid loss in shale reservoirs raises industry and public's concerns from both technical and environmental aspects [19, 234]. Capillary pressure associated with wettability appears to be one of the main driving forces to account for water uptake by shale during hydraulic fracturing. While extensive research has been carried out on contact angle and spontaneous imbibition measurements using shale samples in the presence of low salinity water, most studies have only focused on the interaction of oil-water-inorganic minerals such as quartz, calcite and dolomite. Few studies exist to examine the geochemical controls over the system wettability in the presence of oil-brine-organic matter, which likely contributes to the shale gas and oil adsorption although OM usually takes only 5 wt% of shale rocks [167, 168]. In this paper, we aimed to reveal how organic matter controls shale wettability from geochemical perspective. In particular, we hypothesized that the low salinity slick water shifts the oil and OM surface potentials to be more positive, facilitates the expansion of electrical double layer, which leads to a greater repulsive force between oil/OM surfaces, and thus hydrophilicity. To test the hypothesis, the spontaneous imbibition results reported by Fakcharoenphol et al. were used to verify our geochemical simulations. Surface species and surface potential of oil and organic matters were calculated with consideration of pH, brine salinity and temperature. We

also outline the disjoining pressure between the interfaces of brine-oil and brine-OM, which governs the tendency of attachment or detachment of oil from OM surface.

Our surface complexation modelling shows that decreasing salinity triggers a larger positive surface potential at oil-brine and brine-OM surfaces when pH is lower than 6.5. At pH = 5.75 (Middle Bakken formation fluid pH), lowering salinity from 280,000 to 20,000 ppm increases the surface potential of oil surfaces from 32 to 51 mV, and the same amount of surface potential increase was shown at OM surfaces. Moreover, the surface potential of oil and OM decreases with increasing pH, which even can be shifted from positive to negative. Furthermore, the surface potential of both oil and OM decreases with increasing temperature at *in-situ* pH (from 3.5 to 7). The electrostatic isotherm calculations show that low salinity brine shifts the disjoining pressure from negative (in high salinity brine) to positive, favouring desorption/detachment of oil from OM. Taken together, our surface complexation modelling and disjoining pressure calculation account for at least in part the incremental oil recovery contributed by oil-brine-OM wettability alteration in low salinity brine.

In conclusion, we presented insights to understand the geochemical controls over wettability of oil-brine-organic matter, which likely contributes to the water uptake into shale during hydraulic fracturing apart from the osmotic effect. Our results support the hypothesis that lowering salinity increases oil-OM surface repulsion and triggers a more hydrophilicity system, which partly accounts for the low recovery of flowback water during hydraulic fracturing in shale reservoirs. Knowing surface chemical controls over wettability alteration which can be represented by surface complexation modelling, water uptake into shale matrix and enhanced shale oil recovery may be quantified.

4.7. Supplemental Materials
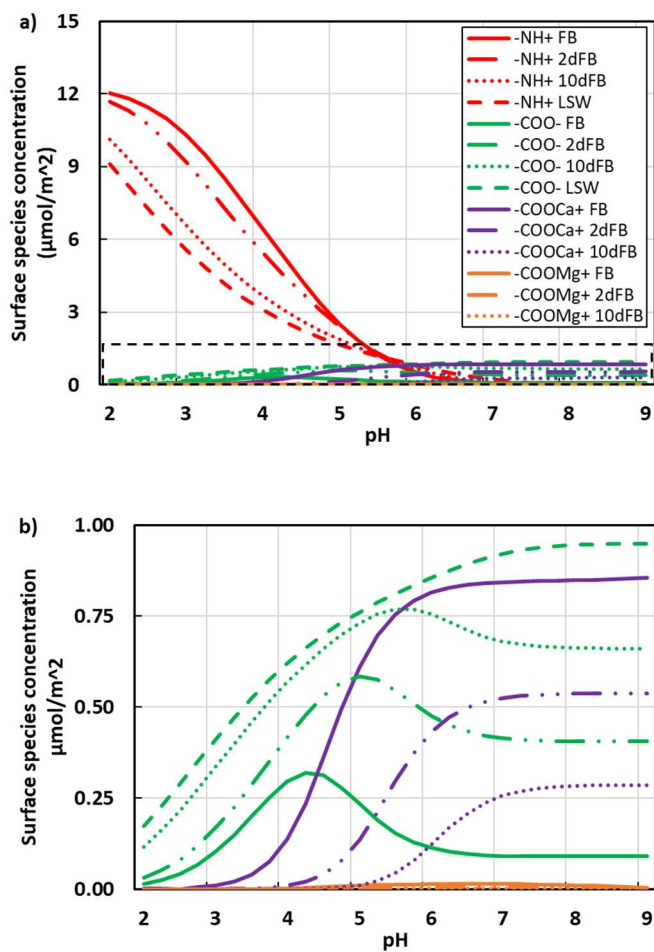
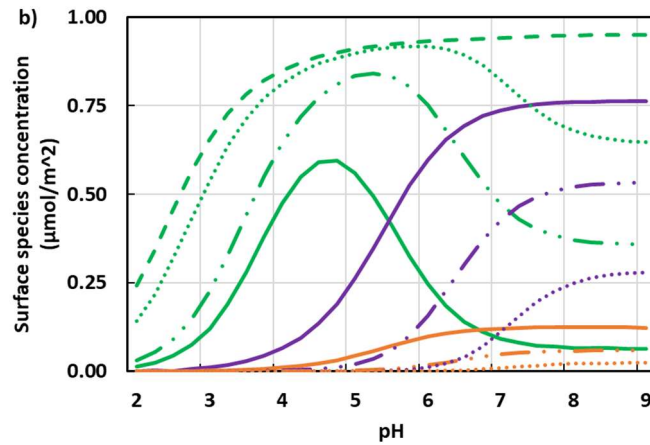
Figure 4-9 a) Oil surface species concentration as a function of pH at 100°C, and b) amplifying picture for low surface species concentration area.
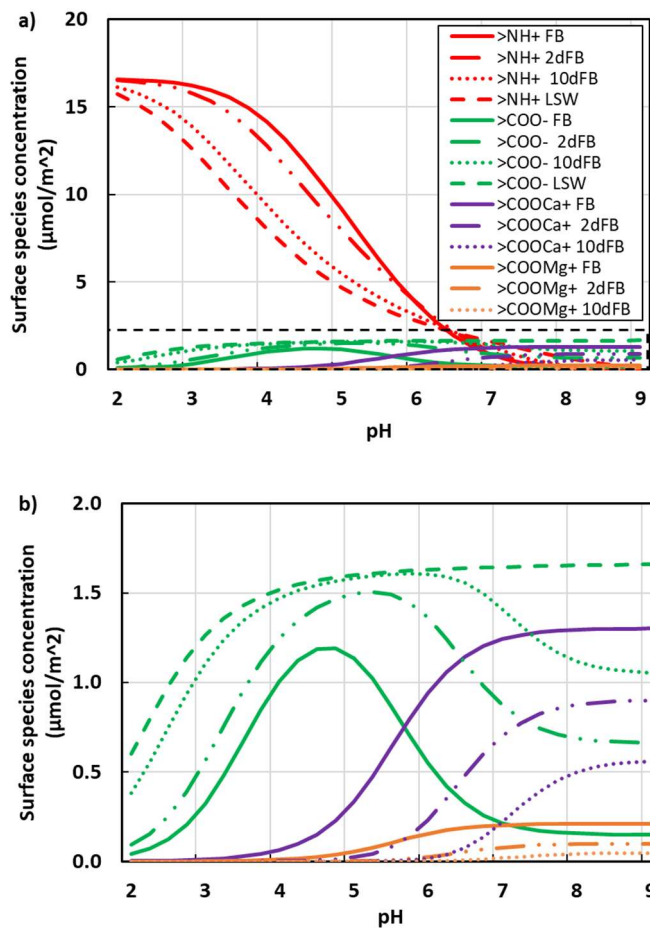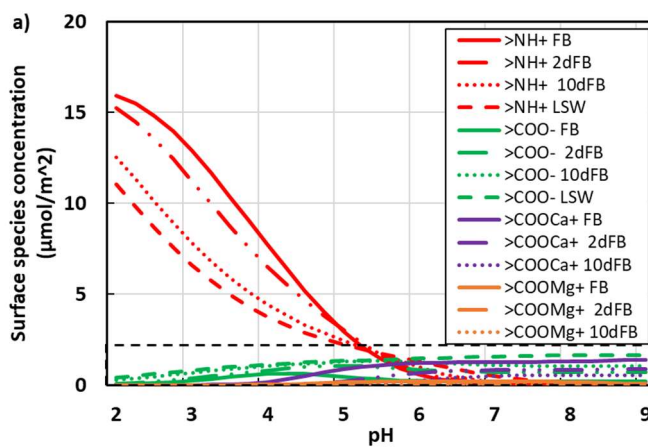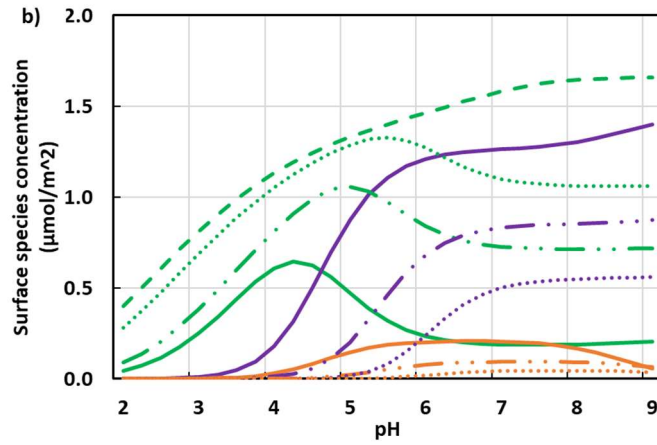
Figure 4-10 a) OM surface species concentration as a function of pH at 100°C, and b) amplifying picture for low surface species concentration area.
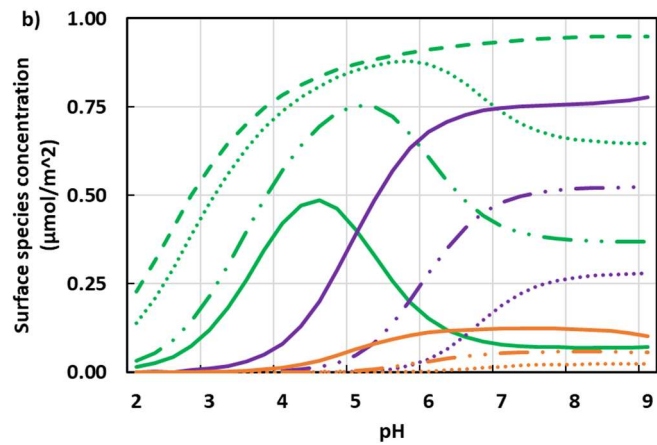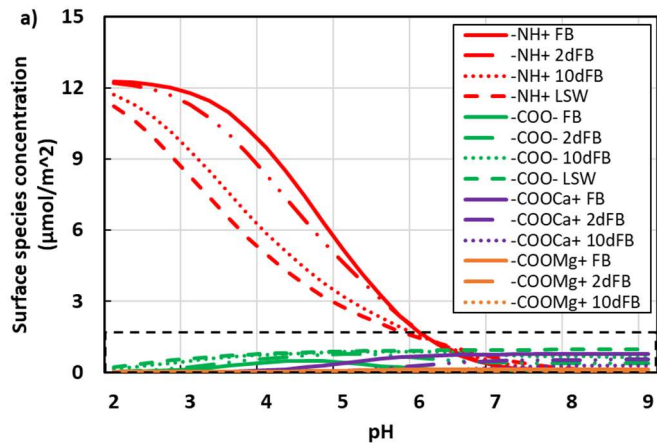
Figure 4-11 a) Oil surface species concentration as a function of pH at 60°C, and b) amplifying picture for low surface species concentration area.
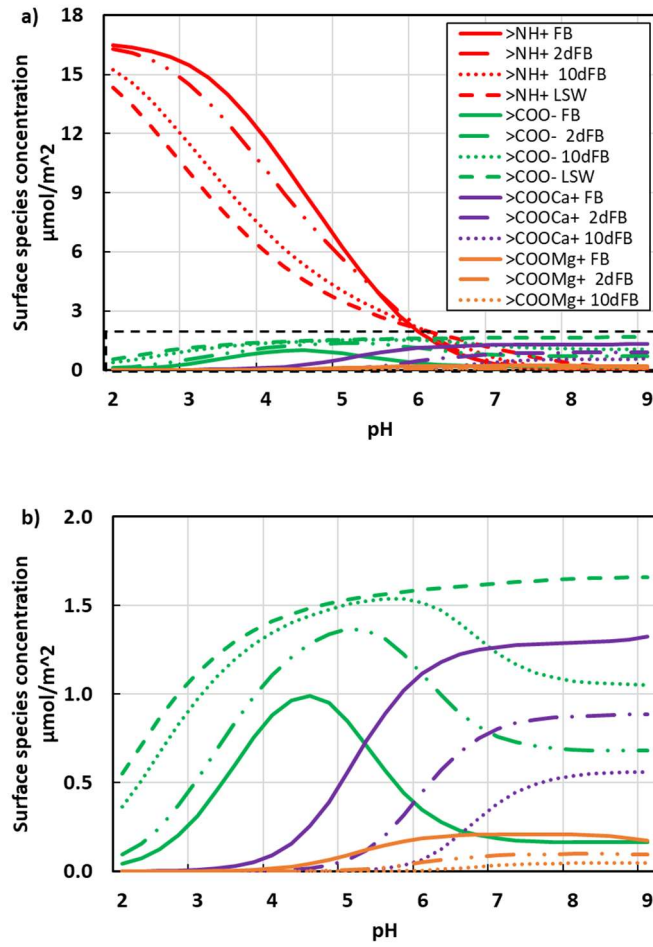
Figure 4-12 a) OM surface species concentration as a function of pH at 60°C, and b) amplifying picture for low surface species concentration area.
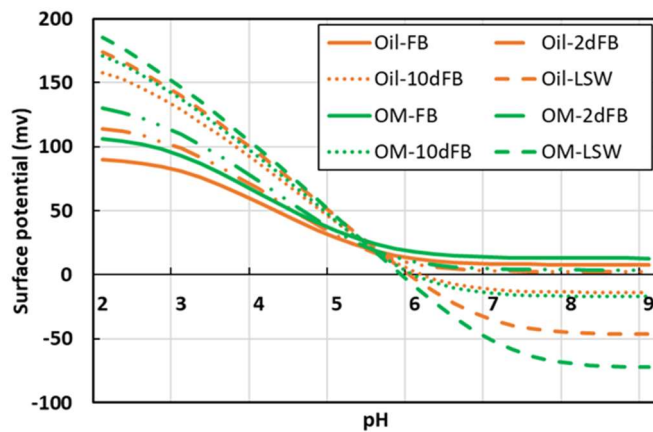
Figure 4-13 Surface potential on oil and organic matter surface as a function of pH at 100°C.
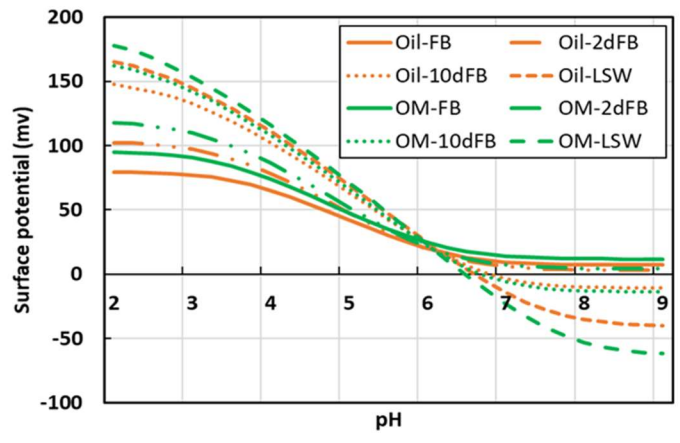
Figure 4-14 Surface potential on oil and organic matter surface as a function of pH at 60ºC.

5. Chapter 5 Interpreting Water Uptake by Shale with Ion Exchange, Surface Complexation, and Disjoining Pressure

5.1. Abstract

Multi-stage hydraulic fracturing is a commonly used method to maximize production from shale gas reservoirs. However, the recovery of flowback water after hydraulic fracturing is relatively low, which gives rise to technical and environmental concerns. Although it is widely accepted that the water uptake is due to physicochemical fluid-shale interactions caused by the capillary forces, much of the researches up to now are just descriptive in nature, and little attention has been paid to quantitatively characterize the fluid-shale interactions thus surface forces from geochemical perspective. In this study, we performed geochemical modelling to explain the results of spontaneous imbibition experiments by published work. We calculated the surface potential of organic matter, quartz and calcite in the presence of 0.1 to 20 wt% NaCl. Moreover, we predicted the local pH using PHREEQC with consideration of ion exchange and mineral dissolution. We also computed the disjoining pressure under constant charge condition.

Results show that a low salinity drives the surface potential of organic matter and inorganic minerals to strongly negative at *in-situ* pH. Disjoining pressure isotherm shows that air-brine-organic matter and air-brine-calcite systems give positive disjoining pressure regardless of salinity, implying a water-wet system. Moreover, a low salinity shifts the disjoining pressure to be more positive for organic matter, suggesting a wettability alteration process. However, the change of disjoining pressure on calcite surface is negligible as a function of salinity. Our results confirm that capillary forces at least partially contribute to the water uptake, and the presence of organic matter likely further facilitates the water uptake due to wettability alteration. This explains in part why a low salinity causes shale expansion and micro-fractures generation in organic-rich reservoirs.

Keywords: Shale gas reservoirs, Water uptake, Wettability, Surface complexation modelling, Disjoining pressure isotherm.

5.2. Introduction

Unconventional shale gas reservoirs have received broad interest within industry due to their large resource volumes [235]. For example, the estimated recoverable shale gas reserves in U.S. is around 17 trillion cubic meters [236], and 15 to 30 trillion cubic meters in China [237]. According to the Energy Information Administration (EIA), shale gas will constitute nearly half of U.S. total natural gas production by 2035 [238]. However, compared to conventional reservoirs such as sandstone, the shale reservoirs have a relative-low permeability (nanodarcy to millidarcy), which prevents the economic development without stimulations [239], such as multi-stage hydraulic fracturing [240, 241] that can create new fractures and activate natural fractures [215]. Hitherto, the application of advanced hydraulic fracturing significantly enhances the gas production efficiency of an individual well and also the stimulated formation volume [242].

To implement multi-stage hydraulic fracturing in shale gas reservoirs, usually 10,000 to 75,000 m^3 water with proppants per well are injected into the formation under high pressures [11]. However, in some cases only less than 30% of the injected water is recovered during production (could be higher depending on the shale plays) [217, 243, 244]. The majority of the injected brine remains in the reservoir, which raises environmental and technical concerns [15, 217]. For example, Boschee [18] reports that the percentage of hydraulic fracturing fluid flowback to ground is approximately 15 to 40% in Bakken shale play. Vidic et al. [17] conclude that the range of flowback water recovery in Marcellus formation is 9 to 53%. Nicot and Scanlon [15, 16] report that over 80% of hydraulic fluid disappeared in Eagle Ford shale play. As a consequence, large amounts of hydraulic fluids with chemical additives may leak into the aquifer and possibly contaminate the potable water [22]. Moreover, the remaining fracturing fluid in shale reservoirs would significantly decrease the relative permeability of gas phase thus gas production rate [19, 20]. Therefore, there is a pressing need to understand the controlling factors of the low water recovery by flowback.

To understand hydraulic fracturing fluids disappearance, a number of mechanisms have been proposed such as gravity induced water segregation and retention at main fractures [72, 245], clay hydration [80], chemical osmotic effect [27, 63, 91], micro-

fracture extension [75, 162], and capillary force [74, 75, 246, 247] which is associated shale wettability. While extensive laboratory works have been done to reveal the mechanisms behind water uptake by shale, much of researches up to now have been just descriptive in nature. Consequently, more quantitative study needs to be made to understand how fluid-shale interactions affect mineral surface species and surface energy, which determines air-fluid-shale wettability and capillary forces.

To understand the wettability in shales, many contact angle measurements have been conducted to characterize the wettability of shale in the presence of oil and various brines. For example, Lan et al., [76] measured the contact angle of oil and water in the presence of air on shale surface using samples from Horn River Basin. They observed that the contact angle in the presence of water is around at 37° while oil can completely spread along the rock surface, implying a hydrophobic shale surface. Similarly, Roshan et al. [91] performed contact angle tests with various ion types, concentrations, pressures and temperatures. Their results indicate that the contact angle of oil is between 6° to 18° while that of water varies between 17° to 62°, which confirms a hydrophobic surface in the presence of brine. However, these contact angle results are contrary to the spontaneous imbibition observations, where shale can imbibe more water than oil [75, 80, 97]. Xu et al. and Ghanbari et al. argue that traditional contact angle measurements on shale surface cannot represent the *in-situ* wettability [20, 63, 108] due to the strong geochemical and geomechanical heterogeneities [248]. Therefore, it is important to directly estimate shale surface energy to predict the wettability associated with fluid-shale interactions.

To achieve this, we performed a geochemical study to characterize the shale wettability and compared our results with published experimental works performed by Xu and Dehghanpour [63]. Specifically, a surface complexation model was performed to compute the surface potential of organic matter, calcite and quartz as a function of pH. We predicted the local pH on the basis of ion exchange between illite and brine. Furthermore, we computed the disjoining pressure isotherm of air-brine-shale system in the presence of 0.1, 1, 10 and 20 wt% NaCl solution at constant charge condition.

5.3. Previous Observations by Xu and Dehghanpour [63]

5.3.1. Horn River Basin formation mineralogy

Given the mineralogy of shale significantly affects the gas-brine-shale system wettability [91, 239], Table 5-1 lists the X-ray Diffraction (XRD) derived composition of three shale samples from Horn River Canada used in spontaneous imbibition experiments by Fort Simpson (FS), Muskwa (M) and Otter Park (OP) [63, 74]. Results show that illite and quartz are dominant minerals followed by calcite, dolomite, chlorite and pyrite.

Table 5-1 Mineralogy of different sections of Horn River Basin (in wt%) [63, 74].

Mineral	Calcite	Quartz	Dolomite	Chlorite
FS	0.5 ± 0.4	29 ± 1.3	2.7 ± 0.3	6.5 ± 0.8
M	0	36.7 ± 1.2	5.2 ± 0.4	4.4 ± 0.4
OP	12.9 ± 0.4	43.6 ± 1.1	2.2 ± 0.5	0
Mineral	Illite	Plagioclase Albite	Pyrite	TOC
FS	55.4 ± 1.7	4.1 ± 0.5	1.7 ± 0.2	1.73
M	48.3 ± 1.5	3.6 ± 0.5	1.7 ± 0.2	2.25
OP	33.8 ± 1.2	4.4 ± 0.4	3.2 ± 0.2	3.01

5.3.2. Fluid properties

Xu and Dehghanpour used 10 and 20 wt% sodium chloride and deionized water as imbibition fluids in their experiments [63]. Table 5-2 shows the fluid density, viscosity and surface tension of brine-air at 25°C. In our geochemical modelling, we added another two NaCl concentrations (1 wt% and 0.1 wt%) to furtherly study the effect of salinity on fluid-rock interactions and shale wettability.

Table 5-2 Properties of fluids used in the spontaneous imbibition tests [63, 249-251].

Fluid	Density (g/cm^3)	Viscosity (cp)	Surface Tension (dyne/cm)
20 wt% NaCl	1.12	1.26	79.00
10 wt% NaCl	1.06	1.04	76.00

| DI water | 1.00 | 0.90 | 72.00 |

5.3.3. Spontaneous imbibition experiments

Spontaneous imbibition tests were performed by Xu and Dehghanpour using an intact shale sample from Horn River Basin in the presence of 10 or 20 wt% NaCl and deionized water [63]. Shale samples were cleaned and dried prior to being put inside an imbibition cell containing NaCl. The mass of the imbibed fluid was recorded periodically during the spontaneous imbibition process. Given that the details of experimental works have been well documented in Xu and Dehghanpour' paper, here we only summarize the main results (Figure 5-1). First, a low NaCl concentration increases the solution uptake for all samples. Second, the capability of imbibing NaCl solution is: Fort Simpson > Muskwa > Otter Park. Third, deionized brine and 10 wt% NaCl facilitate the breakdown of samples (Fort Simpson and Muskwa). To gain a deeper understanding of these results, we therefore performed geochemical modelling.
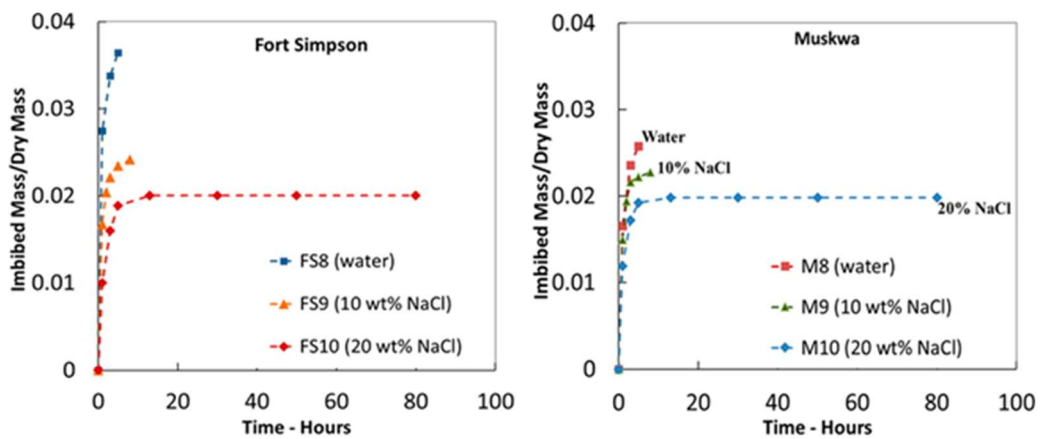
(a)

(b)
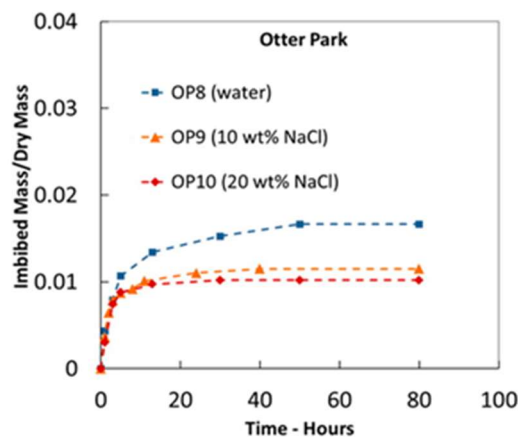
(c)

Figure 5-1 Spontaneous imbibition results for a) FS, b) M and c) OP intact shale sample in the presence of 10 and 20 wt% NaCl and DI water [63]. Due to the breakdown of samples (Fort Simpson and Muskwa), the curves of imbibed mass over time end early.

5.4. Geochemical Modelling

5.4.1. Surface complexation modelling

Since surface energy is governed by surface chemical species [252], a surface complexation model was performed to calculate the surface potential on both organic matter (which represents kerogen in this study) and inorganic minerals (quartz and calcite) as a function of pH. Table 5-3 lists the chemical reactions and corresponding equilibrium constant at 25°C for organic matter, quartz and calcite, respectively [87, 179]. The surface site density and specific area were set at 3.84 $\mu mol/m^2$ and 0.1 m^2/g for quartz [182] and 4.1 $\mu mol/m^2$ and 1 m^2/g for calcite [90, 179], respectively. Since the imbibition experiments were conducted at ambient conditions, the log of CO_2 partial pressure is set at -3.4 in our models. PHREEQC 3.5.0 was used to simulate the surface complexation and ion exchange process, and we used the database of Lawrence Livermore National Laboratory (LLNL) thermo.V8.R6.230 [175] for all the simulations.

Due to the high specific area, organic matter controls the amount of adsorbed gas although TOC constitutes only 1.73 to 3.01 wt% of the sample. Therefore, a surface complexation model was used to calculate surface potential of organic matter. In this work, we assume the ratio of base number (BN) to acid number (AN) of organic matter surface is 10:1 (5 $\mu mol/m^2$ for BN and 0.5 $\mu mol/m^2$ for AN) with a specific area of 200 m^2/g. This assumption is backed up by Fourier transform infrared (FTIR) spectroscopy [178], X-ray photoelectron spectroscopy (XPS) and sulphur X-ray absorption near edge structure (S-XANES) techniques [177]. For example, Huang et al. [178] characterized the structure of bulk organic matter in Silurian shale, China using FTIR. They report that most of the nitrogen atoms are present as the form of pyrrolic and pyridinic groups so that the amount of ammonium is relatively small. In contrast, carboxylic groups are observed although the amount decreases at high temperature [177].

Table 5-3 Input parameters of surface complexation model of organic matter, quartz and calcite [87, 179]. '>' represents the chemical group attached onto the rock surface.

Number	Reaction	$\log K_{25°C}$
	OM	
1	$>NH^+ \leftrightarrow\ >N + H^+$	-6.0
2	$>COOH \leftrightarrow\ >COO^- + H^+$	-5.0
3	$>COOH + Ca^{2+} \leftrightarrow\ >COOCa^+ + H^+$	-3.8
4	$>COOH + Mg^{2+} \leftrightarrow\ >COOMg^+ + H^+$	-4.0
	Quartz	
5	$>SiOH \leftrightarrow\ >SiO^- + H^+$	-4.0
6	$>SiOH + Ca^{2+} \leftrightarrow\ >SiOCa^+ + H^+$	-9.7
7	$>SiOH + CaOH^+ \leftrightarrow\ >SiOCaOH + H^+$	-4.5
	Calcite	
8	$>CaOH + H^+ \leftrightarrow\ >CaOH_2^+$	11.9
9	$>CaOH + HCO_3^- \leftrightarrow\ >CaCO_3^- + H_2O$	5.8
10	$>CaOH_2^+ + SO_4^{2-} \leftrightarrow\ >CaSO_4^- + H_2O$	2.1
11	$>CO_3H \leftrightarrow\ >CO_3^- + H^+$	-5.1
12	$>CO_3H + Ca^{2+} \leftrightarrow\ >CO_3Ca^+ + H^+$	-2.6
13	$>CO_3H + Mg^{2+} \leftrightarrow\ >CO_3Mg^+ + H^+$	-2.6

5.4.2. Ion exchange modelling to predict the local pH

Ion exchange between basal-charged clays in particular the high-content of illite and brine can significantly affect the local pH [82, 84, 187, 188]. This triggers the variation of the chemical surface species at organic matter and inorganic minerals thus surface potential [88, 189, 190]. We therefore performed ion-exchange modelling to determine the *in-situ* pH which would be used as a reference to obtain surface potentials of brine-shale and to calculate the disjoining pressure. To achieve this, we consider the geochemical reactions and corresponding equilibrium constants which are shown in Table 5-4. OP is selected as the simulative objective due to the integrity of imbibition results (Figure 5-1). Since the mineral compositions of OP are very similar to those of FS and M, the simulation results should also apply to them. Zolfaghari et al. [115] reported that the cation exchange capacity (CEC) of OP based on the ammonium acetate method is 3.5 cmol/kg. Therefore, the absolute amount of exchangeable sites

in our model is set as 0.007 mol (the typical CEC of kaolinite is about 10 cmol/kg, and illite and smectite have CEC ranging from 25 to 100 cmol/kg [191]).

Table 5-4 Input parameters of mineral surface ion-exchange [90, 187].

Number	Reaction	log $K_{25°C}$
1	$>Na + H^+ \leftrightarrow >H + Na^+$	4.6
2	$2>Na + Ca^{2+} \leftrightarrow >Ca + 2Na^+$	0.8
3	$>Na + K^+ \leftrightarrow >K + Na^+$	0.7
4	$2>Na + Mg^{2+} \leftrightarrow >Mg + 2Na^+$	0.6

To better simulate the pH variation induced by *in-situ* geochemical reactions with respect to ion types and concentrations, we also considered the mineral dissolution. Table 5-5 lists the dissolution-precipitation equilibrium of calcite ($CaCO_3$), dolomite ($CaMg(CO_3)_2$), quartz (SiO_2) and pyrite (FeS_2) using the database of Lawrence Livermore National Laboratory (LLNL) thermo.V8.R6.230 database [175].

Table 5-5 Reactions and equilibrium constants of calcite, dolomite, quartz and pyrite dissolution-precipitation [175].

Number	Reaction	log $K_{25°C}$
1	$CaCO_3 + H^+ = Ca^{2+} + HCO_3^-$	1.85
2	$CaMg(CO_3)_2 + H^+ = Ca^{2+} + Mg^{2+} + HCO_3^-$	2.51
3	$SiO_2 = SiO_2$	-3.99
4	$FeS_2 + H_2O = 0.25\ H^+ + 0.25\ SO_4^{2-} + Fe^{2+} + 1.75\ HS^-$	-24.65

5.4.3. Disjoining pressure calculation

The disjoining pressure is defined as the interactive force between the interfaces of air-brine and brine-rock [193, 231, 253] with a summation of van-der-Waals force, electrical double layer and structural force described by Eq. 5-1.

$$\Pi_{Total} = \Pi_{Van\ der\ Waals} + \Pi_{electrical} + \Pi_{structural} \qquad \text{Eq. 5-1}$$

where Π_{Total} is the total disjoining pressure; $\Pi_{Van\ der\ Waals}$ is the Van der Waals force; $\Pi_{electrical}$ is the electrical force and $\Pi_{structural}$ is the structural force. The structural force is usually omitted due to its short-range interactions compared to other long-range

interactions such as Van der Waals force and electrical force [163]. Therefore, the total disjoining pressure is formulated as Eq. 5-2.

$$\Pi_{Total} = \Pi_{electrical} - \frac{H}{6\pi L^3}$$ Eq. 5-2

In this study, the London wavelength is 100 nm, electron charge is 1.60×10^{-19} C, dielectric permittivity of vacuum is 8.854×10^{-12} F·m^{-1}, relative permittivity of electrolyte solution is 78.4 and valence of a symmetrical electrolyte solution is 1 [231]. The Hamaker constant of organic matter, quartz and calcite for rock-water-air system is set at -0.24×10^{-20} J, -9.97×10^{-21} J and -2.37×10^{-20} J, respectively [163, 253]. The detail of the total disjoining pressure and the calculation procedures are documented in our previous work [193]. It is worth noting that in the presence of an air-water-rock system, the chemical potential of air-water interface is set at 0 [253]. Besides, we computed the disjoining pressure at constant charge condition to indicate the electrical double layer compression approximation [254].

5.5. Results and Discussion

In this section, we first show the effect of pH and salinity on surface chemical species and surface potential. We then present the local pH predicted by geochemical model and compare the results with values reported by literature. Finally, we outline the isotherm of disjoining pressure for gas-brine-organic matter and gas-brine-calcite systems.

5.5.1. Effect of pH and salinity on surface species concentration

The pH of aqueous solution significantly affects the surface species concentration of organic matter at a given salinity (Figure 5-2). For example, the number of >NH$^+$ decreases significantly with increasing pH due to a shift of Reaction 1 (Table 5-3) towards the right-hand side. However, >COO$^-$ increases slightly with pH, although the increase of >COO$^-$ with pH is relatively distinct at acidic condition which is in line with literatures [88, 182]. >COOCa$^+$ and >COOMg$^+$ are present on organic matter surface but their concentrations are considerably less than those of >NH$^+$ and >COO$^-$ due to the limited dissolution of calcite and dolomite so that we did not show their trends in the figures.

Salinity also impacts the surface species concentration (Figure 5-2). For example, $>NH^+$ increases with increasing salinity when pH is less than 7 largely due to the decrease of activity coefficient of H^+. However, a shift appears when pH is greater than 7, showing a decrease of $>NH^+$ with increasing salinity. With regard to the increased pH due to the ion-exchange in this study (Table 5-6), lowering NaCl salinity from 20 to 0.1 wt% increases the $>NH^+$ concentration from 0.08 to 0.14 μmol/m². For $>COO^-$, decreasing brine salinity slightly increases the surface concentration at a lower pH but a decrease at a pH greater than 7. Similar results were obtained by Brady et al. [179], who show that that lowering NaCl concentration can increase the carboxylic acid concentration on oil surfaces at a low pH.
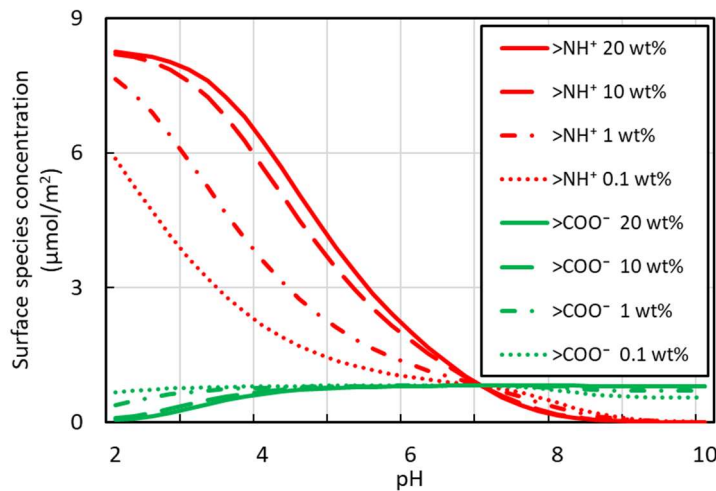
Figure 5-2 Surface chemical species variation at organic matter surfaces over pH in the presence of various salinities.

Figure 5-3 shows the variation of $>SiO^-$ concentration on quartz surface with pH at different salinities. Increasing pH gradually increases $>SiO^-$ concentration due to the Reaction 5 in Table 5-3, which shifts the equilibrium towards right-hand side and it reaches a constant (6.38 μmol/m²) for all salinities at alkaline condition. For example, at a given salinity (20 wt% NaCl), increasing pH from 4 to 8 increases the $>SiO^-$ surface density from 1.39 to 6.35 μmol/m².

Figure 5-3 also shows that decreasing salinity decreases the $>SiO^-$ concentrations. For example, at pH=7, decreasing NaCl concentration from 20 wt% to 10 or 1 to 0.1 wt% decreases $>SiO^-$ concentrations from 6.14 to 5.99 μmol/m² or 4.71 to 2.89 μmol/m², respectively. At an alkaline condition of pH=8.5, lowering NaCl concentration from

20 to 0.1 wt% decreases >SiO⁻ concentration from 6.37 to 5.55 µmol/m². Brady et al. [182] reported the same trend, which shows that increasing pH increases >SiO⁻ concentration on quartz surface while decreasing ionic strength of NaCl decreases the surface site density.
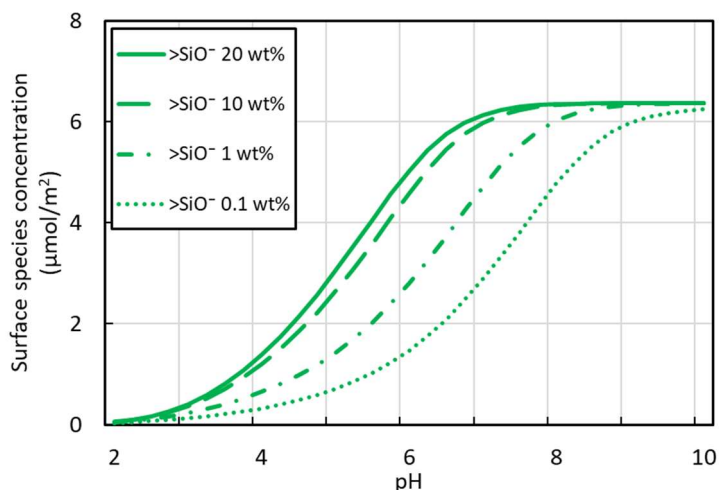
Figure 5-3 Surface chemical species variation at quartz surfaces over pH in the presence of various salinities.

Figure 5-4 depicts the surface chemical species variation on calcite surface with pH at various salinities. The results show that the change of >CaOH$_2^+$ concentration with pH is minor when pH is less than 7, which is due to a high equilibrium constant of the Reaction 8 in Table 3 that is in line with Brady et al. [88] and our previous work [83, 219]. However, >CaOH$_2^+$ decreases at alkaline condition, which is also observed by Chen et al. [189]. For >CO$_3^-$, increasing pH increases the species concentration at acidic condition. The concentration gradually drops when pH is greater than 7. In contrast, >CaCO$_3^-$ and >CO$_3$Ca$^+$ follow the same trend that increasing pH increases the species concentrations.

Figure 5-4 also shows that the change of NaCl salinity leads to a limited effect on the concentration of >CaOH$_2^+$, >CaCO$_3^-$ and >CO$_3$Ca$^+$ at a given pH. However, >CO$_3^-$ increases with lowering salinity when pH is less than 7 due to a decrease of activity coefficient of H$^+$. For example, at pH=5, decreasing salinity from 20 to 0.1 wt% increases the >CO$_3^-$ concentration from 5.23 to 5.45 µmol/m².
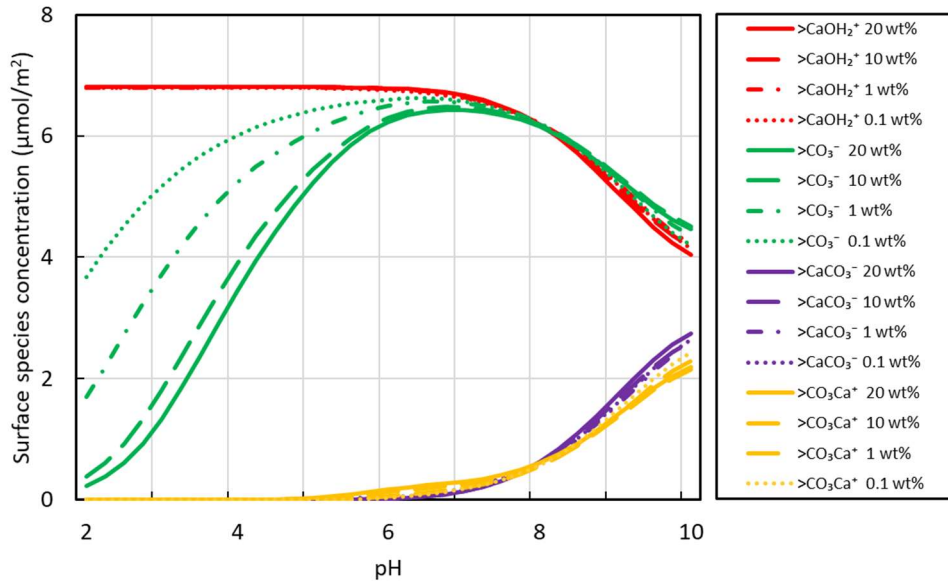
Figure 5-4 Surface chemical species variation at calcite surfaces over pH in the presence of various salinities.

5.5.2. Effect of pH and salinity on surface potential

Since the surface chemical species of organic matter highly depends on pH, we computed the surface potential of organic matter as a function of pH at various salinities. Figure 5-5 shows that pH significantly affects surface potential of organic matter. Specifically, the surface potential decreases with increasing pH with a shift from positive to negative when pH is greater than 7 due to deprotonation of $-NH^+$ and $-COOH$ at alkaline conditions (Reaction 1 and 2 in Table 5-3).

Meanwhile, salinity variation also contributes to the surface potential. Figure 5-5 shows that at both acid and alkaline conditions, increasing salinity decreases absolute value of surface potential. For instance, at *in-situ* pH as a result of ion-exchange (Table 5-6), lowering solution salinity from 20 to 0.1 wt% decreases the organic matter surface potential from -17.6 to -23.8 mV.

Taken together, it appears that both pH and salinity are important to determine the surface potential of the organic matter-brine thus wettability. This will be discussed with disjoining pressure isotherm in the following subsection.
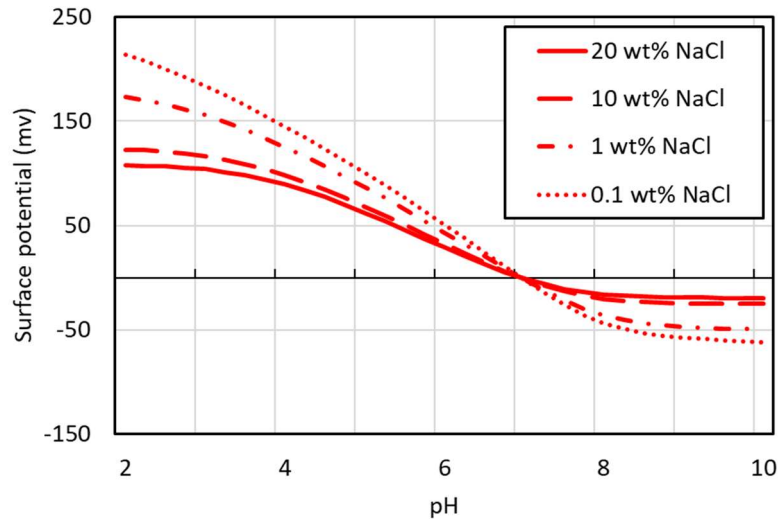
Figure 5-5 Surface potential of OM-brine as a function of pH in the presence of various brines.

Figure 5-6 shows the variation of surface potential of quartz with pH at different salinities. Similar to organic matter, the surface potential of quartz-brine becomes more negative with increasing pH. For example, at a given salinity of 20 wt%, surface potential decreases from -84.1 to -95.2 mV with increasing pH from 6 to 8. This implies a more hydrophilic surface in agreement with the observations reported by Nasralla et al. [255] and Xie et al. [256].

Salinity also significantly affects the quartz surface potential (Figure 5-6). For the pH associated in this study (Table 5-6), decreasing NaCl concentration from 20 to 10 wt% or 1 to 0.1 wt% decreases the surface potential from -95.3 to -110.1 mV or -165.0 to -216.9 mV, respectively. In contrast, for pH=7, decreasing NaCl salinity decreases the surface potential from -93.6 to –107.1 mV.
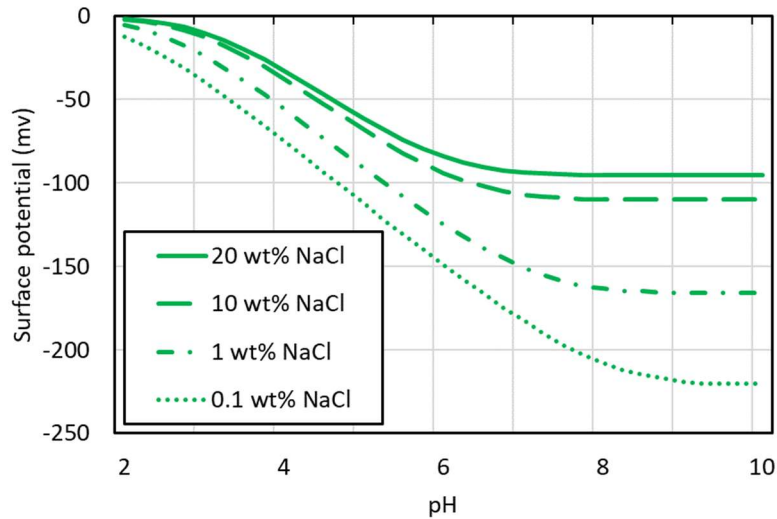
Figure 5-6 Surface potential of quartz-brine as a function of pH in the presence of various brines.

Similar to organic matter and quartz, the surface potential of calcite decreases with increasing pH, while a shift from positive to negative appears at pH=8 (Figure 5-7). For example, for at a salinity of 0.1 wt%, surface potential decreases from 40.8 to -12.9 mV with increasing pH from 6 to 9.

Under acidic conditions, lowering salinity increases the calcite surface potential thus hydrophilicity. For example, at pH=5, lowering salinity from 20 to 0.1 wt% increases the surface potential from 37.2 to 42.0 mV. However, when pH is greater than 8, the variation of NaCl salinity rarely affects calcite surface potential. Our results are supported by Lee et al. [257], who reported that decreasing salinity would increase the thickness of water film on sand surface at acid conditions thus expands the electrical double layer and shifts the surface more water-wet. To summarize, an increase of surface potential indicates that a low NaCl concentration would expand the electrical double layer on organic matter, quartz and calcite surface, which makes the wettability to more water-wet. Therefore, reusing high concentrations flowback water for subsequent fracking may reduce water loss as a result of a less hydrophilic system. However, high salinity water likely compresses electrical double layer, which increases the hydrophobicity and undermines the hydrocarbon production.
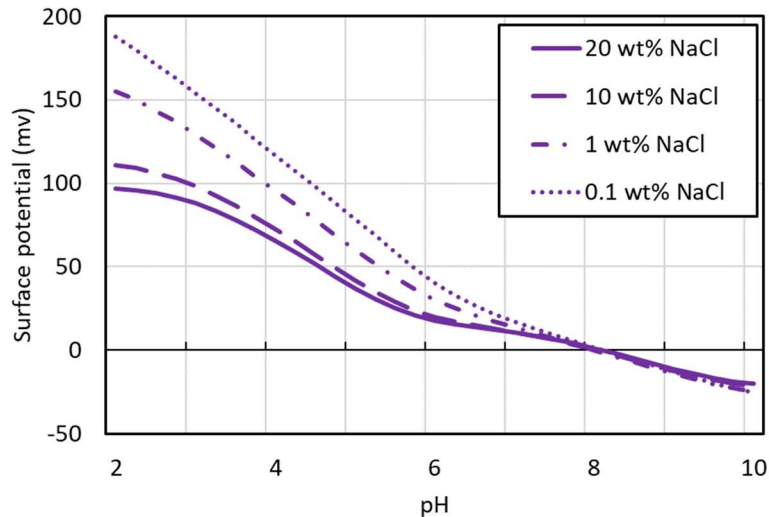
Figure 5-7 Surface potential of calcite-brine as a function of pH in the presence of various brines.

5.5.3. Local pH of shales predicted by geochemical modelling

A high content of basal-charged clays such as illite can trigger ion-exchange process thus increase the local pH due to the Reaction 1 in Table 5-4. Therefore, it is important to determine the *in-situ* pH which will be used as a reference to obtain the surface potentials of brine-shale and subsequently the disjoining pressure. Table 5-6 lists the pH predicted by the illite ion-exchange model with consideration of the dissolution-precipitation equilibrium of calcite, dolomite, quartz and pyrite. All the fluids are in equilibrium with carbon dioxide in the atmosphere to better match the spontaneous imbibition experiments. The results indicate that the pH slightly increases from 8.3 to 8.7 with decreasing the salinity from 20 to 0.1 wt%. This is because decreasing Na^+ concentration will shift the reaction 1 of Table 2-4 to right-hand side thus lowering the local H^+ activity coefficient. The local pH predicted by PHREEQC is also supported by the results from Zolfaghari et al. [115] who reported that the solution pH ranges from 8.0 to 8.5 after saturating the OP sample with deionised water at room temperature and atmospheric pressure. In addition, Xu et al. [185] also measured the solution pH after spontaneous imbibition experiment using a sample from Horn River Basin. Their results show that pH varies from 7.5 to 8.5 in the presence of oxidized imbibing water, and from 8.0 to 9.0 with degassed water. Generally, the local pH predicted by PHREEQC is in agreement with reported value from literature. Our results imply that the flowback water likely exhibits alkaline condition for illite (or

basal-charge planes)-bearing shale reservoirs due to the ion exchange process. To better predict the local disjoining pressure, we used the salinity-dependent pH (Table 5-6) as the reference to quantify the surface potential thus *in-situ* wettability in the following subsection.

Table 5-6 The in-situ solution pH due to illite ion-exchange.

NaCl concentration		20 wt%	10 wt%	1 wt%	0.1 wt%
pH	without CO_2	9.082	9.170	9.535	10.122
	with CO_2	8.336	8.352	8.405	8.714
Surface potential (mV)	organic matter	-17.6	-22.5	-42.8	-55.3
	quartz	-95.3	-110.1	-165.0	-216.9
	calcite	-2.5	-3.5	-5.8	-8.6

5.5.4. Effect of NaCl salinity on disjoining pressure

Figure 5-8 and 5-9 show the total disjoining pressure on organic matter and calcite surface varies with water film thickness at different NaCl salinity. On the basis of the electrical double layer compression approximation model developed by Gregory [254], constant charge condition is suggested to be applied when surface potential is less than 50 mV for a wide range of ionic strength [253]. Given that the quartz surface potential is far beyond 50 mV (Table 5-6), constant charge model may not represent the thermodynamic isotherm on quartz. We therefore only calculated the disjoining pressure of air-brine-organic matter and air-brine-calcite systems as function of salinity. Besides, it is worth noting that the positive disjoining pressure represents the repulsive force, whereas the negative disjoining pressure represents adhesive force [193, 258].

Figure 5-8 shows the disjoining pressure of air-brine-organic matter system under constant charge condition. The total disjoining pressure is always positive for organic matter, indicating a water-wet surface in the presence of air. Lowering salinity from 20 to 10 wt% does not change the disjoining pressure. However, further decreasing salinity to 1 and 0.1 wt% significantly increases the disjoining pressure thus creates a more water-wet system, favouring spontaneous imbibition yielded by capillary forces.

The results explain the wettability alteration process associated with capillary forces triggered by salinity changes, which partially accounts for the increase of the solution uptake for all samples with lowering NaCl concentration.

Our results are also supported by Yang et al., [64] who report that large volume of total organic content could facilitate the propagation of pre-existing micro-fractures in Longmaxi shale samples with organic-rich intervals. This is because with nano meter pore diameters, the capillary pressure of fine-grained organic-rich shale can be as high as 100 MPa [65]. Besides, the NaCl salinity reduction induced disjoining pressure increase enlarges the Debye-length of electrical double layer and the adsorbed water film thickness [55, 66], which in return gives rise to a greater disjoining pressure that serves as a high internal pore pressure to propagate existing micro-fractures in shale samples. On the other hand, the excess imbibed water may weaken shale strength due to the dissolution of minerals such as calcite and dolomite and clay swelling [23]. Consequently, the NaCl salinity reduction leads to more water uptake and the breakdown of shale samples during spontaneous imbibition as shown in Figure 5-1.
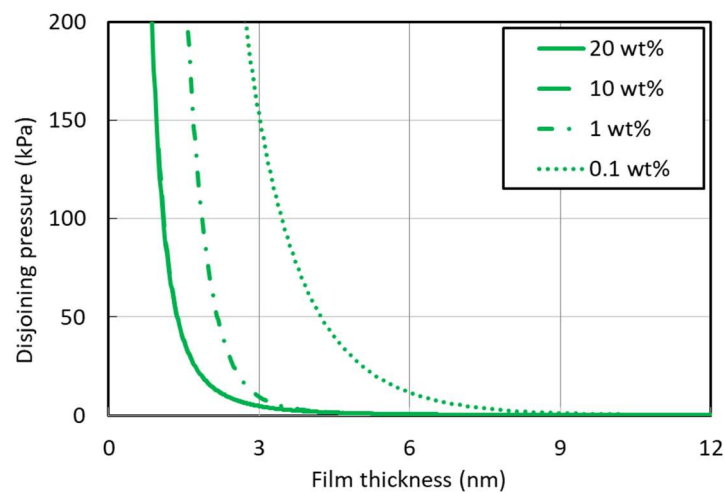
Figure 5-8 Disjoining pressure on organic matter surface changes with film thickness at different NaCl concentration. The results of 20 and 10 wt% are overlapped.

For air-brine-calcite system, the disjoining pressure remains to be positive regardless of solution salinity, whereas the effect of salinity on the increase of disjoining pressure is negligible as shown in Figure 5-9. This implies that capillary force still acts as a driving force for the water uptake although the wettability alteration on calcite surface due to salinity variation is negligible. The primary reason for the minor change of

disjoining pressure over salinity is due to a limited variation of surface potential of brine-calcite at *in-situ* pH (Table 5-6). However, the positive disjoining pressure indicates a high internal pore pressure which likely causes a pre-existing micro-fracture propagation [259]. We therefore conclude that salinity may not significantly increase the hydrophilicity of air-brine-calcite system of Horn River basin, but capillary force remains to serve as a driving force for water uptake in shale when *in-situ* pH is greater than 8. It is worth noting that the disjoining pressure and surface potentials highly depend on the local pH as aforementioned. In this study, due to the specific mineralogy of Horn River basin, the predicted pH of NaCl solution is around 8.3 to 8.7, which leads to the negligible change of calcite surface potential and disjoining pressure. However, if the *in-situ* pH is less than 7 because of the different mineralogy, formation brine compositions and CO_2 injection for fracking or hydrocarbon production, we would expect a significant increase of calcite surface potential due to the NaCl salinity reduction as shown in Figure 5-7. Consequently, the disjoining pressure on calcite surface would tend to more positive and thus alter the wettability to more water-wet.
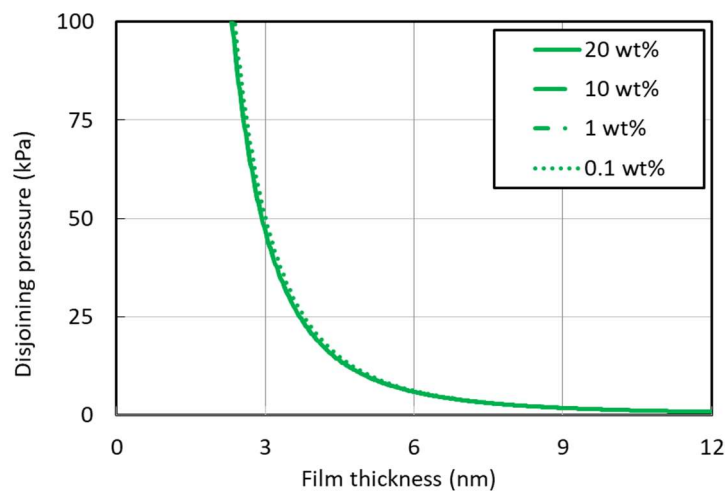
Figure 5-9 Disjoining pressure on calcite surface changes with film thickness at different NaCl concentration.

5.6. Implications and Conclusions

The low recovery of injected water after fracturing in shale gas reservoirs triggers both technical and environmental concerns [217, 243, 244]. While a few mechanisms (e.g., gravity induced water segregation [72, 245], clay hydration [80] and chemical osmotic effect [27, 63, 91]) have been proposed to account for the low recovery of flowback

water, few works have been able to draw any systematic investigation on the quantitative characterization of the fluid-shale interactions thus surface forces from geochemical perspective. In this study, we performed geochemical modelling to interpret Xu and Dehghanpour's spontaneous imbibition experiments [Xu, M., and H. Dehghanpour. *Advances in understanding wettability of gas shales.* Energy & Fuels 28.7 (2014): 4362-4375]. We calculated the surface chemical species and surface potential of organic matter, quartz and calcite in the presence of 0.1, 1, 10 and 20 wt% NaCl solutions. Furthermore, we computed the disjoining pressure isotherm of air-brine-shale system in the presence of 0.1 to 20 wt% NaCl at constant charge condition and compared the results with those in the literature.

Our results show that salinity and pH of brines significantly affect the surface species concentration of organic matter and inorganic minerals and thus surface potential. To be more specific, lowering salinity shifts surface potential of fluid-shale to more negative at *in-situ* pH (8.3 to 8.7). Disjoining pressure isotherm calculations show that decreasing salinity from 1 to 0.1 wt% shifts the disjoining pressure to be more positive for air-brine-organic matter, suggesting a hydrophilicity increase. Besides, air-brine-calcite system also gives a positive disjoining pressure regardless of salinity, implying a more hydrophilic system. The results also suggest that lowering salinity increases the disjoining pressure thus internal pore pressure to cause shale sample expansion and generation of micro-fractures [63, 260]. Taken together, our geochemical modelling accounts for the low recovery of injected water due to (1) the surface forces of organic matter and inorganic materials which is associated with capillary forces, and (2) an increase of the internal pore pressure which gives rise to micro-fracture propagation. Our work provides a first look at how hydraulic fluids affect organic matter and inorganic materials' surface chemical species, surface energy and system wettability, and underscores the importance of a combination of geochemical modelling and thermodynamics to predict fluid-shale interactions thus water uptake by shale.

6. Chapter 6 Effect of the Fluid–Shale Interaction on Salinity: Implications for High-Salinity Flowback Water during Hydraulic Fracturing in Shales

6.1. Abstract

Hydraulic fracturing has been widely implemented to enhance hydrocarbon production from shale reservoirs. However, one of the main challenges during hydraulic fracturing is to understand what factor(s) triggers high salinity of flowback water, which sometimes can be up to 300,000 mg/L. While several mechanisms have been proposed to explain the controlling factor behind the high salinity of flowback water, there has been little discussion about the effect of fluid-shale interactions (e.g., mineral dissolution and surface complexation) on the high salinity, and far less attention has been paid to quantify the contribution of fluid-shale interactions. We thus conducted spontaneous imbibition experiments using deionised water and outcrops from Marcellus, Barnett and Eagle Ford shale plays with minor precipitated salts. We also monitored the pH, electrical conductivity and ion concentrations (Cl^-, K^+, Ca^{2+}, NO_3^-, F^-, Br^- and NH^+) of the surrounding water during spontaneous imbibition process in consecutive four weeks. To quantify the impact of fluid-shale interactions on salinity, we performed geochemical modelling to examine the contribution of mineral dissolution (calcite, albite, quartz, chalcopyrite, pyrite and dolomite) and surface complexation on fluid salinity.

Spontaneous imbibition tests show that Barnett shale plugs imbibed more water than Marcellus and Eagle Ford largely due to the highest content of calcite and lowest content of organic carbon. The order of sequence of pH is Eagle Ford (8.3) > Barnett (8.0) > Marcellus (7.6) in line with prediction of geochemical modelling, confirming that pyrite oxidation plays a significant role in local pH thereby brine composition at ambient condition. Geochemical modelling also shows that salinity increment induced by the fluid-shale interactions is less than 3% of flowback water salinity, suggesting a minor impact of fluid-shale interactions on salinity increase. These findings point out that fluid-fluid and fluid-salt interactions likely play a more important role in high salinity of flowback water during hydraulic fracturing in shales.

Keywords: Shale reservoirs, Flowback water salinity, Fluid-shale interactions, Spontaneous imbibition, geochemical modelling.

6.2. Introduction

The increasing demand for geo-energy has been shifting the industry's attention from conventional to unconventional hydrocarbon resources, typically shale oil and gas. Given the low porosity (usually less than 10%) and ultralow permeability (e.g., tens of nano-darcy to 1 milli-darcy) [239, 261, 262], multi-stage hydraulic fracturing along with horizontal drilling has been commonly implemented to unlock shale oil and gas from subsurface [13, 162, 228, 263]. To fracture shale reservoirs, low salinity hydraulic fluids (usually < 5000 ppm total dissolved solid (TDS)), which is composed of slick water, proppants and other additives, are injected into underground [13, 16, 116, 264]. This process would significantly increase the connectivity of shale formation by creating new fractures combined with activating pre-existing fractures, and thus increases shale hydrocarbon recovery [56, 215, 264].

However, hydraulic fracturing in shales usually results in high salinity of flowback water, sometimes up to 300,000 mg/L, which poses environmental and production issues [11, 27, 110, 112, 116, 265]. For instance, Kurtoglu [109] investigated the water chemistry of three samples from Middle Bakken reservoir. The average TDS is 285,000 mg/L. Hayes [110] reported that the level of TDS of produced water from Marcellus shale play can be as high as 300,000 mg/L with high concentration of Na, Ca, Cl and relatively high level of Ba, Br and Sr. Zolfaghari et al. [115] measured the salinity of flowback water from three formation in Horn River Basin. They reported that the fluid salinity ranges from 40,000 to 70,000 mg/L. Such high concentrations of TDS together with large volumes of trapped water may raise public concerns on the quality of portable water, and burden the post-processing cost of flowback water before reinjection for hydraulic fracturing [18, 20, 120, 217]. Moreover, the mixture of trapped slick water and *in-situ* existing formation brine can interact with shale rock, which may affect rock mechanical properties such as bulk strength [29-33], Young's modulus [35-37, 55], brittleness index [37, 39] and influence the subcritical crack growth [40-42]. Besides, the change of fluid salinity would also affect brine-oil/gas-rock wettability, and thus influence the shale oil and gas production [21, 85, 87, 182,

187, 190]. Therefore, there is a pressing need to understand the controlling factor(s) behind the high salinity flowback water during hydraulic fracturing in shales.

To understand the origin of high salinity flowback water, several potential mechanisms have been proposed, such as i) fluid-fluid interactions which include the mixing of low salinity hydraulic fluids with initial high salinity formation brine [112, 116-118], and diffusion osmosis [29, 115, 119]; ii) fluid-salt interactions, which likely results in a salinity increment due to the dissolution of precipitated salts on fracture surfaces [20, 113, 119]; iii) fluid-shale interactions in particular mineral dissolution [113-115, 117, 119, 120], ion exchange process [21, 115] and surface complexation [85, 88]. For instance, Rowan et al. [121] measured $^{228}Ra/^{226}Ra$ and ^{226}Ra activity of 13 produced water samples from the Marcellus shale play. They conclude that the high saline flowback water was the result of mixing injected slick water with high salinity formation brine. Ghanbari et al. [108] proposed that the salt precipitating on pore and fracture surface may be another source of ions. Zolfaghari et al. [115] performed spontaneous imbibition experiments using shales from Horn River Basin. They attributed the high salinity to the exchangeable ion mobilization from clay minerals. Chermak and Schreiber [120] analysed the trace element data from 9 shale gas reservoirs in the U.S. and proposed that the high saline flowback water was caused by the mineral dissolution. However, Stewart et al. [116] found the opposite, arguing that dissolution of soluble components cannot release enough ions to match the high salinity of produced water, although more quantitative works need to be conducted. Roshan et al. [91] performed contact angle measurements on shale sample with consideration of different ion concentrations and types. Their results imply that the potential determined ions (PDIs) typically the bivalent ions are able to adsorb on the mineral surface through surface complexation and ion exchange, which likely affects the in-situ fluid salinity. Teppen and Miller [122], Ali and Hascakir [47], Abdulsattar et al. [123] pointed out that, for the shales containing a certain amount of clays with high value of cation exchange capacity (CEC) such as smectite and zeolite, cations can be held on the rock negatively charged surfaces of the rock, thereby affecting the flowback water chemistry.

In this context, we aimed to examine the contribution of fluid-shale interactions on high salinity flowback water with a combination of spontaneous imbibition

experiments, water chemistry monitoring and geochemical modelling using outcrops from the Marcellus, Barnett and Eagle Ford shale plays. We monitored the imbibed water chemistry such as pH, conductivity and ion concentrations (Cl^-, K^+, Ca^{2+}, NO_3^-, F^-, Br^- and NH^+) every twenty-four hours during consecutive four weeks. Geochemical modelling incorporating mineral dissolution (calcite, albite, quartz, chalcopyrite, pyrite and dolomite) and surface complexation was performed to quantify the contribution of mineral dissolution and surface complexation on fluid salinity.

6.3. Spontaneous Imbibition Tests

6.3.1. Sample mineralogy

Given that we aimed to investigate the impact of fluid-shale interaction on high salinity flowback water, we selected outcrops samples from the Marcellus, Barnett and Eagle Ford shale plays with negligible precipitated salts and connate water [116]. Besides, considering that mineralogy strongly affects fluid-shale interactions in particular the mineral dissolution and surface complexation, we first examined the mineral compositions of outcrop samples (Table 6-1). The samples were pulverised to ultrafine particle with size of 2 μm and the corresponding mineralogy was analysed by semi-quantitative X-ray diffraction (XRD) in John De Laeter Centre, Curtin University. The results show that all the tested samples are rich in calcite from 66.8% to 77.55%. Samples from Eagle Ford have more quartz and less albite than those from Marcellus and Barnett. The mass percentage of clays is low in all samples. Rock-eval analyses indicate that Eagle Ford sample has higher total organic carbon (TOC, 3.48%) than Marcellus (2.28%) and Barnett (1.22%).

Table 6-1 The mineralogy of tested samples from Marcellus, Barnett and Eagle Ford shale plays (wt%).

	Quartz	Calcite	Albite	Illite	Muscovite	Biotite	Mica
Marcellus	7.15	71.30	10.36	0.22	2.14	0.02	0.01
Barnett	2.64	77.55	10.88	0.03	0.02	0.15	0.00
Eagle Ford	16.66	66.80	8.90	0.25	0.00	0.14	0.00
	Dolomite	Kaolinite	Montmorillonite	Pyrite	Chlorite	Chalcopyrite	TOC
Marcellus	1.20	0.01	0.00	2.95	0.10	4.53	2.28
Barnett	1.26	1.28	0.00	1.29	0.75	4.14	1.22
Eagle Ford	1.13	1.15	0.00	0.81	0.67	3.49	3.48

6.3.2. Experimental procedure

Spontaneous imbibition experiments under ambient conditions were performed as the following procedures: (i) intact shale plugs from Kocurek Industries INC. were cut into small cylinders with a diameter of 38.20 mm and height of 9.85 mm in the Geomechanics and Geophysics laboratory at Commonwealth Scientific and Industrial Research Organization (CSIRO, Perth); (ii) the samples were heated at 105 °C in an oven for 48 hours to evaporate moisture; (iii) the mass of dried sample was measured before the imbibition test; (iv) samples without naked-eye micro-fractures were immersed in deionised (DI) water with volume of 700 mL (Figure 6-1a); (v) the weight of wet samples was measured every 24 hours in the consecutive four weeks to examine the effect of fluid-shale interactions to the water uptake. It is worth noting that only the samples with no visible micro-fractures were selected for spontaneous imbibition tests, which can avoid any hydration-generated micro-fractures.
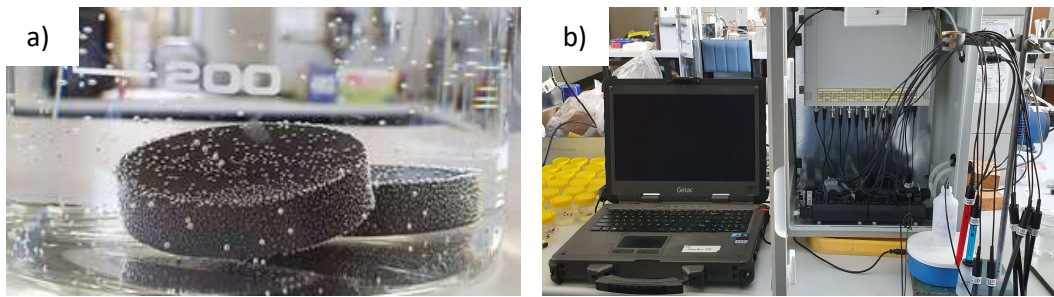
Figure 6-1 a) Spontaneous imbibition experiments using shale samples with DI water. Air bubbles were expelled away from samples' pore network during the imbibition process, and b) ion selective electrodes and monitoring system for water chemistry investigation.

To better characterize the role of fluid-shale interactions in the salinity increment of flowback water, we also continuously monitored the surrounding water chemistry using ion selective electrodes (Figure 6-1b). Fluid properties such as pH, conductivity, and concentration of ions (Cl^-, K^+, Ca^{2+}, NO_3^-, F^-, Br^- and NH^+) were monitored using the corresponding electrodes, which were connected to the ELIT Compact On-Site Fluid Analyser (NICO 2000 LTD.). It is worth noting that the concentration of other ions such as Na^+, Ba^{4+}, SO_4^{2-} were not measured in this study due to the significant interference from other ions. Before water chemistry measurement, all the electrodes were calibrated using standard pH buffers (pH = 10, 7 and 4) and standard solutions

(1000, 100, 10 and 1 mg/L for selected ions). The results were recorded when the value of aforementioned parameters had reached a steady state at each measurement.

6.4. Geochemical Modelling

To quantify how fluid-shale interactions contribute to salinity increment during spontaneous imbibition, surface complexation and mineral dissolution are coupled in the geochemical modelling. We performed surface complexation modelling (SCM) to characterize the extent of ions attaching/detaching from the rock, and the distribution of chemical species after fluid-shale interaction. Table 6-2 lists the surface complexation reactions of calcite, quartz and organic matter (kerogen in this case) and corresponding equilibrium constant at 25°C. It is worth noting that ion exchange on basal-charged clay surfaces (e.g., illite) was not considered in this study due to the negligible content of illite in these samples [21, 187]. We also did not incorporate ion diffusion caused by the osmosis effect [29, 115, 119] because of the low content of clay minerals. The input parameters for the SCM are listed in Table 6-3. All simulations were conducted using PHREEQC V3.5.0 plugged in Notepad++ V6.6.9 with the database of Lawrence Livermore National Laboratory (LLNL) thermo.com.V8.R6.230 [175]. Detailed information on SCM can be found in our previous works [21, 85].

Table 6-2 Geochemical complexation on surface of calcite [89, 182], quartz [85, 182] and organic matter [85]. '>' means the functional group which is attached on mineral surface.

#	Surface complexation reaction	log K_{298K}
	Calcite	
1	$>CaOH + H^+ \leftrightarrow >CaOH^{2+}$	11.9
2	$>CaOH + HCO_3^- \leftrightarrow >CaCO_3^- + H_2O$	5.8
3	$>CaOH_2^+ + SO_4^{2-} \leftrightarrow >CaSO_4^- + H_2O$	2.1
4	$>CO_3H \leftrightarrow >CO_3^- + H^+$	-5.1
5	$>CO_3H + Ca^{2+} \leftrightarrow >CO_3Ca^+ + H^+$	-2.6
	Quartz	
6	$>SiOH \leftrightarrow >SiO- + H^+$	-4.0
7	$>SiOH + Ca^{2+} \leftrightarrow >SiOCa^+ + H^+$	-9.7
8	$>SiOH + CaOH^+ \leftrightarrow >SiOCaOH + H^+$	-4.5

	Organic matter	
9	$>NH^+ \leftrightarrow >N + H^+$	-6.0
10	$>COOH \leftrightarrow >COO^- + H^+$	-5.0
11	$>COOH + Ca^{2+} \leftrightarrow >COOCa^+ + H^+$	-3.8
12	$>COOH + Mg^{2+} \leftrightarrow >COOMg^+ + H^+$	-4.0

Table 6-3 Input parameters of Surface Complexation Modelling.

	Surface site density ($\mu mol/m^2$)	Acid number ($\mu mol/m^2$)	Base number ($\mu mol/m^2$)	Specific area (m^2/g)
Calcite [90, 179]	5	N/A	N/A	2.8
Quartz [182]	3.84	N/A	N/A	0.1
Organic matter [85]	N/A	0.5	5	200

Note: carboxylate and nitrogen base group numbers on organic matter surface are represented by acid and base number [85].

Besides SCM, we also characterized the contribution of mineral dissolution to the salinity variation of imbibed water using PHREEQC. The degree of mineral precipitation-dissolution is represented by saturation indices (SI) [175]. Mineral would tend to precipitate when the SI is positive, while it tends to dissolve when the SI is negative [21, 175]. Based on the XRD analysis, we modelled dissolution of calcite ($CaCO_3$), albite ($NaAlSi_3O_8$), quartz (SiO_2), chalcopyrite ($CuFeS_2$), pyrite (FeS_2) and dolomite ($CaMg(CO_3)_2$) defined by the same database as SCM. Table 6-4 shows the reactions of precipitation-dissolution for these minerals at room temperature. Given that the whole experiment was conducted under atmospheric condition, oxygen and carbon dioxide were set to equilibrate with fluid. The dissolved O_2 can oxidize the pyrite and thus decrease solution pH and affect other mineral dissolution [185]. The dissolved CO_2 can provide extra H^+, which may further influence fluid-shale interactions and water chemistry [21]. The log of partial pressure of CO_2 and O_2 is set as -3.4 and -0.67, which represents their contents in the atmosphere.

Table 6-4 Precipitation-dissolution of calcite, albite, quartz, chalcopyrite, pyrite and dolomite at room temperature [175].

#	Geochemical reactions	$\log K_{298K}$
13	$CaCO_3 + H^+ = Ca^{2+} + HCO_3^-$	1.85
14	$NaAlSi_3O_8 + 4 H^+ = Al^{3+} + Na^+ + 2 H_2O + 3 SiO_2$	2.76

15	$SiO_2 = SiO_2$	-3.99
16	$CuFeS_2 + 2\,H^+ = Cu^{2+} + Fe^{2+} + 2\,HS^-$	-32.56
17	$FeS_2 + H_2O = 0.25\,H^+ + 0.25\,SO_4^{2-} + Fe^{2+} + 1.75\,HS^-$	-24.65
18	$CaMg(CO_3)_2 + 2\,H^+ = Ca^{2+} + Mg^{2+} + 2\,HCO_3^-$	2.51

6.5. Results and Discussions

6.5.1. Water uptake by shale during spontaneous imbibition process

Figure 6-2 shows the normalized weight of DI water imbibition for samples from the Marcellus, Barnett and Eagle Ford shale plays, respectively. Barnett samples imbibed more DI water (1.4%) than Marcellus (1.0%) and Eagle Ford (0.7%) with consideration of measuring error. The variation of the imbibed brines in different shale samples is likely caused by the mineralogy differences. For examples, Barnett samples contain higher calcite contents (77.55%) than Marcellus (71.30%) and Eagle Ford (66.80%, see Table 6-1). The system of fluid-air-calcite likely presents a strong hydrophilicity when fluid salinity is less than 5000 ppm [84, 87, 91]. Therefore, the Barnett samples with higher calcite content imbibed and trapped more water than Marcellus and Eagle Ford. On the other hand, Barnett samples also have the lowest content of hydrophobic organic matter (1.22%) compared to Marcellus (2.28%) and Eagle Ford (3.48%), which may further inhibit water imbibition [108, 266].
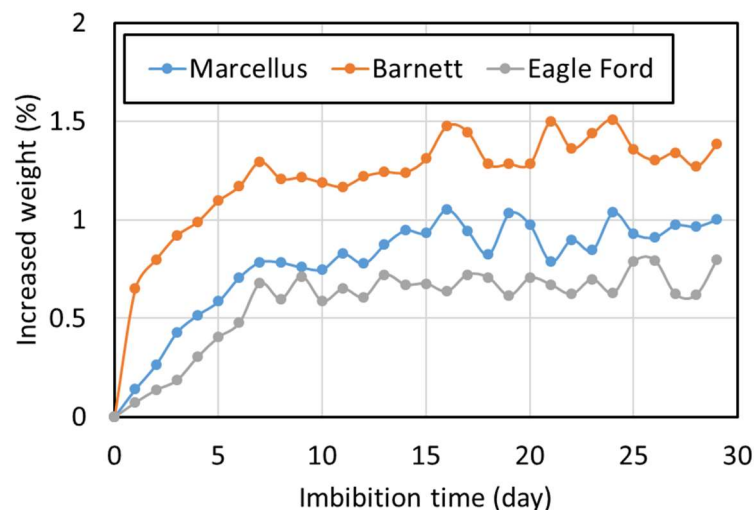
Figure 6-2 Normalized weight of DI water imbibed into dry samples from Marcellus, Barnett and Eagle Ford shale plays at room temperature and atmospheric pressure.

For all tested samples, the increased weight is less than 1.5% which is consistent with observations reported by Roychaudhuri et al. [73], Morsy and Sheng [267] and Zhou et al. [268]. The low amount of water uptake may be due to the limited clay content, especially smectite. Without smectite, shale rocks may not imbibe much of water and would not swell and break up thus generating micro-fractures as observed by Xu and Dehghanpour [63] and Roshan et al. [94]. In this case, water is imbibed mainly by the capillary forces [63, 73] and osmotic pressure [27, 63]. However, the low permeability of the shale matrix significantly prohibits rocks from uptaking water [20, 73] due to high drag forces within the nano-pores in shales, which likely causes the limited water imbibition as observed in Figure 6-2. Besides, without the pre-existing micro-fractures, the low contact area between shale matrix and fluid may further decrease the water uptake [75, 94].

6.5.2. pH variation over time during spontaneous imbibition process

Given the pH of aqueous ionic solution would significantly affect the mineral dissolution and rock surface geochemistry, the pH of the solution was monitored during spontaneous imbibition experiments (Figure 6-3). The order of the sequence of pH is as the following: Eagle Ford (8.3) > Barnett (8.0) > Marcellus (7.6). All the recorded pH values are slightly greater than 7 under ambient conditions, which indicates a weak alkalinity. This result may be caused by the strong reaction between >CaOH and H^+ on calcite surfaces (Reaction 1 in Table 6-2), which reduces the content of hydrogen ions and raises the solution pH. Similar results were reported by Zolfaghari et al. [115] and Xu et al. [185], who found that the DI water pH ranges from 8.0 to 8.5 after imbibition tests. Moreover, fluids saturated with Eagle Ford samples present the highest pH values (Figure 6-3). This is largely attributed to the oxidation of pyrite through the reaction: $FeS_2(s) + 154O_2(g) + 72H_2O(l) \rightarrow Fe(OH)_3(s) + 2H_2SO_4(aq)$ [269], which generates acid (Figure 6-4). Note that Eagle Ford samples contain less pyrite (0.81 wt%) than Barnett (1.29 wt%) and Marcellus (2.95 wt%), which indicates less capacity of buffering over the calcite dissolution in Eagle Ford samples [185]. We indeed tested the impact of pyrite oxidation on pH using geochemical modelling with and without consideration of pyrite oxidation. Our results confirm that pyrite oxidation plays an important role in local pH and brine composition, which is detailed in subsection 6.5.4.1.
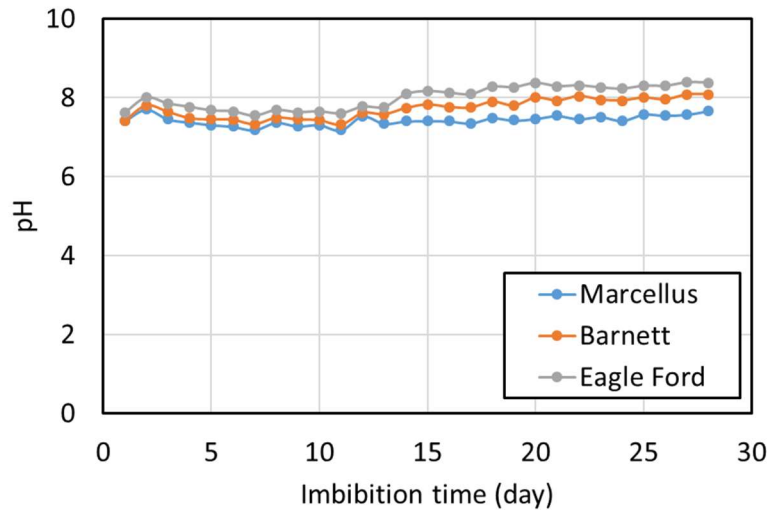
Figure 6-3 Fluid pH varies with imbibition time for rock samples from Marcellus, Barnett and Eagle Ford at room temperature and atmospheric pressure.
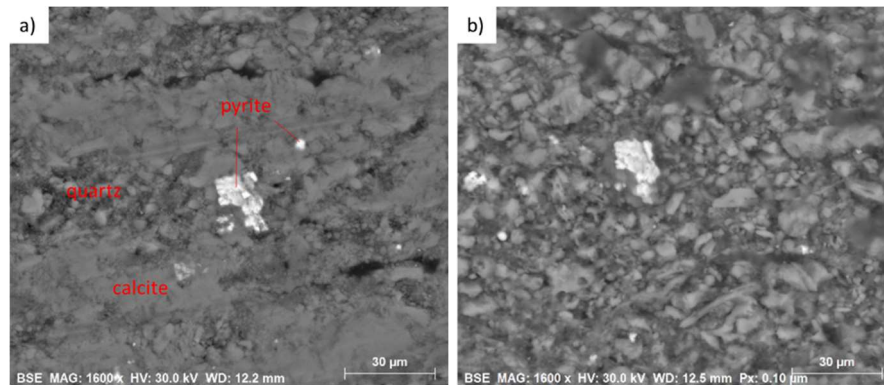
Figure 6-4 Scanning electron microscopy (SEM) images on Marcellus sample surface a) before, and b) after spontaneous imbibition experiments for seven days at ambient conditions. Analysis was conducted using SEM Philips XL 40. It is clearly shown that a portion of pyrite was oxidized and dissolved in water, which may generate extra H^+ and trigger pH reduction as observed in Figure 6-3. Calcite was also partially dissolved, in line with the increment of Ca^{2+} concentration reported in section 6.5.3.

6.5.3. Ion concentration and electrical conductivity

Figures 6-5 a-c show the variation of concentration of Cl^-, K^+ and Ca^{2+} with imbibition time for the Marcellus, Barnett and Eagle Ford shale samples, respectively. The concentrations of other tested ions such as NO_3^-, F^-, Br^- and NH^+ were non-detectable and therefore were not included here. In general, the concentrations of Cl^-, K^+ and Ca^{2+} increase with imbibition time with a similar trend reported by Zolfaghari et al. [115]

and field data reported by Haluszczak et al. [112]. Samples of Marcellus and Barnett have slightly higher Cl⁻ (Figure 6-5a) and K⁺ (Figure 6-5b) concentrations than Eagle Ford. According to the mineralogy, Barnett samples should contain much more Ca^{2+} than Marcellus and Eagle Ford due to the higher content of calcite. However, the concentration of Ca^{2+} for the three tested shales are roughly equivalent at the end of imbibition tests (Figure 6-5c). This result implies that only a little amount of calcite would be dissolved into water when the dissolution reaches equilibrium. Therefore, the contribution of mineral dissolution to high salinity of flowback water should be limited, which would be discussed in the section below.

However, the recorded Cl⁻ concentration is much less than K⁺ and Ca^{2+}, which leads to a relatively high ratio of K^+/Cl^- and Ca^{2+}/Cl^- as shown in Figures 6-5d and 6-5e. One of the possible reasons is that the mobilizable monovalent potassium would not react with minerals through surface complexation (see Table 3-2) and would be leached out from clay minerals [115, 270]. The dissolution of precipitated K-salts and Ca-salts on pore surfaces may also contribute to the high ratio of K^+/Cl^- and Ca^{2+}/Cl^- [115].
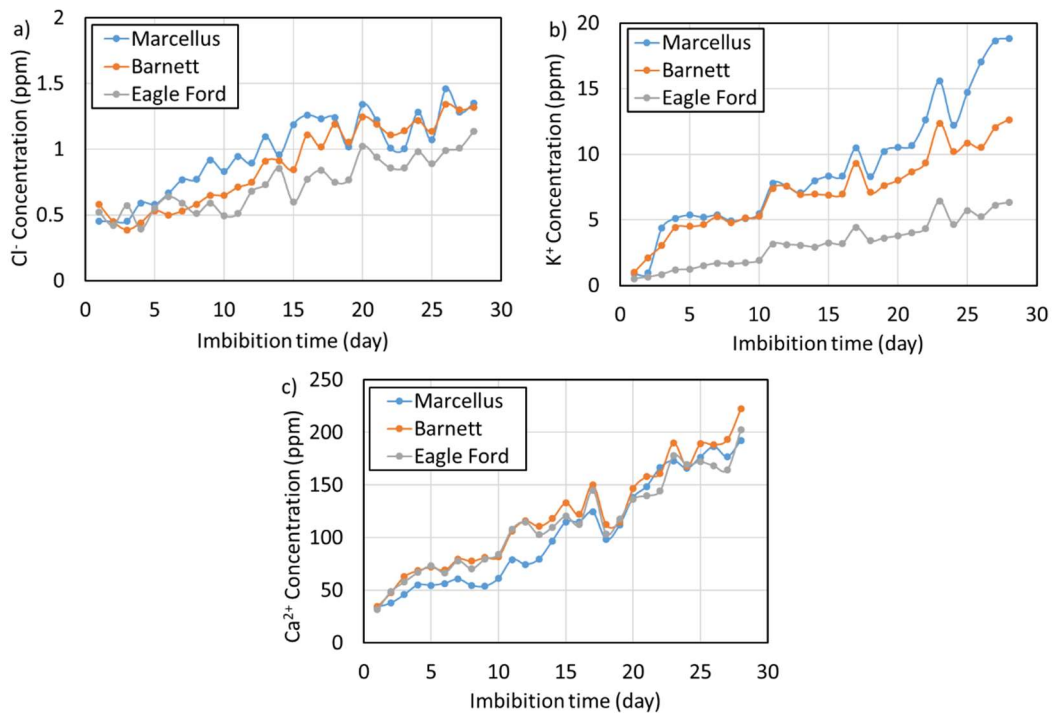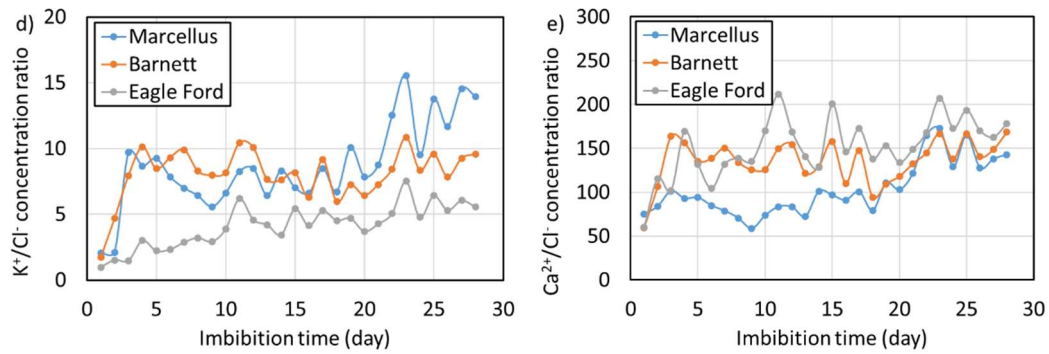
Figure 6-5 Ion concentrations of imbibed fluid versus time for a) Cl^-, b) K^+, c) Ca^{2+}, and ion concentration ratio of d) K^+/Cl^- and e) Ca^{2+}/Cl^- at room temperature and atmospheric pressure.

Although the incremental trends of ion concentration in this study match with field observations, the values of lab-measured ion concentrations are much less than that of the field by several orders of magnitude (e.g., the recorded total ion concentration is around 200 mg/L, whereas the TDS of flowback water after 14 days in Marcellus gas wells can be as high as 228,000 mg/L [112]). This can be attributed to the discrepancy between *in-situ* reservoir and experiment conditions, including fluid-rock contact area, connate formation brine, pre-existing salts, temperature and pressure. Besides, other anions such as HCO_3^- and SO_4^{2-} were not covered in this study. Nevertheless, it is not expected to increase the lab-measured values to such high field level even considering the unmeasured ions [115]. Consequently, our results indicate that fluid-shale interactions play a minor role in high TDS of produced water after hydraulic fracturing. Rather, the fluid-fluid interaction such as mixing of slick water with connate high salinity formation brine, and the fluid-salt interaction such as dissolution of pre-existing salts should account for the observed high salinity.

To verify the recorded ion concentration, we measured samples' electrical conductivity (EC) (Figure 6-6a). All ECs of tested solutions increase over imbibition time, which is in line with the ion concentration variation as shown in Figure 5. Barnett sample's conductivity is slightly higher than Marcellus and Eagle Ford, which may be due to the higher clay content (the kaolinite content of Barnett, Marcellus and Eagle Ford is 1.28%, 0.01% and 1.15%). Clay minerals usually present a greater cation exchange capacity (CEC) [122, 271]. Therefore, the higher clay content of the Barnett samples facilitates ion mobilization, and thus leads to the higher conductivity [115]. The EC versus concentration of Cl^-, K^+ and Ca^{2+} was plotted to further demonstrate

the validity of measured electrical conductivity (see Figures 6-6 b to d). In general, a linear relationship between conductivity and tested ions' concentration was observed, which supports the aforementioned results that conductivity increases with imbibition time and ion concentrations.
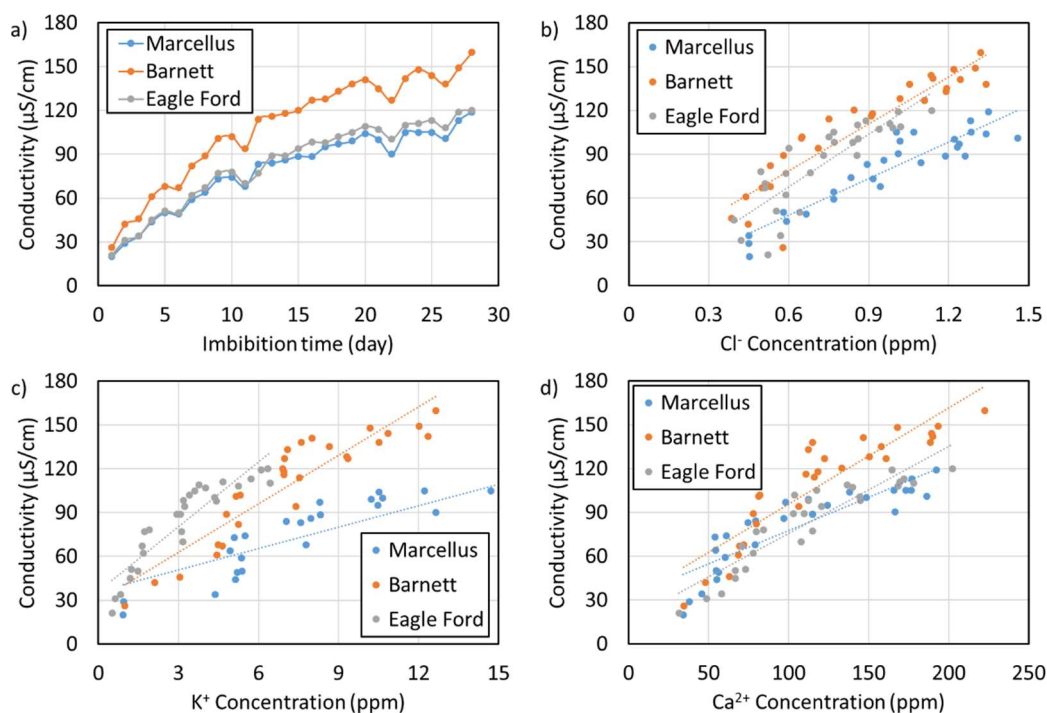
Figure 6-6 a) the EC of imbibed water versus with time, and the measured EC versus concentration of b) Cl⁻, c) K⁻ and d) Ca²⁺ at room temperature and atmospheric pressure.

6.5.4. Geochemical simulation

6.5.4.1. *Effect of fluid-shale interactions on water chemistry*

To validate the experimental results from geochemical perspective, we simulated the fluid chemistry with consideration of mineral dissolution (Table 6-4) and surface complexation (Table 6-2) at the same experimental conditions as spontaneous imbibition. The simulation results show that Eagle Ford has the higher pH (7.579) than Barnett (7.545) and Marcellus (7.483) (Table 6-5), which is in line with the measured pH given in Figure 6-3. However, the measured pH is slightly higher than the simulation results. One of the possible reasons is that in spontaneous imbibition tests, water may not reach all inner pores because of the low connectivity of shales [63]. However, in geochemical modelling, minerals and surface functional groups were

simulated to fully equilibrate with water. In this case, pyrite can complete react with water that contains dissolved O_2 and thus lower the pH [185]. Nevertheless, the predicted pH is still generally in line with experimental results. Clearly, the geochemical prediction supports the experimental observation with respect to pH and brine composition, which are key factors to affect mineral dissolution and surface complexation processes.

Table 6-5 Simulated fluid chemistry after mineral dissolution and surface complexation for Marcellus, Barnett and Eagle Ford samples, respectively.

	pH		Dissolved CO_2 (mol)		Ionic strength (M)		
Marcellus	7.483		4.795×10^{-3}		0.190		
Barnett	7.545		5.731×10^{-3}		0.133		
Eagle Ford	7.579		5.594×10^{-3}		0.107		
Species and concentration (mg/L)							
	AlO_2^-	HCO_3^-	SO_4^{2-}	CO_3^{2-}	Ca^{2+}	Mg^{2+}	Na^+
Marcellus	3.01	21.22	6582.86	0.07	2078.29	71.76	12.2
Barnett	3.88	23.80	4640.91	0.08	1410.86	49.95	8.88
Eagle Ford	4.47	25.27	3723.43	0.09	1134.86	40.73	7.44

Table 6-5 also shows that the TDS due to the fluid-rock interaction is dominated by SO_4^{2-} and Ca^{2+}, which further confirms that the pyrite oxidation and calcite dissolution are the main geochemical processes, resulting in local pH variation. However, the predicted Ca^{2+} concentrations of imbibed water after fluid-shale interaction (Table 6-5) is much higher than the experimental results presented in section 6.5.3. This is attributed to the sufficient mineral-fluid contact and equilibrium of geochemical reactions in geochemical simulation. To be more specific, pyrite oxidization generates H^+, which reacts with calcite and dolomite through the reaction: $FeS_2 + 3.75O_2(aq) + CaMg(CO_3)_2(s) + 1.5H_2O(l) \rightarrow Fe(OH)_3(s) + Ca^{2+}(aq) + 2SO_4^{2-}(aq) + 2CO_2(aq)$ [185]. Therefore, more Ca^{2+} would be released into solution in geochemical simulation compared to spontaneous imbibition experiments. Nevertheless, while all minerals were set to fully react with water, the simulated TDS is still less than 3% of flowback water salinity as reported by field. It is worth noting that the spontaneous imbibition experiments and corresponding geochemical simulations were performed under atmospheric conditions, where the consumed O_2 in water can always be supplemented by O_2 in air. In this case, the

presence of pyrite may significantly affect the pH and brine compositions. While in reservoir conditions, once hydraulic fracturing fluid is injected underground, no more O_2 would be supplied once it reacts with pyrite. Therefore, less H^+ and subsequently Ca^{2+} would be generated, which may further undermine the contribution of fluid-rock interaction on the high salinity of flowback water. Nevertheless, with the combination of experimental results and geochemical modelling, mineral dissolution and surface complexation would play a minor role in high salinity of flowback water.

6.5.4.2.   *Mineral dissolution*

To further validate the geochemical prediction with respect to pH and brine composition, the saturation index as a function of pH for calcite, albite, quartz, chalcopyrite, pyrite and dolomite at room temperature and atmospheric pressure are plotted in Figure 6-7. Given the similar simulated water chemistry of Marcellus, Barnett and Eagle Ford samples, the variations of indices of three shales are almost same so that we only plot the trend of Marcellus. The results indicate that the saturation indices of minerals except for pyrite and chalcopyrite at *in-situ* pH (7.6 based on the imbibition tests and 7.483 based on geochemical simulation) are nearly zero or positive, which means that these minerals tend to precipitate rather than dissolve [21, 175]. Pyrite and chalcopyrite would be completely oxidized by dissolved O_2, which gives a low level of saturation index. Combined with results of water chemistry simulation, we therefore conclude that mineral dissolution and surface complexation reaction would have limited contributions to high salinity of produced water during hydraulic fracturing in shales.
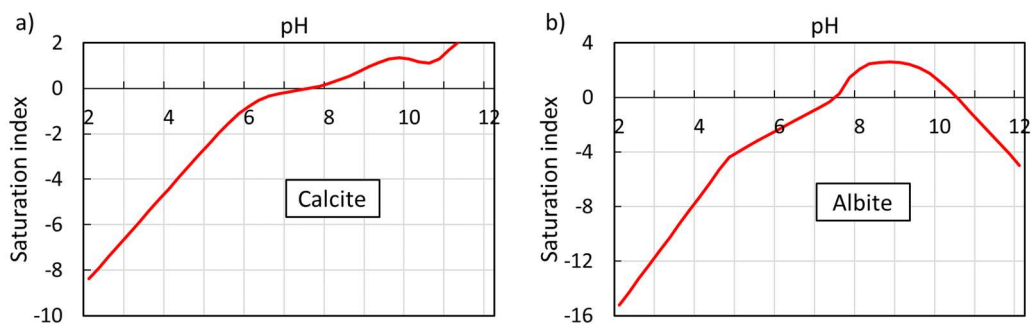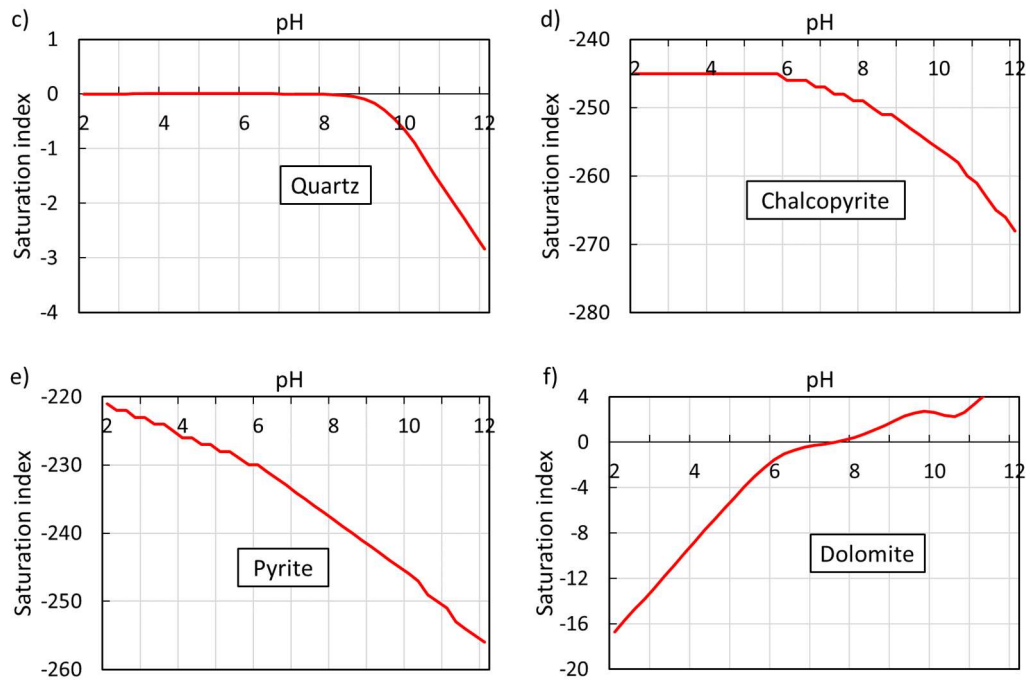
Figure 6-7 Saturation index versus pH of imbibed water for a) calcite, b) albite, c) quartz, d) chalcopyrite, e) pyrite and f) dolomite at ambient conditions.

Now that mineral dissolution has been shown to play a minor role in the high salinity, we suggest that the reported high TDS is due to the high salinity of initial formation brine [116]. This innate brine can be trapped in pores and micro-fractures inside the shale matrix [116, 121]. With the implementation of multi-stage hydraulic fracturing, some of the inner pores and pre-existing micro-fractures would be connected with the main hydraulic fracture. During the flowback process and hydrocarbon production, the mixture of injected fluid and innate formation brine can flow to the wellbore under generated pressure gradients. Besides, this pressure gradient may also prevent underground brines from migrating upward, which further holds the produced high salinity [272, 273].

6.6. Conclusions

In this study, spontaneous imbibition experiments was performed using deionised water and intact outcrops from Marcellus, Barnett and Eagle Ford shale plays under room temperature and atmospheric pressure. The surrounding fluid chemistry such as pH, electrical conductivity and ion concentrations (Cl^-, K^+, Ca^{2+}, NO_3^-, F^-, Br^- and NH^+) was monitored every twenty-four hours in consecutive four weeks. We also performed geochemical modelling to examine the contribution of fluid-shale

interaction such as mineral dissolution and surface complexation to the high salinity of flowback water. The main conclusions can be drew as the following:

- Barnett samples imbibed more deionised water (1.4%) than Marcellus (1.0%) and Eagle Ford (0.7%). This is likely attributed to the higher content of calcite and lower content of hydrophobic organic matter.

- The order of sequence of experimentally measured pH (Eagle Ford (8.3) > Barnett (8.0) > Marcellus (7.6)) is in line with simulation results (Eagle Ford (7.579) > Barnett (7.545) > Marcellus (7.483)), confirming the importance of pyrite oxidation on local pH at ambient condition. The slightly discrepancy in pH magnitude is likely due to the non-equilibrium thermodynamics in particular the pyrite oxidation during spontaneous imbibition process.

- The concentrations of Cl^-, K^+ and Ca^{2+} for tested samples increase over imbibition time. Marcellus samples contain higher K^+ (18 mg/L) than Barnett (13 mg/L) and Eagle Ford (6 mg/L). The concentration of Ca^{2+} (200 mg/L) and Cl^- (1.3 mg/L) are roughly equivalent for all samples at the end of imbibition and are much less than the field observation (e.g., 300,000 mg/L), which suggests that mineral dissolution is minor.

- With consideration of fully reaction between fluid and minerals in geochemical modelling, the maximum TDS of fluid saturated with Marcellus, Barnett and Eagle Ford samples is less than 3% of flowback water salinity. This simulation result is slightly higher than experimental observation due to the fully equilibrium between shale and water, but is still much less than the field observation. This result further confirms that the contribution of mineral dissolution on high salinity flowback water is negligible.

7. Chapter 7 Effect of Pyrite Oxidation on Flowback Water Properties during Hydraulic Fracturing in Calcite-Rich Shales

7.1. Abstract

Megalitres of water with associated dissolved oxygen are injected into shale reservoirs during the hydraulic fracturing process. Pyrite oxidation, if it occurs *in-situ*, can generate extra H^+, thereby dissolving calcite and increasing the salinity of flowback water. The process of calcite dissolution may soften the hydraulic fracture surfaces, resulting in proppants embedment and thus decreasing fracture conductivity for calcite-rich shales. Therefore, it is of vital importance to understand the impact of *in-situ* pyrite oxidation on fluid-shale interactions, particularly calcite dissolution, to help industry screen and design hydraulic fracturing fluids in shales. Spontaneous imbibition experiments were performed using Marcellus shale samples under three conditions: i) ambient conditions, where the fluid was in equilibrium with atmospheric air throughout the tests, ii) limited O_2 condition, where the fluid was free equilibrated with air in a sealed cylinder and iii) vacuum condition, where the fluid in a sealed cylinder was degassed. The pH and ion concentrations were measured upon completion of the experiments. To further explore how pyrite oxidation affects fluid-rock interactions, we performed geochemical simulations with considerations of mineral dissolution (calcite, albite, quartz, chalcopyrite, pyrite and dolomite), surface complexation and the dissolved O_2 on fluid salinity.

The spontaneous imbibition tests show that the salinity of fluids in ambient conditions is higher than the limited or vacuumed saturation fluids, confirming that pyrite oxidation generates H^+ which would dissolve minerals such as calcite and dolomite. This result is also supported by the observed pH and the concentration of dissolved Ca^{2+}. The fluid fully saturated with O_2 has the lowest pH and highest Ca^{2+} compared to limited O_2 saturation condition and degassed condition. Scanning electron microscopy analyses show that brine saturation barely affects the morphology and elemental distribution of pyrite at ambient conditions, suggesting that pyrite oxidation plays a minor role in fluid salinity. Geochemical modelling also indicates that although pyrite oxidation can slightly increase fluid salinity, the salinity increment is less than 5% of reported flowback water salinity, confirming that the dissolved O_2 in hydraulic fracturing fluids has a minor effect on fluid-rock interaction thus the salinity

increment. This work demonstrates that pyrite dissolution at lab-scale would overestimate the impact of fluid-shale interactions and calcite dissolution in reservoir conditions. We prove that pyrite dissolution in *in-situ* conditions results in minor implications for fluid-shale interactions and calcite dissolution. Consequently, we limit intrinsic uncertainty of hydraulic fluid design associated with pyrite oxidization especially for calcite-rich shales.

Keywords: Shale reservoirs, Hydraulic fracturing, Flowback water chemistry, Spontaneous imbibition, Pyrite oxidation.

7.2. Introduction

The prodigious developments of multi-stage horizontal drilling and hydraulic fracturing have been boosting the exploitation of unconventional resources, typically shale oil and gas [234, 274]. To effectively 'unlock' shale gas from tight shale formations which have low porosity and ultra-low permeability (from nanodarcy to millidarcy) [239], approximately 10,000-75,000 m^3 water per well with proppants and other additives such as biocide, corrosion inhibitor and friction reducer are injected underground at high pressure to generate fractures [217, 263]. The generated fractures can communicate and activate pre-existing natural micro-fractures, which increases formation connectivity and thus enhances shale gas production [39, 217]. Afterwards, flowback water (or so-called produced water) combined with hydrocarbons are withdrawn during the production stage and processed before reusing for next fracking [113, 185, 275].

During the implementation of fracking, oxygen that dissolved in the fracturing fluid is introduced to deep, anoxic formations [185]. The extraneous oxygen may react with O_2-sensitive minerals, pyrite in particular, and generate extra H^+, which would further dissolve other minerals such as calcite and dolomite, thereby increasing the salinity of flowback water [91, 115, 121, 185]. It is reported that the total dissolved solids (TDS) of flowback water after fracking can be as high as 280,000 ppm with a certain amount of cations and anions including Na^+, K^+, Ca^{2+}, Mg^{2+}, Fe^{3+}, Ba^{2+}, Cl^-, SO_4^{2-} and also trace metals such as Cr, Cu, Pb, Cd, Hg, Ni, Ag, and Zn [16, 27, 113, 275-278]. For example, Zolfaghari et al. (2016) reported the flowback water compositions of three formations in Horn River Basin, Canada. The field data show that the concentration of

Cl⁻ after 500 hours production can be up to 20,000 to 45,000 mg/L. Blauch et al. investigated major element chemistry (Na^+, K^+, Ca^{2+}, Mg^2, Cl^-, SO_4^{2-}) of flowback water from two Marcellus shale wells. The salinity of collected samples after 30 days production ranges from 117,000 to 124,000 mg/L. Gregory et al. also reported that the average TDS of produced water in late flowback in Marcellus shales is 261,000 mg/L, which contains approximately 148,000 mg/L of Cl^-, 44,000 mg/L of Na^+ and 31,000 mg/L of Ca^{2+}. The high concentrations of TDS covered in flowback water are costly to treat and challenging the protection of groundwater and surface water resources [273, 276]. If the high salinity was triggered by pyrite oxidation associated mineral dissolution, the fracking fluid should be degassed to remove the dissolved O_2 before use so that it could restrain the *in-situ* salinity increment. However, Xu et al. reported that compared to the degassed water used in spontaneous imbibition experiments, the oxic water had negligible effect on the concentration increment of K^+, Na^+ and Cl^-, whereas it can notably increase the concentration of Fe^{2+}/Fe^{3+} and SO_4^{2-}. Our previous work also shows that the salinity increment due to fluid-shale interactions may be less than 5% of reported field flowback water salinity, although more quantitative studies should be performed to unveil the role of pyrite oxidation associated mineral dissolutions on flowback water properties [58].

Moreover, the fluid-rock interactions can affect shale mechanical properties, including bulk strength [29-33], Young's modulus [35-37, 55], brittleness index [37, 39] and subcritical crack growth [40-42, 44, 62]. Published works indicate that the oxidation of pyrite can change pore structure and increase pore networks connectivity, which would facilitate ion transportation from the shale matrix to the generated fractures [185, 279, 280]. For example, Chen et al. oxidized black shale rock from Longmaxi formation using hydrogen peroxide (H_2O_2) to examine the effect of oxidative dissolution on the shale structure. Their results indicate that carbonate and Fe^{2+} associated minerals such as chlorite and pyrite exhibit observable dissolution after the treatment, and the porosity and connectivity of pore networks of shale matrix are enhanced. However, calcite dissolution may also soften and weaken fracture surfaces, resulting in proppants embedment issues and thus decreasing fracture conductivity in calcite-rich shales [35, 48, 158]. For instance, Corapcioglu et al. measured the Young's modulus of Niobrara shale before and after saturation by fracturing fluids for 30 days. They reported that the Young's modulus can be decreased by 80%, which was mainly

caused by the dissolution and weakening of calcite. The significant reduction of Young's modulus negatively impacts the proppants pack on fracture surfaces, which decreases the rock conductivity and thus influencing hydrocarbon production. Consequently, there is a pressing need to quantitatively characterize the role of pyrite oxidation associated calcite dissolution, which can (i) help industry to manage the flowback water chemistry, (ii) evaluate shale formation stimulation/damage, and (iii) screen and design appropriate hydraulic fracturing fluid for calcite-rich shales.

In this study, we aim to examine the contribution of pyrite oxidation on calcite dissolution and the high salinity of flowback water. Spontaneous imbibition experiments using sections from Marcellus and Eagle Ford formations were performed under three conditions: (i) ambient condition, where fluid was free to equilibrate with O_2 in the atmosphere throughout the tests, (ii) limited O_2 condition, where fluid would only react with limited amount of air in a sealed cylinder, and (iii) vacuumed condition, where fluid in the sealed cylinder was degassed. The pH, oxidation-reduction potential (ORP), electrical conductivity (EC) and ion concentrations were measured periodically. To further explore how pyrite oxidation affects fluid-rock interactions, we performed geochemical simulations with consideration of mineral dissolution (calcite, albite, quartz, chalcopyrite, pyrite and dolomite), surface complexation and the dissolved O_2/CO_2 on fluids chemistry.

7.3. Spontaneous Imbibition Experiments

7.3.1. Rock mineralogy

Considering that mineral composition significantly affects fluid-shale interactions such as mineral dissolution and surface complexation, and thus the surrounding fluid properties, we first examined the mineralogy of the outcrop samples from Marcellus and Eagle Ford shale plays (Table 7-1). The results show that all tested samples from both formations are calcite-rich from 66.8 to 71.3%. Eagle Ford rock has a tiny amount of kaolinite (1.15%) but other clay minerals are negligible. Marcellus samples have less quartz but more pyrite than Eagle Ford samples. Besides, Rock-Eval test indicates that the total organic carbon (TOC) of Eagle Ford samples (3.48%) is slightly higher than Marcellus (2.28%).

Table 7-1 The mineralogy of tested shale sample from Marcellus and Eagle Ford (wt%) [58].

	Quartz	Calcite	Albite	Illite	Muscovite	Biotite	Mica
Marcellus	7.15	71.30	10.36	0.22	2.14	0.02	0.01
Eagle Ford	16.66	66.80	8.90	0.25	0.00	0.14	0.00
	Dolomite	Kaolinite	Montmorillonite	Pyrite	Chlorite	Chalcopyrite	TOC
Marcellus	1.20	0.01	0.00	2.95	0.10	4.53	2.28
Eagle Ford	1.13	1.15	0.00	0.81	0.67	3.49	3.48

7.3.2. Spontaneous imbibition tests

To examine the role of pyrite oxidation in mineral dissolution and the subsequent fluids' salinity increment, spontaneous imbibition experiments were performed under three different conditions: (i) ambient condition, where fluid was eligible to access the O_2 from atmosphere throughout the tests, (ii) limited O_2 condition, where fluid would only react with air in limited space of a sealed cylinder, and (iii) vacuumed condition, where fluid in the sealed cylinder was fully degassed (Figure 7-1). The difference between ambient and limited air conditions is that for ambient condition, aqueous O_2 can be always supplemented by equilibration with atmosphere after consumption, while for limited air condition, no more $O_{2(aq)}$ is available once it is consumed before the sealed system is opened).
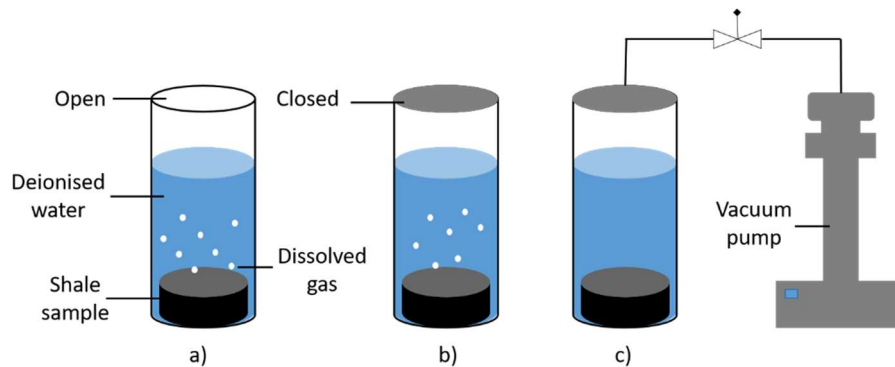
Figure 7-1 Schematic of spontaneous imbibition for a) ambient condition, b) limited O_2 condition and c) vacuum condition.

Spontaneous imbibition experiments under all three conditions follow the steps below: (i) the intact shale plugs were cut into cylinder samples with diameter of 38.0 mm and height of 9.8 mm; (ii) the cut samples were dried in the oven with temperature of 100°C for 48 hrs; (iii) the weight of dry sample was recorded before spontaneous imbibition

experiment; (iv) samples were immersed into 800 mL deionised (DI) water in the 1 L cylinders. The cylinder was kept open throughout the test for ambient condition and was closed for limited O_2 and vacuum conditions. (v) The weight of wet sample at ambient condition was measured every 24 h in consecutive 30 days. For the other two scenarios, weight can only be recorded after cylinder was opened due to the system limitation. Then the samples were keeping saturated in DI water for another 20 days and samples' weight was measured every 24 h during this period. (vi) Fluid chemistry, including pH, electrical conductivity, oxidation-reduction potential and ion concentrations (K^+, Ca^{2+}, NH^+, Cl^-, NO_3^-, F^-, and Br^-), were monitored using ELIT Compact On-Site Fluid Analyzer (NICO 2000, Ltd.) (Figure 7-2) [58]. Before the formal measurement, the corresponding ion-selective electrodes were calibrated by standard pH buffers (pH 4, 7 and 10) and standard solutions (1, 10 100 and 1000 mg/L for the selected ions) [58]. Similar to weight measurement, the fluid chemistry at ambient condition was recorded every 24 h in the first 30 days. For the other two conditions, the fluid properties were measured after opening the cylinder (from the 31st to the 50th day). (vii) The scanning electron microscopy (SEM) analysis was undertaken before and after saturation of representative Marcellus shale samples using a Mira-3 Variable Pressure Field Emission Electron Microscopy (VP-FESEM) with energy dispersive x-ray spectroscopy (EDS) and Electron Backscattered Diffraction (EBSD) located at the Microscopic and Microanalysis Facility (MMF), John De Laeter Centre, Curtin University. The samples were polished, and carbon coated. The imaging was carried out under working conditions (10-15 kev) to provide the variation of morphology and elemental distribution before and after fluid-rock interactions.

Figure 7-2 Ion-selective electrodes for water chemistry measurements during spontaneous imbibition tests [58].

7.4. Geochemical Simulation

To examine the role of fluid-shale interactions in water chemistry during spontaneous imbibition process, mineral dissolution modellings were performed using PHREEQC (V3.5.0 plugged in Notepad++ V7.7.1 with the database of Lawrence Livermore National Laboratory thermo.com.V8.R6.230) [21, 85, 174]. On the basis of mineralogy reported in Table 7-1, calcite ($CaCO_3$), dolomite ($CaMg(CO_3)_2$), quartz (SiO_2), pyrite (FeS_2), chalcopyrite ($CuFeS_2$) and albite ($NaAlSi_3O_8$) were selected to quantify their dissolution ability at *in-situ* conditions. Table 7-2 shows the dissolution reactions of these minerals and the corresponding equilibrium constant at 25°C.

Table 7-2 Mineral dissolution reactions during spontaneous imbibition [174].

Mineral	Geochemical reactions	log K_{298K}
Calcite	$CaCO_3 + H^+ = Ca^{2+} + HCO_3^-$	1.85
Dolomite	$CaMg(CO_3)_2 + 2\ H^+ = Ca^{2+} + Mg^{2+} + 2\ HCO_3^-$	2.51
Quartz	$SiO_2 = SiO_2$	-3.99
Pyrite	$FeS_2 + H_2O = 0.25\ H^+ + 0.25\ SO_4^{2-} + Fe^{2+} + 1.75\ HS^-$	-24.65
Chalcopyrite	$CuFeS_2 + 2\ H^+ = Cu^{2+} + Fe^{2+} + 2\ HS^-$	-32.56
Albite	$NaAlSi_3O_8 + 4\ H^+ = Al^{3+} + Na^+ + 2\ H_2O + 3\ SiO_2$	2.76

Calcite surface complexation modelling (SCM) was also performed to characterize the ion attachment-detachment ability from the surface of these calcite-rich shale samples, which may affect fluid salinity variations. Table 7-3 lists the surface complexation reactions on calcite surfaces at room temperature [89, 182]. The surface site density of calcite was set to 5.0 $\mu mol/m^2$ and specific area 2.8 m^2/g [90, 179].

Table 7-3 Calcite surface complexation reactions at room temperature [89, 182].

Geochemical reactions	log K_{298K}
$>CaOH + H^+ = >CaOH_2^+$	11.9
$>CaOH + HCO_3^- = >CaCO_3^- + H_2O$	5.8
$>CaOH_2^+ + SO_4^{2-} = >CaSO_4^- + H_2O$	2.1
$>CO_3H = >CO_3^- + H^+$	-5.1
$>CO_3H + Ca^{2+} = >CO_3Ca^+ + H^+$	-2.6

Given that the dissolved O_2 in fluids at ambient and limited air conditions can oxidize certain minerals (particularly pyrite and chalcopyrite), and thus affect *in-situ* pH and other geochemical reactions, the O_2/fluids equilibrations were considered in this work. Table 7-4 lists the main reactions associated with O_2-related geochemical processes [174]. Meanwhile, dissolved CO_2 can generate extra H^+ and promote calcite dissolution. Therefore, we also combined CO_2-related reactions with other geochemical reactions as aforementioned (Table 4-5) [174, 281, 282]. The input of log of partial pressure of CO_2 and O_2 is set as -3.4 and -0.67.

Table 7-4 Batch reactions of dissolved O_2 [174].

Geochemical reactions	log K_{298K}
$0.5\ O_2 + Cl^- = ClO^-$	-15.1
$O_2 + Cl^- = ClO_2^-$	-23.1
$1.5\ O_2 + Cl^- = ClO_3^-$	-17.3
$2\ O_2 + Cl^- = ClO_4^-$	-15.7
$2\ H^+ + 2\ SO_3^{2-} = S_2O_4^{2-} + 0.5\ O_2 + H_2O$	-25.2
$2\ SO_3^{2-} = S_2O_6^{2-} + 2\ e^-$	41.8
$2\ SO_3^{2-} + 1.5\ O_2 + 2\ H^+ = 2\ SO_4^{2-} + H_2O$	70.7
$0.5\ O_2 + 2\ HS^- = S_2^{2-} + H_2O$	33.3
$O_2 + H^+ + 3\ HS^- = S_3^{2-} + 2\ H_2O$	79.4
$1.5\ O_2 + 2\ H^+ + 4\ HS^- = S_4^{2-} + 3\ H_2O$	125.3
$H^+ + Fe^{2+} + 0.25\ O_2 = Fe^{3+} + 0.5\ H_2O$	8.5
$2\ H_2O + Fe^{2+} = Fe(OH)_2 + 2\ H^+$	-20.6
$3\ H_2O + Fe^{3+} = Fe(OH)_3 + 3\ H^+$	-12

Table 7-5 Batch reactions of dissolved CO_2 [174, 281, 282].

Geochemical reactions	log K_{298K}
$CO_{2(aq)} + H_2O = H_2CO_3$	-2.6
$CO_{2(g)} + H_2O = H^+ + HCO_3^-$	-7.8
$H_2CO_3 = H^+ + HCO_3^-$	-3.8
$HCO_3^- = H^+ + CO_3^{2-}$	-10.3
$HCO_3^- + H^+ = CO_2 + H_2O$	6.3

7.5. Results and Discussions

7.5.1. Water update

Figure 7-3 shows the weight increment of dry samples from Marcellus and Eagle Ford shale plays at ambient, limited air and vacuum conditions, respectively. As aforementioned, samples at all conditions were immersed in DI water from the 1st day. The sample weight at ambient conditions was measured every 24 hours (from the 1st to 30th day in Figure 7-3). The weight at limited air and vacuum conditions could only be recorded once the sealed cylinder was open (from the 31st to 50th day). It can be seen that most of the water uptake occurs during the first several days and thereafter the sample weight slowly reaches a plateau. After 30 days of saturation, the sample at ambient condition imbibed more water (0.70% for Eagle Ford) than limited air (0.63%) and vacuum (0.56%) conditions. This result can be attributed to the different capability of three tests in contact with oxygen. For ambient conditions, the O_2 in the atmosphere is free to equilibrate with the imbibition fluid so that the fluid contains the maximum amount of aqueous O_2. The $O_{2(aq)}$ can oxidize pyrite through the reaction:

$$FeS_2 + 154 \, O_2 + 7 \, H_2O \rightarrow Fe(OH)_3 + 2 \, H_2SO_4$$
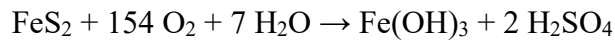
and generate H^+ [185, 269]. These extra H^+ would then dissolve calcite and increase rock internal connectivity and thus facilitate water uptake. However, for limited air and vacuum conditions, the shale samples and fluids have very limited access to O_2 compared to ambient condition. Therefore, pyrite is hardly to be oxidized and much less H^+ would be generated to dissolve carbonate. As a result, the shale samples at these two conditions remain tight and low connectivity, which is harder to imbibe water.
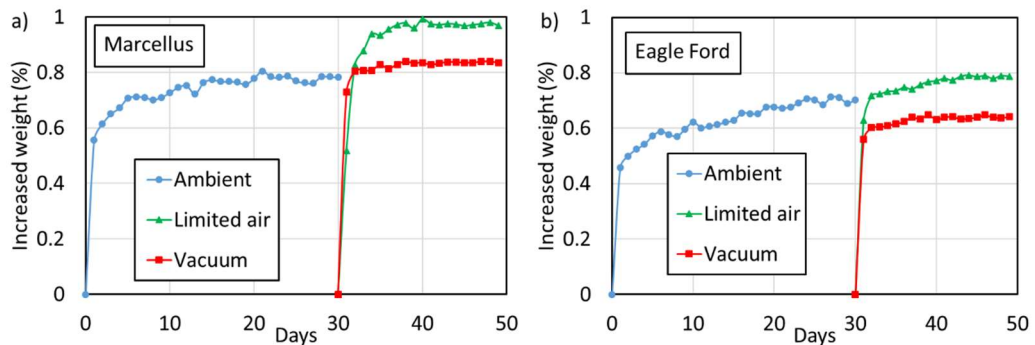
Figure 7-3 Weight increment of shale samples from a) Marcellus and b) Eagle Ford shale plays at ambient, limited air and vacuum conditions, respectively.

However, once the fluids at limited air and vacuum conditions are able to access O_2 in the atmosphere (from the 31st to 50th day in Figure 7-3), the shale rocks can quickly imbibe water. Samples at initially limited air condition even imbibed more water than ambient conditions. One of the possible reasons is that rock sample can still react with the small amount of $O_{2(aq)}$ available during the sealed imbibition process. Although the extent of this pyrite oxidation and calcite dissolution is weaker and slower than the ambient condition, these reactions still take place. Once the cylinder is opened and imbibition water gets in contact with air, the new dissolved O_2 would further oxidize pyrite and release more H^+. Consequently, micro-fractures in the rock at limited air conditions would reach deeper parts of the sample and the connectivity would be further enhanced. Therefore, the rock at initially limited air conditions imbibed more water than the ambient condition as observed in Figure 7-3.

7.5.2. pH and ORP

Fluid pH is another indicator that represents the extent of *in-situ* geochemical reactions such as pyrite oxidization, and strongly affects mineral dissolution. Figure 7-4 shows the results of varying pH with spontaneous imbibition time for Marcellus and Eagle Ford shale samples at three O_2 levels. With consideration of measuring errors, pH at ambient condition slightly fluctuates around 8.0 during the whole imbibition process. This weak alkalinity is mainly caused by the strong reaction: $>CaOH + H^+ = >CaOH^{2+}$ (Table 7-3) that takes place on calcite surfaces, which decreases H^+ concentrations and increases *in-situ* pH. Besides, calcite dissolution can consume extra H^+ generated by pyrite oxidation, which would also increase pH. Similar results were observed by Xu et al. [185], Zolfaghari et al. [115] and Zeng et al. [58], who reported that the pH of DI water after spontaneous imbibition tests would range from 8.0 to 8.5.
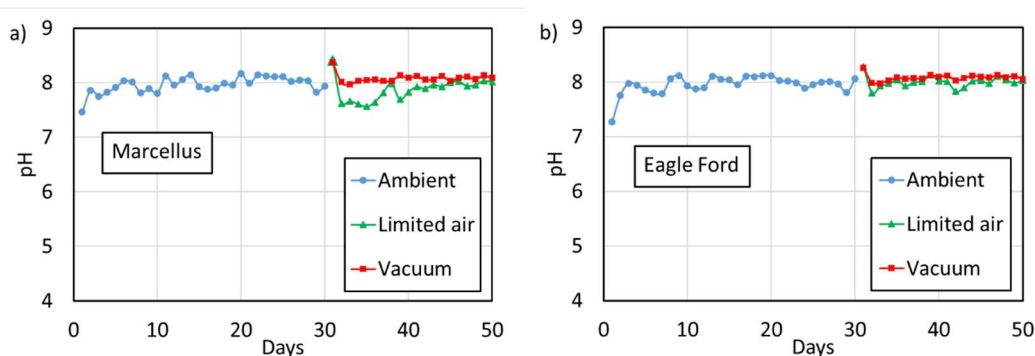
Figure 7-4 pH varies with imbibition time for a) Marcellus and b) Eagle Ford shale samples at ambient, limited air and vacuum conditions, respectively.

For the limited air and vacuum conditions, fluid pH presents higher values (8.4 for Marcellus and 8.28 for Eagle Ford) compared to ambient conditions. Since under limited O_2 or anoxic environments, the reaction of pyrite oxidation becomes limited, which releases less H^+ than in an aerobic environment. However, the complexation between calcite surface groups >CaOH and H^+ is not affected. Therefore, fluids of these two cases show higher pH. Once the sealed fluids come into contact with air, the pH under these two conditions rapidly drops back to the same level as ambient conditions. These results indicate the importance of aqueous O_2 in regulating *in-situ* pH and calcite dissolution, which directly affects the ion concentrations of the surrounding fluids that will be discussed in subsection 7.5.4.

We also monitored oxidation-reduction potential (ORP, also known as redox potential of the fluids during the imbibition progress (Figure 7-5). The ORP is a measurement of the ability of a chemical species or molecule to lose electrons (oxidation) or acquire electrons (reduction) to another chemical species or molecule [283, 284]. A positive ORP value indicates an oxidizing environment. In this experiment, the ORP at limited air condition after coming in contact with air has a higher average value than ambient or vacuum conditions for both Marcellus and Eagle Ford shale samples. In other words, when fluid at limited air condition can equilibrate with air, it would have greatest ability to oxidize pyrite and chalcopyrite. Consequently, calcite can be dissolved by the released H^+ and micro-pores/micro-fractures would be generated. This process enhances the connectivity of whole pore networks, and also explains why sample at initially limited air condition can imbibe highest amount of water after contacting with air.
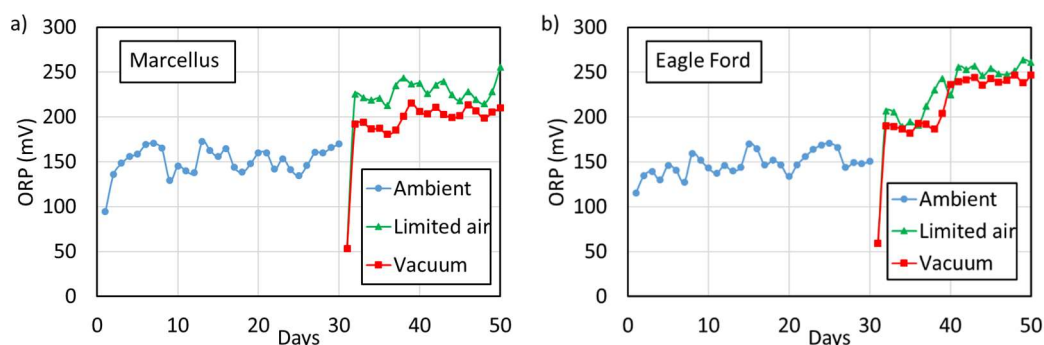
Figure 7-5 Oxidation-reduction potential varies with imbibition time for a) Marcellus and b) Eagle Ford shale samples at ambient, limited air and vacuum conditions, respectively.

7.5.3. Ion centration and EC

The concentrations of Cl^-, K^+ and Ca^{2+} of the fluid varying with spontaneous imbibition time at different O_2 level are presented in Figure 7-6. Concentrations of the other measured ions such as NH^+, NO_3^-, F^-, and Br^- were not detectable. After 30 days imbibition, the concentrations of these ions at limited air and vacuum conditions are much less than ambient condition. Combined with observations of water uptake and pH, this result again shows that the anoxic environment would weaken the pyrite oxidation and release less H^+ to dissolve calcite. As a result, fewer concentrations of Cl^-, K^+ and Ca^{2+} can be generated at low $O_{2(aq)}$ levels. Because the real underground conditions in shale fields are mostly similar to the limited air condition in the experiments, where pyrite can only react with the O_2 dissolved in the injected hydraulic fracturing fluid, our results imply that the traditional experiment of ambient spontaneous imbibition at lab-scale would overestimate the impact on fluid-shale interactions at reservoir conditions. In other words, although the lab measured fluid salinity is much less than the field records by several orders of magnitude (e.g., the lab-measured salinity of Marcellus is around 350 to 450 mg/L, whereas the TDS of flowback water form Marcellus gas wells can be as high as 228,000 mg/L [112]), we may still overestimate the level of aqueous ions generated through fluid-shale interactions.
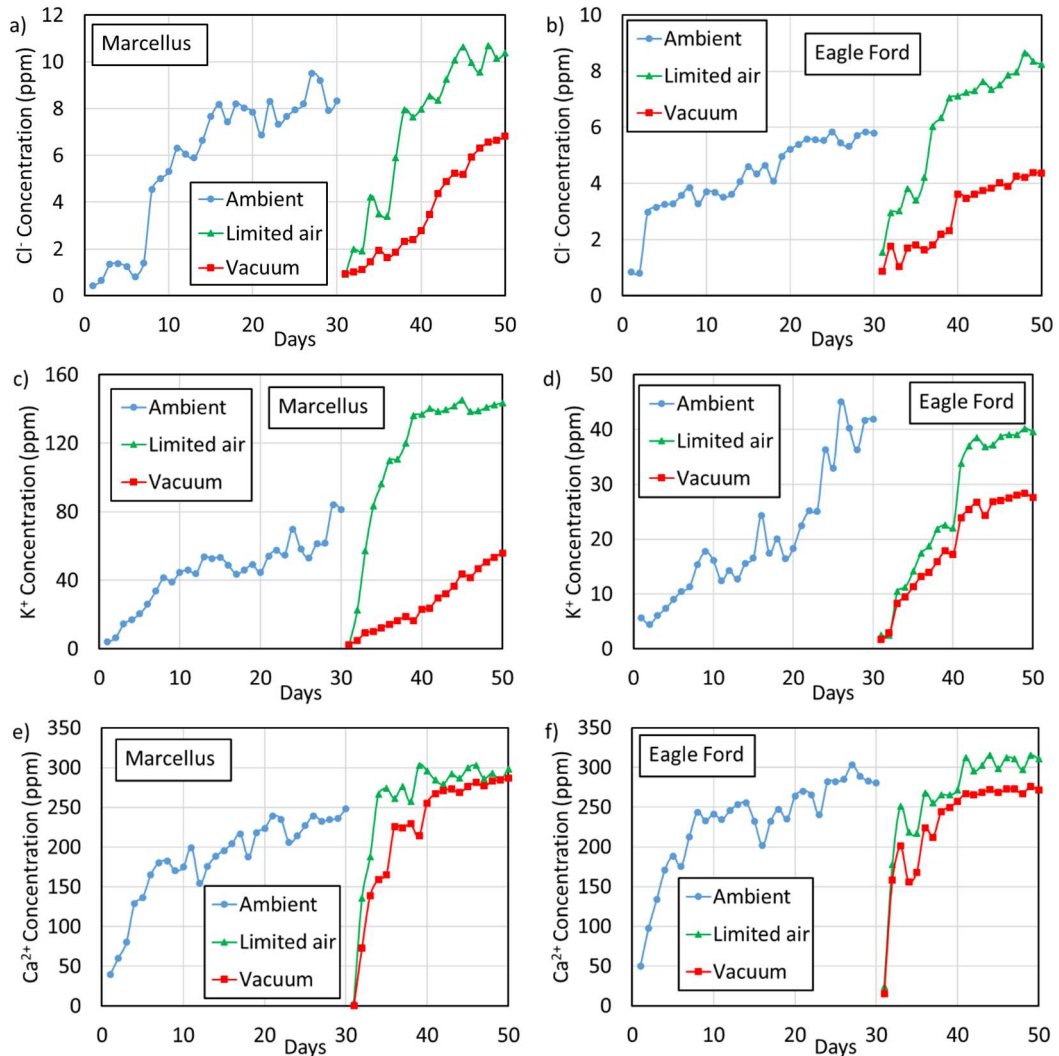
Figure 7-6 Ion concentration for Marcellus and Eagle Ford shale samples varies with imbibition time for Cl⁻, K⁺ and Ca²⁺ at ambient, limited air and vacuum conditions, respectively.

When the fluids at limited air and vacuum conditions come in contact with air (from the 31st to 50th day in Figure 7-6), the concentration of Cl⁻, K⁺ and Ca²⁺ increases rapidly. The ion concentrations at initially limited air condition is even higher than the continuously ambient condition at the end of experiments. As aforementioned, the pyrite oxidation and calcite dissolution can still take place at low $O_{2(aq)}$ levels in the sealed cylinder. Once the fluid is able to equilibrate with air, micro-fractures can extend to the deeper part of the rock, and thus generate more ions. Meanwhile, the pre-existing salts precipitated on the surface of micro-pores and micro-fractures could also dissolve into the imbibed fluids and increase salinity. Given that the fluid salinity at the end of these experiments is only 2% of field observations, our results imply that the fluid-shale interactions (pyrite oxidation and calcite dissolution) and salt

dissolution may not be the main source of the aqueous ions; the mixing of fracturing water with high salinity formation brine should play the dominant role in the high TDS of flowback water during hydraulic fracturing.
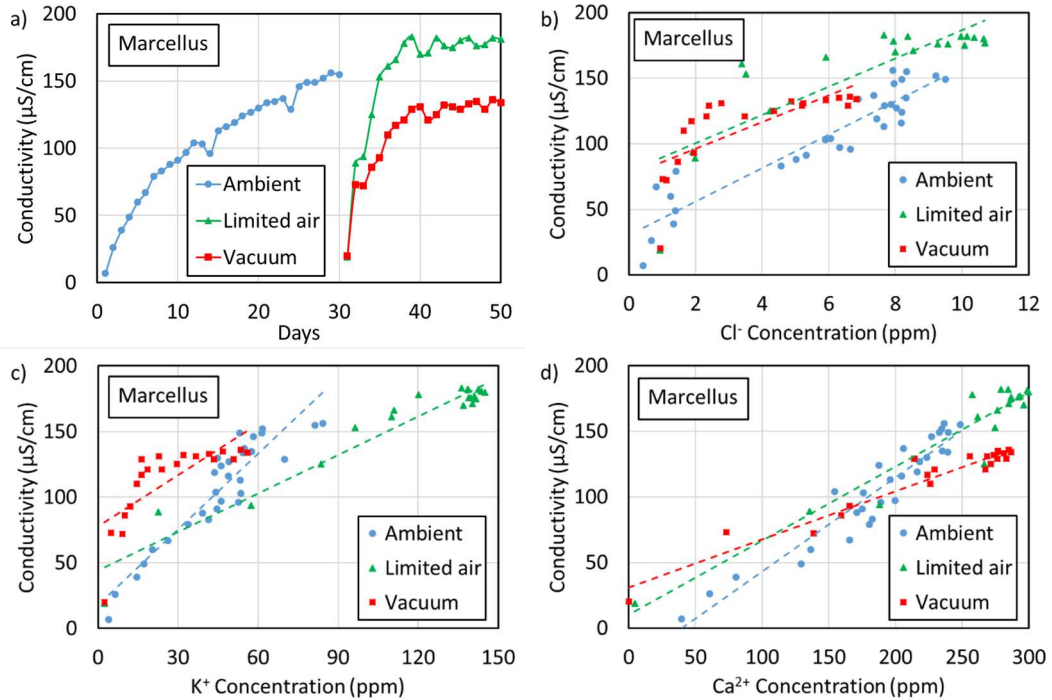
Figure 7-7 a) Electrical conductivity of surrounding fluid regarding Marcellus sample varies with imbibition time. b-d) EC versus concentration of Cl^-, K^+ and Ca^{2+} at ambient, limited air and vacuum conditions, respectively.
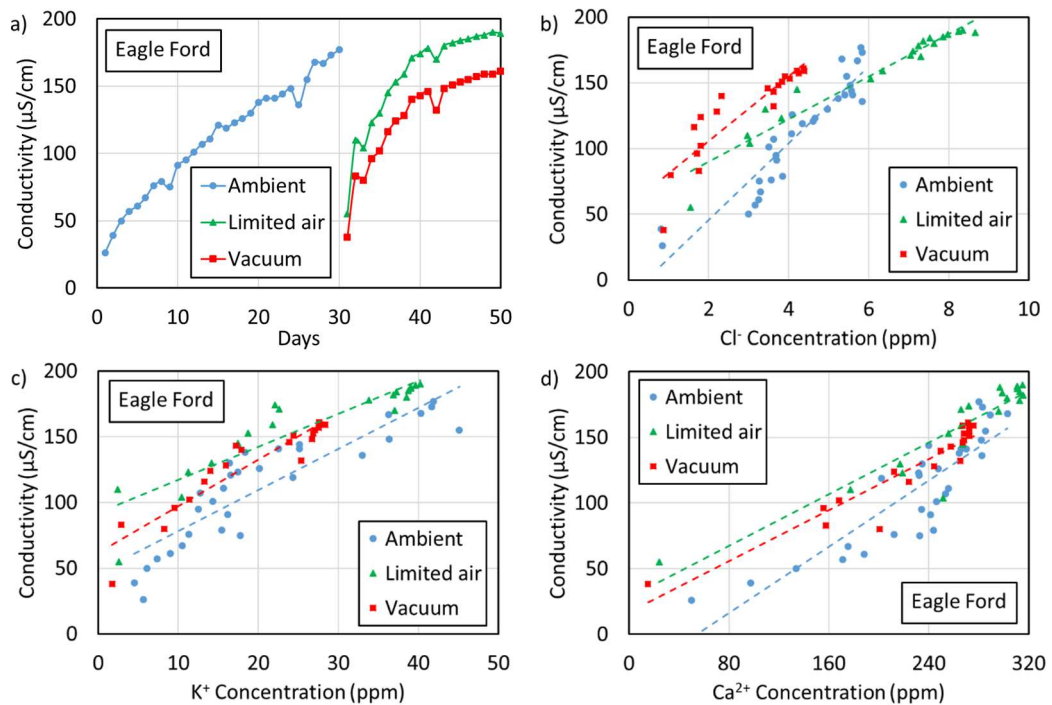
Figure 7-8 a) Electrical conductivity of surrounding fluid regarding Eagle Ford sample varies with imbibition time. b-d) EC versus concentration of Cl$^-$, K$^+$ and Ca^{2+} at ambient, limited air and vacuum conditions, respectively.

Electrical conductivity (EC) of imbibed fluid with respect to the Marcellus (Figure 7-7a) and Eagle Ford (Figure 7-8a) samples was also monitored to examine the accuracy of recorded ion concentrations. In general, the EC gradually increases with imbibition time when fluids are able to equilibrate with atmospheric air, which is in line with results of ion concentrations shown in Figure 7-8. At the end of 30 days imbibition, the EC under ambient conditions is much higher than that under limited air and vacuum conditions, which again indicates that pyrite oxidation and the subsequent calcite dissolution would not likely occur in anoxic environments. Panels b-d of Figures 7-7 and 7-8 show the relationship between EC and the concentration of Cl$^-$, K$^+$ and Ca^{2+}, respectively. The linear relationship further proves that ion concentration and EC increase with imbibition time as the result of fluid-shale interactions.

7.5.4. Scanning electron microscopy analyses

To directly observe the changes of pyrite before and after fluid-rock interactions, we performed SEM imaging using Marcellus shale samples that were saturated in water under ambient conditions. The SEM results integrated with X-ray Diffraction (XRD) analysis show that the samples consist of primary pyrite crystals and pyrite framboids associated with other inorganic minerals such as calcite, quartz, illite and kaolinite (Figure 7-9 and 7-10). After 10 days water saturation, we did not observe significant changes of the morphology of pyrite (Figure 7-9). From the EDS-SEM images (Figure 7-10), we also noticed that no obvious changes of elemental distribution appeared on pyrite surfaces after water saturation. The Marcellus shale comprised of Fe and S due to the pyrite and there is no OH$^-$ ion addition due to the saturation. Combined with the spontaneous imbibition results, the SEM analyses indicate that although pyrite oxidation can take place during the fluid-rock interaction process, and can slightly affect the water chemistry such as pH and EC, it still plays a minor role in the fluid salinity increment. In other words, although pyrite oxidation would facilitate calcite dissolution at lab-scale (in terms of the ambient conditions where O$_2$ can always keep equilibrating with water), we may still overestimate the its impact on fluid-shale

interactions and calcite dissolution at reservoir conditions, where much less amount of dissolved O_2 can exist in the formation brine.
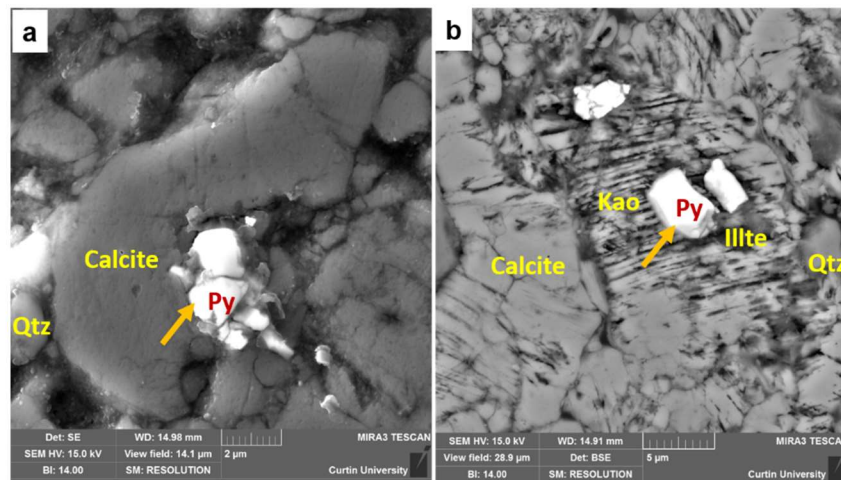
Figure 7-9 The SEM images showing pyrite presence in the shale indicated by orange arrows, a) secondary electron (SE) imaging before brine saturation, and b) back-scattered imaging after saturation. Kao and Qtz stands for kaolinite and quartz in the figure respectively.
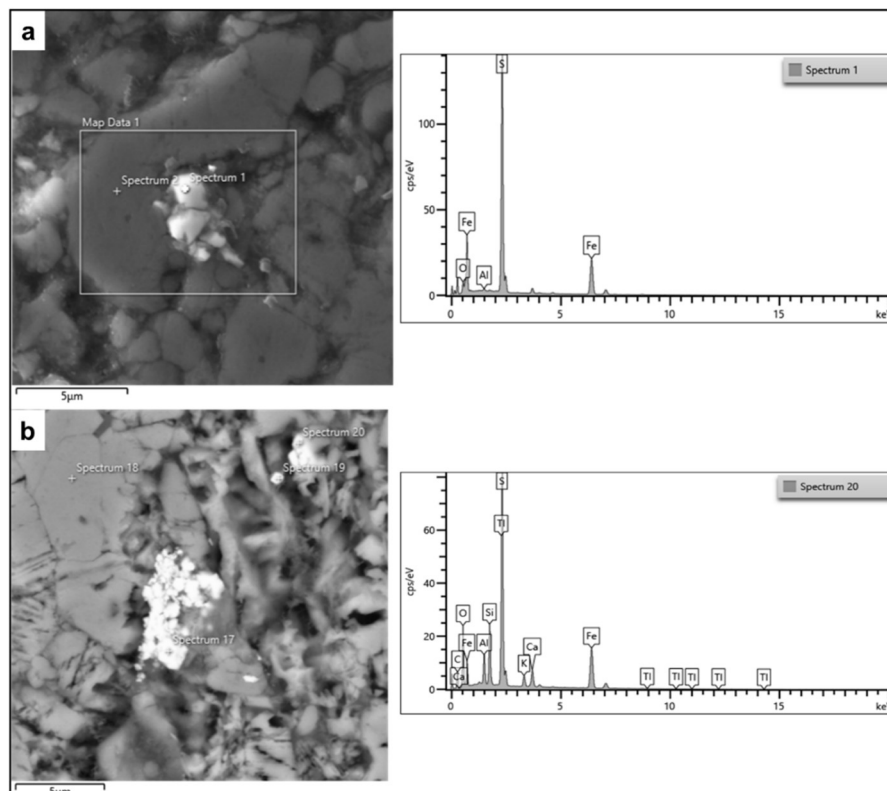
Figure 7-10 The SEM images and EDS showing elemental distribution of pyrite a) Secondary electron (SE) image and spectrum 1 illustrating Fe and S ions before brine saturation, and b) back-scattered image and spectrum 20 showing Fe and S ions after saturation.

7.5.5. Geochemical simulation

To further understand how fluid-shale interactions (pyrite oxidation, mineral dissolution and surface complexation) affect the water properties, PHREEQC was used to model fluid chemistry using Marcellus shale samples at different $O_{2(aq)}$ level (Table 7-6). All the minerals were set to be able to fully react with fluid so that we could examine the maximum possible level of fluid salinity after fluid-rock interactions. The results show that fluid pH under ambient conditions is lower than limited air and vacuum conditions, where the trend is in line with the observation from spontaneous imbibition tests. The simulated pH at vacuum conditions (9.72) is higher than experimental measurement (8.40). One of the possible reasons is that in the geochemical modelling regarding vacuum conditions, the whole system is under a completely anoxic environment. For the experiments, although the system was being vacuumed, a small amount of O_2 could still be trapped in the micro-pores of the shale samples [185]. The trapped O_2 would partly react with pyrite and generate H^+, which decreases the *in-situ* pH. However, the limited O_2 would be totally consumed before the sealed system is reopened. This is why none of the dissolved O_2 is present after fluid-shale interactions in the simulation for limited air and vacuum conditions (Table 7-6), and the experimental measured ORP under these two conditions is much less than ambient conditions (Figure 7-5).

Table 7-6 Simulated fluid chemistry regarding Marcellus samples under ambient, limited air and vacuum conditions at room temperature.

	pH	Ionic strength (M)	Dissolved O_2 (mol/L)	Dissolved CO_2 (mol/L)
Ambient	7.50	0.169	2.631×10^{-4}	1.316×10^{-5}
Limited air	7.95	0.006	0	2.453×10^{-5}
Vacuum	9.72	0.0005	0	4.723×10^{-8}

Main chemical species and concentrations (mg/L)										
	Na^+	Mg^{2+}	Ca^{2+}	Fe^{2+}	$Fe(OH)_2^+$	AlO_2^-	HCO_3^-	CO_3^{2-}	SO_4^{2-}	$Fe(OH)_4^-$	TDS*
Ambient	7.8	45.4	1303.6	0	263.6	1996.6	15.3	0.05	4139.0	42.3	7813.7
Limited air	2.1	1.7	43.4	20.7	0	5.3	62.5	0.31	104.6	0	240.6
Vacuum	2.0	0.2	5.2	0	0	5.1	6.7	1.7	0	0	20.9

* The concentration of other aqueous ions such as Fe^{3+} is less than 1.0×10^{-7} and therefore not included in the TDS.

Table 7-6 also shows that the TDS of fluid at ambient condition (7813.7 mg/L) is much higher than the limited air (240.6 mg/L) and vacuum conditions (20.9 mg/L), which is in accordance with the experimental measurements of ion concentrations and electrical conductivity. For the limited air condition that would be the most similar to the real reservoir environment, SO_4^{2-} which originated from pyrite and chalcopyrite oxidation, and HCO_3^- and Ca^{2+} from calcite dissolution, are the main ions contributing to the total salinity. Only small amounts of Na^+ (2.1 mg/L) can be generated through albite dissolution based on the simulation. However, the salinity of Na^+ of flowback water can be as high as 35,000 to 45,000 mg/L [113, 276]. The discrepancy of Na^+ concentration and TDS between geochemical simulation/lab experiments and field observations implies that pyrite oxidation associated mineral dissolution may play a negligible role in the salinity increment. The production of intrinsic high saline groundwaters should dominantly account for the high salinity of flowback water during hydraulic fracturing. Besides, the salt packages that can be within the big chunk of shales but negligible in the small samples may also contribute to the salinity increment.

7.6. Conclusions

In this study, the effect of pyrite oxidation on water chemistry (pH, oxidation-reduction potential, electrical conductivity and ion concentration) during spontaneous imbibition process was investigated at three different dissolved O_2 levels using calcite-rich Marcellus and Eagle Ford shale samples. Geochemical modelling, which combines mineral dissolution and surface complexation, was performed to further interpret the source of high salinity of flowback water during hydraulic fracturing. The key results of this work are summarized as follows:

- Shale samples under ambient conditions uptake a higher volume of water, and the fluids have higher values of ORP but lower pH than the limited air and vacuum conditions after 30 days imbibition, suggesting that pyrite oxidation can facilitate calcite dissolution by generating extra H^+ and thus likely communicate pore networks and enhance rock connectivity.
- Once fluids at limited air and vacuum conditions are able to source O_2 from air, the amount of imbibed water, fluid salinity and electrical conductivity can

rapidly increase, which confirms that pyrite oxidization process play an import role at ambient condition with continuous contact with O_2 from air.

- The fluid salinity under limited air conditions, which is the most similar to the reservoir conditions in terms of aqueous O_2 concentrations, is much less than that of the ambient conditions, indicating that traditional imbibition experiment where fluids can always equilibrate with air would overestimate the impact of pyrite oxidization process in shale at real reservoir conditions.

- SEM analyses show that brine saturation barely affects the morphology and elemental distribution of pyrite at ambient conditions, implying that pyrite oxidation would play a minor role in fluid salinity at reservoir conditions.

- Spontaneous imbibition tests, SEM analyses and geochemical modelling indicate that lab-measured fluid salinity is only ~2% of field observations. This result implies that the mixing of injected fracturing fluid with high salinity formation brines rather than mineral dissolution may account for the high TDS of flowback water during hydraulic fracturing in calcite-rich.

8. Chapter 8 Role of brine composition on rock surface energy and its implications for subcritical crack growth in calcite

8.1. Abstract

Subcritical crack growth in calcite-bearing reservoirs plays a vital role in rock deformation. Published experimental results show that fluid-rock interactions likely affects rock surface energy and triggers fracture propagation. However, much of research up to now has been only descriptive in nature, impairing a substantial interpretation to predict subcritical crack growth. In this study, we developed a physicochemical model to relate fluid-calcite interaction in particular surface potential to surface energy in light of capacitance theory. To test the model, we calculated calcite surface chemical species and surface potential as a function of pH, ion type and fluid salinity using surface complexation modelling. Moreover, we compared the predicted surface energy with Bergsaker et al.'s experimental measurements.

Our results confirm that fluid chemistry would affect calcite surface species distribution and surface energy. At high acidic condition, lowering salinity increases surface potential of brine-calcite. At alkaline condition, lowering salinity decreases surface potential in the presence of $MgSO_4$ and $MgCl_2$ but increases that of Na_2SO_4. Furthermore, pH would affect the level of bonding-capable divalent such as Ca^{2+} through the equilibrium of calcite dissolution-precipitation, and thus indirectly influence surface energy. Our results unveil the importance of fluid-rock interactions on subcritical crack growth and shed light on hydrocarbon exploitation and CO_2 capture and storage in carbonate reservoirs. These findings also delineate the inner connection between geochemical and geo-mechanical properties at subsurface.

Keywords: Subcritical crack growth; Fluid-rock interaction; Surface potential; Surface energy; Fluid chemistry.

8.2. Introduction

Subcritical crack growth represents the slow fracture propagation at stress below the threshold of dynamic rupture [41, 285, 286]. It plays a significant role in Earth's crust deformation [64, 287], hydrocarbons exploitation [46, 75, 149], CO_2 capture and storage (CCS) [138] and mechanical weathering and rock erosion [288-290]. Since

inception of the concept proposed by Atkinson in 1984 [285], the effect of fluid-rock interaction on subcritical crack growth and rock geomechanical properties has long been intriguing scientists [41, 46]. According to the Griffith fracture propagation theory [291], an existing crack likely propagates when the energy release rate G (J/m^2) of rupture is greater than the rock surface energy γ_s (J/m^2), which is stated as:

$$G_0 - 2\gamma_s^e = 0 \hspace{4cm} \text{Eq. 8-1}$$

where G_0 and γ_s^e are the mechanical energy release rate and surface tension at given equilibrium conditions. Alteration of *in-situ* chemical environment may change the value of G_0 thus either prompts or restrains the crack propagation [40, 46, 64, 292].

Previous studies have shown that fluid properties such as electrolyte concentrations [44, 135, 293] and pH [294, 295] can influence the subcritical crack growth in silicate materials, including quartz [295-297], granite [288, 289, 294] and sandstone [44, 45, 288, 298]. For instance, Martin [296], and Martin and Durham [297] investigated the influence of water vapour pressure on crack growth in quartz. They found that water vapour pressure would significantly affect crack growth in quartz at room temperature. Nara et al. [45] used double-torsion with combination of load relaxation method to test the effects of temperature and humidity on subcritical crack growth in sandstone. The results show that humidity and clay content in sandstone would significantly affect subcritical crack growth and formation long-term stability. Nara et al. [135] also investigated the effect of NaCl concentrations on subcritical crack velocity of sandstone in water. They found that increasing electrolyte concentrations up to 1 M decreased crack velocity but further increasing salinity would increase crack velocity again. Kudo et al. [294] investigated the effect of solution pH on crack growth in granite under tensile stress. The results show that with both solutions of pH = 3 (H_2SO_4) and pH = 11 (NaOH), transgranular crack within quartz grains can significantly increase under low crack velocities (10^{-7} m/s).

Besides the silicate materials, experimental studies have confirmed that the crack growth velocity in carbonate typically the calcite is also affected by the content of water, brine compositions and salinity [42, 149, 299-302]. For example, Røyne et al. [287] used a double-torsion apparatus to evaluate the effect of water content on subcritical crack growth in calcite crystal. They found that increasing water

concentration of glycol-water mixtures decreases the upper bounds of surface energy for crack propagation. Bergsaker et al. [64] measured crack growth velocity in calcite single crystals with different ion species including Na_2SO_4, $NaCl$, $MgSO_4$ and $MgCl_2$ and pH (5 to 7.5). The results show that the energy release rate G_0 is strongly affected by the fluids composition but is independent of pH. Rostom et al. [41] also used the modified double-torsion setup to investigate how NaCl salinities influence the calcite subcritical crack propagation. They found that a low NaCl concentration (less than 0.8 M) can decrease the surface energy, favouring rock weakening effect, whereas G_0 would increase if NaCl concentration is higher than 1 M. Nara et al. [302] investigated the effect of surrounding environment on subcritical crack growth in marble, and they observed that increasing ambient temperature and/or temperature can increase crack velocity.

To interpret the experimental results and understand the subcritical crack growth, a few mechanisms have been proposed, including stress corrosion [41, 303, 304], mineral dissolution [305, 306], surface energy alteration [40, 41] and electrical double layer expansion due to rock-water interaction [135, 307]. Charles [303] proposed a stress corrosion model to explain the bonds weakening at tip of crack as a result of chemical environmental changes. He claimed that the Si-O bond of glass is easier to break up in the presence of water vapour. Detwiler [305] measured the fracture aperture changes during dissolution experiments using textured glass and KH_2PO_4 crystal samples. The results show that dissolution controlled by reaction kinetics and hydrodynamics plays a vital role in fracture extensions. Rostom et al. [41] measured subcritical crack velocity of different fluids by changing the concentration of NH_4Cl and NaCl. They observed that the crack velocity is affected by fluid chemistry and they attributed this phenomenon to the modification of electrostatic repulsion forces between two fractures surfaces.

Hitherto, both experimental works and theories indicate that the chemical environmental changes can influence the surface energy which likely triggers subcritical crack growth. However, the existing accounts barely quantify how fluid-carbonate interactions affect subcritical crack extension, which impairs the prediction of rock mechanical properties. In this work, we developed a physical model to relate fluid-calcite interaction in particular surface potential to surface energy in light of

capacitance theory. To test this model, we calculated calcite surface chemical species and surface potential as a function of pH (2 to 10), ion type (Na$_2$SO$_4$, NaCl, MgSO$_4$ and MgCl$_2$) and ionic strength (0.012 to 1.2 M) using surface complexation model and the predicted surface energy were compared with Bergsaker et al.'s experimental measurements.

8.3. Methodologies

In the section, we first briefly review the experimental works on subcritical crack growth performed by Bergsaker et al. [64]. Then a surface complexation modelling is presented for the calculation of calcite surface species and surface potential.

8.3.1. Experimental observations by Bergsaker et al.

Bergsaker et al. measured the velocity of subcritical crack growth in calcite single crystal using a double torsion apparatus in the presence of different fluid pH (5 to 7.5), fluid compositions (Na$_2$SO$_4$, NaCl, MgSO$_4$ and MgCl$_2$) and ionic strength (0.012 to 1.2 M) [64]. All solutions were saturated with CaCO$_3$ and the experiments were performed under room temperature (23±1.5ºC), atmospheric pressure and ambient humidity conditions. Details of the experiment please refer to [Bergsaker et al. The effect of fluid composition, salinity, and acidity on subcritical crack growth in calcite crystals. *Journal of Geophysical Research: Solid Earth* 121.3 (2016): 1631-1651]. Here we summarize the main conclusions from that research:

1. pH ranging from 5 to 7.5 does not significantly affect the calcite surface energy when solution is saturated with CaCO$_3$;

2. With consideration of the variability of measurement, lowering ionic strength of NaCl, MgSO$_4$ and MgCl$_2$ from 1.2 M to 0.012M decreases the average energy release rate during micro-cracks propagating (0.32 to 0.28 J/m^2 for NaCl, 0.34 to 0.30 J/m^2 for MgSO$_4$, and 0.32 to 0.31 J/m^2 for MgCl$_2$);

3. Decreasing ionic strength of Na$_2$SO$_4$ from 1.2 to 0.012 M somehow increases the energy release rate from 0.27 to 0.36 J/m^2.

8.3.2. Surface complexation model

Surface complexation model (SCM) has been widely used to evaluate the adsorption of metal ions and oil on organic and inorganic minerals [21, 85, 204, 308]. In SCM, all the surface reactions are explicitly expressed with consideration of surface species and aqueous ions [209, 308]. The surface charge therefore develops as a result of chemical and hydrogen bonds between surface sites and ions in electrolyte. Consequently, it is a function of electrolyte composition, concentration and pH, as well as it depends on mineral lattice structure. In this work, a SCM developed by Pokrovsky et al. and Brady et al. is used to calculate the surface species concentration, surface potential and *in-situ* pH for different ion type and ionic strength (Table 8-1) [88, 308]. Details of SCM on calcite surface are documented in our previous works [87, 186]. The specific area and site density of calcite are set as 1 m^2/g and 4.1 $\mu mol/m^2$ [186]. Calcite and CO_2 dissolution are involved in all reactions at ambient condition using PHREEQC 3.5.0 with database of Lawrence Livermore National Laboratory (LLNL) thermo.V8.R6.230 [175]. Dissolved O_2 is not covered because it could oxidize minerals such as pyrite but has negligible effect on calcite [185].

Table 8-1 Input parameters for surface complexation reactions of calcite [88, 186, 308]. '>' represents the chemical species are attached on the calcite surface.

Number	Reaction	log K_{298k}
R1	$>CaOH + H^+ \leftrightarrow >CaOH_2^+$	11.85
R2	$>CaOH + HCO_3^- \leftrightarrow >CaCO_3^- + H_2O$	5.8
R3	$>CaOH_2^+ + SO_4^{2-} \leftrightarrow >CaSO_4^- + H_2O$	2.1
R4	$>CO_3H \leftrightarrow >CO_3^- + H^+$	-5.1
R5	$>CO_3H + Ca^{2+} \leftrightarrow >CO_3Ca^+ + H^+$	-2.6
R6	$>CO_3H + Mg^{2+} \leftrightarrow >CO_3Mg^+ + H^+$	-2.6

8.4. Model Development

One important step in our model is to related surface potential, which is associated with geochemistry such as surface chemical species, to the energy release rate of rupture. This correlation is built on the basis of capacitance theory and can be presented through Lippmann classical equation. The Lippmann classical equation describes the change of surface tension of interface between the polarizable electrode

and ionic solution [196, 197]. It has been widely applied on liquid-solid interface to interpret the wetting phenomenon [198-201]. According to the derivation made by Kramer [199] and Linford [202], for liquid electrodes, if the boundary conditions of derivation like constant temperature T, pressure p, chemical potential μ and strain ε are considered explicitly, we have

$$(\frac{\partial \gamma}{\partial E})_{T,p,\mu,\varepsilon} = -q \qquad \text{Eq. 8-2}$$

where γ, E and q represent surface tension (J/m^2), electrode potential (V) and charge (C), respectively. For general solid electrodes, if the strain is potential-dependent, we have the generalized Lippmann equation [201, 203]

$$\frac{d\gamma}{dE} = -q - (\gamma - f)\frac{d\varepsilon}{dE} \qquad \text{Eq. 8-3}$$

where f is the surface stress (J/m^2). For most of the solid electrodes especially the planar flat electrode, the dε/dE can be neglected [199, 201]. Therefore, the classical Lippmann equation is given by

$$\frac{d\gamma}{dE} = -q \qquad \text{Eq. 8-4}$$

Van Cappellen et al. [204] developed a constant capacitance model (CCM) using surface complexation on carbonatite-brine interface. The results imply that for carbonated surface such as calcite and dolomite, the double layer capacitance c (F/m^2) can be set as a constant in the presence of homogeneous solution. This is because the change of capacitance by a factor of two would not significantly affect the surface charges [204, 205]. For example, the surface charge difference of $MnCO_3$ is less than 0.005 mmol/m^2 in presence of high ($I = 1$ M) and low ($I = 0.032$ M) ionic strength [204]. The results have also been confirmed by microscopic and spectroscopic investigations [204, 206-211]. Meanwhile, a more complex model named Charge Distribution MUltiSIte Complexation (CD-MUSIC) also uses the constant capacitance [211, 212], although it specifies two capacitances, where c_1 is the capacitance of the interface between solid surface and the centre of the Stern layer, and c_2 corresponds to the capacitance from Stern layer centre to the starting point of the EDL [170, 174]. Therefore, if capacitance at specific ionic strength is considered as potential-independent, Eq. 8-4 can be rearranged as

$$\gamma - \gamma_0 = -\frac{1}{2}c(E - E_0)^2 = -\frac{1}{2}\frac{q^2}{c} \qquad \text{Eq. 5-5}$$

If we define the uncharged surface potential as Φ, then

$$\Phi = E - E_0 \qquad \text{Eq. 8-6}$$

Subsequently, the general Lippmann Equation can be stated as

$$\gamma - \gamma_0 = -\frac{1}{2}c\Phi^2 = -\frac{1}{2}\frac{q^2}{c} \qquad \text{Eq. 8-7}$$

Eq. 8-7 suggests that if the surface potential changes from Φ_1 to Φ_2, the surface tension would change as

$$\gamma_2 - \gamma_1 = -\frac{1}{2}(c_2\Phi_2^2 - c_1\Phi_1^2) \qquad \text{Eq. 8-8}$$

where γ_1 and γ_2, Φ_1 and Φ_2, c_1 and c_2 are the surface tension or surface energy, surface potential, and capacitance at different ionic strength, respectively. By substituting Eq. 8-1 into Eq. 8-8, we finally get the correlation between surface potential and energy release rate during fracture propagation.

$$G_{02} - G_{01} = -(c_2\Phi_2^2 - c_1\Phi_1^2) \qquad \text{Eq. 8-9}$$

where G_{01} and G_{02} are the energy release rate at different ionic strength. Eq. 8-9 indicates that the change of surface energy is affected by both capacitance of EDL and surface potential.

8.5. Results and Discussion

Given that calcite surface potential is determined by surface geochemistry, we first examined the effect of pH, ion type and salinity on surface chemical species. To verify the established model, we then compared the simulation results of energy release rate to the experimental values measured by Bergsaker et al. [64].

8.5.1. Effect of pH and ionic strength on calcite surface species

The pH of solution strongly affects the chemical species on calcite surface. Figure 5-1 shows the correlations between pH and chemical species in the presence of NaCl at different ionic strength. The variation of functional groups with pH and ionic strength

for MgCl$_2$ and Na$_2$SO$_4$ can be found in Supplement Materials (Figures 5-7 and 5-8). For NaCl, the change of >CaCO$_3^-$ and >CO$_3$Ca$^+$ follow the same trend that the species concentrations increase with increasing pH, whereas the concentrations of >CaOH$_2^+$ and >CO$_3^-$ decrease when pH is greater than 7. In contrast, >CaOH$_2^+$ density keeps constant at acidic condition while >CO$_3^-$ density gradually increases. The main reason is that at acidic condition, the high H$^+$ concentration shifts the Reaction 1 to right-hand side and Reaction 4 and 5 to left-hand side so that >CaOH$_2^+$ can keep a high level while >CO$_3^-$ and >CO$_3$Ca$^+$ density is negligible. When pH is greater than 7, the drop of H$^+$ level tends to reverse these reactions and triggers the corresponding changes as shown in Figure 5-1.

Solution salinity also affects the chemical species distribution, but that influence is relatively limited for particular sorts of functional group if calcite only contacts with NaCl (Figure 5-1). The concentrations of >CaCO$_3^-$ and >CaOH$_2^+$ do not vary significantly if decreasing the ionic strength from 1.2 to 0.012 M. At alkaline condition especially with pH greater than 8.5, the low ionic strength slightly increases >CO$_3$Ca$^+$ concentration. The only exception is >CO$_3^-$. The low ionic strength significantly increases the >CO$_3^-$ concentration when pH is less than 7. For example, >CO$_3^-$ concentration increases from 5.54 to 6.46 μmol/m^2 with decreasing ionic strength from 1.2 to 0.012 M at pH of 5. This is because at alkaline condition, dissolution of calcite is highly restricted thus Ca^{2+} concentration does not significantly change when varying ionic strength. However, lowering salinity at acidic condition facilitates the calcite dissolution thus affects the concentrations of >CO$_3$Ca$^+$ and indirectly >CO$_3^-$ through equilibrium of Reactions 4 and 5. Therefore, if calcite only contacts with NaCl, pH would affect divalent cation (Ca^{2+}) concentrations by controlling the calcite dissolution-precipitation and thus indirectly influence the surface species.
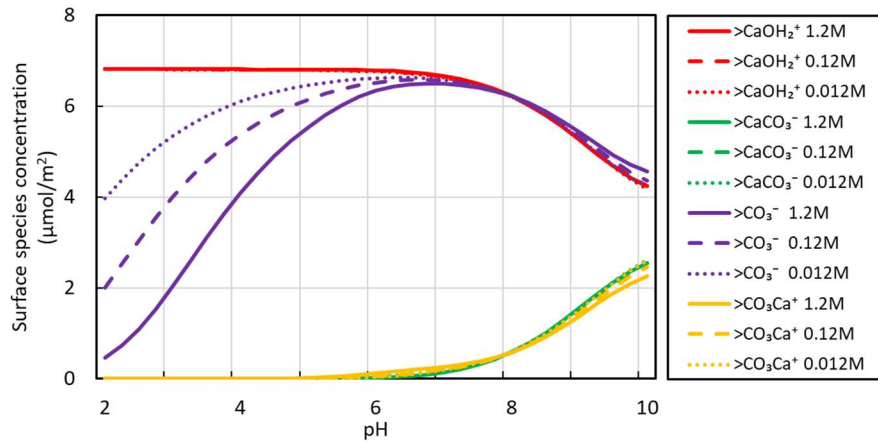
Figure 8-1 Surface species of calcite varies with pH and ionic strength in the presence of NaCl.

In contrast to NaCl, more complex changes of functional groups on calcite surface are observed when it is in presence in $MgSO_4$ (Figure 8-2). The effect of pH on surface species with $MgSO_4$ is similar to that of NaCl when pH is greater than 7 that the concentrations of $>CaCO_3^-$ and $>CO_3Mg^+$ increase whereas $>CaOH_2^+$ and $>CO_3^-$ decrease. At acidic condition, the amount of $>CaCO_3^-$ is negligible due to the competition with $>CaSO_4^-$ and $>CaOH_2^+$, $>CO_3Mg^+$ and $>CO_3^-$ densities increase with increasing pH. However, the variation of $>CaSO_4^-$ and $>CaOH_2^+$ concentrations depends on local pH and ionic strength. For example, lowering ionic strength always decreases the $>CaSO_4^-$ concentration, but $>CaSO_4^-$ density at low ionic strength (0.012 M) keeps dropping with increasing pH while it will first increase then decrease at alkaline condition if under high ionic strength (1.2 M). Similar results were documented by Chen et al., who reported that decreasing solution salinity can increase the concentration of $>CO_3^-$ and decrease $>CO_3Ca^+$ [87].
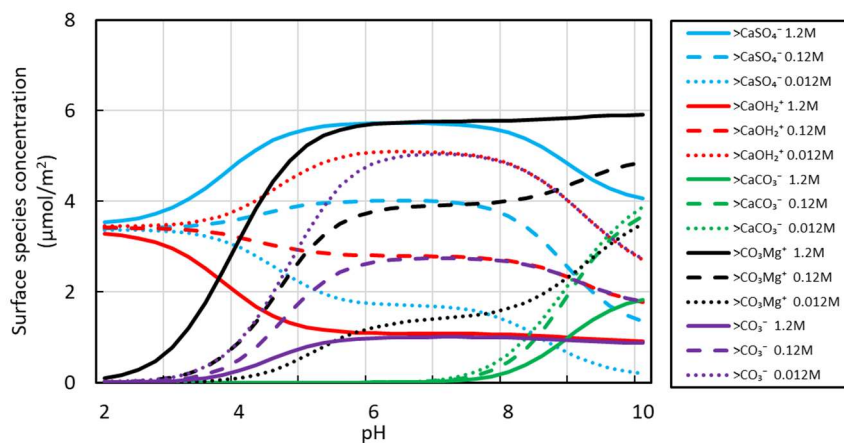
Figure 8-2 Surface species of calcite varies with pH and ionic strength in the presence of $MgSO_4$.

8.5.2. Effect of pH and ionic strength on surface potential

pH affects surface potential by changing the equilibrium of protonation and deprotonation of Reaction 1 and 4 to 6. Figures 8-3 and 8-4 show the variation of surface potential of EDL with pH in the presence of NaCl and $MgSO_4$ solution. The curves for $MgCl_2$ and Na_2SO_4 can be found in Supplemental Materials (Figures 8-9 and 8-10). For NaCl, $MgCl_2$ and Na_2SO_4, increasing pH decreases the surface potential for all ionic strengths. For instance, the calcite surface potential with NaCl drops from 44.05 to -13.20 mV when increasing pH from 5 to 9. In contrast, the trend of surface potential in the presence of $MgSO_4$ varies with salinity (Figure 8-4). At acidic condition especially with pH less than 5, decreasing H^+ level increases surface potential at high ionic strength (1.2 M) while decreases at low ionic strength (0.012 M). However, all the surface potentials keep constant with pH from 6 to 8 and gradually decrease at highly alkaline condition. It is worth noting that a high absolute value of surface potential would expand the EDL, thicken water film and strengthen the repulsion forces between fracture surfaces thus facilitating crack propagation [41, 193, 257]. Therefore, if we could enhance the acidity for NaCl and $MgCl_2$ by injecting CO_2 and alkalinity for Na_2SO_4 at calcite-rich formations, it could be expected that the *in-situ* subcritical crack growth would be strengthened.
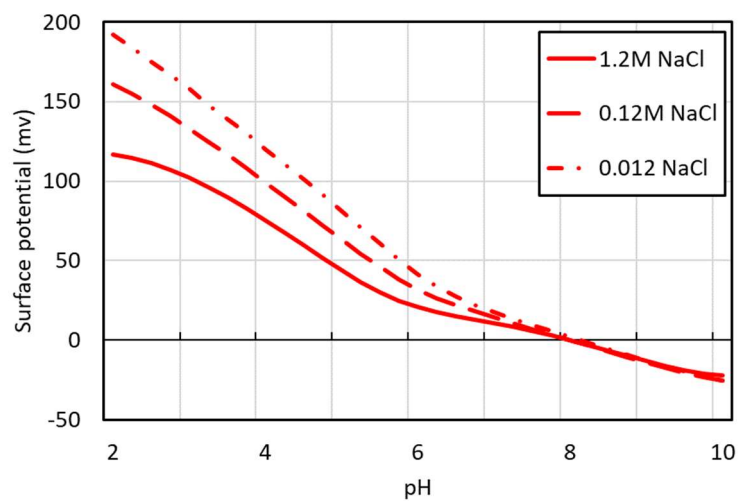
Figure 8-3 Surface potential of calcite varies with pH and ionic strength in the presence of NaCl.
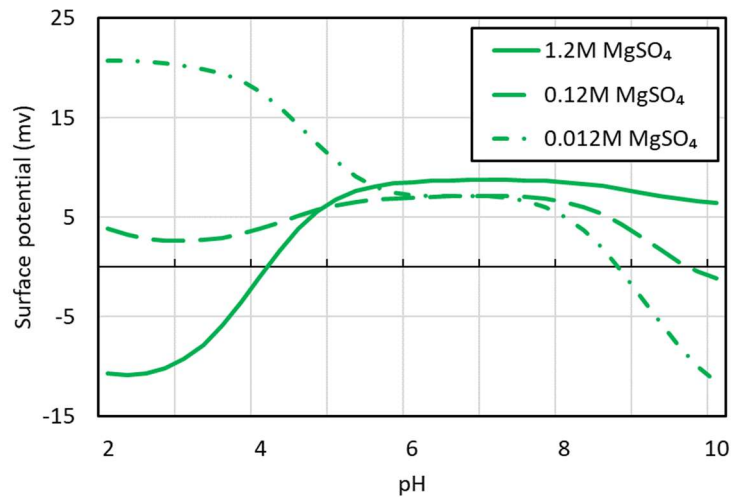
Figure 8-4 Surface potential of calcite varies with pH and ionic strength in the presence of MgSO₄.

Besides pH, solution salinity also affects surface potential. Under highly acidic condition, a low ionic strength always increases surface potential. For instance, increasing ionic strength for $MgSO_4$ from 0.012 to 1.2 M shifts the surface potential from negative (-9.28 mV) to positive (19.90 mV) at pH of 3.5. When pH is greater than 8, lowering salinity significantly decreases the surface potential for $MgSO_4$ and $MgCl_2$ but leads to an increase for Na_2SO_4. For NaCl, the change of ionic strength slightly decreases the surface potential, e.g. from -18.71 to -19.70 mV at pH of 9.5. This small degree of change compared to other fluids could be attributed to the intrinsic fluid compositions.

We know that calcite surface chemistry is strongly affected by the divalent ions such as Ca^{2+}, Mg^{2+} and SO_4^{2-}, which can bond with functional groups (Reaction 3, 5 and 6) thus alter surface species concentration and surface potential. The concentrations of divalent ions in $MgSO_4$, $MgCl_2$ and Na_2SO_4 solution are controlled by fluid salinity. Subsequently, any change of ionic strength would directly affect the level of these bonding-capable ions and the calcite surface geochemistry. Besides, the protonation and deprotonation competition through Reaction 1 and 4 to 6 would also change the presence of $>CaOH_2^+$, $>CO_3^-$, $>CO_3Ca^+$ and $>CO_3Mg^+$. Therefore, the variations of surface species concentration and surface potential of these fluids are influenced by both pH and salinity as shown in Figure 8-2 and 8-4.

In contrast, for NaCl solution, all the aqueous divalent cations such as Ca^{2+} derive from the calcite dissolution which is mainly controlled by the level of H^+ [309]. At acidic condition, calcite tends to dissolve at low ionic strength (Figure 8-5). Therefore, varying NaCl salinity can change the level of bonding-capable Ca^{2+} so as the surface species and surface potential. However, when pH is greater than 8.5, the saturation index of calcite is positive so it tends to precipitate. As a result, changing NaCl salinity does not significantly affect Ca^{2+} level. This is the reason why the surface species and surface potential barely change with NaCl salinity at alkaline condition as shown in Figures 8-1 and 8-3. Given the *in-situ* pH of NaCl solution saturated with calcite is approximately 8.3 (Table 8-2), we could expect from Figure 8-3 that changing NaCl ionic strength would not significantly affect the calcite surface potential, which leads to a limited influence on surface energy alteration.
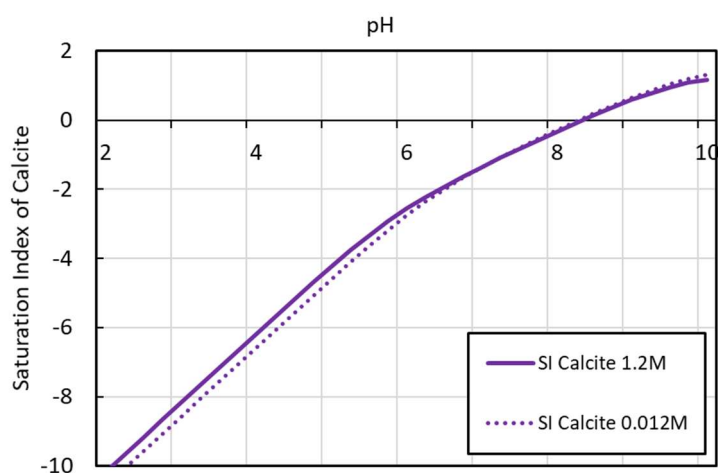
Figure 8-5 Equilibrium of calcite dissolution-precipitation in NaCl solution. The negative and positive saturation index at in-situ pH represents that calcite tends to dissolute and precipitate, respectively.

8.5.3. Correlation of surface potential and surface energy

Once we get the surface potential, the surface energy can be calculated based on Eq. 8-9 and compared with experimentally measured values. If subscript 1 and 2 represent the state of parameters at high (1.2 M) and low (0.012 M) ionic strength, and we substitute the corresponding capacitance and surface potential at *in-situ* pH of Table 8-2 into Eq. 8-9, we can get the difference of surface energy as a result of salinity change. Figure 8-6 shows the matching results of energy release rate (ΔG_0^s) predicted by the physical model and the experimental energy release rate (ΔG_0) measured by

Bergsaker et al. for all solutions. Given the minor deviations, we tentatively conclude that the induced surface energy release rate could predict the actual value of subcritical crack growth in calcite.

Table 8-2 Values of predicted surface potential and capacitance used to match experimental results.

	pH		Surface potential (mV)		Capacitance (F/m^2)	
	1.2M	0.012M	Φ_1	Φ_2	C_1 *	C_2
NaCl	8.353	8.304	-4.7	-2.6	2000	200
MgSO$_4$	8.383	8.314	8.2	3.4	500	50
MgCl$_2$	8.252	8.295	33.6	11.1	9	0.9
Na$_2$SO$_4$	8.473	8.332	-28.1	-10.4	100	10

* The capacitance is calculated by the equation $c = \dfrac{\sqrt{I}}{\alpha}$, where I is the ionic strength and α is an empirical parameter related to dielectric properties of EDL [308].
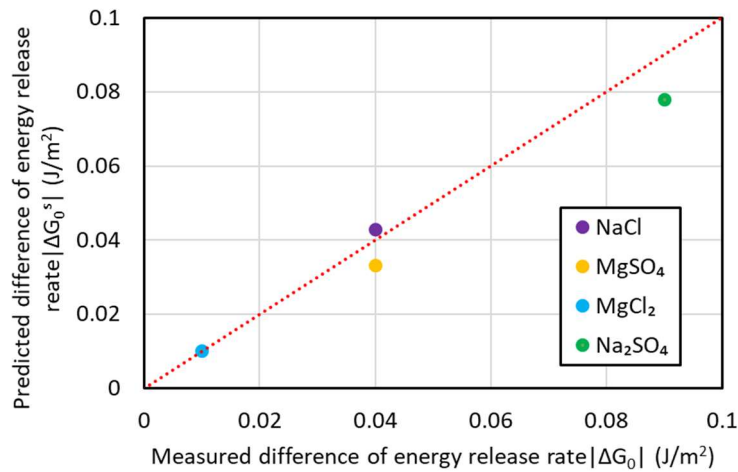
Figure 8-6 Deviations between the measured energy release rate ΔG_0 and simulated results ΔG_0^s.

Compared to the capacitances used for MgSO$_4$, MgCl$_2$ and Na$_2$SO$_4$, we set high capacitance values for NaCl to match the experimental measurements. This is because a relatively low surface potential in the presence of NaCl is observed at slightly alkaline condition (Table 8-2). If we shift the chemical environment to higher acidity, it is expected from Figure 8-3 that the surface potential of NaCl would significantly increase so that the corresponding capacitance would drop to a low value. For example,

Pokrovsky et al. simulated the Zn adsorption on goethite, hematite and other oxides surface with $I = 0.01$ M mixture of $NaNO_3$ and HNO_3 [310]. The reported pH can be as low as 3.64 so that the capacitance was set as 1 F/m^2. Van Cappellen et al. used low capacitance of 30 F/m^2 for $I = 0.032$ M and high value of 168 F/m^2 for $I = 1$ M [204]. Considering that the fluid with single composition in natural environment scarcely exists, the 'real' capacitance of the complex fluid would therefore fall in a reasonable range. Nevertheless, we provide a potential approach to evaluate the subcritical crack growth from geochemical perspective. This new method can be taken together with experimental works such as double torsion apparatus to better interpret the effect of fluid-rock interaction on subcritical crack growth.

8.5.4. Implications

Aforementioned model and mechanisms of fluid-rock interactions on subcritical crack growth have at least four implications. The first one is on CO_2-assisted enhanced oil recovery (EOR). CO_2-assisted EOR is considered as one of the environmentally friendly and economic means to yield additional oil recovery [83, 281]. When the carbonated water with low pH (low as 2.6 to 3 [281, 311]) is injected into underground, the H^+ would react with formation rock and cause the calcite and dolomite dissolution, which increases divalent ions' concentration such as Ca^{2+} and Mg^{2+}. Meanwhile, the pH of injected carbonated water can increase to 5.5 to 8 [223, 309, 311] due to the calcite buffering effect. At this range of pH, the increment of divalent ions' concentration would increase surface potential (Figure 8-9), thereby decreasing surface energy and facilitating subcritical crack growth. This process would not only take place at the near-wellbore region, but would also prevail at deeper formation. This is because the high level of the calcium at advancing front would transport from injectors to producers throughout the reservoirs, which increases the surface potential at pore surfaces and thus results in subcritical crack growth. This process poses a threat of channelling (or permeability increment) between injectors and producers during the long-term carbonated water flooding.

The second implication of fluid-rock interactions on subcritical crack growth is on carbon dioxide capture and storage in carbonate formations. CCS has been identified as a feasible technique to alleviate anthropogenic CO_2 emission [312, 313]. Currently, the processed CO_2 is injected underground and mixed with formation brine. The in-

situ pH would therefore drop to a low level as result of CO_2-brine-carbonate interaction. For example, Chen et al. pointed out that the pH of 1 M NaCl and 50 mM $CaCl_2$ mixture with carbonation can be as low as 3 at pressure of 3000 psi and 25°C [281]. At such high acidity, calcite and dolomite dissolution would occur, which increases surface potential as a result of Ca^{2+} increment and thus decreases the surface energy. This process would favour subcritical crack growth, resulting in increasing of permeability, which may help sequestrating CO_2 underground. However, the induced subcritical crack growth may cause wellbore instability and leakage problem. Besides, subcritical crack growth may also change the rock permeability during CCS, which brings challenges to predict CO_2 plume migration.

The third implication of this work is on hydraulic fracturing design in unconventional typically the calcite-bearing shales [46, 149]. To fracture shale formation and extract gas and oil economically, low total dissolved solids (TDS) slick water (typically less than 5000 ppm) would be injected into underground [13, 162]. The injected low salinity fluid would change the surface chemistry of minerals as showed in previous sections thus prompt micro-fracture propagation, enhancing reservoir connectivity and hydrocarbon recovery. This process has been confirmed by monitoring micro-seismic events during pump-off stage [314, 315] and can be attributed to the fluid-rock interactions as a result of chemical environmental change [42]. Our work quantitatively predicts the effect of fluid chemistry on fracture surface energy alteration and provides a lens for hydraulic fracturing fluid design.

The fourth implication of fluid-rock interactions on subcritical crack growth is on weathering. Mechanical weathering is environmentally dependent process that commonly observed in carbonate and calcite-rich sandstone rocks [290, 316]. The correlation between rock surface potential and surface energy established in this work provides insights to understand the impact of pore fluid chemistry [41, 135] on subcritical crack growth thereby the weathering. For example, lowering ionic strength of the pore fluids likely increases rock surface potential thereby decreasing the surface energy needed for crack propagation. This process would induce subcritical crack growth and affect the long-term stability of rock mass.

8.6. Conclusions

The long-term subcritical crack growth is one of the main mechanisms to explain the carbonate deformation [41, 285]. Published experimental results imply that fluid-calcite interaction likely affects calcite surface energy and leads to subcritical crack growth [40, 41, 46]. However, there has been little quantitative analysis of how fluid-rock interaction influences this geomechanical phenomenon. In this study, we developed a physical model to relate surface potential of EDL to surface energy needed to propagate crack in light of capacitance theory. We also tested the model using the experimental data reported by [Bergsaker et al. The effect of fluid composition, salinity, and acidity on subcritical crack growth in calcite crystals. *Journal of Geophysical Research: Solid Earth* 121.3 (2016): 1631-1651].

Our results show that calcite surface potential is a function of solution pH, fluid composition and ionic strength, which can be predicted using surface complexation model. pH would affect the Ca^{2+} level through the equilibrium of calcite dissolution-precipitation thus indirectly influence surface energy. At high acidic condition, a low fluid salinity would increase surface potential for all tested solutions. At alkaline condition, lowering salinity decreases surface potential of $MgSO_4$ and $MgCl_2$ but increases that of Na_2SO_4. The effects of ionic strength of NaCl on surface potential is considerably restricted due to the limited divalent ions concentration such as Ca^{2+}, Mg^{2+} and SO_4^{2-}, which are capable to bond with functional groups on calcite surface. Furthermore, the predicted energy release rate ΔG_0^s is generally in line with the experimental measurement ΔG_0 reported by Bergsaker et al. Our physical model therefore builds an overall framework to quantify how fluid-calcite interactions affect surface energy and subsequent subcritical crack growth.

8.7. Supplemental Materials
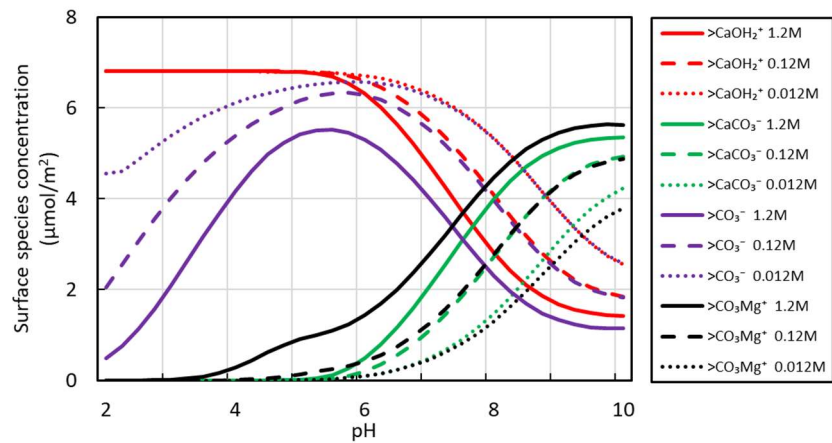
Figure 8-7 Surface species of calcite varies with pH and ionic strength in the presence of MgCl$_2$.
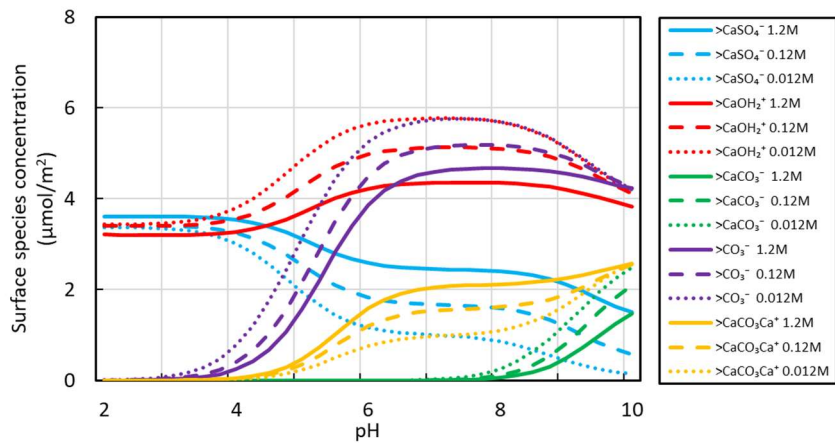
Figure 8-8 Surface species of calcite varies with pH and ionic strength in the presence of Na$_2$SO$_4$.
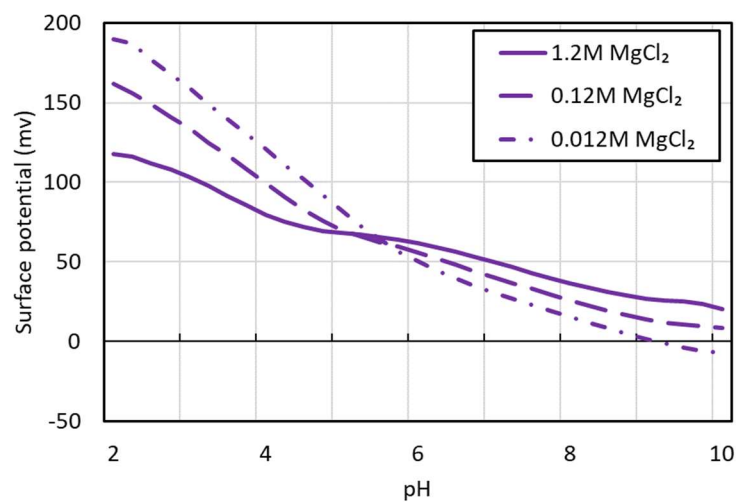
Figure 8-9 Surface potential of calcite varies with pH and ionic strength in the presence of $MgCl_2$.
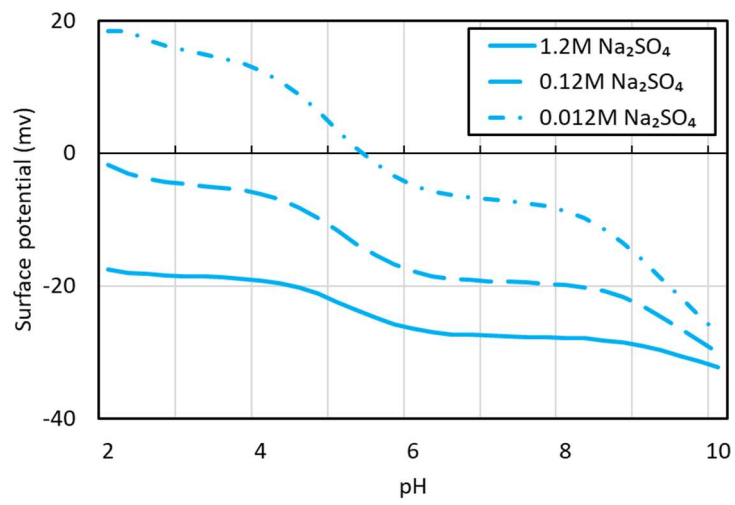
Figure 8-10 Surface potential of calcite varies with pH and ionic strength in the presence of Na_2SO_4.

9. Chapter 9 Interpreting micromechanics of fluid-shale interactions with geochemical modelling and disjoining pressure: Implications for calcite-rich and quartz-rich shales

9.1. Abstract

Fluid-shale interactions appear to significantly affect shale micromechanical properties, which regulate fracture network propagation during multistage hydraulic fracturing in shales and thus the gas production. While published works confirm that fluid-shale interactions can reduce Young's modulus and rock strength compared to dry shale samples, few attentions have been paid to unveil the nature of the physics with a combination of geochemical modelling and disjoining pressure isotherm, and fewer works have envisaged the effect of mineralogy (calcite-rich or quartz-rich rock) on shale weakening with presence of aqueous liquids. We hypothesize that fluid-mineral interactions likely generate electrical double layer force between mineral surfaces which would shift the disjoining pressure from strongly negative (mineral-air-mineral) to less negative or even positive (mineral-fluid-mineral) thus triggering Young's modulus reduction. To test the hypothesis, geochemical modellings including minerals dissolution (calcite, dolomite, quartz, pyrite and illite) and surface complexation were performed together with disjoining pressure isotherm using literature experimental data, accounting for the Young's modulus reduction induced by fluid-shale interactions.

The geochemical modelling shows that the amount of mineral dissolution at *in-situ* condition is negligible, and thus may play a minor role in Young's modulus. Disjoining isotherm shows that both calcite and quartz (plane-plane geometry) give a strong negative disjoining pressure generated by van der Waals force and structural force in the presence of air, whereas the disjoining pressure can be shifted from strongly negative to less negative for calcite and even positive for quartz in presence of fluids due to the electrostatic force, suggesting a Young's modulus reduction due to the weaker adhesion in line with literature experimental data. This work provides an overall conceptual framework, which supports the hydraulic fracturing fluid design and treatment in shale reservoirs from geochemical and disjoining pressure isotherm perspectives.

Keywords: Shale reservoirs; Fluid-rock interactions; Young's modulus; Geochemical modelling; Disjoining pressure isotherm.

9.2. Introduction

The increasing demand of geo-energy has shifted the gravitation of petroleum industry from conventional to unconventional resources development worldwide, particularly in the United States [273, 317, 318], Canada [74, 319, 320], Australia [239, 321, 322] and China [2, 162, 323]. Due to the low permeability (tens of nano-darcy to milli-darcy [239]) of shale reservoirs, the economic production from shale is not viable without a combination of horizontal drilling and multistage hydraulic fracturing [217]. To fracture shale reservoirs, a huge amount of water (10,000 to 75,000 m^3 per well [11]) with additives such as salts (NaCl and KCl) and the proppants (sands or tiny ceramic beads) are injected into subsurface at high pressure [13, 273, 276]. The injected proppants can hold the pre-existing and induced micro-fractures open and thus enhance the formation productivity [276, 324].

Published works have shown that fluid-rock interaction can affect the rock geomechanical properties such as Young's modulus [35-37], compressive strength [29-33], brittleness index [37, 39] and subcritical crack growth [40-43]. This is typically true for the shale reservoirs that are rich in calcite and quartz. For instance, Bergsaker et al. [64] investigated the effect of fluid composition and salinity on calcite subcritical crack growth using double torsion apparatus. The results show that lowering salinity of Na_2SO_4 from 0.4M to 0.004M could strengthen the calcite crystal, whereas the calcite weakening was observed when lowering the same salinity for NaCl. They suggest that mineral dissolution is not the controlling factor in subcritical crack propagation, whereas the ion adsorption on calcite grains and the corresponding surface charge change may attribute to the observed rock weakening. Al-Bazali et al. [133] experimentally investigated the impact of water content on shale compressive strength. They observed that higher water activity can trigger larger shale strength reduction. Akrad et al. [35] measured Young's modulus of the shale samples with different mineralogy before and after saturating with 2 wt% KCl. They reported that the samples containing more calcite have a greater Young's modulus reduction than those rich in quartz. The weakening effect of shale would lead to proppants embedment

issues, which may undermine the fracture conductivity and thus decrease hydrocarbon production [35, 325].

While experimental works have demonstrated that fluid-shale interactions can weaken the rock strength, few of them have quantified the physics behind this phenomenon, [307] and fewer researches have looked beyond the effect of mineralogy (calcite or quartz-rich) on shale weakening from geochemical perspective. Therefore, we aimed to provide an overall conceptual framework which would predict how the fluid-shale interaction influences the geomechanical properties, and help the hydraulic fracturing design and treatment in shale reservoirs. We hypothesize that fluid-mineral interactions would trigger extra electrical double layer force between mineral subsurfaces and lead to Young's modulus reduction, compared to the dry sample conditions where only van der Waals force and structural force contribute to the disjoining pressure. To be more specific, we hypothesize that 1) a shift of disjoining pressure from strongly negative (in air condition without fluid-rock interactions) to less negative or even positive (with fluid-rock interactions) leads to Young's modulus reduction of shale, and 2) the reduction of Young's modulus would be more distinct in calcite-rich shales compared to quartz-rich shales. To test the assumptions, we first simulated the dissolution of minerals (calcite, dolomite, quartz, pyrite and illite) at *in-situ* conditions using data from Akrad et al. [35]. Then, a complexation modelling on surface of organic matter (OM, which represents the kerogen in this work to differentiate the inorganic minerals), quartz, calcite and dolomite are performed to calculate the corresponding surface species distributions and surface potential as function of pH and KCl salinity. Moreover, the obtained surface potential is used to predict the disjoining pressure between calcite-calcite and quartz-quartz surfaces, accounting for the reduction of Young's modulus in calcite-rich and quartz-rich shales after fluid-rock interactions.

9.3. Experimental Observations

To test our hypothesis, experimental data from Akrad et al. [35] are adopted because their work covers a wide range of shale formations with different mineralogy (e.g., calcite-rich, quartz-rich and clay-rich shales) in the United States. To be more specific, the Young's modulus of intact samples from Barnett, Bakken, Eagle Ford and Haynesville shale plays were measured using nano-indentation techniques before and

after saturation with fracturing fluid (2 wt% KCl with slick water) at room and high temperature (300 ºF) and under atmospheric pressure. As the non-destructive measurement technique, the nano-indentation is perfect to determine the Young's modulus on tiny samples by recording force and displacement. Table 9-1 shows the mineralogy of the tested samples using Quantitative Evaluation of Minerals by Scanning Electron Microscopy (QEMSCAN), and the total organic content (TOC) by pyrolysis test, which are well documented in their work [35].

Table 9-1 Mineralogy and TOC of targeted samples for Young's modulus measurement (wt%)[35].

Formation	Dolomite	Pyrite	Calcite	Quartz	I/S[a]	TOC	E[b] reduction (%)
Lower Bakken	10	13	0	21	47	17.18	22
Middle Bakken	4	1	77	11	4	0.45	52
Barnett	1	2	12	59	21	4.4	32
Eagle Ford	2	6	77	3	8	4.99	70
Haynesville	0	5	2	28	57	3.53	6

[a]I/S represents the mixture of illite and smectite.

[b]E represents Young's modulus of tested samples measured by nanoindentation.

The main conclusions from Akrad et al. [35] can be summarized as the following: 1) Young's modulus decreases in all samples saturated with 2 wt% KCl solution compared to the dry samples, and 2) calcite-rich shales give a higher percentage of reduction in Young's modulus compared to quartz-rich shales (30 to 50% reduction for calcite-rich samples, and 10 to 30% for quartz-rich samples).

9.4. Methodology

9.4.1. Mineral dissolution-precipitation

Given that mineral dissolution was assumed to govern the rock mechanical properties during hydraulic fracturing as supposed by Akrad et al. [35], we first examined the extent of mineral dissolution induced by fluid-shale interactions. The extent of such dissolution-precipitation of any mineral can be represented by the saturation index as shown in Eq. 9-1 [175]:

$$Saturation\ Index(mineral) = log\left(\frac{IAP}{K}\right)$$
<div align="right">Eq. 9-1</div>

where *IAP* is the ion activity product of the solution, and *K* is the equilibrium constant of the dissolution-precipitation reaction for a given mineral. The mineral will tend to dissolve into the solutions when the saturation index is negative, whereas it would precipitate when that value is positive [21, 175]. According to the reported mineralogy of shale samples in Table 9-1, minerals including quartz (SiO_2), calcite ($CaCO_3$), dolomite ($CaMg(CO_3)_2$), pyrite (FeS_2) and illite ($K_{0.6}Mg_{0.25}Al_{1.8}Al_{0.5}Si_{3.5}O_{10}(OH)_2$) are incorporated in this study. The corresponding dissolution reactions and equilibrium constants for these minerals are listed in Table 9-2, which are defined by the Lawrence Livermore National Laboratory (LLNL) thermo.com.V8.R6.230 database [175]. PHREEQC V3.5.0 was used to perform the modelling of mineral dissolution and the surface complexation which will be introduced in the following subsection.

Table 9-2 Dissolution-precipitation reactions and equilibrium constants for quartz, calcite, dolomite, pyrite and illite [21, 175].

Number	Reactions	log K_{298K}
1	$SiO_2 = SiO_2$	-3.99
2	$CaCO_3 + H^+ = Ca^{2+} + HCO_3^-$	1.85
3	$CaMg(CO_3)_2 + 2 H^+ = Ca^{2+} + Mg^{2+} + 2 HCO_3^-$	2.51
4	$FeS_2 + H_2O = 0.25 H^+ + 0.25 SO_4^{2-} + Fe^{2+} + 1.75 HS^-$	-24.65
5	$K_{0.6}Mg_{0.25}Al_{1.8}Al_{0.5}Si_{3.5}O_{10}(OH)_2 + 8 H^+ = 0.25 Mg^{2+} + 0.6 K^+ + 2.3 Al^{3+} + 3.5 SiO_2 + 5 H_2O$	9.026

Note: Calcite, dolomite and illite tend to dissolve in the solution while quartz and illite tend to precipitate at room temperature.

9.4.2. Surface potential calculation

To test our hypothesis that fluid-mineral interactions likely generates electrical double layer force which shifts the disjoining pressure from strongly negative to less negative or even positive, we first calculated the mineral surface potential. Surface potential is defined as the electrostatic potential energy on a charged surface [163]. If surface charge density and surrounding fluid chemistry is given, then the Grahame equation can be used to calculate the surface potential [163]. Meanwhile, to capture how the individual mineral reacts with electrolyte solution, we performed surface complexation modelling separately on organic matter, quartz, calcite and dolomite to predict the corresponding surface species concentration, surface charge density and

thus the surface potential. The surface complexation reactions and corresponding equilibrium constants are listed in Table 9-3.

In this study, the surface site density for quartz, calcite and dolomite are set to 3.84 [182], 5 [90, 179] and 8 μmol/m^2 [183, 184], and the specific area are set to 0.1, 2.8 and 1.7 m^2/g [21, 85], respectively. For organic matter, the site density for acid number (AN) and base number (BN) are set to 0.5 and 5 μmol/m^2 and the specific area is 200 m^2/g [85]. All the surface complexation reactions are simulated with consideration of aforementioned mineral dissolution-precipitation process. Besides, the effect of CO_2 and O_2 in atmosphere is also incorporated in the simulation to better mimic the experimental conditions. The aqueous CO_2 can generate extra H^+ that affects the complexation reaction on mineral surface as shown in Table 9-3, while the dissolved O_2 can affect electrolyte salinity, pH and accelerate pyrite oxidation [185]. The log of partial pressure of CO_2 and O_2 is set to -3.4 and -0.67, which represents the corresponding content in the atmosphere [21].

Table 9-3 Surface complexation reactions of organic matter, quartz, calcite and dolomite and corresponding equilibrium constants.

Number	Reaction	log K_{298K}
	Organic Matter[a]	
6	$>NH^+ \leftrightarrow >N + H^+$	-6.0
7	$>COOH \leftrightarrow >COO^- + H^+$	-5.0
8	$>COOH + Ca^{2+} \leftrightarrow >COOCa^+ + H^+$	-3.8
9	$>COOH + Mg^{2+} \leftrightarrow >COOMg^+ + H^+$	-4.0
	Quartz[b]	
10	$>SiOH \leftrightarrow >SiO^- + H^+$	-4.0
11	$>SiOH + Ca^{2+} \leftrightarrow >SiOCa^+ + H^+$	-9.7
12	$>SiOH + CaOH^+ \leftrightarrow >SiOCaOH + H^+$	-4.5
	Calcite[b]	
13	$>CaOH + H^+ \leftrightarrow >CaOH_2^+$	11.9
14	$>CaOH + HCO_3^- \leftrightarrow >CaCO_3^- + H_2O$	5.8
15	$>CaOH_2^+ + SO_4^{2-} \leftrightarrow >CaSO_4^- + H_2O$	2.1
16	$>CO_3H \leftrightarrow >CO_3^- + H^+$	-5.1
17	$>CO_3H + Ca^{2+} \leftrightarrow >CO_3Ca^+ + H^+$	-2.6
	Dolomite[c]	

18	$>MgOH + H^+ \leftrightarrow >MgOH_2^+$	10.6
19	$>MgOH - H^+ \leftrightarrow >MgO^-$	-12.0
20	$>MgOH + CO_3^{2-} + 2 H^+ \leftrightarrow >MgHCO_3 + H_2O$	23.5
21	$>MgOH + CO_3^{2-} + H^+ \leftrightarrow >MgHCO_3^- + H_2O$	15.4
22	$>MgOH + HCO_3^- \leftrightarrow >MgCO_3^- + H_2O$	5.8
23	$>MgOH_2^+ + SO_4^{2-} \leftrightarrow >MgSO_4^- + H_2O$	2.1
24	$>CO_3H \leftrightarrow >CO_3^- + H^+$	-4.8
25	$>CO_3H + Mg^{2+} \leftrightarrow >CO_3Mg^+ + H^+$	-2.0

[a] Surface complexation reactions for organic matter are obtained from Zeng et al. [85]. ">" means the functional group is attached on the mineral surface.

[b] The reactions for calcite and dolomite are obtained from Brady et al. [89, 182] and Chen et al. [186].

[c] The reactions for >MgOH of dolomite are obtained from Pokrovsky et al. [183, 184]. Reactions for >CaOH of dolomite are set as same as the calcite.

9.4.3. Disjoining pressure isotherm

The interaction between two surfaces should incorporate electrostatic force, van der Waals force and structural force, which was first proposed by Derjaguin, Landau, Verwey and Overbeek and is well-known as the DLVO theory [192, 231] and is expressed as:

$$\Pi_{Total} = \Pi_{van\ der\ Waals} + \Pi_{electrostatic} + \Pi_{structural} \qquad \text{Eq. 9-2}$$

where Π_{Total} is the total disjoining pressure between two surfaces, Pa; $\Pi_{van\ der\ Waals}$ is the van der Waals force, Pa; $\Pi_{electrostatic}$ is the electrostatic force, Pa; and $\Pi_{structural}$ is the structural force, Pa. It is worth noting that the disjoining pressure between mineral surfaces can represent the rock strength to a certain extent [54]. The negative disjoining pressure corresponds to adhesive force which can attract the adjacent mineral surfaces and therefore indicates a high rock strength, whereas the positive disjoining pressure represents the repulsive force which tends to separate surfaces [54, 163]. By shifting disjoining pressure from negative to positive, the repulsive force between two close surfaces would weaken the rock and decrease the yield and bulk modulus and thus the whole rock strength [60].

At an air condition, only van der Waals force contributes to the disjoining pressure because the electrical double layer (EDL) is assumed to be negligible without fluid-rock interaction [163]. The van der Waals force of two similar flat surfaces (the geometric contact of calcite-calcite and quartz-quartz is assumed to be the plane-plane) is defined by [163, 194]:

$$\Pi_{van\ der\ Waals} = -\frac{H}{6\pi D^3}$$ Eq. 9-3

Where H is the Hamaker constant, J; D is the distance between two mineral interfaces, m.

In presence of fluid, fluid-rock interactions affect the rock surface chemical species thus the surface charge density. Therefore, electrostatic force needs to be considered together with van der Waals force in the disjoining pressure isotherm calculation. The electrostatic force for two similar flat surfaces with constant surface potential is given by [163, 194]:

$$\Pi_{electrostatic} = \left(\frac{\kappa^2}{2\pi}\right) Z e^{-\kappa D}$$ Eq. 9-4

where κ is the reciprocal Debye length, m^{-1}; Z is the interaction constant, J m^{-1}. The reciprocal Debye length is expressed by:

$$\kappa = \left(\sum_i \rho_{\infty i} e^2 z_i^2 / \varepsilon_0 \varepsilon k T\right)^{0.5}$$ Eq. 9-5

where $\rho_{\infty i}$ is the number density of ion i at bulk solution; e is the electronic charge, C; z_i is the valency of ion i, ε_0 is the dielectric constant or permittivity of vacuum, C/(V m); ε is the relative permittivity of water, C/(V m); k is the Boltzmann constant, J/K; T is the absolute temperature, K.

The interaction constant Z in Eq. 9-4 is defined by:

$$Z = 64\pi\varepsilon_0\varepsilon(kT/e)^2 \tanh^2(ze\Psi_0/4kT)$$ Eq. 9-6

where Ψ_0 is the surface potential, mV.

In this simulation, the electronic charge e is set to be 1.602×10^{-19} C, the dielectric constant ε_0 is 8.85×10^{-12} C/(V m), the relative permittivity of water ε is 78.4 C/(V m),

and the Boltzmann constant k is 1.381×10^{-23} J/K [163, 193]. The Hamaker constant for calcite and quartz is set to be 10.1×10^{-20} and 8.86×10^{-20} J at vacuum or air condition, and 1.44×10^{-20} and 1.02×10^{-20} J at water condition at temperature of 298K, respectively [195].

The structural force between two surfaces is calculated by [326]:

$$\Pi_{structural} = A_k exp\left(-\frac{D}{D_s}\right)$$
Eq. 9-7

where A_k is the coefficient, Pa, and D_s is the characteristic decay length, m. In this context, A_k is set to 1.5×10^{10} Pa and D_s is 0.05 nm [193, 326].

To calculate the disjoining pressure between calcite and quartz surfaces, we first performed the Surface Complexation Modelling for specific mineral with consideration of mineral dissolution-precipitation in different KCl solutions to get the *in-situ* pH. The obtained pH is then used to determine the surface potential to predict the corresponding disjoining pressure as shown in Table 9-4 in section 9.5.3. It is worth noting that in this study, the samples from Middle Bakken (M-Bakken) which is calcite-rich (77 wt%) and Barnett which is quartz-rich (59 wt%) are used as the modelling targets to differentiate the role of calcite and quartz in Young's modulus. To furtherly reveal the effect of KCl concentration on the system geochemical and geomechanical properties and enlighten the designing of hydraulic fracturing fluid, we covered three different salinities (5, 2 and 0.5 wt% KCl). It is worth noting that we did not consider the effect of air atomic structure on disjoining pressure for the interaction between rock and air [327]. Effect of temperature is also not included in this work due to a lack of data on the standard enthalpy change ΔH when calculating the equilibrium constant for surface complexation [85], and also on the Hamaker constant H when calculating the van der Waals force at high temperature.

9.5. Results and Discussions

In this section, the effects of pH and KCl salinity of the fracturing fluid on mineral dissolution and surface potential are introduced first. Then the calculated *in-situ* surface potential is used to predict the disjoining pressure, which accounts for the fluid-rock interactions on micromechanics of shales. The distributions of surface species varying with pH for organic matter, quartz, calcite and dolomite can be found in

Supplemental Materials. We recall that all the physics-based geomechanical calculations in this study are built on the experimental results reported by Akrad et al., which was focused on shale-KCl interaction. This simplified fluid medium is only partially realistic for unconventional shale reservoirs, where the flowback or produced water usually contain a large amount of other ions such as sodium, calcium, magnesium and sulphate [110, 111, 328]. Nevertheless, we proposed a potential framework to characterize the rock mechanical properties from a geochemical perspective, which may contribute to furtherly understand the *in-situ* geomechanical-geochemical interactions.

9.5.1. Effect of mineral dissolution

Figures 9-1a to 1e illustrate the variation of saturation index with pH and salinity (5, 2 and 0.5 wt% KCl) for calcite, dolomite, quartz, pyrite and illite with consideration of all minerals dissolution-precipitation for Middle Bakken and Barnett shales, respectively. Results show that KCl concentration has a negligible effect on saturation index for all the tested minerals. For calcite and dolomite, the saturation index increases from negative to positive at the turning point of pH = 8 (Figures 9-1a and 1b), which is in agreement with Rossum and Merrill [125]. The saturation index for quartz roughly remains null and becomes negative when pH is greater than 8.5 (Figure 9-1c). For illite (Figure 9-1e), the saturation index increases first with pH at acid condition then decreases at basic condition, which is in line with the observations reported by Truche et al. [329] and Smith et al. [330] The saturation index of pyrite is extremely low (less than -220) for all pH ranges as shown in Figure 9-1d. This is because pyrite can be easily oxidized by the dissolved O_2 in solution [185]. The generated H^+ during pyrite oxidization then react with calcite and dolomite through following reaction, which produces CO_2 and buffer the system pH [185].

$$FeS_2 + 3.75O_2(aq) + CaMg(CO_3)_2(s) + 1.5H_2O(l) \rightarrow Fe(OH)_3(s) + Ca^{2+}(aq) + 2SO_4^{2-}(aq) + 2CO_2(aq)$$
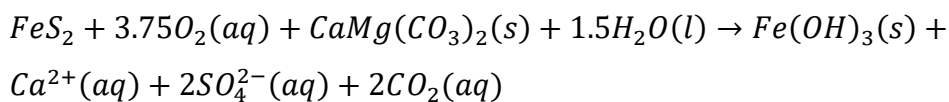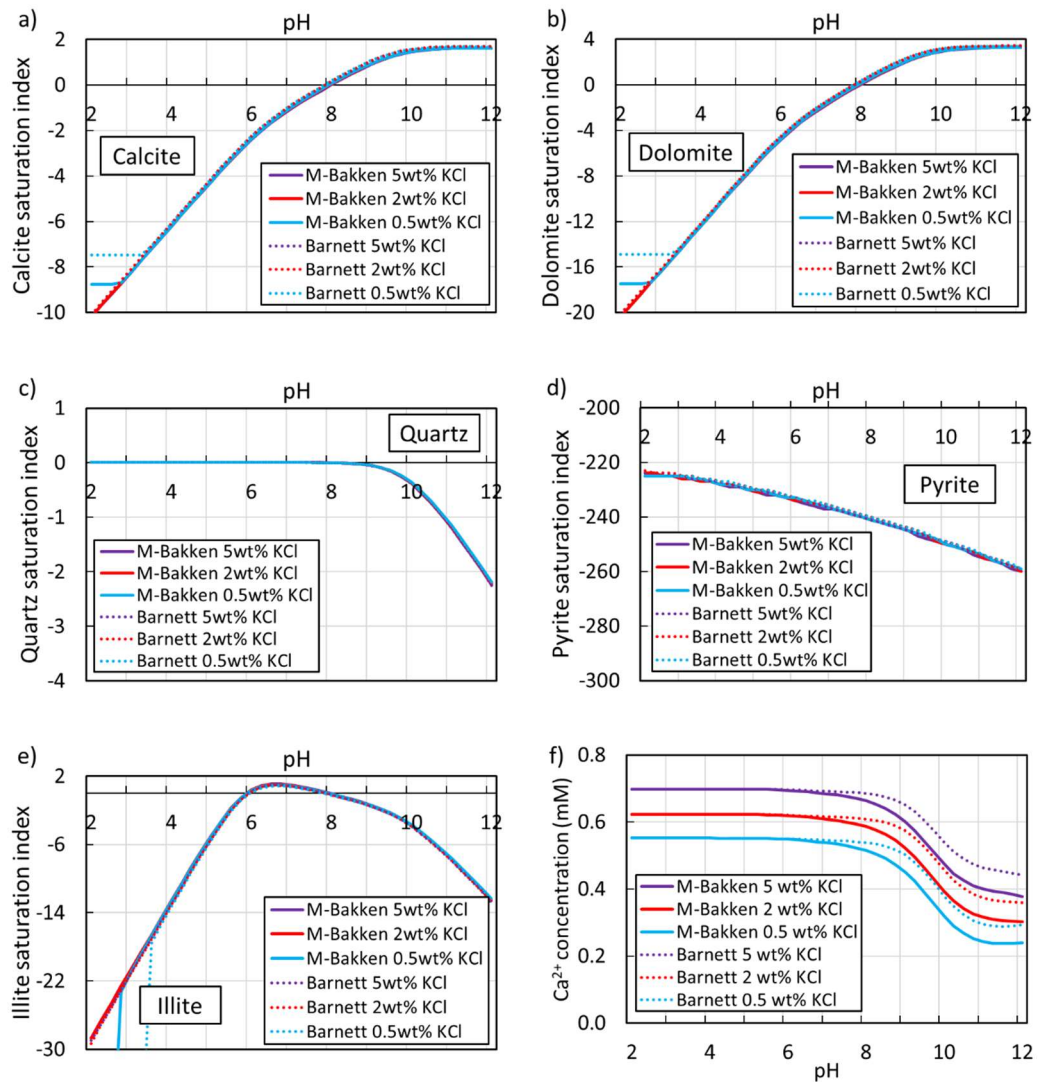
Figure 9-1 Saturation index varies with pH and KCl salinity for a) calcite, b) dolomite, c) quartz, d) pyrite and e) illite, and f) the Ca^{2+} concentration of KCl solution with different salinity after the equilibrium of mineral dissolution-precipitation at 298K. Fluid is set as the excess reactant because of the tiny size (length of millimetres) of the samples used in nanoindentation tests [51]. The solid lines represent Middle Bakken and dot lines represent the Barnett sample.

Given that the *in-situ* pH for the KCl solution is around 8.25 (7.974 for 5 wt%, 7.831 for 2 wt% and 7.813 for 0.5 wt% as simulated by PHREEQC) when it is equilibrated with minerals and CO_2 in the atmosphere at room temperature, the saturation indexes for all the tested minerals at that pH are nearly zero. This implies that mineral dissolution is negligible at this condition not only for the calcite as speculated by Akrad et al. [35], but also for dolomite, quartz, pyrite and illite. It is also worth noting that the dissolution of mineral is a long-term progress and highly depends on the acidity

and cationic ions such as Mg^{2+}, Cu^{2+}, Zn^{2+} and Pb^{2+} in the solutions [126, 331]. In this experiment, the water used only contains the monovalent ions (K^+ and Cl^-) that would not act complexation with functional groups on mineral surface (see Table 6-3). As a result, the possible calcite solubility is considerably limited [124, 127, 332]. Therefore, we rule out the possibility that mineral dissolution may play a significant role in rock weakening thus the Young's modulus reduction.

Moreover, we also calculated Ca^{2+} concentration in solution when the system reaches equilibrium of mineral dissolution-precipitation as illustrated in Figure 9-1f, which shows that lowering KCl salinity slightly decreases the Ca^{2+} level as a result of surface complexation of $>CO_3Ca^+$. This is because decreasing salinity likely increases hydrogen activity coefficient thus shifting the Reaction 17 towards right-hand side. At basic condition for a given salinity, Ca^{2+} concentration decreases with increasing pH due to the strong calcite/dolomite precipitation, which is in line with the results of Figures 9-1a and 1b. At the *in-situ* pH of 8, the Ca^{2+} concentration ranges from 0.5 to 0.7 mM for all tested salinity, which means only 0.35 to 0.49 wt% of calcite dissolves in water and is consistent with the results reported by Langmuir [124]. Since the only source of calcium in solution is the calcite/dolomite dissolution (the existing precipitated salts on mineral surface cannot measured and are not considered in this study; even if the precipitated salts could dissolve in solution, the increased aqueous Ca^{2+} would furtherly restrain the $CaCO_3$ dissolution through the Reaction 2 in Table 9-2), such low level of Ca^{2+} concentration in return indicates that the mineral dissolution at this experimental condition is relatively weak, and should not be responsible for the high Young's modulus reduction (30 to 50%) for calcite-rich sample.

9.5.2. Effect of pH and salinity on surface potential

Given that mineral dissolution plays a negligible role in shale rock weakening, to further test our hypothesis, we computed surface potential of various minerals in presence of different KCl salinity. Figures 9-2a to 2d show that increasing pH decreases the surface potential for all tested minerals. Figure 9-2b illustrates that quartz surface potential would remain negative under all pH conditions. For instance, increasing pH from 6 to 8 would decrease the surface potential from -141 to -195 mV for Middle Bakken with 2 wt% KCl. For organic matter (Figure 9-2a), calcite (Figure

9-2c) and dolomite (Figure 9-2d), the increase of alkalinity shifts surface potential from positive to negative when pH is greater than 7, 9 and 8.5, respectively. Similar results were observed by Zeng et al. [21, 62], who reported that surface potential of organic matter, quartz and calcite decreases with increasing pH.
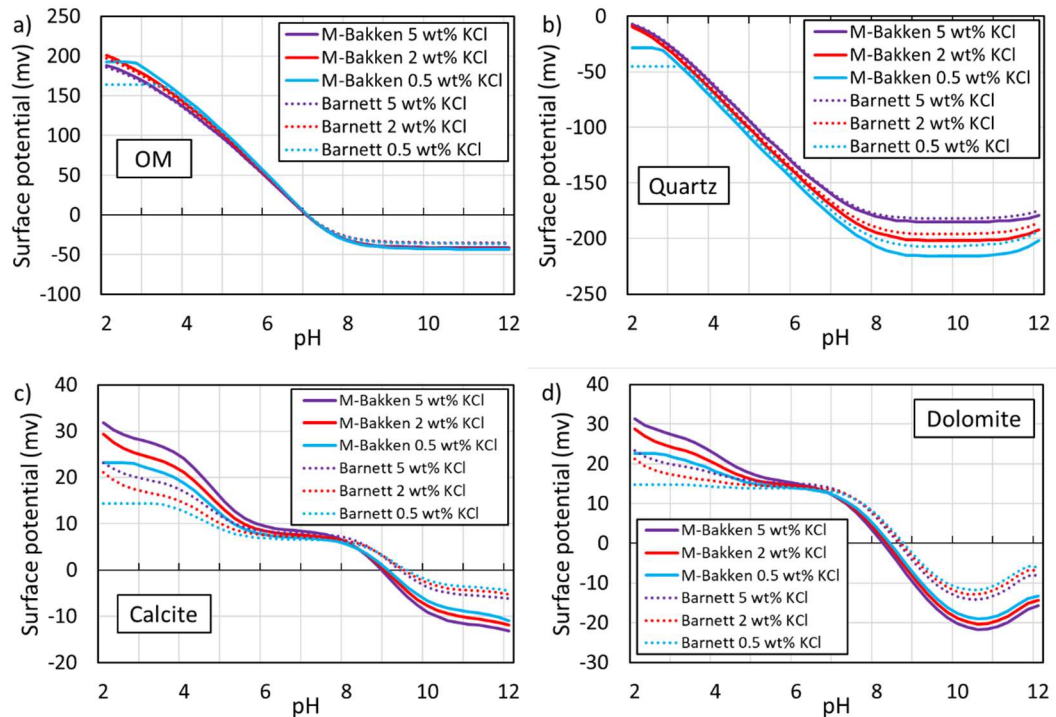
Figure 9-2 Surface potential varies with pH and KCl salinity for a) organic matter (OM), b) quartz, c) calcite, and d) dolomite at 298K for the tested Middle Bakken and Barnett samples with consideration of mineral dissolution and precipitation. Fluid is set as the excess reactant because of the tiny size (length of millimetres) of the samples used in nanoindentation tests [51].

For organic matter, lowering concentration from 5 to 0.5 wt% would increase the surface potential at acidic condition and slightly decrease the potential at basic condition (Figure 9-2a). For quartz, the reduction of KCl salinity decrease the surface potential regardless of pH, but the higher the pH, the greater surface potential drop (Figure 9-2b). Different from OM and quartz, the effect of KCl concentration on calcite and dolomite's surface potential changes with pH (Figure 9-2c and 2d). At acid condition, decreasing salinity would decrease the surface potential. When pH is greater than 8 for calcite and 7 for dolomite, lowering salinity increases the surface potential. To calculate the disjoining pressure and thus test the hypothesis to interpret Akrad et

al. [35] experimental results, surface potential of calcite and quartz at different KCl salinity is reported in Table 9-4.

Table 9-4 The surface potential of calcite and quartz used for calculating disjoining pressure and the measured zeta potential at in-situ pH.

KCl concentration			5 wt%	2 wt%	0.5 wt%
Simulation[a]		pH	7.97	7.83	7.81
	Calcite	Surface potential (mV)	5.60	5.87	6.14
	Quartz[c]		-180	-195	-207
Measurement[b]	Calcite	pH	8.59	8.42	8.39
		Zeta potential (mV)	1.82	-0.06	-2.37
	Quartz	pH	7.45	7.38	7.36
		Zeta potential (mV)	-7.37	-14.68	-28.90

[a] The surface potential of calcite and quartz (parts of the intact shale sample) from the simulation, which combines surface complexation modeling and mineral dissolution-precipitation, is used to calculate the electrostatic force and the disjoining pressure to match the experimental conditions reported by Akrad et al. [35]).

[b] The zeta potential is measured by mixing the powder of pure calcite and quartz crystal with KCl solutions, which is not representative for the real case but shows the similar variation trend.

[c] The estimation of disjoining pressure on mineral surface would be highly accurate when the surface potential is between -25 and 25 mV using plane-plane model described in section 3.3 [326]. Beyond this range, the predicted result may deviate from the true value but still generally reflect the variation tendency.

9.5.3.   Disjoining pressure of calcite-rich and quartz-rich shales

Figure 9-3a shows that both calcite and quartz surfaces return a strong negative disjoining pressure generated by van der Waals force and structural force in presence of air without fluid-mineral interactions. Calcite gives a slightly lower disjoining pressure compared to quartz when the film distance is less than 1 nm due to the greater Hamaker constant of the van der Waals force [195]. However, after fluid-mineral interactions, disjoining pressure between calcite-calcite surfaces becomes less negative, for example only -3.04 kPa at film thickness of 6 nm (Figure 9-3b) compared with -24.8 kPa in the air. This shift becomes even more pronounced for quartz, which

shows a positive disjoining pressure regardless of salinity after fluid-quartz interaction. Decreasing salinity does not result in the change of disjoining pressure for calcite-calcite system due to the negligible change of surface potential at *in-situ* pH (Figures 9-2c and 2d). However, for quartz-quartz system, decreasing salinity does shift the maximum disjoining pressure towards more positive due to the increase of surface potential in magnitude. As aforementioned, the negative disjoining pressure represents adhesive force which can attract the adjacent mineral surfaces thus a high rock strength, whereas the positive disjoining pressure represents the repulsive force which would separate surfaces thus a low rock strength [163]. Therefore, our disjoining pressure isotherm predicts the trend of the Young's modulus reduction before and after fluid-mineral interactions.
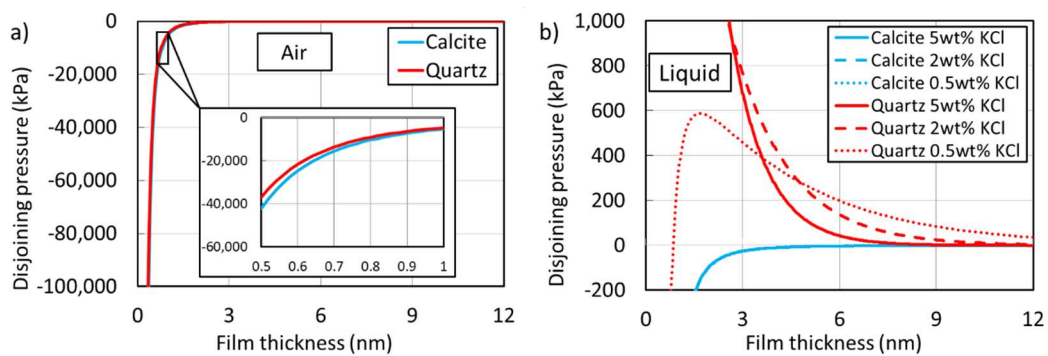
Figure 9-3 Disjoining pressure varies with thickness of film on calcite and quartz surface at a) air without fluid-rock interactions, and b) liquid condition with fluid-rock interactions. Curves of calcite in KCl solution with different concentrations are overlaped.

Disjoining pressure isotherm (Figure 9-3b) also predicts that with fluid-mineral interactions, quartz-rich shales may give a greater reduction of Young's moduli compared to calcite-rich shales because the disjoining pressure is shifted from strongly negative to positive for quartz, but it remains negative in calcite-rich shales. However, our prediction contradicts the experimental result reported by Akrad et al. [18], which shows that calcite-rich shales give a higher reduction in Young's modulus compared to quartz-rich shales (30 to 50% reduction for calcite-rich samples, and 10 to 30% for quartz-rich samples). Four explanations for this discrepancy are proposed in the followings.

First, given that the calcite-calcite and quartz-quartz interactions may play a major role in micromechanics characteristics for calcite-rich and quartz-rich shales, we focused

on the impact of calcite-brine-calcite and quartz-brine-quartz in this study. However, it is worth noting that other and more complex interactions such as calcite-quartz, calcite-OM, quartz-OM and clay minerals may also contribute to the shale micromechanics, which can be quantified using the methodology proposed in this study.

Second, rhombohedral cleavage structure of calcite likely plays an additional role in its micromechanics with fluid-rock interactions. To be more specific, in the present calculation, the KCl solution is considered to have equal chance to enter the surfaces between calcite-calcite and quartz-quartz. In fact, the rhombohedral cleavage structure of calcite [333-336] provides it sub-layers or alternating layers as shown in Figure 4a. In other words, the disjoining pressure would play a role in calcite rock strength between not only the bulk surfaces, but also the intersected cleavage planes inside the bulk. Rather, quartz not exhibiting such rhombohedral cleavage structure, all Si and O atoms are tightly bonded together [337, 338]. Consequently, calcite structures would contribute more to the disjoining pressure decrease thus the Young's modulus reduction.
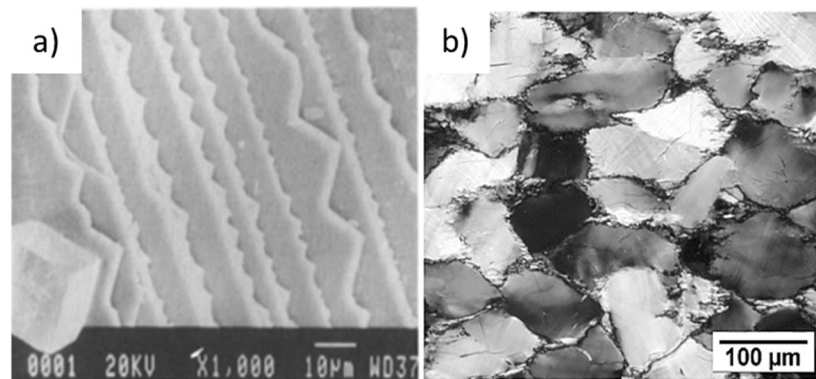
Figure 9-4 a) The calcite cleavage fracture on rhombohedral cleavage planes (from Schultz et al. [336]), and b) the quartz grains sturcture after recrystallization imaged by light-optical micrograph (from Stipp and Tullis [339]).

Third, the disjoining pressure calculation of quartz is based on the plane-plane model, which means two adjacent quartz are contacted through flat surfaces. However, quartz grains can contact each other either by plane or point especially after recrystallization at high temperature as shown in Figure 9-4b [339]. Disjoining pressure with point-point geometry would be much less than plane-plane geometry [163, 313]. Therefore, the current calculated disjoining pressure of quartz may be overestimated.

Fourth, the disjoining pressure curves presented in Figure 9-3 assumes that mineral dissolution is the only mechanism for increasing the ionic strength. However, the salinity of innate shale formation brine can be as high as 300,000 mg/L [110, 115]. After drying in the oven, these salts can precipitate on the surface of pores and micro-fractures inside the rock. When the rock is saturated with KCl solution, the precipitated salts can dissolve again, which would increase the solution salinity. Besides, other possible source of ions such as osmosis effect, which may lead to the discrepancy between experimental observations and simulated results, was not incorporated in this work.

9.6. Implications and Conclusions

Hydraulic fracturing is currently an indispensable means to economically unlock shale oil and gas. Although published works show that during hydraulic fracturing, fluid-shale interactions play a significant role in rock mechanical properties, e.g., Young's modulus [35-37], compressive strength [29-31], brittleness index [37, 39] and subcritical crack growth [40-42], the nature of physics remains unclear thus posing risks to predict the micromechanical behaviour of shale. In this work, we aimed to reveal the controlling factor(s) of micromechanics of shale before and after fluid-mineral interactions from geochemical and disjoining pressure isotherm perspectives. Mineral dissolution and surface complexation were modelled with consideration of KCl concentration (5, 2 and 0.5 wt%) and solution pH (2 to 12) using published data. The obtained calcite and quartz surface potential at *in-situ* condition were then used to calculate the disjoining pressure of calcite and quartz system.

Geochemical modelling shows that saturation index for calcite, dolomite, quartz, pyrite and illite at *in-situ* pH (8.25) is almost zero, implying that mineral dissolution may play a negligible role in shale strength such as Young's modulus reduction. Surface complexation modelling shows that the surface potential of organic matter, quartz, calcite and dolomite decreases with increasing pH. Surface potential of organic matter, calcite and dolomite decreases with increasing salinity at acidic condition except for quartz, which shows the opposite trend. Disjoining pressure calculations show that in air condition without fluid-mineral interactions, quartz-rich and calcite-rich shales give a strongly negative disjoining pressure, indicating a high rock strength thus high Young's Modulus. However, with presence of fluid, the disjoining pressure

can be shifted from strongly negative to slightly negative (for calcite-rich shale) and even positive (for quartz-rich shales), indicating a reduction of rock strength. However, with fluid-mineral interactions, our prediction contradicts the experimental result reported by Akrad et al. [35], which shows that calcite-rich shales give a higher reduction in Young's modulus compared to quartz-rich shales. We tentatively believe that rhombohedral cleavage structure of calcite and the geometry contact of minerals likely play a significant role in the micromechanical properties with fluid-rock interactions. Our work also implies that a hydrophilic system (inorganic materials of shale) likely promotes the effect of fluid-rock interaction on its micromechanics because such system favours water imbibition thus electrostatic force and disjoining pressure. However, the effect of fluid-mineral interactions on shale may be minor in a hydrophobic system, which prevents the water imbibition process. Our study reveals the mechanisms of rock weakening effect after fluid-shale interactions from subsurface physicochemical perspective. These findings would also help to screen the appropriate slick water when performing hydraulic fracturing in calcite-rich and quartz-rich shale reservoirs.

9.7. Supplemental Materials
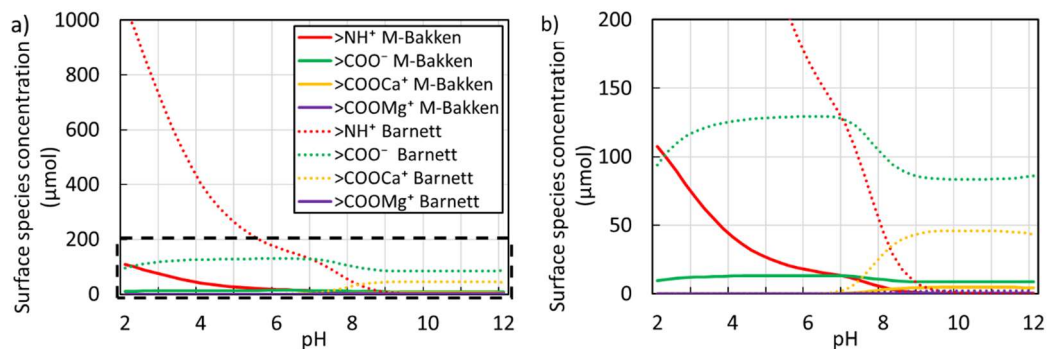
Figure 9-5 Organic matter surface species concentration varies with pH for tested Middle Bakken and Barnett sample at a) the whole scale, and b) low concentration area.
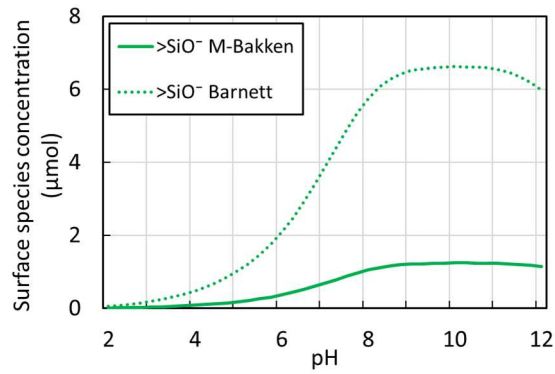
Figure 9-6 Quartz surface species concentration varies with pH for tested Middle Bakken and Barnett sample.
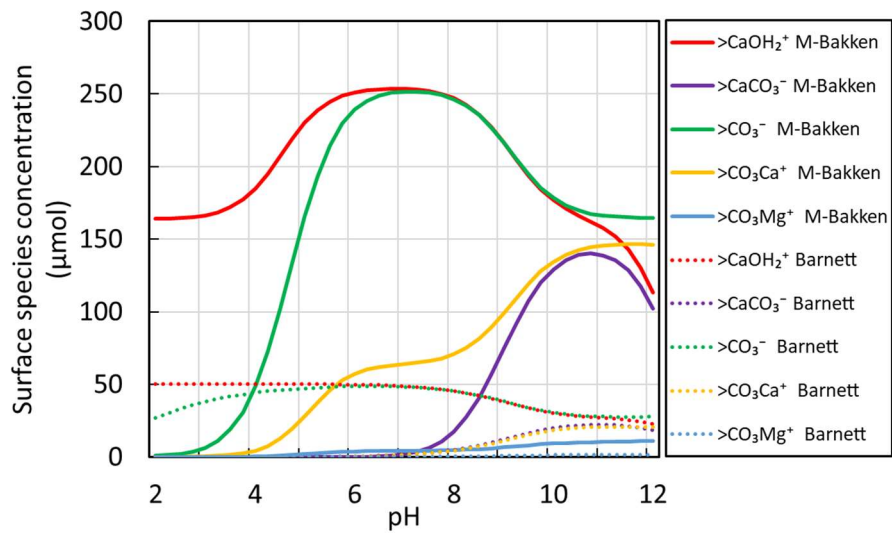
Figure 9-7 Calcite surface species concentration varies with pH for tested Middle Bakken and Barnett sample.
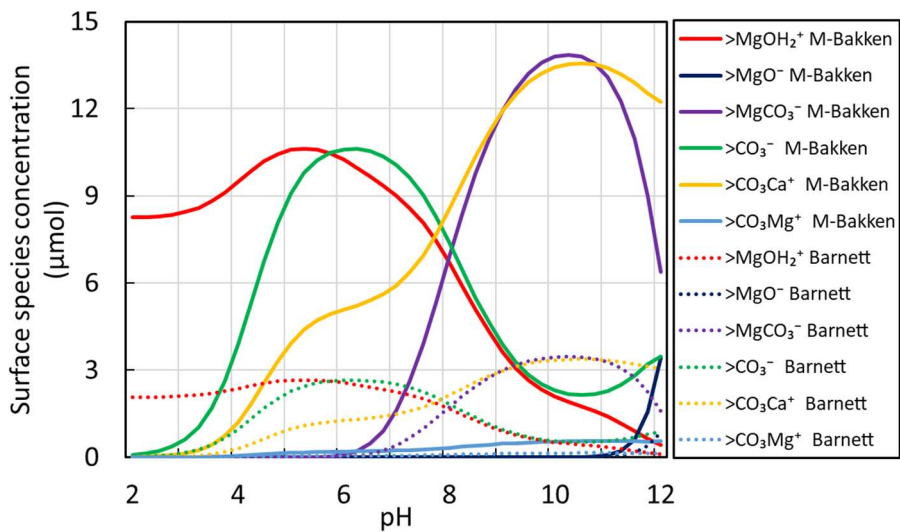
Figure 9-8 Dolomite surface species concentration varies with pH for tested Middle Bakken and Barnett sample.

10. Chapter 10 Effect of Fluid-rock Interactions on Shales Micromechanics

10.1. Abstract

Multi-stage hydraulic fracturing combined with horizontal drilling has been widely implemented to enhance oil/gas production from shale reservoirs. One method of reservoir stimulation is to use low-salinity fracturing fluid that mixes with existing high-salinity formation brine. This process either activates existing natural fractures or generates new fractures thus enhances reservoir communication. However, it is still unclear how the *in-situ* geochemistry change would affect shale surface energy and fracture/micro-fracture propagation, and far less research has investigated the effect of salinity on shale micromechanics. This impedes the proper evaluation of hydraulic fracturing influence on the stability of shale reservoirs with different mineralogy. In this study, the strength of shale samples with different composition at different saturation conditions were measured using nano-indentation techniques together with atomic force microscopy (AFM) and scanning electron microscopy (SEM). In addition, geochemical modelling with the combination of surface complexation and disjoining pressure isotherm were performed to examine the role of physicochemical reactions on shale micromechanical properties.

Nano-indentation tests confirm that brine saturation can decrease samples' indentation moduli regardless of mineralogy. We also found that decreasing salinity would further decrease indentation modulus of calcite-, quartz- and illite-rich shale samples by 43.8%, 19.2%, and 33.3%, suggesting that rock micromechanics are indeed affected by the geochemistry. Compared to dry condition, calcite- and quartz-rich shales have greater indentation moduli reduction after low salinity brine saturation (64.3% and 45.4%) than the illite-rich sample (32.2%), indicating that fluid-rock interactions associated with shale micromechanics are also influenced by mineralogy. Thermodynamics calculation shows that the shift of the disjoining pressure isotherm from strongly negative to positive likely plays an important role in shale weakening rather the mineral dissolution before and after water saturation. Taken together, these findings provide a new understanding of surface energy induced micromechanics of shale through geochemical modelling together with thermodynamics.

10.2. Introduction

During the transition of world energy structure from traditional fossil fuels to renewable energy (e.g., hydrogen), unconventional resources typically the shale gas reservoir plays an important role because of its abundant deposit and cleaner than coal and oil [1, 2]. Shale is a fine-grained sedimentary rock which mainly consists of certain amounts of organic matter (kerogen) and inorganic materials such as quartz, calcite, dolomite, pyrite and clay minerals (e.g., kaolinite, smectite and illite, etc.) [4-7]. Given the low porosity and relatively low permeability (ranges from nanodarcy to millidarcy [8, 9]), a combination of horizontal drilling and multi-stage hydraulic fracturing is indispensable to extract shale gas economically. To improve formation connectivity, low salinity fracturing fluids are commonly injected underground under high pressure, which can create new fractures whilst activating existing natural fractures and thus enhance the production efficiency [217, 242, 340]. Meanwhile, several reservoir and rock parameters need to be considered to maximize the hydraulic fracturing performance including permeability, porosity, compressibility, Young's modulus, Poisson's ratio, toughness and *in-situ* stress, etc [25, 26, 341, 342]. Considering that shales contain high salinity formation brine (sometimes can be up to 280,000 mg/L [27]), when the low salinity water-based hydraulic fracturing fluids (less than 5,000 mg/L [13]) enter the reservoir, the mixing process can not only affect the *in-situ* geochemistry, but also influence the aforementioned design factors typically the mechanical behaviours [28]. Therefore, it is of vital importance to investigate how the shale mechanical properties are governed by the fluid-shale interactions.

Laboratories experiments from last two decades have demonstrated that saturating rock with water would weaken or soften the rock and change its mechanical properties such as compressive strength [29-34], Young's modulus [35-38], brittleness index [37, 39], and may also affect the crack growth even under subcritical conditions [40-46]. However, it is still far from clear to understand the role of water in rock weakening. Current proposed mechanisms of fluid-rock interactions induced rock strength reduction include mineral dissolution and degradation [35, 47-53], clay hydration and swelling [30, 31, 54-56], pyrite oxidation and associated secondary carbonate dissolution [57-59], and the change of rock surface energy and disjoining pressure [40,

60-62]. For example, Al-Bazali et al. [133] measured shale compressive strength under different water saturation in biaxial test. The results show that exposing shale with higher content of water can lead to a larger shale strength decrease, which is mainly caused by the calcite dissolution. Lin and Lai [143] reported that for Barnett shale, increasing 1% of water content would roughly decrease Young's modulus by 6.1 ‰. Liu et al. [144] tested the compressive strength and Young's modulus of shale through water absorption and uniaxial compression experiments. Their results indicate that the rock mechanical properties are also affected by the system wettability: the compressive strength and Young's modulus would decrease when shale is under 'water-absorbing' state. Lyu et al. [18] performed uniaxial compressive strength tests on shale rocks saturated with deionised water, NaCl, KCl and $CaCl_2$ solution. They reported that samples with saline water presented lower swelling tendency and strength reduction compared to the pure water. Adding K^+ can furtherly decrease the strength reduction by preventing clay swelling. These results from macroscopic rock mechanical tests, typically the uniaxial compression test and triaxial test, have clearly demonstrated that fluid-rock interaction would undoubtedly soften shale rocks. The aqueous ions such as Ca^{2+}, Mg^{2+}, and SO_4^{2-} etc., which can react with rock by attaching to or detaching from the specific functional groups on mineral surfaces, can affect shale surface energy, lead to electrical double layer expansion and generate repulsion force between two adjacent mineral particles or sublayers, and thus control the rock strength [60, 61].

To further understand the comprehensively physicochemical mechanisms behinds macroscopic observations, it is crucial to study the contribution of fluid-rock interactions to rock mechanics from shale mineralogy. Meanwhile, the development of nano-indentation technology makes the characterization of rock properties from the mineral perspective possible [343-346]. This technique uses sample with much less geometry, and can provide information of rock strength by applying force of indenter on sample surface only in the depth of tens of nanometers [51]. Therefore, we have the chance to take a glance at how fluid-rock interactions affect the micromechanical properties on mineral itself without worrying about other factors such as internal structures such as pore and micro-fracture networks, mineral cementation, bedding plane orientation and dislocation creep [51, 55]. Although fluid-rock interactions on rock mechanical behaviours have been widely reported from both meso and micro-scale, most of the research up to now have been only descriptive in nature and lack of

quantitative characterization of fluid-rock interactions induced rock weakening. Moreover, much fewer works have been conduct to interpret how the brine salinity can affect shale micromechanics, which fails to capture the geochemical contributions to shale weakening during the mixing of low salinity hydraulic fracturing fluid and high salinity per-existing formation brine. In this study, we thus aim to measure the strength of shale samples with different mineralogy (calcareous, siliceous and argillaceous shale) under different saturation conditions (dry, high salinity and low salinity saturation) through nano-indentation tests with combination of atomic force microscopy (AFM) and scanning electron microscopy (SEM), and understand the effect of fluid-rock interaction on shale micromechanics from physicochemical perspective.

10.3. Methodology

10.3.1. Shale samples

Three samples (TH-1, TH-5 and TH-6) from Goldwyer Formation shale, Canning Basin, Western Australia with different mineral composition were selected for this study (Figure 10-1). The sample TH-1 is calcareous or calcite-rich shale with higher percentage of calcite (>55%), whereas, TH-5 is found to be argillaceous or clay-rich shale (mainly illite >60%) and sample-TH-6 is siliceous shale with about >45% silica minerals (quartz and feldspar). The averaged total organic carbon (TOC) content for the samples-TH-1, TH-5 and TH-6 is recorded as 0.1 wt%, 1.14 wt% and 2.25 wt%. The SEM analysis was carried out before and after fluid treatment on these samples by using a Mira-3 Variable Pressure Field Emission Electron Microscopy (VP-FESEM) having energy dispersive x-ray spectroscopy (EDS) and electron backscattered diffraction (EBSD). The digital images of mineral abundance and distribution were provided by TESCAN Integrated Mineral Analyser (TIMA; see Figure 10-2). All rock samples were mounted in the resin and then polished to make the surface smooth. The polished samples were carbon coated, and the analysis was carried out under working conditions (10-15 Kev) and about 15-20 mm working distance.

Figure 10-1 Shale rock specimens mounted with resin that rich in (from left to right) calcite (TH-1), clay (mainly illite, TH-5) and quartz (TH-6), respectively.
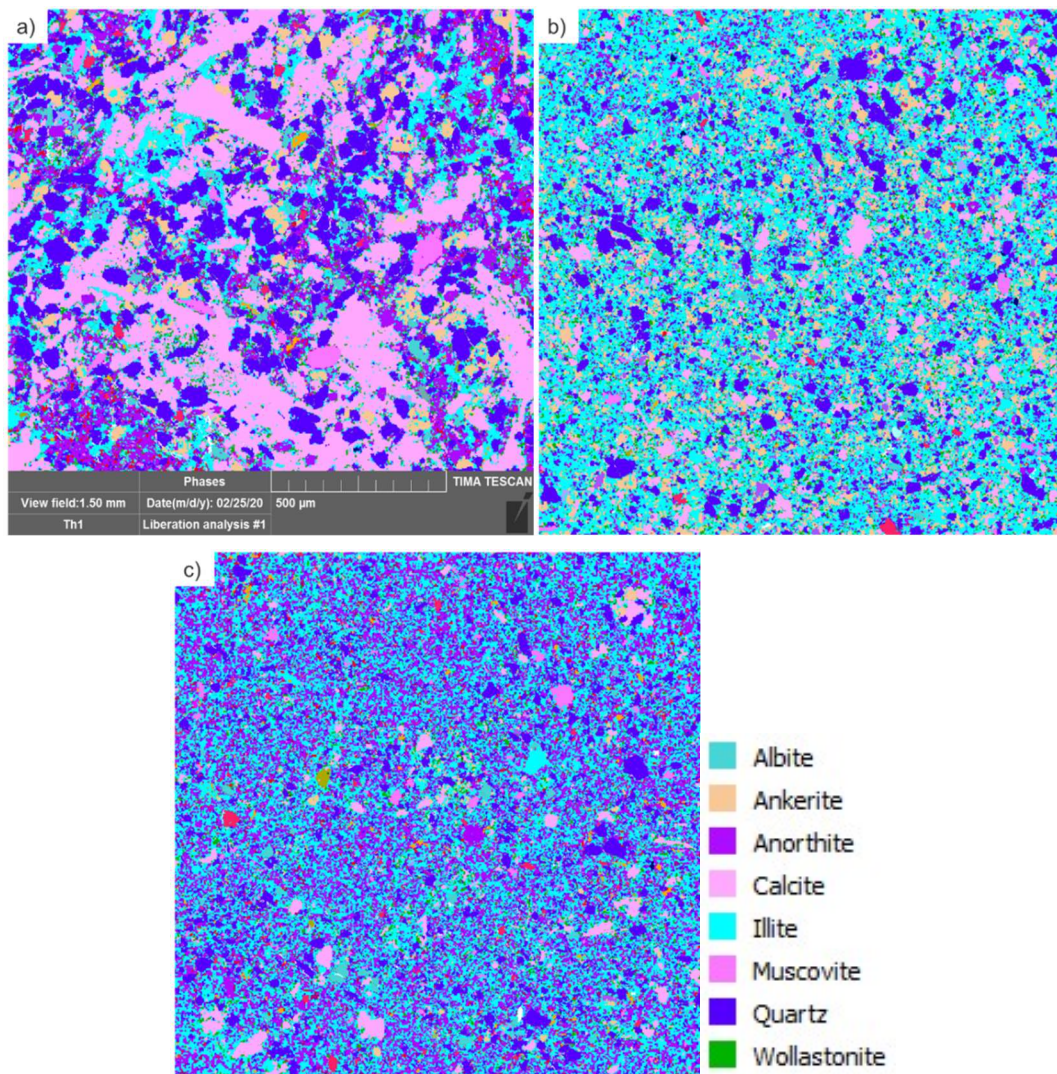
Figure 10-2 Mineral abundance and distribution imaged by TIMA for a) calcite-rich TH-1, b) illite-rich TH-5 and c) quartz-rich TH-6 shale samples [347].

10.3.2. Saturation fluids

Ion types and concentrations would affect mineral surface species concentration, surface potential, surface energy and disjoining pressure. The pre-existing formation brine usually contain extremely high amount of total dissolved solids (TDS) where sometimes can be up to 300,000 mg/L [110, 348]. However, the typical TDS of injected hydraulic fracturing fluid is less than 5,000 mg/L [13]. Therefore, to investigate how the brine compositions can affect shale rock micromechanics, we used two types of brine in this study. The high salinity water (HSW) containing 1 M NaCl + 0.05 M CaCl2 represents the high salinity formation brine, whereas low salinity water (LSW) with 0.01 M NaCl + 0.005 M CaCl2 represents the low salinity fracturing fluids. After the initial tests at dry condition, including the TIMA, SEM, nanoindentation and AFM, all samples were saturated with HSW for 21 days at ambient conditions and then examined by SEM, nanoindentation and AFM again. Afterwards, the samples were saturated with LSW for another 21 days at ambient conditions. Upon the completion of the saturation, the samples were examined in the third round to characterize the influence of fluid-rock interactions on sample mechanical properties.

10.3.3. Nano-indentation test

The micromechanical properties of shale samples were measured using Fischer-Cripps Ultra Micro Indentation System equipped with a Berkovich indenter [213]. In each test, we examined 64 test points on an 8 × 8 network with 50 μm spacing between adjacent points. It should be added that the measurements were conducted on the same area before and after the tests to assure consistency of the indentation results. The maximum applied force was set as 50 mN. It is worth also noting that the directly acquired data from this measurement is indentation modulus. The relationship between indentation modulus and Young's modulus is given by [214]:

$$M = \frac{E}{1-\nu^2} \qquad \text{Eq. 10-1}$$

Where M is indentation modulus, GPa; E is the Young's modulus, GPa; ν is the Poisson's ratio. Given the constant Poisson's ratio of the sample, we can indirectly quantify the change of Young's modulus of the rocks before and after brine exposure

by comparing the change of indentation modulus, and thus characterize the effect of fluid-rock interactions on shale mechanical behavior.

10.3.4. Atomic force microscopy test

AFM is a perfect tool to provide detail surface topography at nano scale. In this study, we used Nano-surf-C3000 controller ECS 204 equipped with Nano surf Cantilever to analyse shale surface structures [349]. This equipment is able to characterize the surface roughness before and after brine treatment and thus can test our purposes that how fluid-rock interactions typically the brine salinity would affect shale micromechanics.

10.3.5. Geochemical modelling

To predict the disjoining pressure between two adjacent mineral particles or sublayers and consequently evaluate the rock strength, the first step is to calculate the mineral surface potential. Surface potential is defined as the electrical potential between the charged surface of a particle and any point in the suspension [163, 350]. For edge charged minerals such as calcite, dolomite and quartz, the surface species can either detach H^+ or attach bonding-capable ions such as Ca^{2+}, Mg^{2+}, and SO_4^{2-} from surrounding solutions and change the surface charge distribution so as the surface potential. If we know the charge density on mineral surface and the water chemistry, the classic *Grahame* equation and *Poisson-Boltzmann* equation can be used to calculate the surface potential in electrolyte solution [61, 62, 163]. Details of the calculation procedures can be found in our previous work [61]. Table 7-1 lists the major surface complexation reactions at room temperature for calcite and quartz used in this study. It is also worth noting that the surface complexation was not simulated on illite surface given its basal-charge type in nature with negligible edge-charges [88].

Table 10-1 Surface complexation reactions for calcite [89, 182] and quartz [62] and associated equilibrium constant at 298K. ">" represent the attachment of specific surface species to mineral surface. Reactions for group of >CaOH of dolomite are set as same as the calcite.

Surface complexation reaction	log K_{298K}	#Eq.
Calcite		

$>CaOH + H^+ = >CaOH_2^+$	11.9	2
$>CaOH + HCO_3^- = >CaCO_3^- + H_2O$	5.8	3
$>CaOH_2^+ + SO_4^{2-} = >CaSO_4^- + H_2O$	2.1	4
$>CO_3H = >CO_3^- + H^+$	-5.1	5
$>CO_3H + Ca^{2+} = >CO_3Ca^+ + H^+$	-2.6	6
Quartz		
$>SiOH = >SiO^- + H^+$	-4	15
$>SiOH + Ca^{2+} = >SiOCa^+ + H^+$	-9.7	16
$>SiOH + CaOH^+ = >SiOCaOH + H^+$	-4.5	17

Once surface potential of specific mineral at given water chemistry is obtained, we can then calculate the disjoining pressure. Disjoining pressure is defined as the distance dependence of the interaction between two adjacent surfaces [193, 231]. The negative disjoining pressure acts as adhesive force which tends to hold the mineral particles together. When disjoining pressure is positive, it would act as the repulsive force and weaken particles interconnections and thus decrease intact rock strength [60].

Based on the classic Derjaguin-Landau-Verwey-Overbeek or DLVO theory, the disjoining pressure can be calculated by [193]:

$$\Pi_{Total} = \Pi_{van \, der \, Waals} + \Pi_{electrostatic} + \Pi_{structural} \qquad \text{Eq. 10-18}$$

where Π_{Total} is the total disjoining pressure between two surfaces, Pa; $\Pi_{van \, der \, Waals}$ is the van der Waals force, Pa; $\Pi_{electrostatic}$ is the electrostatic force, Pa; and $\Pi_{structural}$ is the structural force, Pa. The *van der Waals* force between two flat surfaces (calcite consists of thin sublayers due to the rhombohedral cleavage structure [333-336] so that we assume it presents plane-plane contact) is given by [163]:

$$\Pi_{van \, der \, Waals-plane} = -\frac{H}{6\pi D^3} \qquad \text{Eq. 10-19}$$

where H is the *Hamaker* constant, J; D is the distance between two mineral interfaces, m. While for quartz which is constituted by individual particles, the contact area among adjacent grains should be much less than the calcite. Therefore, we used point-point contact model to calculate *van der Waals* force for quartz and it is defined by [163]:

$$\Pi_{van \, der \, Waals-point} = -\frac{H}{6D^2}\left(\frac{R_1 R_2}{R_1 + R_1}\right) \qquad \text{Eq. 10-20}$$

where R_1 and R_2 are the radius of two contacted quartz grains (assuming the grain is sphere), m, and R_1, $R_2 \gg D$.

The electrostatic force of plane-plane contact for calcite and point-point contact for quartz is respectively given by [163]:

$$\Pi_{electrostatic-plane} = \left(\frac{\kappa^2}{2\pi}\right) Z e^{-\kappa D} \qquad \text{Eq. 10-21}$$

$$\Pi_{electrostatic} \quad = \kappa \left(\frac{R_1 R_2}{R_1 + R_1}\right) Z e^{-\kappa D} \qquad \text{Eq. 10-22}$$

where κ is the reciprocal *Debye* length, m^{-1}; Z is the interaction constant, J m^{-1}. The reciprocal Debye length is expressed by:

$$\kappa = \left(\sum_i \rho_{\infty i} e^2 z_i^2 / \varepsilon_0 \varepsilon k T\right)^{0.5} \qquad \text{Eq. 10-23}$$

where $\rho_{\infty i}$ is the number density of ion i at bulk solution; e is the electronic charge, C; z_i is the valency of ion i, ε_0 is the dielectric constant or permittivity of vacuum, C/(V m); ε is the relative permittivity of water, C/(V m); k is the *Boltzmann* constant, J/K; T is the absolute temperature, K. The interaction constant Z in Eq. 10-21 is defined by:

$$Z = 64\pi \varepsilon_0 \varepsilon (kT/e)^2 tanh^2 (ze\Psi_0 / 4kT) \qquad \text{Eq. 10-24}$$

where Ψ_0 is the surface potential, mV.

The structural interaction is defined by [163]:

$$\Pi_{structural} = A_k exp\left(-\frac{D}{D_s}\right) \qquad \text{Eq. 10-25}$$

where A_k is the coefficient, Pa; D_s is the characteristic decay length from exponential model, m [193].

In this research, the dielectric constant ε_0 is set as 8.85×10^{-12} C/(V m), water relative permittivity ε is 78.4 C/(V m), electronic charge e is 1.602×10^{-19} C, and the *Boltzmann* constant k is 1.381×10^{-23} J/K [163, 193]. The *Hamaker* constant for calcite and quartz is set as 10.1×10^{-20} and 8.86×10^{-20} J at vacuum or air condition, and 1.44×10^{-20} and 1.02×10^{-20} J at water condition at temperature of 298K, respectively [195]. The radius of two contacted quartz particles is set to same as 0.3 nm [351] so that does not meet

the requirement using point-point model. Therefore, plane-plane model is also applied to calculate disjoining pressure between quartz particles. The A_k is set as 1.5×10^{10} Pa and D_s is 0.05 nm [193, 326].

10.4. Results

10.4.1. Nano-indentation tests

Figure 10-3 and Figure 10-4 show the measured and mapped indentation moduli by nano-indentation at dry, HSW and LSW saturation conditions of calcite-rich, quartz-rich and clay-rich samples, respectively. It is clearly shown that HSW saturation would markedly decrease the indentation modulus for calcite-rich (37.5% reduction) and quartz-rich (32.4% reduction) shale samples, but seem to have negligible effect on illite-rich specimen. Decreasing salinity can further lead to indentation modulus decrease by 43.8% for calcite-rich sample, 19.2% for quartz-rich sample and for 33.3% illite-rich sample (Table 10-2). Overall, saturating dry shale specimens with LSW decrease the indentation modulus by 64.3% for calcite-rich sample, 45.4% for quartz-rich sample and 32.2% for illite-rich sample. In other words, the strength of calcareous and argillaceous shale is more sensitive to low salinity brine than the siliceous shale.
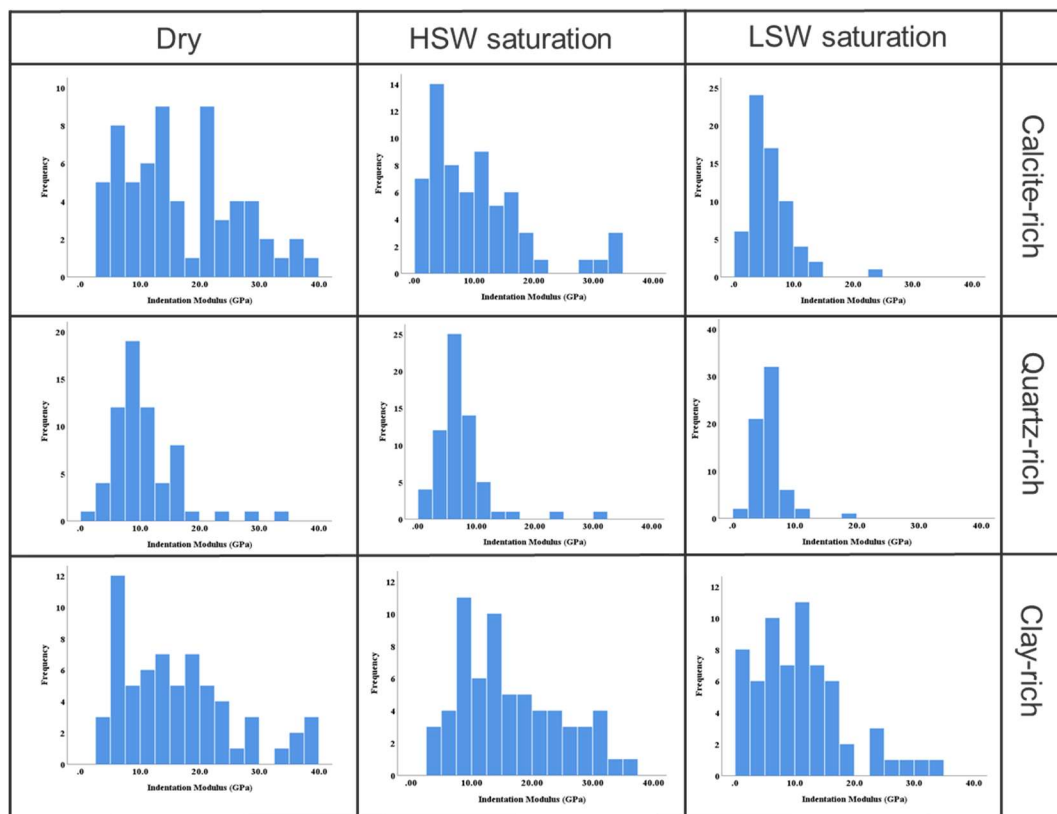
Figure 10-3 Measured indentation moduli with frequency at dry, HSW and LSW saturation conditions of calcite-rich, quartz-rich and clay-rich samples, respectively.
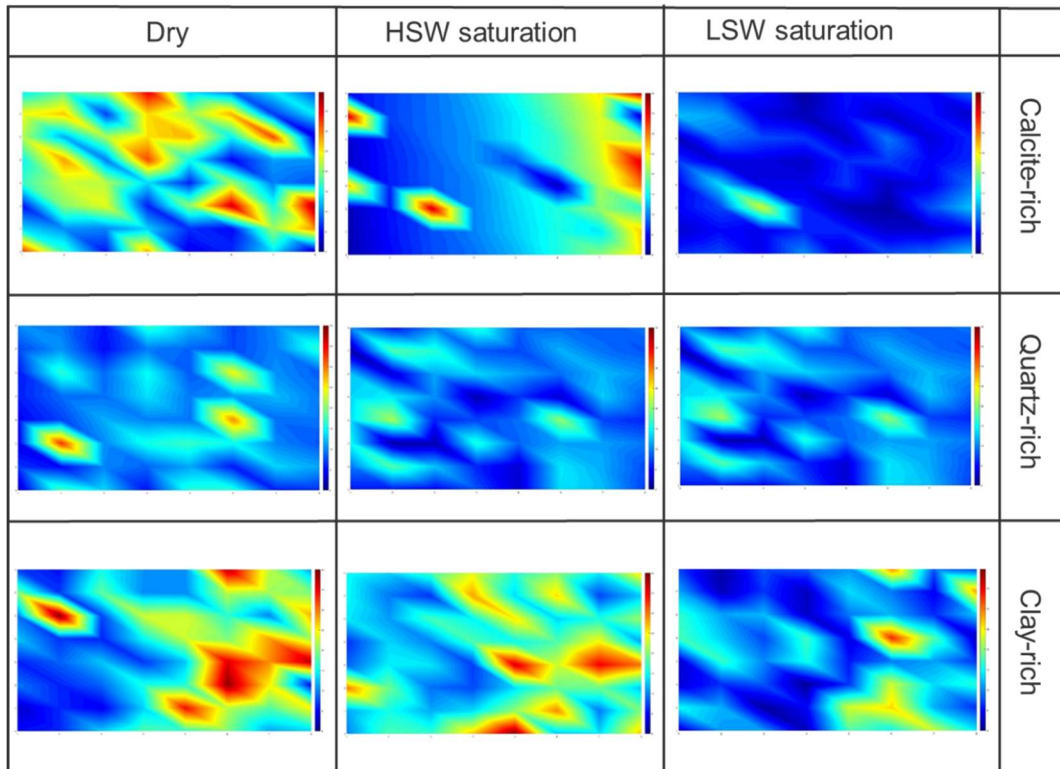
Figure 10-4 Mapped indentation moduli with frequency at dry, HSW and LSW saturation conditions of calcite-rich, quartz-rich and clay-rich samples, respectively. The red point/area presents higher indentation modulus and blue point/area indicate lower indentation modulus.

Table 10-2 Summarization of average indentation moduli from nano-indentation tests.

Indentation Modulus (GPa)	Calcite-rich	Quartz-rich	Clay-rich
Dry	16.8	10.8	16.21
High Salinity	10.5	7.3	16.5
Low Salinity	6	5.9	11

10.4.2. Atomic force microscopy imaging

To further examine the role of fluid-rock interactions in shale micromechanics, AFM tests were conducted on all sample surface before and after fluid treatment to probe the surface roughness. Figure 10-5 shows the 2D AFM topographic images for calcite-rich, quartz-rich and clay-rich samples at dry, HSW and LSW saturation conditions,

respectively. Compared to dry samples, HSW saturation surprisingly decreases the surface roughness for all types of shale (Table 10-3). After HSW treatment on dry samples, the surface roughness reduce by 12.5% for calcite-rich specimen, 33.8% for clay-rich specimen, and 49.2% for quartz-rich specimen. On the other hand, compared to dry samples, the subsequent LSW treatment increases the surface roughness by 18.5% for calcite-rich sample, 41.5% for quartz-rich sample and 54.7% for illite-rich sample.
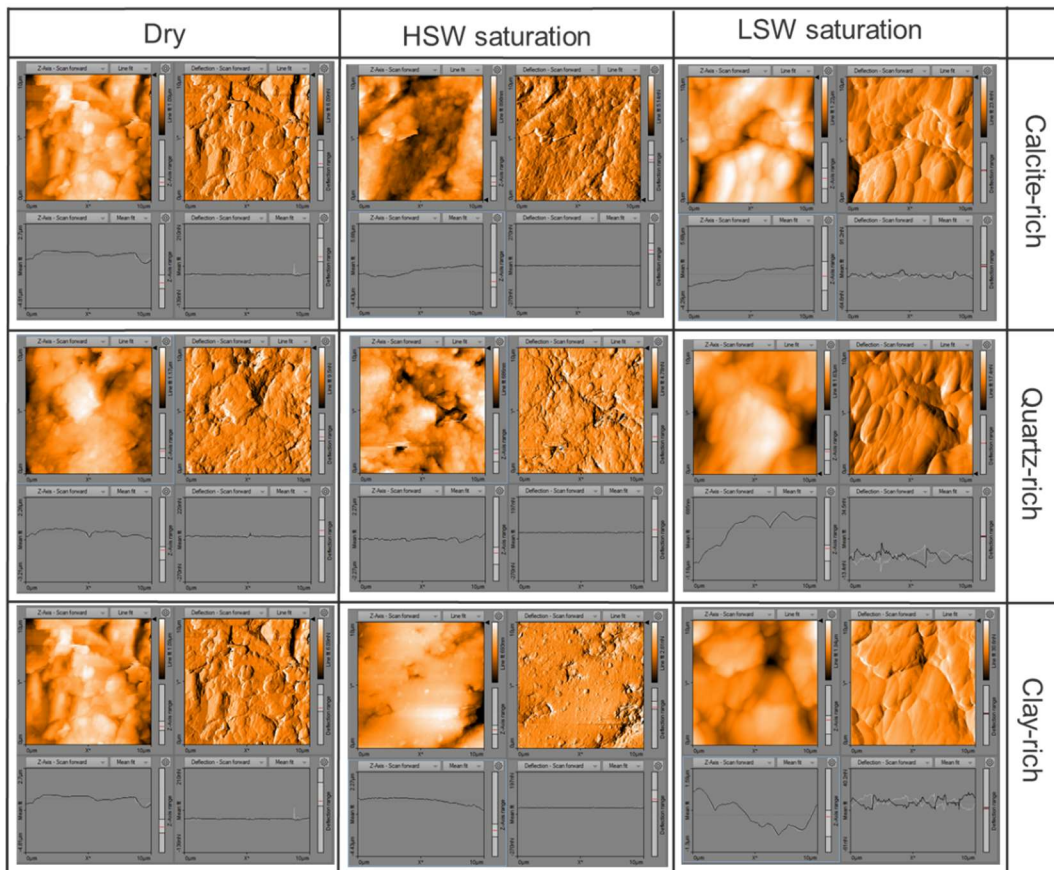
Figure 10-5 2D AFM topographic images for calcite-rich, quartz-rich and clay-rich samples at dry, HSW and LSW saturation conditions, respectively.

Table 10-3 Summarization of the mean roughness on targeted area from AFM.

Surface roughness (nm)	Calcite-rich	Quartz-rich	Clay-rich
Dry	168	183	139
High Salinity	147	98	92
Low Salinity	199	259	215

10.4.3. Surface morphology analysis

To characterize the effect of fluid-rock interactions on shale surface morphology and microstructures, we also conducted SEM tests on all samples at dry and LSW saturation, respectively (Figure 10-6). For quartz-rich and clay-rich samples, we successfully located the same positions on specimen surface at different saturation conditions and thus can directly examine how fluid-rock interactions affect micro-fracture propagation. For calcite, although the tested locations were not the same, the qualitative analysis on rock surface with similar morphology can still provide evidence of fluid-exposure induced micro-fracture extension. In general, we did not observe noticeable change on surface structure for all tested samples. Compared to dry samples, the saturation process did not generate any new micro-fracture or extend the existing micro-fracture networks even for the clay-rich specimen. Some pyrite particles on clay surface were dissolved after LSW saturation, which may be due to the oxidation process with aqueous O_2 and associated dissolution [21, 352].
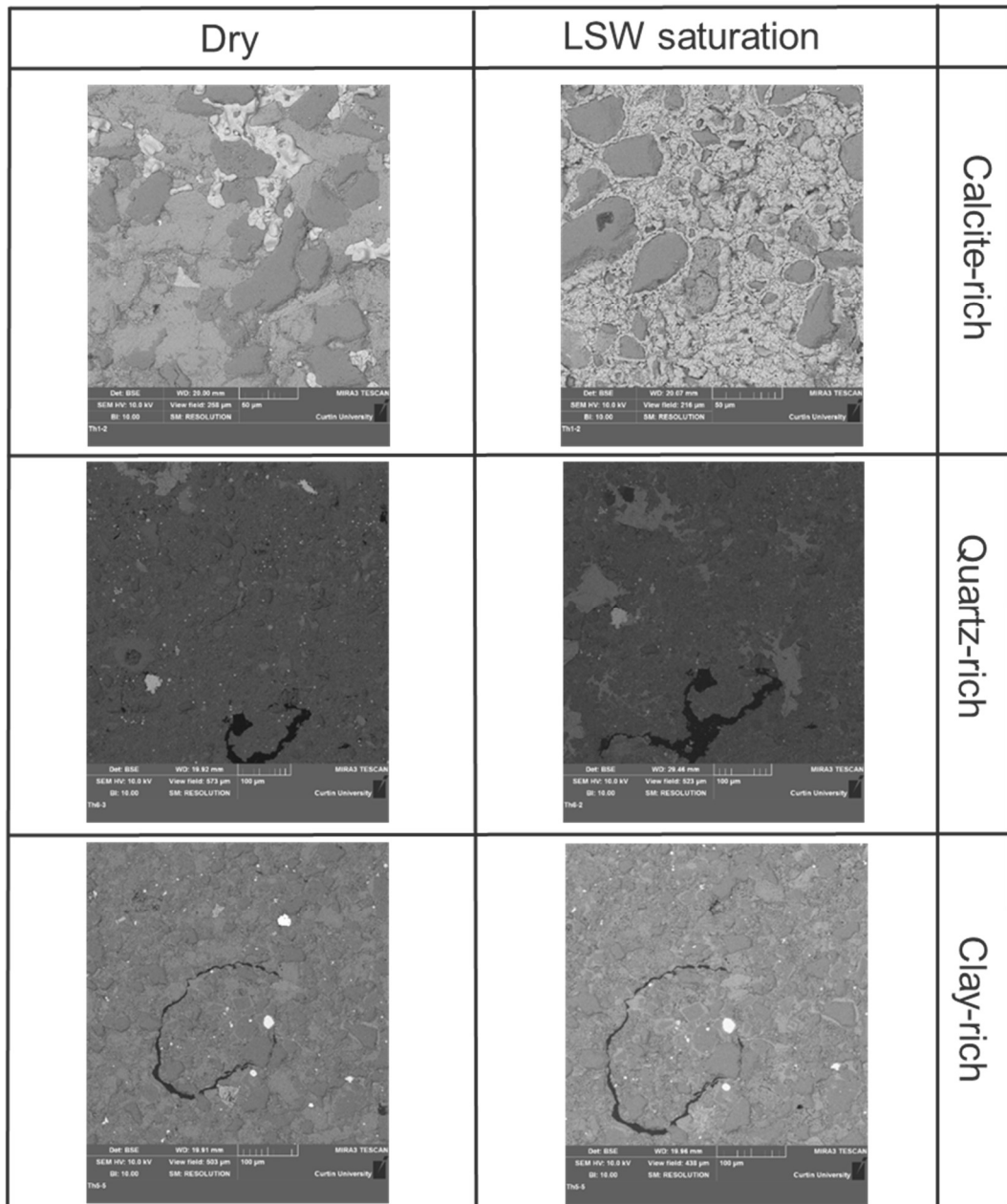
Figure 10-6 SEM surface morphology for calcite-rich, quartz-rich and clay-rich samples at dry, HSW and LSW saturation conditions, respectively.

10.5. Discussions

10.5.1. Effect of water saturation on shale micromechanics

Aforementioned results from nano-indentation and AFM tests clearly show that saturating dry shale sample into water (no matter what shale mineralogy and water chemistry) can decrease its Young's modulus and increase surface roughness, and thus lead to rock weakening/softening. The reasons of water saturation induced rock weakening were mainly attributed to the mineral dissolution and degradation [35, 47-

53], clay hydration and swelling [30, 31, 54-56], pyrite oxidation and associated secondary carbonate dissolution [57-59], and the reduction of friction angle and cohesion force [154, 353, 354]. However, in this study we propose that the water saturation process would change rock surface potential and surface energy, which can also contribute to bulk strength and elastic modulus. This process can be characterized with disjoining pressure isotherm between adjacent mineral sublayers (calcite) and particles (quartz), indicating rock strength reduction. Table 10-4 shows the calculated calcite and quartz surface potential at given pH at HSW and LSW saturation conditions, respectively. Then we used calculated surface potential to predict disjoining pressure isotherm for calcite and quartz at dry (Figure 10-7), HSW and LSW saturation conditions (Figure 10-8).

Table 10-4 Calculated surface potential (SP, mV) based on surface complexation modelling.

	HSW		LSW	
	pH	SP	pH	SP
Calcite	7.6	36.6	7.8	24.1
Quartz	6.3	-104.8*	6.8	-172.5

* The prediction of disjoining pressure on mineral surface are more accurate when the surface potential is between −25 and 25 mV [61, 326]. Beyond this range, the disjoining pressure calculation may deviate from the true value but would still reflect the variation trend.
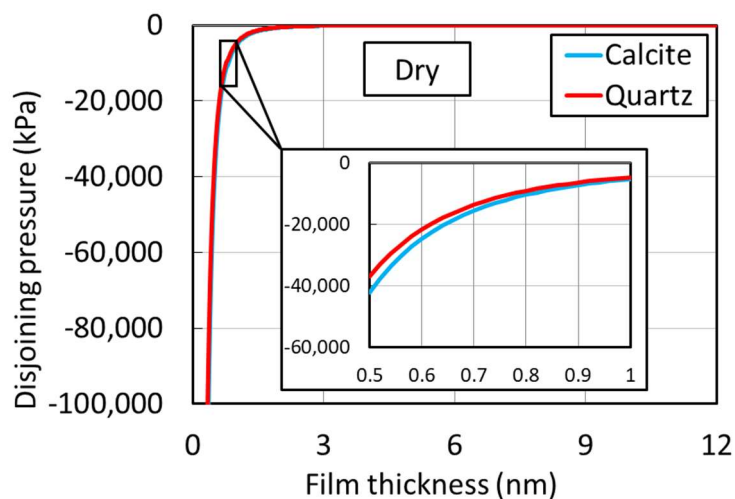
Figure 10-7 Disjoining pressure as function of film thickness on calcite and quartz subsurface at dry condition [61].
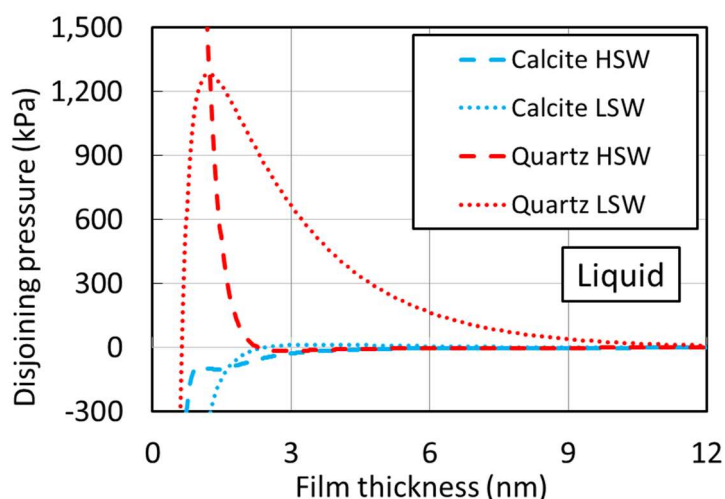
Figure 10-8 Disjoining pressure as function of film thickness on calcite and quartz subsurface at HSW, LSW and DI saturation conditions.

Our results show that the disjoining pressure on calcite and quartz surface exhibits negative at dry condition, which tends to attract adjacent sublayers and particles together. This is probably because that for dry samples, only *van der Waals* force takes effect on disjoining pressure (the contribution from structural force is very limited due to its nature of short-range interactions [193]), and it is always negative. Therefore, dry shale rocks usually present a higher strength [60]. After water treatment (regardless the brine salinity and shale mineralogy), the aqueous ions can react with specific surface species and form electrical double-layer between two sublayer surfaces [60, 61]. In this case, the positive electrostatic force also contributes to the total disjoining pressure, which leads to a shift of it from strong negative to less negative and even positive [193]. As a result, the attraction force between surfaces becomes weaker and in some cases alters to repulsion force. This process may weaken the connections among mineral surfaces and particles and thus decrease the shale strength at microscale.

10.5.2. Effect of brine salinity on shale micromechanics

Figure 10-8 also shows that decreasing brine salinity from 1 M NaCl + 0.05 M CaCl$_2$ to 0.01 M NaCl + 0.005 M CaCl$_2$ can shift the disjoining pressure from negative to positive, which corresponds to the force change from attraction to repulsion. For example, at film thickness of 3 nm, the saturation from HSW to LSW increases the disjoining pressure from -27.5 to 13.4 mV for calcite and from -15.8 to 666.5 mV for

quartz. This huge shift would trigger electrical double layer expansion and thus further weaken mineral connections. This also explains why decreasing salinity would decrease the indentation modulus observed in nano-indentation tests in section 3.2. To the best of our knowledge, we have not seen any report related to the effect of salinity on shale micromechanics. However, similar results on carbonate were found by Megawati et al. [60], who reported that decreasing Na_2SO_4 ionic strength from 0.657 to 0.03 can reduce chalk bulk and yield modulus.

Similar to the nano-indentation results, from the AFM tests, we observed an increase of surface roughness after saturating dry samples with HSW. The results show that HSW treatments decrease the surface roughness for all types of shale. Figure 10-6 suggests that this is likely due to the salts participation on rock surface. Given the HSW contains high concentration of NaCl and $CaCl_2$, the aqueous salt could precipitate from brine and form as crystal particles (see images of HSW saturation in Figure 5). The generated crystal particles then filled in the uneven area and thus slightly decrease the surface roughness. The assumption of this process can be also supported by the subsequent LSW saturation results. We cleaned the surface of samples with deionised water before saturating them into LSW. Therefore, most of the precipitated salts crystal should be flushed out. The tiny amounts of rudimental salts particles, if they still exist on the rock surface, would also re-dissolve into LSW. As the results, the surface toughness increase again and higher than the dry samples' values.

10.5.3. Effect of mineralogy on shale micromechanics

Our nano-indentation results show that calcite-rich and quartz-rich shale samples are more sensitive to fluid-rock interactions than the clay-rich samples as they present a greater indentation modulus reduction after brine saturation. One of the possible reasons is that calcite and quartz are edge-charged minerals, where the surface species or functional groups present on the edge or surface of mineral [61, 179]. Therefore, the surface species, such as >CaOH and >CO_3H for calcite and >SiOH for quartz, can interact with surrounding brine and release H^+ or attach aqueous ions (the extent of reaction depends on the equilibrium constant and ion concentrations, see Table 10-1). In other words, brine chemistry would control the surface charge, surface potential, surface energy and also affect the disjoining pressure for edge-charged minerals, and thus plays a significant role in rock weakening. However, illite belongs to basal-

charged mineral, where the majority of function groups locate in the basal or inner part of the rock [21]. Therefore, illite tends to react with fluid through the ion exchange process rather than surface complexation [90]. Consequently, illite-rich shales becomes less sensitive to saturated brine and has lower indentation modulus reduction than calcite and quartz as shown in Table 10-2. Similar observations were reported by Akrad et al. [35], who found that clay-rich Haynesville shales have less Young's modulus reduction (6%) than calcite-rich Eagle Ford shales (70%) and quartz-rich Barnett shales (32%) after saturation with 2.0 wt% KCl slickwater.

If aforementioned assumption is sufficient, we would expect to see the same trend of surface roughness change from AFM tests, where the surface roughness of calcite-rich and quartz-rich samples should present a greater increase than illite-rich sample. However, the results show that the final LSW treatment has a higher increase of surface roughness (54.7%) than 18.5% calcite-rich (18.5%) and quartz-rich (41.5%) sample when comparing to initial dry condition. This discrepancy implies that besides the disjoining pressure and electrical double layer expansion, there should be other factors, which also contribute to the shale micromechanics. In fact, we only considered the interactions between calcite-calcite and quartz-quartz when calculating the disjoining pressure isotherm. The more complex system such as calcite-clay, quart-clay and calcite-calcite were not covered (due to the fact that disjoining pressure would only present different behavior when the fill thickness is less than 9 nm as shown in Figure 10-8, it is unreasonable to calculate the disjoining pressure among different types of mineral through the simple weighting method). Nevertheless, our geochemical simulations explain how the water saturation and fluid chemistry can affect shale micromechanics typically the indentation or Young's modulus.

By combining shale micromechanics from this study with the widely reported mesoscale shale properties from triaxial tests, we would be able to better understand how the fluid-rock interactions affect the mechanical behaviors of shale with different mineralogy. Given the calcareous and siliceous shales present a higher reduction of indentation modulus and strength in LSW than the argillaceous shale, the injection of low salinity hydraulic fracturing fluid would decrease the rock yield point and fracture initiation pressure for fracture propagation. Therefore, the hydraulic fracturing performance in calcite- and quartz-rich shales would be more pronounced as the

fracture networks in these reservoirs can be better developed, which improves the formation connectivity and thus the production efficiency. However, for the soft clay-rich shales, the low salinity induced rock weakening may intensify the issues proppants embedment on fracture surface. In this case, the hydraulic fracture conductivity would dramatically decrease and impede the hydrocarbon flow and ultimate productivity [161].

10.6. Conclusions

Fluid-rock interactions play important roles in shale mechanical behaviors during hydraulic fracturing. In this study, we measured the strength of shale sample with different mineralogy under different saturation conditions through nano-indentation tests. Topography on sample surface, which can reveal surface structure and roughness at microscale, was imaged by the atomic force microscopy measurement. Moreover, scanning electron microscopy tests were performed on each sample before and after brine exposure to detect any fluid-rock interactions induced micro-fracture generation or propagation. Besides, a geochemical interpretation with combination of surface complexation modelling and disjoining pressure isotherm was provided to further understand the effect of fluid-rock interaction on shale micromechanics from geochemical perspective.

Nano-indentation tests confirm that water saturation can decrease the indentation moduli of all tested samples. Decreasing salinity can further decrease indentation modulus of calcareous, siliceous and argillaceous shale samples by 43.8%, 19.2% and 33.3%, suggesting that the low salinity water would change shale in-situ geochemistry such as surface potential and surface energy and thus affect the mechanics behaviors. From the mineralogy perspective, calcite- and quartz-rich shales present greater indentation moduli reduction after low salinity brine saturation (64.3% and 45.4%) than the illite-rich sample (32.2%). These results implying that for shales rich in edge-charge minerals such as calcite and quartz, the injection of low salinity hydraulic fracturing fluid would decrease fracture initiation pressure and facilitate fracture propagation and hydrocarbon productivity. While for the shales rich in basal-charged mineral typically clays, the low salinity saturation may further soften the rock and lead to proppants embedment on fracture surface, which impairing the fracture conductivity and long-term production efficiency.

11. Concluding Remarks and Future Works Outlook

Hitherto, large-scale multi-stage hydraulic fracturing with combination of horizontal drilling have been widely implemented in the industry. This process can stimulate tight shale gas reservoirs by generating new fractures and activating pre-existing natural fractures and thus improve the reservoir transmissibility and the ultimate productivity. During the hydraulic fracturing process, hydraulic fracturing fluids containing the low salinity slick water (typically less than 5,000 mg/L) with other additives are injected underground at high pressure. To generate hydraulic fracturing network, a large volume of water is needed during the implementation of hydraulic fracturing (approximately 10,000 to 75,000 m^3 for a single well per annum). However, the flowback water recovery is only 10 to 50% for some shale reservoirs. The majority of injected fluids remain underground, which raises both technical and environmental concerns. Although several mechanisms have been proposed to explain the water loss, most previous works are only descriptive in nature. Quantitative understanding of fluid-shale interactions induced water uptake still remains challenging due to the lack of fundamental studies on the geochemical driven in shale systems. In particular, the process of fluid-rock interactions triggered shale wettability alteration is still unclear.

Besides, the *in-situ* geochemistry change by mixing of low salinity fracturing fluids with pre-existing high salinity formation brine can also affect rock mechanical properties and micro-fracture propagation and thus control the extra water uptake. However, fewer works have quantitatively interpreted how fluid-rock interactions can affect shale surface energy and the mechanical behaviours.

This study aims to systematically investigate the role of fluid-rock interactions in water uptake during hydraulic fracturing in shales from (1) geochemical properties, including the surface species concentrations, surface potential, wettability alteration and flowback water chemistry such as pH, ion concentration, oxidation-reduction potential and electrical conductivity, and (2) geomechanical properties, including surface energy, energy release rate at the tip of crack, bulk strength, Young's modulus and surface roughness. Multiple tools of physicochemical modellings and experimental works have been applied to interpret the role fluid-shale interactions on water uptake from both geochemical and geomechanical perspectives. The main conclusions are obtained as follows.

11.1. Geochemistry controls over wettability alteration in shale gas reservoirs and the capillary associated water uptake

The surface complexation modelling shows that decreasing salinity triggers a larger positive surface potential at oil-brine and brine-OM surfaces when pH is lower than 6.5. At pH = 5.75 (Middle Bakken formation fluid pH), lowering salinity from 280,000 to 20,000 ppm increases the surface potential of oil surfaces from 32 to 51 mV, and the same amount of surface potential increase was shown at OM surfaces. Moreover, the surface potential of oil and OM decreases with increasing pH, which even can be shifted from positive to negative. Furthermore, the surface potential of both oil and OM decreases with increasing temperature at *in-situ* pH (from 3.5 to 7). The electrostatic isotherm calculations show that low salinity brine shifts the disjoining pressure from negative (in high salinity brine) to positive, favouring desorption/detachment of oil from OM. Taken together, our surface complexation modelling and disjoining pressure calculation account for at least in part the incremental oil recovery contributed by oil-brine-OM wettability alteration in low salinity brine.

Meanwhile, our results show that salinity and pH of brines significantly affect the surface species concentration of organic matter and inorganic minerals and thus surface potential. To be more specific, lowering salinity shifts surface potential of fluid-shale to more negative at *in-situ* pH (8.3 to 8.7). Disjoining pressure isotherm calculations show that decreasing salinity from 1 to 0.1 wt% shifts the disjoining pressure to be more positive for air-brine-organic matter, suggesting a hydrophilicity increase. Besides, air-brine-calcite system also gives a positive disjoining pressure regardless of salinity, implying a more hydrophilic system. The results also suggest that lowering salinity increases the disjoining pressure thus internal pore pressure to cause shale sample expansion and generation of micro-fractures [63, 260]. Taken together, our geochemical modelling accounts for the low recovery of injected water in part due to (1) the surface forces of organic matter and inorganic materials which is associated with capillary forces, and (2) an increase of the internal pore pressure which gives rise to micro-fracture propagation.

11.2. Fluid-rock interactions play minor role in the contribution of high total dissolved solids of flowback water during hydraulic fracturing

From the mineralogy perspective, Barnett samples imbibed more deionised water (1.4%) than Marcellus (1.0%) and Eagle Ford (0.7%). This is likely attributed to the higher content of calcite and lower content of hydrophobic organic matter. The order of sequence of experimentally measured pH (Eagle Ford (8.3) > Barnett (8.0) > Marcellus (7.6)) is in line with simulation results (Eagle Ford (7.579) > Barnett (7.545) > Marcellus (7.483)), confirming the importance of pyrite oxidation on local pH at ambient condition. The slightly discrepancy in pH magnitude is likely due to the non-equilibrium thermodynamics in particular the pyrite oxidation during spontaneous imbibition process. Besides, the concentrations of Cl^-, K^+ and Ca^{2+} for tested samples increase over imbibition time. Marcellus samples contain higher K^+ (18 mg/L) than Barnett (13 mg/L) and Eagle Ford (6 mg/L). The concentration of Ca^{2+} (200 mg/L) and Cl^- (1.3 mg/L) are roughly equivalent for all samples at the end of imbibition and are much less than the field observation (e.g., 300,000 mg/L), which suggests that mineral dissolution is minor. Consequently, with consideration of fully reaction between fluid and minerals in geochemical modelling, the maximum TDS of fluid saturated with Marcellus, Barnett and Eagle Ford samples is less than 3% of flowback water salinity. This simulation result is slightly higher than experimental observation due to the fully equilibrium between shale and water, but is still much less than the field observation. This result further confirms that the contribution of mineral dissolution on high salinity flowback water is negligible.

From oxygen content and pyrite oxidation perspective, shale samples under ambient conditions uptake a higher volume of water, and the fluids have higher values of ORP but lower pH than the limited air and vacuum conditions after 30 days imbibition, suggesting that pyrite oxidation can facilitate calcite dissolution by generating extra H^+ and thus likely communicate pore networks and enhance rock connectivity. Once fluids at limited air and vacuum conditions are able to source O_2 from air, the amount of imbibed water, fluid salinity and electrical conductivity can rapidly increase, which confirms that pyrite oxidization process play an import role at ambient condition with continuous contact with O_2 from air. Furthermore, the fluid salinity under limited air conditions, which is the most similar to the reservoir conditions in terms of aqueous

O$_2$ concentrations, is much less than that of the ambient conditions, indicating that traditional imbibition experiment, where fluids can always equilibrate with air, would overestimate the impact of pyrite oxidization process in shale at real reservoir conditions. SEM analyses show that brine saturation barely affects the morphology and elemental distribution of pyrite at ambient conditions, implying that pyrite oxidation would play a minor role in fluid salinity at reservoir conditions. In summary, spontaneous imbibition tests, SEM analyses together with geochemical modelling indicate that lab-measured fluid salinity is only ~2% of field observations. This result implies that the mixing of injected fracturing fluid with high salinity formation brines accounts for the high TDS of flowback water during hydraulic fracturing rather than mineral dissolution in calcite-rich shales.

11.3.   Wettability alteration induced hydrophilicity would decrease the surface energy threshold for fracture initiation and thus facilitate fracture propagation

With consideration of the variability of measurement, lowering ionic strength of NaCl, MgSO$_4$ and MgCl$_2$ from 1.2 M to 0.012M decreases the average energy release rate during micro-cracks propagating (0.32 to 0.28 J/m^2 for NaCl, 0.34 to 0.30 J/m^2 for MgSO$_4$, and 0.32 to 0.31 J/m^2 for MgCl$_2$) [64]. The physicochemical modelling results show that calcite surface potential is a function of solution pH, fluid composition and ionic strength, which can be predicted using surface complexation model. pH would affect the Ca^{2+} level through the equilibrium of calcite dissolution-precipitation thus indirectly influence surface energy. At high acidic condition, a low fluid salinity would increase surface potential for all tested solutions. At alkaline condition, lowering salinity decreases surface potential of MgSO$_4$ and MgCl$_2$ but increases that of Na$_2$SO$_4$. The effects of ionic strength of NaCl on surface potential is considerably restricted due to the limited divalent ions concentration such as Ca^{2+}, Mg^{2+} and SO$_4^{2-}$, which are capable to bond with functional groups on calcite surface. Furthermore, the predicted energy release rate ΔG_0^s is generally in line with the experimental measurement ΔG_0 reported by Bergsaker et al. This physicochemical model therefore builds an overall framework to quantify how fluid-calcite interactions affect surface energy and subsequent subcritical crack growth.

11.4. Edge-charged minerals such as calcite and quartz and basal-charged mineral typically illite play different roles in shale weakening during hydraulic fracturing

The nano-indentation results show that calcite-rich and quartz-rich shale samples are more sensitive to fluid-rock interactions than the clay-rich samples as they present a greater indentation modulus reduction after brine saturation. HSW saturation would markedly decrease the indentation modulus for calcite-rich (37.5% reduction) and quartz-rich (32.4% reduction) shale samples, but seem to have negligible effect on illite-rich specimen. Decreasing salinity can further lead to indentation modulus decrease by 43.8% for calcite-rich samples, 19.2% for quartz-rich samples and for 33.3% illite-rich samples (Table 7-2). Overall, saturating dry shale specimens with LSW decreases the indentation modulus by 64.3% for calcite-rich samples, 45.4% for quartz-rich samples and 32.2% for illite-rich samples. This is mainly caused by different mineral structure. The surface species, such as >CaOH and $>CO_3H$ for calcite and >SiOH for quartz, can interact with surrounding brine and release H^+ or attach aqueous ions. In other words, brine chemistry would control the surface charge, surface potential, surface energy and also affect the disjoining pressure for edge-charged minerals, and thus plays a significant role in rock weakening. However, for basal-charged mineral like illite, the majority of function groups locate in the basal or inner part of the rock. Therefore, illite tends to react with fluid through the ion exchange process rather than surface complexation [90].

Meanwhile, geochemical modelling also shows that saturation index for calcite, dolomite, quartz, pyrite and illite at *in-situ* pH (8.25) is almost zero, implying that mineral dissolution may play a negligible role in shale strength such as Young's modulus reduction. Surface complexation modelling shows that the surface potential of organic matter, quartz, calcite and dolomite decreases with increasing pH. Surface potential of organic matter, calcite and dolomite decreases with increasing salinity at acidic condition except for quartz, which shows the opposite trend. Disjoining pressure calculations show that in air condition without fluid-mineral interactions, quartz-rich and calcite-rich shales give a strongly negative disjoining pressure, indicating a high rock strength thus high Young's Modulus. However, with presence of fluid, the disjoining pressure can be shifted from strongly negative to slightly negative (for

calcite-rich shale) and even positive (for quartz-rich shales), indicating a reduction of rock strength. However, with fluid-mineral interactions, our prediction contradicts the experimental result reported by Akrad et al. [35], which shows that calcite-rich shales give a higher reduction in Young's modulus compared to quartz-rich shales. We believe that rhombohedral cleavage structure of calcite and the geometry contact of minerals likely play a significant role in the micromechanical properties with fluid-rock interactions.

11.5. Future Works Outlook

In this work, we have studied the effect of fluid-rock interactions on shale geochemical and geomechanical behaviours, which may shed lights on the low recovery of flowback water during hydraulic fracturing in shale gas reservoirs. The future works are suggested as follows.

1. From geochemical perspective, the current geochemical modellings on organic matter and inorganic minerals are performed at room temperature and atmospheric pressure. New geochemical tools need to be developed under high temperature and high pressure to assess the impact of fluid-shale interactions on wettability alteration under reservoir conditions.

2. From geomechanical perspective, we have seen the distinct influence of the fluid-rock interactions on shale mechanical properties particular the Young's modulus at microscale through the nano-indentation experiments. However, it is still unclear whether the geochemistry-controlled mechanical behaviours alteration can be upscaled to core-scale and reservoir-scale. Therefore, macroscopic experiments such as triaxial compression tests with combination of micro-seismicity monitoring and micro-CT scanning are calling for to further assess how the fluid-rock interactions can affect shale mechanical properties at a larger size under confining environments.

3. Furthermore, in this study, pH, aqueous ion composition and concentration were considered as the main geochemical variables when assessing the shale wettability alteration and rock strength. The effect of CO_2 and H_2 injection on shale geochemical and geomechanical behaviours can be also explored to provide more insights for maintaining the long-term stability of shale caprock

for CO_2 Capture and Storage and Underground H_2 Storage to achieve the global objective of net-zero Carbon Emission in near future.

References

1. Ross, D.J. and R.M. Bustin, *The importance of shale composition and pore structure upon gas storage potential of shale gas reservoirs.* Marine and petroleum Geology, 2009. **26**(6): p. 916-927.

2. Hao, F., H. Zou, and Y. Lu, *Mechanisms of shale gas storage: Implications for shale gas exploration in China.* AAPG bulletin, 2013. **97**(8): p. 1325-1346.

3. Wu, Y.-S., et al., *A Generalized Framework Model for the Simulation of Gas Production in Unconventional Gas Reservoirs.* SPE Journal, 2014. **19**(05): p. 845-857.

4. Sondergeld, C.H., et al., *Petrophysical Considerations in Evaluating and Producing Shale Gas Resources*, in *SPE Unconventional Gas Conference.* 2010, Society of Petroleum Engineers: Pittsburgh, Pennsylvania, USA.

5. Kale, S.V., C.S. Rai, and C.H. Sondergeld. *Petrophysical characterization of Barnett shale.* in *SPE Unconventional Gas Conference.* 2010. Society of Petroleum Engineers.

6. Clarkson, C.R., et al., *Pore structure characterization of North American shale gas reservoirs using USANS/SANS, gas adsorption, and mercury intrusion.* Fuel, 2013. **103**: p. 606-616.

7. Clarkson, C.R., et al., *Production analysis of tight-gas and shale-gas reservoirs using the dynamic-slippage concept.* SPE journal, 2012. **17**(01): p. 230-242.

8. Singh, H. and F. Javadpour. *Nonempirical apparent permeability of shale.* 2013. Unconventional Resources Technology Conference (URTEC).

9. Sakhaee-Pour, A. and S. Bryant, *Gas permeability of shale.* SPE Reservoir Evaluation & Engineering, 2012. **15**(04): p. 401-409.

10. Wang, L., et al., *Advances in improved/enhanced oil recovery technologies for tight and shale reservoirs.* Fuel, 2017. **210**: p. 425-445.

11. Zolfaghari, A., H. Dehghanpour, and D. Bearinger, *Produced Flowback Salts vs. Induced-Fracture Interface: A Field and Laboratory Study.* SPE Journal, 2019. **Preprint**(Preprint): p. 13.

12. Arthur, J.D., et al. *Evaluating the environmental implications of hydraulic fracturing in shale gas reservoirs.* in *SPE Americas E&P environmental and safety conference.* 2009. Society of Petroleum Engineers.

13. Barati, R. and J.T. Liang, *A review of fracturing fluid systems used for hydraulic fracturing of oil and gas wells.* Journal of Applied Polymer Science, 2014. **131**(16).

14. Zolfaghari, A., H. Dehghanpour, and D. Bearinger, *Produced Flowback Salts vs. Induced-Fracture Interface: A Field and Laboratory Study.* SPE Journal, 2019. **24**(03): p. 1309-1321.

15. Nicot, J.-P., et al., *Source and Fate of Hydraulic Fracturing Water in the Barnett Shale: A Historical Perspective.* Environmental Science & Technology, 2014. **48**(4): p. 2464-2471.

16. Scanlon, B.R., R.C. Reedy, and J.P. Nicot, *Will water scarcity in semiarid regions limit hydraulic fracturing of shale plays?* Environmental Research Letters, 2014. **9**(12): p. 124011.

17. Vidic, R.D., et al., *Impact of shale gas development on regional water quality.* Science, 2013. **340**(6134): p. 1235009.

18. Boschee, P., *Produced and Flowback Water Recycling and Reuse: Economics, Limitations, and Technology.* Oil and Gas Facilities, 2014. **3**(01): p. 16-21.

19. Javadpour, F., M. McClure, and M. Naraghi, *Slip-corrected liquid permeability and its effect on hydraulic fracturing and fluid loss in shale.* Fuel, 2015. **160**: p. 549-559.

20. Singh, H., *A critical review of water uptake by shales.* Journal of Natural Gas Science and Engineering, 2016. **34**: p. 751-766.

21. Zeng, L., et al., *Interpreting Water Uptake by Shale with Ion Exchange, Surface Complexation, and Disjoining Pressure.* Energy & Fuels, 2019. **33**(9): p. 8250-8258.

22. Kargbo, D.M., R.G. Wilhelm, and D.J. Campbell, *Natural gas plays in the Marcellus Shale: Challenges and potential opportunities.* 2010, ACS Publications.

23. Roberson, T.W., *Environmental concerns of hydraulically fracturing a natural gas well.* Utah Envtl. L. Rev., 2012. **32**: p. 67.

24. Rivard, C., et al., *An overview of Canadian shale gas production and environmental concerns.* International Journal of Coal Geology, 2014. **126**: p. 64-76.

25. Suboyin, A., M.M. Rahman, and M. Haroun, *Hydraulic fracturing design considerations, water management challenges and insights for Middle Eastern shale gas reservoirs.* Energy Reports, 2020. **6**: p. 745-760.

26. Yew, C.H. and X. Weng, *Mechanics of hydraulic fracturing.* 2014: Gulf Professional Publishing.

27. Fakcharoenphol, P., et al., *The Effect of Osmotic Pressure on Improve Oil Recovery from Fractured Shale Formations*, in *SPE Unconventional Resources Conference.* 2014, Society of Petroleum Engineers: The Woodlands, Texas, USA.

28. Osiptsov, A.A., *Fluid mechanics of hydraulic fracturing: a review.* Journal of petroleum science and engineering, 2017. **156**: p. 513-535.

29. Al-Bazali, T., *The impact of water content and ionic diffusion on the uniaxial compressive strength of shale.* Egyptian Journal of Petroleum, 2013. **22**(2): p. 249-260.

30. Lyu, Q., et al., *Experimental investigation on the mechanical behaviours of a low-clay shale under water-based fluids.* Engineering Geology, 2018. **233**: p. 124-138.

31. Lal, M., *Shale Stability: Drilling Fluid Interaction and Shale Strength*, in *SPE Asia Pacific Oil and Gas Conference and Exhibition.* 1999, Society of Petroleum Engineers: Jakarta, Indonesia. p. 10.

32. Lu, Y., et al., *A mechanical model of borehole stability for weak plane formation under porous flow.* Petroleum Science and Technology, 2012. **30**(15): p. 1629-1638.

33. Lu, Y., et al., *Influence of porous flow on wellbore stability for an inclined well with weak plane formation.* Petroleum Science and Technology, 2013. **31**(6): p. 616-624.

34. Velcin, H., et al., *Experimental Reactivation of Shear-fractured Berea and Boise Sandstones by Brine or Liquid CO2 Injection at Depth.* Journal of Geophysical Research: Solid Earth, 2020. **125**(2): p. e2019JB018281.

35. Akrad, O.M., J.L. Miskimins, and M. Prasad. *The effects of fracturing fluids on shale rock mechanical properties and proppant embedment.* in *SPE Annual Technical Conference and Exhibition.* 2011. Society of Petroleum Engineers.

36. Kang, Y., et al., *Strengthening shale wellbore with silica nanoparticles drilling fluid.* Petroleum, 2016. **2**(2): p. 189-195.

37.   Lyu, Q., et al., *Experimental investigation of mechanical properties of black shales after CO2-water-rock interaction.* Materials, 2016. **9**(8): p. 663.

38.   Dautriat, J., et al., *Remote monitoring of the mechanical instability induced by fluid substitution and water weakening in the laboratory.* Physics of the Earth and Planetary Interiors, 2016. **261**: p. 69-87.

39.   Feng, R., et al., *Brittleness Index: From Conventional to Hydraulic Fracturing Energy Model.* Rock Mechanics and Rock Engineering, 2019.

40.   Røyne, A., K.N. Dalby, and T. Hassenkam, *Repulsive hydration forces between calcite surfaces and their effect on the brittle strength of calcite-bearing rocks.* Geophysical Research Letters, 2015. **42**(12): p. 4786-4794.

41.   Rostom, F., et al., *Effect of fluid salinity on subcritical crack propagation in calcite.* Tectonophysics, 2013. **583**: p. 68-75.

42.   Yan, W., et al., *Effects of Fluid Conditions on Subcritical Crack Growth in Tight Sandstone*, in *52nd U.S. Rock Mechanics/Geomechanics Symposium.* 2018, American Rock Mechanics Association: Seattle, Washington. p. 7.

43.   Shen, W., F. Yang, and Y.-P. Zhao, *Unstable crack growth in hydraulic fracturing: The combined effects of pressure and shear stress for a power-law fluid.* Engineering Fracture Mechanics, 2020. **225**: p. 106245.

44.   Nara, Y., M. Tanaka, and T. Harui, *Evaluating long-term strength of rock under changing environments from air to water.* Engineering Fracture Mechanics, 2017. **178**: p. 201-211.

45.   Nara, Y., et al., *Effects of humidity and temperature on subcritical crack growth in sandstone.* International Journal of Solids and Structures, 2011. **48**(7-8): p. 1130-1140.

46.   Chen, X., P. Eichhubl, and J.E. Olson, *Effect of water on critical and subcritical fracture properties of Woodford shale.* Journal of Geophysical Research: Solid Earth, 2017. **122**(4): p. 2736-2750.

47.   Ali, M. and B. Hascakir, *Water/Rock Interaction for Eagle Ford, Marcellus, Green River, and Barnett Shale Samples and Implications for Hydraulic-Fracturing-Fluid Engineering.* SPE Journal, 2017. **22**(01): p. 162-171.

48.   Corapcioglu, H., J. Miskimins, and M. Prasad, *Fracturing Fluid Effects on Young's Modulus and Embedment in the Niobrara Formation*, in *SPE Annual Technical Conference and Exhibition.* 2014, Society of Petroleum Engineers: Amsterdam, The Netherlands. p. 17.

49.   Dieterich, M., B. Kutchko, and A. Goodman, *Characterization of Marcellus Shale and Huntersville Chert before and after exposure to hydraulic fracturing fluid via feature relocation using field-emission scanning electron microscopy.* Fuel, 2016. **182**: p. 227-235.

50.   Du, J., et al., *Shale softening: Observations, phenomenological behavior, and mechanisms.* Applied Clay Science, 2018. **161**: p. 290-300.

51.   Lebedev, M., M.E. Wilson, and V. Mikhaltsevitch, *An experimental study of solid matrix weakening in water-saturated Savonnières limestone.* Geophysical Prospecting, 2014. **62**(6): p. 1253-1265.

52.   Mikhaltsevitch, V., M. Lebedev, and B. Gurevich, *Laboratory measurements of the effect of fluid saturation on elastic properties of carbonates at seismic frequencies.* Geophysical Prospecting, 2016. **64**(4): p. 799-809.

53.   Risnes, R., et al., *Water weakening of chalk—Mechanical effects of water–glycol mixtures.* Journal of Petroleum Science and Engineering, 2005. **48**(1-2): p. 21-36.

54. Demarco, M.M., et al., *The impact of partial water saturation on rock strength: an experimental study on sandstone [Der Einfluss einer partiellen Wassersättigung auf die mechanischen Gesteinseigenschaften: eine Fallstudie an Sandsteinen]*. Zeitschrift der Deutschen Gesellschaft für Geowissenschaften, 2007. **158**(4): p. 869-882.

55. Lu, Y., et al., *Characterization of Shale Softening by Large Volume-Based Nanoindentation*. Rock Mechanics and Rock Engineering, 2019.

56. Pedlow, J. and M. Sharma, *Changes in Shale Fracture Conductivity due to Interactions with Water-Based Fluids*, in *SPE Hydraulic Fracturing Technology Conference*. 2014, Society of Petroleum Engineers: The Woodlands, Texas, USA. p. 19.

57. Rimstidt, J.D. and D.J. Vaughan, *Pyrite oxidation: a state-of-the-art assessment of the reaction mechanism*. Geochimica et Cosmochimica acta, 2003. **67**(5): p. 873-880.

58. Zeng, L., et al., *Effect of the Fluid–Shale Interaction on Salinity: Implications for High-Salinity Flowback Water during Hydraulic Fracturing in Shales*. Energy & Fuels, 2020. **34**(3): p. 3031-3040.

59. Woo, I., et al., *Evaluation of the impact of pyrite oxidation on rock characteristics and environment by laboratory tests*. Environmental earth sciences, 2013. **69**(6): p. 1821-1829.

60. Megawati, M., A. Hiorth, and M. Madland, *The impact of surface charge on the mechanical behavior of high-porosity chalk*. Rock mechanics and rock engineering, 2013. **46**(5): p. 1073-1090.

61. Zeng, L., et al., *Interpreting micromechanics of fluid-shale interactions with geochemical modelling and disjoining pressure: Implications for calcite-rich and quartz-rich shales*. Journal of Molecular Liquids, 2020: p. 114117.

62. Zeng, L., et al., *Role of brine composition on rock surface energy and its implications for subcritical crack growth in calcite*. Journal of Molecular Liquids, 2020. **303**: p. 112638.

63. Xu, M. and H. Dehghanpour, *Advances in Understanding Wettability of Gas Shales*. Energy & Fuels, 2014. **28**(7): p. 4362-4375.

64. Bergsaker, A.S., et al., *The effect of fluid composition, salinity, and acidity on subcritical crack growth in calcite crystals*. Journal of Geophysical Research: Solid Earth, 2016. **121**(3): p. 1631-1651.

65. Civan, F., *instrumental and laboratory techniques for characterization OF reservoir rock*, in *Reservoir Formation Damage*. 2007, Gulf Professional Publishing Burlington. p. 154-173.

66. Agbalaka, C.C., et al. *The effect of wettability on oil recovery: A review*. in *SPE Asia Pacific Oil and Gas Conference and Exhibition*. 2008. Society of Petroleum Engineers.

67. Siddiqui, M.A.Q., et al., *Current understanding of shale wettability: A review on contact angle measurements*. Earth-Science Reviews, 2018. **181**: p. 1-11.

68. Borysenko, A., et al., *Experimental investigations of the wettability of clays and shales*. Journal of Geophysical Research: Solid Earth, 2009. **114**(B7).

69. Bai, B., et al., *Rock characterization of Fayetteville shale gas plays*. Fuel, 2013. **105**: p. 645-652.

70. Elgmati, M.M., et al. *Submicron-pore characterization of shale gas plays*. in *North American unconventional gas conference and exhibition*. 2011. Society of Petroleum Engineers.

71. Morsy, S., A. Gomaa, and J.J. Sheng, *Improvement of Mancos Shale Oil Recovery by Wettability Alteration and Mineral Dissolution*, in *SPE Improved Oil Recovery Symposium*. 2014, Society of Petroleum Engineers: Tulsa, Oklahoma, USA. p. 10.

72. Engelder, T., L.M. Cathles, and L.T. Bryndzia, *The fate of residual treatment water in gas shale.* Journal of Unconventional Oil and Gas Resources, 2014. **7**: p. 33-48.

73. Roychaudhuri, B., T.T. Tsotsis, and K. Jessen, *An experimental investigation of spontaneous imbibition in gas shales.* Journal of Petroleum Science and Engineering, 2013. **111**: p. 87-97.

74. Dehghanpour, H., et al., *Liquid Intake of Organic Shales.* Energy & Fuels, 2012. **26**(9): p. 5750-5758.

75. Dehghanpour, H., et al., *Spontaneous Imbibition of Brine and Oil in Gas Shales: Effect of Water Adsorption and Resulting Microfractures.* Energy & Fuels, 2013. **27**(6): p. 3039-3049.

76. Lan, Q., et al., *A comparative investigation of shale wettability: the significance of pore connectivity.* Journal of Natural Gas Science and Engineering, 2015. **27**: p. 1174-1188.

77. Habibi, A., et al., *Advances in understanding wettability of tight oil formations: a Montney case study.* SPE Reservoir Evaluation & Engineering, 2016. **19**(04): p. 583-603.

78. Liang, L., J. Xiong, and X. Liu, *Experimental study on crack propagation in shale formations considering hydration and wettability.* Journal of Natural Gas Science and Engineering, 2015. **23**: p. 492-499.

79. Li, J., et al., *Water Sorption and Distribution Characteristics in Clay and Shale: Effect of Surface Force.* Energy & Fuels, 2016. **30**(11): p. 8863-8874.

80. Makhanov, K., et al., *Liquid uptake of gas shales: A workflow to estimate water loss during shut-in periods after fracturing operations.* Journal of Unconventional Oil and Gas Resources, 2014. **7**: p. 22-32.

81. Takahashi, S. and A.R. Kovscek, *Wettability estimation of low-permeability, siliceous shale using surface forces.* Journal of Petroleum Science and Engineering, 2010. **75**(1): p. 33-43.

82. Chen, Y., et al., *Drivers of pH increase and implications for low salinity effect in sandstone.* Fuel, 2018. **218**: p. 112-117.

83. Xie, Q., et al., *A pH-resolved wettability alteration: implications for CO2-assisted EOR in carbonate reservoirs.* Energy & Fuels, 2017. **31**(12): p. 13593-13599.

84. PBrady, P.V., et al., *Altering wettability to recover more oil from tight formations.* Journal of Unconventional Oil and Gas Resources, 2016. **15**: p. 79-83.

85. Zeng, L., et al., *Wettability alteration induced water uptake in shale oil reservoirs: A geochemical interpretation for oil-brine-OM interaction during hydraulic fracturing.* International Journal of Coal Geology, 2019. **213**: p. 103277.

86. Aladasani, A., B. Bai, and Y.-S. Wu. *Investigating Low Salinity Waterflooding Recovery Mechanisms in Carbonate Reservoirs.* in *SPE EOR Conference at Oil and Gas West Asia*. 2012.

87. Chen, Y., et al., *Oil/water/rock wettability: Influencing factors and implications for low salinity water flooding in carbonate reservoirs.* Fuel, 2018. **215**: p. 171-177.

88. Brady, P.V. and G. Thyne, *Functional Wettability in Carbonate Reservoirs.* Energy & Fuels, 2016. **30**(11): p. 9217-9225.

89. Brady, P.V., J.L. Krumhansl, and P.E. Mariner, *Surface Complexation Modeling for Improved Oil Recovery*, in *SPE Improved Oil Recovery Symposium*. 2012, Society of Petroleum Engineers: Tulsa, Oklahoma, USA.

90. Brady, P.V. and J.L. Krumhansl, *Surface Complexation Modeling for Waterflooding of Sandstones.* 2013.

91. Roshan, H., et al., *On wettability of shale rocks.* Journal of Colloid and Interface Science, 2016. **475**: p. 104-111.

92. Pan, B., et al., *CO2 and CH4 Wettabilities of Organic-Rich Shale.* Energy & Fuels, 2018. **32**(2): p. 1914-1922.

93. Mirchi, V., et al. *Dynamic interfacial tensions and contact angles of surfactant-in-brine/oil/shale systems: implications to enhanced oil recovery in shale oil reservoirs.* in *SPE Improved Oil Recovery Symposium*. 2014. Society of Petroleum Engineers.

94. Roshan, H., et al., *Mechanisms of water adsorption into partially saturated fractured shales: An experimental study.* Fuel, 2015. **159**: p. 628-637.

95. XIE, L., et al., *Experimental investigations of the mineral wettability in shale and its influence factors.* Acta Geologica Sinica (English Edition), 2015. **1**.

96. MILLS, R., *THE EVAPORATION AND CONCENTRATION OF WATERS ASSOCIATED WITH PETROLEUM.*

97. Odusina, E.O., C.H. Sondergeld, and C.S. Rai, *NMR Study of Shale Wettability*, in *Canadian Unconventional Resources Conference*. 2011, Society of Petroleum Engineers: Calgary, Alberta, Canada. p. 15.

98. Lan, Q., et al., *Water Loss versus Soaking Time: Spontaneous Imbibition in Tight Rocks*, in *SPE/EAGE European Unconventional Resources Conference and Exhibition*. 2014, Society of Petroleum Engineers: Vienna, Austria.

99. Gale, J.F., et al., *Natural fractures in shale: A review and new observationsNatural Fractures in Shale: A Review and New Observations.* AAPG bulletin, 2014. **98**(11): p. 2165-2216.

100. Loucks, R.G., et al., *Spectrum of pore types and networks in mudrocks and a descriptive classification for matrix-related mudrock pores.* AAPG bulletin, 2012. **96**(6): p. 1071-1098.

101. Sun, Y., B. Bai, and M. Wei, *Microfracture and Surfactant Impact on Linear Cocurrent Brine Imbibition in Gas-Saturated Shale.* Energy & Fuels, 2015. **29**(3): p. 1438-1446.

102. Meng, M., et al., *Monitor the process of shale spontaneous imbibition in co-current and counter-current displacing gas by using low field nuclear magnetic resonance method.* Journal of Natural Gas Science and Engineering, 2015. **27**: p. 336-345.

103. Zhou, Z., et al., *Experimental investigation of the effect of imbibition on shale permeability during hydraulic fracturing.* Journal of Natural Gas Science and Engineering, 2016. **29**: p. 413-430.

104. Ge, H.-K., et al., *Experimental investigation of shale imbibition capacity and the factors influencing loss of hydraulic fracturing fluids.* Petroleum Science, 2015. **12**(4): p. 636-650.

105. Yang, L., et al., *The effect of microstructure and rock mineralogy on water imbibition characteristics in tight reservoirs.* Journal of Natural Gas Science and Engineering, 2016. **34**: p. 1461-1471.

106. Roshan, H., et al., *Investigation of the kinetics of water uptake into partially saturated shales.* Water Resources Research, 2016. **52**(4): p. 2420-2438.

107. Takeda, M., et al. *Development and application of chemical osmosis simulator based on TOUGH2.* in *2012 TOUGH2 Symposium.* 2012. Lawrence Berkeley National Laboratory Berkeley, California.

108. Ghanbari, E. and H. Dehghanpour, *Impact of rock fabric on water imbibition and salt diffusion in gas shales.* International Journal of Coal Geology, 2015. **138**: p. 55-67.

109. Kurtoglu, B., *Integrated reservoir characterization and modeling in support of enhanced oil recovery for Bakken.* 2013, Colorado School of Mines. Arthur Lakes Library.

110. Hayes, T.D., *Sampling and analysis of water streams associated with the development of Marcellus shale gas.* 2009: Gas Technology Institute.

111. Zolfaghari, A., et al., *Advances in Flowback Chemical Analysis of Gas Shales*, in *SPE Annual Technical Conference and Exhibition.* 2015, Society of Petroleum Engineers: Houston, Texas, USA.

112. Haluszczak, L.O., A.W. Rose, and L.R. Kump, *Geochemical evaluation of flowback brine from Marcellus gas wells in Pennsylvania, USA.* Applied Geochemistry, 2013. **28**: p. 55-61.

113. Blauch, M.E., et al., *Marcellus Shale Post-Frac Flowback Waters - Where is All the Salt Coming from and What are the Implications?*, in *SPE Eastern Regional Meeting.* 2009, Society of Petroleum Engineers: Charleston, West Virginia, USA. p. 20.

114. Jiang, X., *Flowback quality characterization for horizontal wells in Wattenberg field.* 2013, Colorado State University.

115. Zolfaghari, A., et al., *Laboratory and field analysis of flowback water from gas shales.* Journal of Unconventional Oil and Gas Resources, 2016. **14**: p. 113-127.

116. Stewart, B.W., et al., *Origin of brines, salts and carbonate from shales of the Marcellus Formation: Evidence from geochemical and Sr isotope study of sequentially extracted fluids.* Applied Geochemistry, 2015. **60**: p. 78-88.

117. Harrison, A.L., et al., *Element release and reaction-induced porosity alteration during shale-hydraulic fracturing fluid interactions.* Applied Geochemistry, 2017. **82**: p. 47-62.

118. Capo, R.C., et al., *The strontium isotopic evolution of Marcellus Formation produced waters, southwestern Pennsylvania.* International Journal of Coal Geology, 2014. **126**: p. 57-63.

119. Ghanbari, E., et al., *Flowback Volumetric and Chemical Analysis for Evaluating Load Recovery and Its Impact on Early-Time Production*, in *SPE Unconventional Resources Conference Canada.* 2013, Society of Petroleum Engineers: Calgary, Alberta, Canada.

120. Chermak, J.A. and M.E. Schreiber, *Mineralogy and trace element geochemistry of gas shales in the United States: Environmental implications.* International Journal of Coal Geology, 2014. **126**: p. 32-44.

121. Rowan, E.L., et al., *Geochemical and isotopic evolution of water produced from Middle Devonian Marcellus shale gas wells, Appalachian basin, PennsylvaniaGeochemistry of Produced Water from Marcellus Shale Water, PA.* Aapg Bulletin, 2015. **99**(2): p. 181-206.

122. Teppen, B.J. and D.M. Miller, *Hydration energy determines isovalent cation exchange selectivity by clay minerals.* Soil Science Society of America Journal, 2006. **70**(1): p. 31-40.

123. Abdulsattar, Z.R., *Physicochemical Interactions of Source-Rocks with Injected Water-Based Fluids.* 2015.

124. Langmuir, D., *Stability of calcite based on aqueous solubility measurements.* Geochimica et Cosmochimica Acta, 1968. **32**(8): p. 835-851.

125. Rossum, J.R. and D.T. Merrill, *An evaluation of the calcium carbonate saturation indexes.* Journal-American Water Works Association, 1983. **75**(2): p. 95-100.

126. Lea, A.S., et al., *Microscopic effects of carbonate, manganese, and strontium ions on calcite dissolution.* Geochimica et Cosmochimica Acta, 2001. **65**(3): p. 369-379.

127. Dolgaleva, I.V., et al., *Modeling of the Effect of pH on the Calcite Dissolution Kinetics.* Theoretical Foundations of Chemical Engineering, 2005. **39**(6): p. 614-621.

128. Baud, P., W. Zhu, and T.f. Wong, *Failure mode and weakening effect of water on sandstone.* Journal of Geophysical Research: Solid Earth, 2000. **105**(B7): p. 16371-16389.

129. Wasantha, P.L.P. and P.G. Ranjith, *Water-weakening behavior of Hawkesbury sandstone in brittle regime.* Engineering Geology, 2014. **178**: p. 91-101.

130. Liu, H., et al., *Effect of water imbibition on uniaxial compression strength of sandstone.* International Journal of Rock Mechanics and Mining Sciences, 2020. **127**: p. 104200.

131. Cai, X., et al., *Water-Weakening Effects on the Mechanical Behavior of Different Rock Types: Phenomena and Mechanisms.* Applied Sciences, 2019. **9**(20): p. 4450.

132. Chen, G., et al., *Weakening effects of the presence of water on the brittleness of hard sandstone.* Bulletin of Engineering Geology and the Environment, 2019. **78**(3): p. 1471-1483.

133. Al-Bazali, T., et al., *Factors controlling the compressive strength and acoustic properties of shales when interacting with water-based fluids.* International Journal of Rock Mechanics and Mining Sciences, 2008. **45**(5): p. 729-738.

134. Gupta, I., et al., *Water Weakening: A Laboratory Study of Marcellus, Woodford, Eagle Ford, and Wolfcamp Shales.* SPE Reservoir Evaluation & Engineering, 2019. **22**(02): p. 418-427.

135. Nara, Y., et al., *Influences of electrolyte concentration on subcritical crack growth in sandstone in water.* Engineering geology, 2014. **179**: p. 41-49.

136. Wu, Y.-S., *Multiphase fluid flow in porous and fractured reservoirs.* 2015: Gulf professional publishing.

137. Alemu, B.L., et al., *Caprock interaction with CO2: A laboratory study of reactivity of shale with supercritical CO2 and brine.* Applied Geochemistry, 2011. **26**(12): p. 1975-1989.

138. Leung, D.Y., G. Caramanna, and M.M. Maroto-Valer, *An overview of current status of carbon dioxide capture and storage technologies.* Renewable and Sustainable Energy Reviews, 2014. **39**: p. 426-443.

139. Marcon, V. and J.P. Kaszuba, *Carbon dioxide–brine–rock interactions in a carbonate reservoir capped by shale: Experimental insights regarding the evolution of trace metals.* Geochimica et Cosmochimica Acta, 2015. **168**: p. 22-42.

140. Flesch, S., et al., *Hydrogen underground storage—Petrographic and petrophysical variations in reservoir sandstones from laboratory experiments under simulated reservoir conditions.* International Journal of Hydrogen Energy, 2018. **43**(45): p. 20822-20835.

141. Hemme, C. and W. Van Berk, *Hydrogeochemical modeling to identify potential risks of underground hydrogen storage in depleted gas fields.* Applied Sciences, 2018. **8**(11): p. 2282.

142. Zivar, D., S. Kumar, and J. Foroozesh, *Underground hydrogen storage: A comprehensive review.* International Journal of Hydrogen Energy, 2020.

143. Lin, S. and B. Lai. *Experimental investigation of water saturation effects on Barnett shale's geomechanical behaviors.* in *SPE Annual Technical Conference and Exhibition.* 2013. Society of Petroleum Engineers.

144. Liu, D., et al., *Experimental investigation on the mechanical and acoustic emission characteristics of shale softened by water absorption.* Journal of Natural Gas Science and Engineering, 2018. **50**: p. 301-308.

145. Zhang, J., et al., *Compressive Strength and Acoustic Properties Changes in Shale with Exposure to Water-Based Fluids*, in *Golden Rocks 2006, The 41st U.S. Symposium on Rock Mechanics (USRMS).* 2006, American Rock Mechanics Association: Golden, Colorado. p. 12.

146. Hemphill, T., et al., *Direct Strength Measurements of Shale Interaction with Drilling Fluids*, in *Abu Dhabi International Petroleum Exhibition and Conference.* 2008, Society of Petroleum Engineers: Abu Dhabi, UAE. p. 8.

147. Khodja, M., et al., *Shale problems and water-based drilling fluid optimisation in the Hassi Messaoud Algerian oil field.* Applied Clay Science, 2010. **49**(4): p. 383-393.

148. Gomez, S.L. and W. He, *Fighting Wellbore Instability: Customizing Drilling Fluids Based on Laboratory Studies of Shale-Fluid Interactions*, in *IADC/SPE Asia Pacific Drilling Technology Conference and Exhibition.* 2012, Society of Petroleum Engineers: Tianjin, China. p. 10.

149. Aderibigbe, A.A. and R.H. Lane, *Rock/Fluid Chemistry Impacts on Shale Fracture Behavior*, in *SPE International Symposium on Oilfield Chemistry.* 2013, Society of Petroleum Engineers: The Woodlands, Texas, USA. p. 10.

150. Pagels, M., et al. *Quantifying fracturing fluid damage on reservoir rock to optimize production.* in *Unconventional Resources Technology Conference.* 2013. Society of Exploration Geophysicists, American Association of Petroleum ….

151. Almasoodi, M.M., Y.N. Abousleiman, and S.K. Hoang, *Viscoelastic Creep of Eagle Ford Shale: Investigating Fluid-Shale Interaction*, in *SPE/CSUR Unconventional Resources Conference – Canada.* 2014, Society of Petroleum Engineers: Calgary, Alberta, Canada. p. 8.

152. Yuan, W., et al., *Experimental Investigation of Interactions between Water and a Lower Silurian Chinese Shale.* Energy & Fuels, 2014. **28**(8): p. 4925-4933.

153. Yang, Z., et al., *Micromechanical Characterization of Fluid-Shale Interactions via Nanoindentation*, in *SPE Asia Pacific Hydraulic Fracturing Conference.* 2016, Society of Petroleum Engineers: Beijing, China. p. 14.

154. Cheng, W., Y. Jin, and M. Chen, *Reactivation mechanism of natural fractures by hydraulic fracturing in naturally fractured shale reservoirs.* Journal of Natural Gas Science and Engineering, 2015. **23**: p. 431-439.

155.   Kererat, C., *Effect of oil-contamination and water saturation on the bearing capacity and shear strength parameters of silty sandy soil.* Engineering Geology, 2019. **257**: p. 105138.

156.   Papamichos, E., M. Brignoli, and F. Santarelli, *An experimental and theoretical study of a partially saturated collapsible rock.* Mechanics of Cohesive-frictional Materials: An International Journal on Experiments, Modelling and Computation of Materials and Structures, 1997. **2**(3): p. 251-278.

157.   Duong, T.V., et al., *Effects of fines and water contents on the mechanical behavior of interlayer soil in ancient railway sub-structure.* Soils and foundations, 2013. **53**(6): p. 868-878.

158.   Alramahi, B. and M.I. Sundberg, *Proppant Embedment And Conductivity of Hydraulic Fractures In Shales*, in *46th U.S. Rock Mechanics/Geomechanics Symposium*. 2012, American Rock Mechanics Association: Chicago, Illinois. p. 6.

159.   Zhang, J., et al. *Experimental and numerical studies of reduced fracture conductivity due to proppant embedment in shale reservoirs*. in *SPE Annual Technical Conference and Exhibition*. 2014. OnePetro.

160.   Mueller, M. and M. Amro. *Indentaion hardness for improved proppant embedment prediction in shale formations*. in *SPE European Formation Damage Conference and Exhibition*. 2015. Society of Petroleum Engineers.

161.   Sayed, M.A., G.A. Al-Muntasheri, and F. Liang, *Development of shale reservoirs: Knowledge gained from developments in North America.* Journal of Petroleum Science and Engineering, 2017. **157**: p. 164-186.

162.   Lu, Y., et al., *Analytical modelling of wettability alteration-induced micro-fractures during hydraulic fracturing in tight oil reservoirs.* Fuel, 2019. **249**: p. 434-440.

163.   Israelachvili, J.N., *Intermolecular and surface forces.* 2011: Academic press.

164.   Cercignani, C., *The boltzmann equation*, in *The Boltzmann equation and its applications*. 1988, Springer. p. 40-103.

165.   Winslow, A.M., *Numerical solution of the quasilinear Poisson equation in a nonuniform triangle mesh.* Journal of computational physics, 1966. **1**(2): p. 149-172.

166.   Sharp, K.A. and B. Honig, *Calculating total electrostatic energies with the nonlinear Poisson-Boltzmann equation.* The Journal of Physical Chemistry, 1990. **94**(19): p. 7684-7692.

167.   Wang, X., et al., *Molecular simulation of CO_2/CH_4 competitive adsorption in organic matter pores in shale under certain geological conditions.* Petroleum Exploration and Development, 2016. **43**(5): p. 841-848.

168.   Kruk, M. and M. Jaroniec, *Gas Adsorption Characterization of Ordered Organic−Inorganic Nanocomposite Materials.* Chemistry of Materials, 2001. **13**(10): p. 3169-3183.

169.   Zhang, T., et al., *Effect of organic-matter type and thermal maturity on methane adsorption in shale-gas systems.* Organic Geochemistry, 2012. **47**: p. 120-131.

170.   Parkhurst, D.L. and C. Appelo, *User's guide to PHREEQC (Version 2): A computer program for speciation, batch-reaction, one-dimensional transport, and inverse geochemical calculations.* 1999.

171.   Davis, J.A., R.O. James, and J.O. Leckie, *Surface ionization and complexation at the oxide/water interface: I. Computation of electrical double layer*

properties in simple electrolytes. Journal of Colloid and Interface Science, 1978. **63**(3): p. 480-499.

172. McLaughlin, S., G. Szabo, and G. Eisenman, *Divalent ions and the surface potential of charged phospholipid membranes.* The Journal of general physiology, 1971. **58**(6): p. 667-687.

173. Israelachvili, J.N., *6 - Van der Waals Forces*, in *Intermolecular and Surface Forces (Third Edition)*, J.N. Israelachvili, Editor. 2011, Academic Press: San Diego. p. 107-132.

174. Parkhurst, D.L. and C. Appelo, *Description of input and examples for PHREEQC version 3--A computer program for speciation, batch-reaction, one-dimensional transport, and inverse geochemical calculations.* 2013.

175. Parkhurst, D.L. and C. Appelo, *Description of input and examples for PHREEQC version 3: a computer program for speciation, batch-reaction, one-dimensional transport, and inverse geochemical calculations.* 2013, US Geological Survey.

176. Cao, T., et al., *A comparative study of the specific surface area and pore structure of different shales and their kerogens.* Science China Earth Sciences, 2015. **58**(4): p. 510-522.

177. Kelemen, S.R., et al., *Direct Characterization of Kerogen by X-ray and Solid-State 13C Nuclear Magnetic Resonance Methods.* Energy & Fuels, 2007. **21**(3): p. 1548-1561.

178. Huang, L., et al., *Thermodynamic and Structural Characterization of Bulk Organic Matter in Chinese Silurian Shale: Experimental and Molecular Modeling Studies.* Energy & Fuels, 2017. **31**(5): p. 4851-4865.

179. Brady, P.V. and J.L. Krumhansl, *A surface complexation model of oil–brine–sandstone interfaces at 100°C: Low salinity waterflooding.* Journal of Petroleum Science and Engineering, 2012. **81**: p. 171-176.

180. Zeng, L., et al., *Interpreting Water Uptake by Shale with Ion Exchange, Surface Complexation, and Disjoining Pressure.* Energy & Fuels, 2019.

181. Naghibi, H., A. Tamura, and J.M. Sturtevant, *Significant discrepancies between van't Hoff and calorimetric enthalpies.* Proceedings of the National Academy of Sciences, 1995. **92**(12): p. 5597-5599.

182. Brady, P.V., et al., *Electrostatics and the Low Salinity Effect in Sandstone Reservoirs.* Energy & Fuels, 2015. **29**(2): p. 666-677.

183. Pokrovsky, O.S., J. Schott, and F. Thomas, *Dolomite surface speciation and reactivity in aquatic systems.* Geochimica et Cosmochimica Acta, 1999. **63**(19): p. 3133-3143.

184. Pokrovsky, O., et al., *Surface speciation models of calcite and dolomite/aqueous solution interfaces and their spectroscopic evaluation.* Langmuir, 2000. **16**(6): p. 2677-2688.

185. Xu, M., et al., *Effects of Dissolved Oxygen on Water Imbibition in Gas Shales.* Energy & Fuels, 2018. **32**(4): p. 4695-4704.

186. Chen, Y., et al., *Electrostatic Origins of CO 2-Increased Hydrophilicity in Carbonate Reservoirs.* Scientific reports, 2018. **8**(1): p. 17691.

187. Chen, Y., Q. Xie, and A. Saeedi, *Role of ion exchange, surface complexation, and albite dissolution in low salinity water flooding in sandstone.* Journal of Petroleum Science and Engineering, 2019. **176**: p. 126-131.

188. Austad, T., A. Rezaeidoust, and T. Puntervold, *Chemical Mechanism of Low Salinity Water Flooding in Sandstone Reservoirs.* 2010, Society of Petroleum Engineers.

189. Chen, Y., et al., *Electrostatic Origins of CO2-Increased Hydrophilicity in Carbonate Reservoirs.* Scientific Reports, 2018. **8**(1): p. 17691.

190. Xie, Q., et al., *The low salinity effect at high temperatures.* Fuel, 2017. **200**: p. 419-426.

191. Rengasamy, P. and G. Churchman, *Cation exchange capacity, exchangeable cations and sodicity.* 1999.

192. Pashley, R.M., *DLVO and hydration forces between mica surfaces in Li+, Na+, K+, and Cs+ electrolyte solutions: A correlation of double-layer and hydration forces with surface cation exchange properties.* Journal of Colloid and Interface Science, 1981. **83**(2): p. 531-546.

193. Xie, Q., et al., *Extended DLVO-based estimates of surface force in low salinity water flooding.* Journal of Molecular Liquids, 2016. **221**: p. 658-665.

194. Al Maskari, N.S., Q. Xie, and A. Saeedi, *Role of Basal-Charged Clays in Low Salinity Effect in Sandstone Reservoirs: Adhesion Force on Muscovite using Atomic Force Microscope.* Energy & Fuels, 2019. **33**(2): p. 756-764.

195. Bergström, L., *Hamaker constants of inorganic materials.* Advances in colloid and interface science, 1997. **70**: p. 125-169.

196. Badiali, J.P. and J. Goodisman, *Lippmann equation and the ideally polarizable electrode.* The Journal of Physical Chemistry, 1975. **79**(3): p. 223-232.

197. Lippmann, G., *Relations entre les phénomènes électriques et capillaires.* 1875, Gauthier-Villars Paris, France:.

198. Mugele, F. and J.-C. Baret, *Electrowetting: from basics to applications.* Journal of physics: condensed matter, 2005. **17**(28): p. R705.

199. Kramer, D., *Dependence of surface stress, surface energy and surface tension on potential and charge.* Physical Chemistry Chemical Physics, 2008. **10**(1): p. 168-177.

200. Grahame, D.C., *The electrical double layer and the theory of electrocapillarity.* Chemical reviews, 1947. **41**(3): p. 441-501.

201. Lipkowski, J., et al., *Comments on the thermodynamics of solid electrodes.* Journal of Electroanalytical Chemistry, 1998. **452**(2): p. 193-197.

202. Linford, R., *The derivation of thermodynamic equations for solid surfaces.* Chemical Reviews, 1978. **78**(2): p. 81-95.

203. Proost, J., *Thermodynamic issues associated with combined cyclic voltammetry and wafer curvature measurements in electrolytes.* Journal of Solid State Electrochemistry, 2005. **9**(10): p. 660-664.

204. Van Cappellen, P., et al., *A surface complexation model of the carbonate mineral-aqueous solution interface.* Geochimica et Cosmochimica Acta, 1993. **57**(15): p. 3505-3518.

205. Sø, H.U., et al., *Competitive adsorption of arsenate and phosphate onto calcite; experimental results and modeling with CCM and CD-MUSIC.* Geochimica et Cosmochimica Acta, 2012. **93**: p. 1-13.

206. Martin-Garin, A., d.P. Van Cappellen, and L. Charlet, *Aqueous cadmium uptake by calcite: A stirred flow-through reactor study.* Geochimica et Cosmochimica Acta, 2003. **67**(15): p. 2763-2774.

207. Arakaki, T. and A. Mucci, *A continuous and mechanistic representation of calcite reaction-controlled kinetics in dilute solutions at 25 C and 1 atm total pressure.* Aquatic Geochemistry, 1995. **1**(1): p. 105-130.

208. Pokrovsky, O.S., J. Schott, and F. Thomas, *Processes at the magnesium-bearing carbonates/solution interface. I. A surface speciation model for magnesite.* Geochimica et cosmochimica acta, 1999. **63**(6): p. 863-880.

209. Pokrovsky, O., et al., *Surface speciation of Ca and Mg carbonate minerals in aqueous solutions: A combined potentiometric, electrokinetic, and DRIFT surface spectroscopy approach.* Min. Mag. A, 1998. **62**: p. 1196-1197.

210. Nilsson, Ö. and J. Sternbeck, *A mechanistic model for calcite crystal growth using surface speciation.* Geochimica et Cosmochimica Acta, 1999. **63**(2): p. 217-225.

211. Wolthers, M., L. Charlet, and P. Van Cappellen, *The surface chemistry of divalent metal carbonate minerals; a critical assessment of surface charge and potential data using the charge distribution multi-site ion complexation model.* American Journal of science, 2008. **308**(8): p. 905-941.

212. Hiemstra, T. and W.H. Van Riemsdijk, *A surface structural approach to ion adsorption: the charge distribution (CD) model.* Journal of colloid and interface science, 1996. **179**(2): p. 488-508.

213. Akhondzadeh, H., et al., *Pore-scale analysis of coal cleat network evolution through liquid nitrogen treatment: A Micro-Computed Tomography investigation.* International Journal of Coal Geology, 2020. **219**: p. 103370.

214. Cripps, A.C.F. and C. Anthony, *Nanoindentation.* Mechanical Engineering Series (New York, NY: Springer-Verlag 2002)(Cited on pages 48, 51, 52 and 76.), 2004.

215. Gandossi, L., *An overview of hydraulic fracturing and other formation stimulation technologies for shale gas production.* Eur. Commisison Jt. Res. Cent. Tech. Reports, 2013.

216. Abramova, A., et al., *Analysis of the modern methods for enhanced oil recovery.* Energy Science and Technology, 2015. **3**: p. 118-148.

217. King, G.E., *Thirty Years of Gas Shale Fracturing: What Have We Learned?*, in *SPE Annual Technical Conference and Exhibition.* 2010, Society of Petroleum Engineers: Florence, Italy. p. 50.

218. Chen, T., et al., *"Peeling Off" Mechanism of Asphaltenes from Solid/Liquid Interface in the Presence of a Highly Charged Amphiphilic Macromolecule.* Energy & Fuels, 2016. **30**(11): p. 9250-9259.

219. Xie, Q., et al., *pH effect on wettability of oil/brine/carbonate system: Implications for low salinity water flooding.* Journal of Petroleum Science and Engineering, 2018. **168**: p. 419-425.

220. Mahani, H., et al., *Electrokinetics of Carbonate/Brine Interface in Low-Salinity Waterflooding: Effect of Brine Salinity, Composition, Rock Type, and pH on ζ-Potential and a Surface-Complexation Model.* SPE Journal, 2016.

221. Chen, Y., et al., *Excess H+ Increases Hydrophilicity during CO2-Assisted Enhanced Oil Recovery in Sandstone Reservoirs.* Energy & Fuels, 2019.

222. RezaeiDoust, A., T. Puntervold, and T. Austad, *Chemical Verification of the EOR Mechanism by Using Low Saline/Smart Water in Sandstone.* Energy & Fuels, 2011. **25**(5): p. 2151-2162.

223. Song, J., et al., *Surface complexation modeling of calcite zeta potential measurements in brines with mixed potential determining ions (Ca2+, CO32−, Mg2+, SO42−) for characterizing carbonate wettability.* Journal of Colloid and Interface Science, 2017. **506**: p. 169-179.

224. Cho, Y., et al., *Rock Characterization in Unconventional Reservoirs: A Comparative Study of Bakken, Eagle Ford, and Niobrara Formations*, in *SPE Low Perm Symposium.* 2016, Society of Petroleum Engineers: Denver, Colorado, USA.

225. Li*, H., et al. *Characterizing the middle Bakken: Laboratory measurement and rock typing of the Middle Bakken formation*. in *Unconventional Resources Technology Conference, San Antonio, Texas, 20-22 July 2015*. 2015. Society of Exploration Geophysicists, American Association of Petroleum Geologists, Society of Petroleum Engineers.

226. Kennedy, M.J., D.R. Pevear, and R.J. Hill, *Mineral surface control of organic carbon in black shale*. Science, 2002. **295**(5555): p. 657-660.

227. Smith, M.G. and R.M. Bustin, *Production and preservation of organic matter during deposition of the Bakken Formation (Late Devonian and Early Mississippian), Williston Basin*. Palaeogeography, Palaeoclimatology, Palaeoecology, 1998. **142**(3): p. 185-200.

228. Palisch, T.T., M. Vincent, and P.J. Handren, *Slickwater Fracturing: Food for Thought*. SPE Production & Operations, 2010. **25**(03): p. 327-344.

229. Buckley, J.S. and N.R. Morrow, *Characterization of Crude Oil Wetting Behavior by Adhesion Tests*, in *SPE/DOE Enhanced Oil Recovery Symposium*. 1990, 1990 Copyright 1990, Society of Petroleum Engineers, Inc.: Tulsa, Oklahoma.

230. Takahashi, S. and A.R. Kovscek, *Spontaneous countercurrent imbibition and forced displacement characteristics of low-permeability, siliceous shale rocks*. Journal of Petroleum Science and Engineering, 2010. **71**(1): p. 47-55.

231. Hirasaki, G., *Wettability: fundamentals and surface forces*. SPE Formation Evaluation, 1991. **6**(02): p. 217-226.

232. Busireddy, C. and D.N. Rao. *Application of DLVO theory to characterize spreading in crude oil-brine-rock systems*. in *SPE/DOE Symposium on Improved Oil Recovery*. 2004. Society of Petroleum Engineers.

233. Karraker, K.A. and C.J. Radke, *Disjoining pressures, zeta potentials and surface tensions of aqueous non-ionic surfactant/electrolyte solutions: theory and comparison to experiment*. Advances in Colloid and Interface Science, 2002. **96**(1): p. 231-264.

234. Kargbo, D.M., R.G. Wilhelm, and D.J. Campbell, *Natural Gas Plays in the Marcellus Shale: Challenges and Potential Opportunities*. Environmental Science & Technology, 2010. **44**(15): p. 5679-5684.

235. Wang, Q., et al., *Natural gas from shale formation–the evolution, evidences and challenges of shale gas revolution in United States*. Renewable and Sustainable Energy Reviews, 2014. **30**: p. 1-28.

236. Rahm, D., *Regulating hydraulic fracturing in shale gas plays: The case of Texas*. Energy Policy, 2011. **39**(5): p. 2974-2981.

237. Zhang, J.-c., et al., *Exploration potential of shale gas resources in China*. Natural Gas Industry, 2008. **6**.

238. Administration, U.E.I., *Annual Energy Outlook 2011: With Projections to 2035*. 2011: Government Printing Office.

239. Rezaee, R., *Fundamentals of gas shale reservoirs*. 2015: John Wiley & Sons.

240. Yu, W., H. Lashgari, and K. Sepehrnoori, *Simulation Study of CO2 Huff-n-Puff Process in Bakken Tight Oil Reservoirs*, in *SPE Western North American and Rocky Mountain Joint Meeting*. 2014, Society of Petroleum Engineers: Denver, Colorado. p. 16.

241. Ding, W., et al., *Fracture development in shale and its relationship to gas accumulation*. Geoscience Frontiers, 2012. **3**(1): p. 97-105.

242. Qian, B., et al., *Application of zipper-fracturing of horizontal cluster wells in the Changning shale gas pilot zone, Sichuan Basin.* Natural Gas Industry B, 2015. **2**(2-3): p. 181-184.

243. Mantell, M. *Recycling and reuse of produced water to reduce freshwater use in hydraulic fracturing operations.* in *Research Triangle Park: EPA Hydraulic Fracturing Study Water Acquisition Workshop.* 2013.

244. Sharma, M. and S. Agrawal. *Impact of liquid loading in hydraulic fractures on well productivity.* in *SPE hydraulic fracturing technology conference.* 2013. Society of Petroleum Engineers.

245. Ezulike, O., et al., *Flowback fracture closure: A key factor for estimating effective pore volume.* SPE Reservoir Evaluation & Engineering, 2016. **19**(04): p. 567-582.

246. Roshan, H., et al., *Investigation of the kinetics of water uptake into partially saturated shales.* Water Resources Research, 2016. **52**(4): p. 2420-2438.

247. Ghanbari, E. and H. Dehghanpour, *Impact of rock fabric on water imbibition and salt diffusion in gas shales.* International Journal of Coal Geology, 2015. **138**(Supplement C): p. 55-67.

248. Yang, J., et al., *Nanoscale geochemical and geomechanical characterization of organic matter in shale.* Nature Communications, 2017. **8**(1): p. 2179.

249. Hai-Lang, Z. and H. Shi-Jun, *Viscosity and density of water+ sodium chloride+ potassium chloride solutions at 298.15 K.* Journal of Chemical & Engineering Data, 1996. **41**(3): p. 516-520.

250. Aveyard, R. and S.M. Saleem, *Interfacial tensions at alkane-aqueous electrolyte interfaces.* Journal of the Chemical Society, Faraday Transactions 1: Physical Chemistry in Condensed Phases, 1976. **72**: p. 1609-1617.

251. Horibe, A., S. Fukusako, and M. Yamada, *Surface tension of low-temperature aqueous solutions.* International journal of thermophysics, 1996. **17**(2): p. 483-493.

252. Qiao, C., et al., *A Mechanistic Model for Wettability Alteration by Chemically Tuned Water Flooding in Carbonate Reservoirs.* 2015, Society of Petroleum Engineers: SPE Journal.

253. Tokunaga, T.K., *Correction to DLVO-Based Estimates of Adsorbed Water Film Thicknesses in Geologic CO2 Reservoirs.* Langmuir, 2013. **29**(9): p. 3152-3152.

254. Gregory, J., *Interaction of unequal double layers at constant charge.* Journal of Colloid and Interface Science, 1975. **51**(1): p. 44-51.

255. Nasralla, R.A. and H.A. Nasr-El-Din, *Double-Layer Expansion: Is It a Primary Mechanism of Improved Oil Recovery by Low-Salinity Waterflooding?* SPE Reservoir Evaluation & Engineering, 2014. **Volume 17**(Issue 01, 2014): p. Pages 49-59.

256. Xie, Q., et al., *Investigation of Electrical Surface Charges and Wettability Alteration by Ions Matching Waterflooding.* International Symposium of the Society of Core Analysts, 2012.

257. Lee, S.Y., et al., *Low Salinity Oil Recovery: Increasing Understanding of the Underlying Mechanisms*, in *SPE Improved Oil Recovery Symposium.* 2010, Society of Petroleum Engineers: Tulsa, Oklahoma, USA. p. 11.

258. Karraker, K.A. and C.J. Radke, *Disjoining pressures, zeta potentials and surface tensions of aqueous non-ionic surfactant/electrolyte solutions: theory and comparison to experiment.* Advances in Colloid and Interface Science, 2002. **96**(1–3): p. 231-264.

259. Yang, L., et al., *Imbibition inducing tensile fractures and its influence on in-situ stress analyses: A case study of shale gas drilling.* Journal of Natural Gas Science and Engineering, 2015. **26**: p. 927-939.

260. Chen, X., et al., *Effect of Water on Fracture Mechanical Properties of Shales.* Journal of Geophysical Research: Solid Earth, 2019. **0**(0).

261. Dong, T., et al., *Porosity characteristics of the Devonian Horn River shale, Canada: Insights from lithofacies classification and shale composition.* International Journal of Coal Geology, 2015. **141-142**: p. 74-90.

262. Chalmers, G.R.L., D.J.K. Ross, and R.M. Bustin, *Geological controls on matrix permeability of Devonian Gas Shales in the Horn River and Liard basins, northeastern British Columbia, Canada.* International Journal of Coal Geology, 2012. **103**: p. 120-131.

263. Arthur, J.D., B. Bohm, and M. Layne, *Hydraulic fracturing considerations for natural gas wells of the Marcellus Shale.* 2009.

264. Edwards, R.W.J. and M.A. Celia, *Shale Gas Well, Hydraulic Fracturing, and Formation Data to Support Modeling of Gas and Water Flow in Shale Formations.* Water Resources Research, 2018. **54**(4): p. 3196-3206.

265. Chapman, E.C., et al., *Geochemical and Strontium Isotope Characterization of Produced Waters from Marcellus Shale Natural Gas Extraction.* Environmental Science & Technology, 2012. **46**(6): p. 3545-3553.

266. Milliken, K.L., et al., *Organic matter–hosted pore system, Marcellus Formation (Devonian), PennsylvaniaGeohorizon.* AAPG Bulletin, 2013. **97**(2): p. 177-200.

267. Morsy, S. and J.J. Sheng, *Imbibition Characteristics of the Barnett Shale Formation*, in *SPE Unconventional Resources Conference*. 2014, Society of Petroleum Engineers: The Woodlands, Texas, USA.

268. Zhou, D., et al., *Scaling of counter-current imbibition processes in low-permeability porous media.* Journal of Petroleum Science and Engineering, 2002. **33**(1-3): p. 61-74.

269. Caldeira, C.L., et al., *Pyrite oxidation in alkaline solutions: nature of the product layer.* International Journal of Mineral Processing, 2003. **72**(1): p. 373-386.

270. Keller, W. and L.M. da Costa, *Comparative chemical compositions of aqueous extracts from representative clays.* American Mineralogist, 1989. **74**(9-10): p. 1142-1146.

271. Morrow, C.P., et al., *Structure, Energetics, and Dynamics of Smectite Clay Interlayer Hydration: Molecular Dynamics and Metadynamics Investigation of Na-Hectorite.* The Journal of Physical Chemistry C, 2013. **117**(10): p. 5172-5187.

272. Kolesar Kohl, C.A., et al., *Strontium isotopes test long-term zonal isolation of injected and Marcellus formation water after hydraulic fracturing.* Environmental science & technology, 2014. **48**(16): p. 9867-9873.

273. Vengosh, A., et al., *A Critical Review of the Risks to Water Resources from Unconventional Shale Gas Development and Hydraulic Fracturing in the United States.* Environmental Science & Technology, 2014. **48**(15): p. 8334-8348.

274. Vengosh, A., et al., *The Effects of Shale Gas Exploration and Hydraulic Fracturing on the Quality of Water Resources in the United States.* Procedia Earth and Planetary Science, 2013. **7**: p. 863-866.

275. Fakhru'l-Razi, A., et al., *Review of technologies for oil and gas produced water treatment.* Journal of Hazardous Materials, 2009. **170**(2): p. 530-551.

276. Gregory, K.B., R.D. Vidic, and D.A. Dzombak, *Water Management Challenges Associated with the Production of Shale Gas by Hydraulic Fracturing.* Elements, 2011. **7**(3): p. 181-186.

277. Lebas, R.A., et al. *Development and use of high-TDS recycled produced water for crosslinked-gel-based hydraulic fracturing.* in *SPE Hydraulic Fracturing Technology Conference.* 2013. Society of Petroleum Engineers.

278. Lord, P., et al., *Recycling Water: Case Studies in Designing Fracturing Fluids Using Flowback, Produced, and Nontraditional Water Sources*, in *SPE Latin-American and Caribbean Health, Safety, Environment and Social Responsibility Conference.* 2013, Society of Petroleum Engineers: Lima, Peru. p. 5.

279. Chen, Q., et al., *Change in composition and pore structure of Longmaxi black shale during oxidative dissolution.* International Journal of Coal Geology, 2017. **172**: p. 95-111.

280. Jin, L., et al., *Evolution of porosity and geochemistry in Marcellus Formation black shale during weathering.* Chemical Geology, 2013. **356**: p. 50-63.

281. Chen, Y., et al., *Excess H+ Increases Hydrophilicity during CO2-Assisted Enhanced Oil Recovery in Sandstone Reservoirs.* Energy & Fuels, 2019. **33**(2): p. 814-821.

282. Yutkin, M.P., et al., *Bulk and surface aqueous speciation of calcite: implications for low-salinity waterflooding of carbonate reservoirs.* Vol. 23. 2018.

283. Chuan, M., G. Shu, and J. Liu, *Solubility of heavy metals in a contaminated soil: effects of redox potential and pH.* Water, Air, and Soil Pollution, 1996. **90**(3-4): p. 543-556.

284. Suslow, T.V., *Oxidation-reduction potential (ORP) for water disinfection monitoring, control, and documentation.* 2004.

285. Atkinson, B.K., *Subcritical crack growth in geological materials.* Journal of Geophysical Research: Solid Earth, 1984. **89**(B6): p. 4077-4114.

286. Xu, M., A. Gupta, and H. Dehghanpour, *How significant are strain and stress induced by water imbibition in dry gas shales?* Journal of Petroleum Science and Engineering, 2019. **176**: p. 428-443.

287. Røyne, A., J. Bisschop, and D.K. Dysthe, *Experimental investigation of surface energy and subcritical crack growth in calcite.* Journal of Geophysical Research: Solid Earth, 2011. **116**(B4).

288. Meredith, P. and B. Atkinson, *Fracture toughness and subcritical crack growth during high-temperature tensile deformation of Westerly granite and Black gabbro.* Physics of the Earth and Planetary Interiors, 1985. **39**(1): p. 33-51.

289. Nara, Y., et al., *Effects of relative humidity and temperature on subcritical crack growth in igneous rock.* International Journal of Rock Mechanics and Mining Sciences, 2010. **47**(4): p. 640-646.

290. Eppes, M.C. and R. Keanini, *Mechanical weathering and rock erosion by climate-dependent subcritical cracking.* Reviews of Geophysics, 2017. **55**(2): p. 470-508.

291. Griffith, A.A., *VI. The phenomena of rupture and flow in solids.* Philosophical transactions of the royal society of london. Series A, containing papers of a mathematical or physical character, 1921. **221**(582-593): p. 163-198.

292. Shchukin, E.D., et al., *Effects of adsorption–active media on the mechanical propreties of catalysts and adsorbents.* Colloids and Surfaces A: Physicochemical and Engineering Aspects, 2006. **282-283**: p. 287-297.

293. Nara, Y., et al., *Precipitation of minerals on rock kept in water with different calcium ion concentrations.* Zairyo (Online), 2018. **67**(7): p. 730-737.

294. Kudo, Y., et al., *Stress-induced crack path in Aji granite under tensile stress.* pure and applied geophysics, 1992. **138**(4): p. 641-656.

295. Atkinson, B.K. and P.G. Meredith, *Stress corrosion cracking of quartz: a note on the influence of chemical environment.* Tectonophysics, 1981. **77**(1-2): p. T1-T11.

296. Martin III, R.J., *Time-dependent crack growth in quartz and its application to the creep of rocks.* Journal of Geophysical Research, 1972. **77**(8): p. 1406-1419.

297. Martin III, R.J. and W.B. Durham, *Mechanisms of crack growth in quartz.* Journal of Geophysical Research, 1975. **80**(35): p. 4837-4844.

298. Nara, Y., et al., *Influence of relative humidity on fracture toughness of rock: implications for subcritical crack growth.* International Journal of Solids and Structures, 2012. **49**(18): p. 2471-2481.

299. Croizé, D., et al., *Experimental mechanical and chemical compaction of carbonate sand.* Journal of Geophysical Research: Solid Earth, 2010. **115**(B11).

300. Henry, J.P., J. Paquet, and J. Tancrez. *Experimental study of crack propagation in calcite rocks.* in *International Journal of Rock Mechanics and Mining Sciences & Geomechanics Abstracts.* 1977. Elsevier.

301. Atkinson, B. *Fracture toughness of Tennessee sandstone and Carrara marble using the double torsion testing method.* in *International journal of rock mechanics and mining sciences & geomechanics abstracts.* 1979. Elsevier.

302. Nara, Y., et al., *Influence of surrounding environment on subcritical crack growth in marble.* Tectonophysics, 2017. **706**: p. 116-128.

303. Charles, R., *Static fatigue of glass. I.* Journal of Applied Physics, 1958. **29**(11): p. 1549-1553.

304. Wiederhorn, S. and L. Bolz, *Stress corrosion and static fatigue of glass.* Journal of the American Ceramic Society, 1970. **53**(10): p. 543-548.

305. Detwiler, R.L., *Experimental observations of deformation caused by mineral dissolution in variable-aperture fractures.* Journal of Geophysical Research: Solid Earth, 2008. **113**(B8).

306. Ellis, B.R., et al., *Dissolution-driven permeability reduction of a fractured carbonate caprock.* Environmental engineering science, 2013. **30**(4): p. 187-193.

307. Binazadeh, M., et al., *Effect of electrostatic interactions on water uptake of gas shales: the interplay of solution ionic strength and electrostatic double layer.* Energy & Fuels, 2016. **30**(2): p. 992-1001.

308. Pokrovsky, O., J. Schott, and J. Mielczarski, *Surface speciation of dolomite and calcite in aqueous solutions.* Encyclopedia of surface and colloid science, 2002. **4**: p. 5081-5095.

309. Al Mahrouqi, D., J. Vinogradov, and M.D. Jackson, *Zeta potential of artificial and natural calcite in aqueous solution.* Advances in colloid and interface science, 2017. **240**: p. 60-76.

310. Pokrovsky, O.S., J. Viers, and R. Freydier, *Zinc stable isotope fractionation during its adsorption on oxides and hydroxides.* Journal of Colloid and Interface Science, 2005. **291**(1): p. 192-200.

311. Steel, L., E. Mackay, and M.M. Maroto-Valer, *Experimental investigation of CO2-brine-calcite interactions under reservoir conditions.* Fuel Processing Technology, 2018. **169**: p. 122-131.

312. Beinlich, A. and H. Austrheim, *In situ sequestration of atmospheric CO2 at low temperature and surface cracking of serpentinized peridotite in mine shafts.* Chemical Geology, 2012. **332-333**: p. 32-44.

313. Xie, Q., et al., *Fines migration during CO2 injection: Experimental results interpreted using surface forces.* International Journal of Greenhouse Gas Control, 2017. **65**: p. 32-39.

314. Inamdar, A.A., et al. *Evaluation of stimulation techniques using microseismic mapping in the Eagle Ford Shale.* in *Tight Gas Completions Conference.* 2010. Society of Petroleum Engineers.

315. Feng, Y. and K. Gray, *Discussion on field injectivity tests during drilling.* Rock Mechanics and Rock Engineering, 2017. **50**(2): p. 493-498.

316. Eppes, M.C., B.I. Magi, and R. Keanini. *Real-time Observations of Rock Cracking and Weather Provide Insights into Thermal Stress-Related Processes of Mechanical Weathering.* in *AGU Fall Meeting Abstracts.* 2015.

317. Medlock, K.B., *Modeling the implications of expanded US shale gas production.* Energy Strategy Reviews, 2012. **1**(1): p. 33-41.

318. Jacoby, H.D., F.M. O'SULLIVAN, and S. Paltsev, *The influence of shale gas on US energy and environmental policy.* Economics of Energy & Environmental Policy, 2012. **1**(1): p. 37-52.

319. Ross, D.J. and R.M. Bustin, *Characterizing the shale gas resource potential of Devonian–Mississippian strata in the Western Canada sedimentary basin: Application of an integrated formation evaluation.* AAPG bulletin, 2008. **92**(1): p. 87-125.

320. Ross, D.J. and R.M. Bustin, *Shale gas potential of the lower Jurassic Gordondale member, northeastern British Columbia, Canada.* Bulletin of Canadian Petroleum Geology, 2007. **55**(1): p. 51-75.

321. Labani, M.M., et al., *Evaluation of pore size spectrum of gas shale reservoirs using low pressure nitrogen adsorption, gas expansion and mercury porosimetry: A case study from the Perth and Canning Basins, Western Australia.* Journal of Petroleum Science and Engineering, 2013. **112**: p. 7-16.

322. Knaus, E., et al., *An overview of oil shale resources.* Oil Shale: A Solution to the Liquid Fuel Dilemma, 2010. **1**.

323. Chengzao, J., M. Zheng, and Y. Zhang, *Unconventional hydrocarbon resources in China and the prospect of exploration and development.* Petroleum Exploration and Development, 2012. **39**(2): p. 139-146.

324. Lu, Y. and K.P. Chen, *Productivity-Index Optimization for Hydraulically Fractured Vertical Wells in a Circular Reservoir: A Comparative Study With Analytical Solutions.* SPE Journal, 2016. **21**(06): p. 2208-2219.

325. Alramahi, B. and M. Sundberg. *Proppant embedment and conductivity of hydraulic fractures in shales.* in *46th US Rock Mechanics/Geomechanics Symposium.* 2012. American Rock Mechanics Association.

326. Hirasaki, G., *Interfacial phenomena in petroleum recovery.* NR Morrow (ed.), 1991: p. 23-76.

327. Zhu, X. and Y.-P. Zhao, *Atomic Mechanisms and Equation of State of Methane Adsorption in Carbon Nanopores.* The Journal of Physical Chemistry C, 2014. **118**(31): p. 17737-17744.

328. Kurtoglu, B., et al., *A Rock and Fluid Study of Middle Bakken Formation: Key to Enhanced Oil Recovery*, in *SPE/CSUR Unconventional Resources Conference – Canada.* 2014, Society of Petroleum Engineers: Calgary, Alberta, Canada. p. 19.

329. Truche, L., et al., *Kinetics of pyrite to pyrrhotite reduction by hydrogen in calcite buffered solutions between 90 and 180°C: Implications for nuclear waste disposal.* Geochimica et Cosmochimica Acta, 2010. **74**(10): p. 2894-2914.

330. Smith, M.M., Z. Dai, and S.A. Carroll, *Illite dissolution kinetics from 100 to 280°C and pH 3 to 9.* Geochimica et Cosmochimica Acta, 2017. **209**: p. 9-23.

331. Elzinga, E.J., A.A. Rouff, and R.J. Reeder, *The long-term fate of Cu2+, Zn2+, and Pb2+ adsorption complexes at the calcite surface: An X-ray absorption spectroscopy study.* Geochimica et Cosmochimica Acta, 2006. **70**(11): p. 2715-2725.

332. Plummer, L.N. and E. Busenberg, *The solubilities of calcite, aragonite and vaterite in CO2-H2O solutions between 0 and 90°C, and an evaluation of the aqueous model for the system CaCO3-CO2-H2O.* Geochimica et Cosmochimica Acta, 1982. **46**(6): p. 1011-1040.

333. Rachlin, A.L., G.S. Henderson, and M.C. Goh, *An atomic force microscope (AFM) study of the calcite cleavage plane: Image averaging in Fourier space.* American Mineralogist, 1992. **77**(9-10): p. 904-910.

334. Maslova, M., L. Gerasimova, and W. Forsling, *Surface properties of cleaved mica.* Colloid Journal, 2004. **66**(3): p. 322-328.

335. Skinner, A.J., J.P. LaFemina, and H.J. Jansen, *Structure and bonding of calcite: a theoretical study.* American Mineralogist, 1994. **79**(3-4): p. 205-214.

336. Schultz, R.A., M.C. Jensen, and R.C. Bradt, *Single crystal cleavage of brittle materials.* International Journal of Fracture, 1994. **65**(4): p. 291-312.

337. Devine, R.A., *The physics and technology of amorphous SiO2.* 2012: Springer Science & Business Media.

338. Calabrese, E. and W.B. Fowler, *Electronic energy-band structure of α quartz.* Physical review B, 1978. **18**(6): p. 2888.

339. Stipp, M. and J. Tullis, *The recrystallized grain size piezometer for quartz.* Geophysical Research Letters, 2003. **30**(21).

340. Mayerhofer, M.J., et al., *What Is Stimulated Reservoir Volume?* SPE Production & Operations, 2010. **25**(01): p. 89-98.

341. Wu, Y., et al., *Multiscale elastic anisotropy of a shale characterized by cross-scale big data nanoindentation.* International Journal of Rock Mechanics and Mining Sciences, 2020. **134**: p. 104458.

342. Luo, S., et al., *Cross-scale characterization of the elasticity of shales: Statistical nanoindentation and data analytics.* Journal of the Mechanics and Physics of Solids, 2020. **140**: p. 103945.

343. Ulm, F.-J. and Y. Abousleiman, *The nanogranular nature of shale.* Acta Geotechnica, 2006. **1**(2): p. 77-88.

344. Bennett, K.C., et al., *Instrumented nanoindentation and 3D mechanistic modeling of a shale at multiple scales.* Acta Geotechnica, 2015. **10**(1): p. 1-14.

345. Yang, Z., et al. *Micromechanical characterization of fluid-shale interactions via nanoindentation*. in *SPE Asia Pacific Hydraulic Fracturing Conference*. 2016. Society of Petroleum Engineers.

346. Zhang, G., Z. Wei, and R.E. Ferrell, *Elastic modulus and hardness of muscovite and rectorite determined by nanoindentation*. Applied Clay Science, 2009. **43**(2): p. 271-281.

347. Iqbal, M.A., et al., *Shale lithofacies controls on porosity and pore structure: an example from Ordovician Goldwyer Formation, Canning Basin, Western Australia*. Journal of Natural Gas Science and Engineering, 2021: p. 103888.

348. Osselin, F., et al., *Quantifying the extent of flowback of hydraulic fracturing fluids using chemical and isotopic tracer approaches*. Applied Geochemistry, 2018. **93**: p. 20-29.

349. Mahesar, A.A., et al., *Morphological and petro physical estimation of Eocene tight carbonate formation cracking by cryogenic liquid nitrogen; a case study of Lower Indus basin, Pakistan*. Journal of Petroleum Science and Engineering, 2020. **192**: p. 107318.

350. Ohshima, H., T.W. Healy, and L.R. White, *Accurate analytic expressions for the surface charge density/surface potential relationship and double-layer potential distribution for a spherical colloidal particle*. Journal of colloid and interface science, 1982. **90**(1): p. 17-26.

351. Jiu, B., et al., *Growth Mechanism of Siliceous Cement in Tight Sandstone and Its Influence on Reservoir Physical Properties*. Energies, 2018. **11**(11): p. 3133.

352. Zeng, L., et al., *Effect of Pyrite Oxidation on Flowback Water Properties During Hydraulic Fracturing in Calcite-Rich Shales*, in *SPE Asia Pacific Oil & Gas Conference and Exhibition*. 2020, Society of Petroleum Engineers: Virtual. p. 16.

353. Igwe, O. and H. Fukuoka, *The effect of water-saturation on the stability of problematic slopes at the Iva Valley area, Southeast Nigeria*. Arabian Journal of Geosciences, 2015. **8**(5): p. 3223-3233.

354. Li, B., et al., *Shear strength of rock fractures under dry, surface wet and saturated conditions*. Rock Mechanics and Rock Engineering, 2020: p. 1-18.

Appendix

A. Attribution Statement

Zeng, L., Chen, Y., Hossain, M. M., Saeedi, A., & Xie, Q. (2019). Wettability alteration induced water uptake in shale oil reservoirs: A geochemical interpretation for oil-brine-OM interaction during hydraulic fracturing. *International Journal of Coal Geology, 213*, 103277.

Name	Conception and design	Acquisition of data&method	Data conditioning& manipulation	Analysis&statistical method	Interpretation& discussion	Final approval
Lingping Zeng*	✓	✓	✓	✓	✓	✓
Signature:						
Yongqiang Chen				✓	✓	✓
Signature:						
Md Mofazzal Hossain						✓
Signature:						
Ali Saeedi						✓
Signature:						
Quan Xie	✓	✓		✓	✓	✓
Signature:						
I acknowledge that these represent my contribution to the above research output.						

*In this study, I designed the conception and methodology of the geochemical modelling in oil-brine-OM system with my supervisor. I independently conducted all geochemical simulations and derived final data, and interpreted and discussed these data with other authors. I also wrote the manuscript and revised the manuscript based on comments from co-authors and anonymous reviewers.

Zeng, L., Chen, Y., Lu, Y., Lau, H. C., Hossain, M. M., Saeedi, A., & Xie, Q. (2019). Interpreting water uptake by shale with ion exchange, surface complexation, and disjoining pressure. *Energy & Fuels, 33*(9), 8250-8258.

Name	Conception and design	Acquisition of data&method	Data conditioning& manipulation	Analysis&statistical method	Interpretation& discussion	Final approval
Lingping Zeng*	✓	✓	✓	✓	✓	✓
Signature:						
Yongqiang Chen				✓	✓	✓
Signature:						
Yunhu Lu					✓	✓
Signature:						
Hon-Chuang Lau					✓	✓
Signature:						
Md Mofazzal Hossain						✓
Signature:						
Ali Saeedi						✓
Signature:						
Quan Xie	✓			✓	✓	✓
Signature:						
I acknowledge that these represent my contribution to the above research output.						

*In this study, I designed the conception and methodology of the geochemical modelling in gas-brine-shale system with my supervisor. I independently conducted all geochemical simulations and derived final data, and interpreted and discussed these data with other authors. I also wrote the manuscript and revised the manuscript based on comments from co-authors and anonymous reviewers.

Zeng, L., Reid, N., Lu, Y., Hossain, M. M., Saeedi, A., & Xie, Q. (2020). Effect of the fluid–shale interaction on salinity: implications for high-salinity flowback water during hydraulic fracturing in shales. *Energy & Fuels, 34*(3), 3031-3040.

Name	Conception and design	Acquisition of data&method	Data conditioning& manipulation	Analysis&statistical method	Interpretation& discussion	Final approval
Lingping Zeng*	✓	✓	✓	✓	✓	✓
Signature:						
Nathan Reid		✓		✓	✓	✓
Signature:						
Md Mofazzal Hossain						✓
Signature:						
Ali Saeedi						✓
Signature:						
Quan Xie	✓				✓	✓
Signature:						
I acknowledge that these represent my contribution to the above research output.						

*In this study, I designed the conception and methodology with my supervisor. I independently conducted all spontaneous imbibition experiments and measured water chemistry, and interpreted and discussed these data with other authors. I also wrote the manuscript and revised the manuscript based on comments from co-authors and anonymous reviewers.

Zeng, L., Iqbal, M. A., Reid, N., Lagat, C., Hossain, M. M., Saeedi, A., & Xie, Q. (2020, November). Effect of Pyrite Oxidation on Flowback Water Properties During Hydraulic *Fracturing in Calcite-Rich Shales. In SPE Asia Pacific Oil & Gas Conference and Exhibition.* Society of Petroleum Engineers.

Name	Conception and design	Acquisition of data&method	Data conditioning& manipulation	Analysis&statistical method	Interpretation& discussion	Final approval
Lingping Zeng*	✓	✓	✓	✓	✓	✓
Signature:						
Muhammad Atif Iqbal			✓		✓	✓
Signature:						
Nathan Reid				✓	✓	✓
Signature:						
Christopher Lagat				✓		✓
Signature:						
Md Mofazzal Hossain						✓
Signature:						
Ali Saeedi						✓
Signature:						
Quan Xie	✓				✓	✓
Signature:						
I acknowledge that these represent my contribution to the above research output.						

*In this study, I designed the conception and methodology with my supervisor. I independently conducted all spontaneous imbibition experiments and measured water chemistry, and interpreted and discussed these data with other authors. I was in charge

of the initial manuscript drafting and further revising. I also wrote the manuscript and revised the manuscript based on comments from co-authors and anonymous reviewers.

Zeng, L., Chen, Y., Lu, Y., Hossain, M. M., Saeedi, A., & Xie, Q. (2020). Role of brine composition on rock surface energy and its implications for subcritical crack growth in calcite. *Journal of Molecular Liquids*, *303*, 112638.

Name	Conception and design	Acquisition of data&method	Data conditioning& manipulation	Analysis&statistical method	Interpretation& discussion	Final approval
Lingping Zeng*	✓	✓	✓	✓	✓	✓
Signature:						
Yongqiang Chen					✓	✓
Signature:						
Yunhu Lu						✓
Signature:						
Md Mofazzal Hossain						✓
Signature:						
Ali Saeedi						✓
Signature:						
Quan Xie	✓			✓	✓	✓
Signature:						
I acknowledge that these represent my contribution to the above research output.						

*In this study, I designed the conception and methodology of the physicochemical modelling by linking surface potential to surface energy to predict micro-fracture propagation. I independently conducted all geochemical simulations and derived final data, and interpreted and discussed these data with other authors. I also wrote the manuscript and revised the manuscript based on comments from co-authors and anonymous reviewers.

Zeng, L., Lu, Y., Al Maskari, N. S., Chen, Y., Hossain, M. M., Saeedi, A., ... & Xie, Q. (2020). Interpreting micromechanics of fluid-shale interactions with geochemical modelling and disjoining pressure: Implications for calcite-rich and quartz-rich shales. *Journal of Molecular Liquids, 319*, 114117.

Name	Conception and design	Acquisition of data&method	Data conditioning& manipulation	Analysis&statistical method	Interpretation& discussion	Final approval
Lingping Zeng*	✓	✓	✓	✓	✓	✓
Signature:						
Yunhu Lu					✓	✓
Signature:						
Nasser S. Al Maskari					✓	✓
Signature:						
Yongqiang Chen				✓	✓	✓
Signature:						
Md Mofazzal Hossain						✓
Signature:						
Ali Saeedi						✓
Signature:						
Jeremie Dautriat						✓
Signature:						
Quan Xie	✓	✓		✓	✓	✓
Signature:						

I acknowledge that these represent my contribution to the above research output.

*In this study, I designed the conception and methodology with my supervisor on the physicochemical modelling to interpret impact of fluid-rock interactions on shale mechanical properties. I independently conducted all geochemical simulations and derived final data, and interpreted and discussed these data with other authors. I also wrote the manuscript and revised the manuscript based on comments from co-authors and anonymous reviewers.

B. Copyright Agreement

The Copyright Agreements between the journals and author to reuse the published papers in this thesis are listed as following.

Role of brine composition on rock surface energy and its implications for subcritical crack growth in calcite

Author: Lingping Zeng,Yongqiang Chen,Yunhu Lu,Md Mofazzal Hossain,Ali Saeedi,Quan Xie

Publication: Journal of Molecular Liquids

Publisher: Elsevier

Date: 1 April 2020

© 2020 Published by Elsevier B.V.

Interpreting micromechanics of fluid-shale interactions with geochemical modelling and disjoining pressure: Implications for calcite-rich and quartz-rich shales

Author: Lingping Zeng,Yunhu Lu,Nasser S. Al Maskari,Yongqiang Chen,Md Mofazzal Hossain,Ali Saeedi,Jeremie Dautriat,Quan Xie

Publication: Journal of Molecular Liquids

Publisher: Elsevier

Date: 1 December 2020

© 2020 Elsevier B.V. All rights reserved.

Copyright Clearance Center | Marketplace™

Society of Petroleum Engineers (SPE) - License Terms and Conditions

Order Date	23-Feb-2021	Type of Use	Republish in a thesis/dissertation
Order license ID	1099351-1	Publisher	Society of Petroleum Engineers
ISBN-13	9781613997093	Portion	Chapter/article

LICENSED CONTENT

Publication Title	Asia Pacific Oil & Gas Conference and Exhibition (20APOG)	Country	United States of America
		Rightsholder	Society of Petroleum Engineers (SPE)
Date	01/01/2020	Publication Type	e-Book
Language	English		

REQUEST DETAILS

Portion Type	Chapter/article	Rights Requested	Main product
Page range(s)	SPE-202322-MS	Distribution	Worldwide
Total number of pages	16	Translation	Original language of publication
Format (select all that apply)	Electronic	Copies for the disabled?	No
Who will republish the content?	Academic institution	Minor editing privileges?	No
Duration of Use	Life of current and all future editions	Incidental promotional use?	No
Lifetime Unit Quantity	Up to 499	Currency	AUD

NEW WORK DETAILS

Title	Effect of Pyrite Oxidation on Flowback Water Properties During Hydraulic Fracturing in Calcite-Rich Shales	Institution name	Curtin University
		Expected presentation date	2021-03-10
Instructor name	Lingping Zeng		

ADDITIONAL DETAILS

Order reference number	N/A	The requesting person / organization to appear on the license	Lingping Zeng, Curtin University

REUSE CONTENT DETAILS

Title, description or numeric reference of the portion(s)	Asia Pacific Oil & Gas Conference and Exhibition (20APOG)	Title of the article/chapter the portion is from	Effect of Pyrite Oxidation on Flowback Water Properties During Hydraulic Fracturing in Calcite-Rich Shales
Editor of portion(s)	N/A		
Volume of serial or monograph	N/A	Author of portion(s)	Lingping Zeng
Page or page range of portion	SPE-202322-MS	Issue, if republishing an article from a serial	N/A
		Publication date of portion	2020-01-01